For Reference

NOT TO BE TAKEN FROM THIS ROOM

Ex libris
universitatis
albertaensis

QUAECUMQUE VERA

THE UNIVERSITY OF ALBERTA

VOLTAMMETRY OF SOME METALLOPORPHYRINS

by

© SCOTT HINMAN

A THESIS

SUBMITTED TO THE FACULTY OF GRADUATE STUDIES AND RESEARCH
IN PARTIAL FULFILMENT OF THE REQUIREMENTS FOR THE DEGREE
DOCTOR OF PHILOSOPHY

DEPARTMENT OF CHEMISTRY

EDMONTON, ALBERTA

FALL, 1983

Digitized by the Internet Archive
in 2023 with funding from
University of Alberta Library

https://archive.org/details/Hinman1983

ABSTRACT

The electrochemistry of some zinc, manganese, and iron complexes of meso-tetraphenylporphin at oxidizing potentials has been investigated by cyclic voltammetry and thin layer spectroelectrochemistry. The anodic reactions of the complexes investigated appear to be associated with the porphyrin ligand rather than the central metal atom. One-electron oxidation at a Pt electrode in non-coordinating solvents such as dichloromethane results in general in the formation of stable π-cation radicals. Abstraction of a single electron from the complex acetatotetraphenylporphinatomanganese(III) is followed by homogeneous reactions which lead eventually to the formation of an acetoxyisoporphyrin cationic complex.

Removal of an electron from the π-cation radical complexes results in the formation of π-dications. These are powerful electrophiles and may react further with neutral or anionic nucleophiles to yield isoporphyrin cations. In all cases, the formation of isoporphyrin complexes leads to the appearance of a new reversible anodic wave and a new irreversible cathodic wave in the cyclic voltammetry of the porphyrin complexes. The new voltammetric waves should prove to be useful diagnostic criteria for the involvement of isoporphyrin formation in studies of porphyrin electrochemistry.

During the course of the work, some electrochemical methodology was developed which is promising for porphyrin electrochemical studies in particular, and organic and bioelectrochemistry in general. Semi-quantitative calculations of the resistance-induced potential distribution at thin layer electrodes were performed, and these led to the design of a thin layer cell which allows the use of potential sweep rates an order of magnitude greater than those normally used in thin layer voltammetry, even when working in highly resistive media. The use of specular reflectance spectroscopy to monitor the ac voltammetric response is discussed, and the application of this technique to the determination of heterogeneous charge transfer rate parameters is illustrated.

ACKNOWLEDGEMENTS

Special thanks are due to the many members of the Chemistry Department at the University of Alberta, and especially the members of my supervisory committee, who contributed to my education and offered helpful advice throughout this work.

Thanks also go to Kathy and Pamela, who remembered who I was when I came home.

Financial support from the Alberta Heritage Foundation for Medical Research during the last two years this work was conducted is gratefully acknowledged.

TABLE OF CONTENTS

CHAPTER PAGE

1. INTRODUCTION AND BACKGROUND MATERIAL ON THE PORPHYRINS.......... 1
    - 1.1 Introduction.......... 1
    - 1.2 Structure and Nomenclature of Porphyrins and Their Metal Complexes.......... 7
    - 1.3 Primary Redox Behaviour of Porphyrins and Metalloporphyrins.......... 14
    - 1.4 Coordination Chemistry of Manganese Porphyrins.......... 22
        - 1.4.1 Mn(III) Porphyrins.......... 23
        - 1.4.2 Mn(II) Porphyrins.......... 32
        - 1.4.3 Mn(IV) and Mn(V) Porphyrins.......... 33

2. EXPERIMENTAL.......... 36
    - 2.1 Preparation of Compounds.......... 36
        - 2.1.1 Zn(II)TPP.......... 36
        - 2.1.2 $(CH_3CO_2)Mn(III)TPP$.......... 37
        - 2.1.3 XMn(III)TPP; X = Cl^-, Br^-, I^-, ClO_4^-, $CF_3CO_2^-$.......... 38
        - 2.1.4 $(CH_3O)Mn(III)TPP$.......... 42
        - 2.1.5 $(Et4N^+)(CH_3CO_2^-)$, $(Me_4N^+)(CF_3CO_2^-)$.......... 44
    - 2.2 Electrochemical Experiments.......... 45

CHAPTER PAGE

2.2.1 Reference Electrodes.................. 45
2.2.2 Electrochemical Cell for Voltammetric Experiments........................... 46
2.2.3 Solvents, Supporting Electrolytes and Other Reagents........................ 48
2.2.4 Electrochemical Instrumentation....... 52
2.2.5 Transmission Spectroelectrochemistry.. 54
2.2.6 Other Experiments.................... 56

3. VOLTAMMETRY AND COULOMETRY AT IMMERSED THIN LAYER ELECTRODES.. 57
3.1 Introduction.............................. 57
3.2 Linear Sweep Voltammetry at Thin Layer Electrodes................................. 62
3.3 Effects of Solution Resistance on the Thin Layer Voltammetric Response................. 66
3.4 Experimental.............................. 86
3.5 Results and Discussion.................... 90
3.6 Chronocoulometry at Immersed Thin Layer Electrodes................................. 104

4. ALTERNATING CURRENT METHODS........................ 108
4.1 Introduction.............................. 108
4.2 Background to AC Voltammetry................. 112

CHAPTER PAGE

4.3 Spectroscopic Determination of the AC Voltammetric Response........................ 122
4.4 Results and Discussion........................ 139
4.5 Electrochemical Cell and Instrumentation for SMACRS................................ 153
4.6 AC Voltammetry With Background Correction.... 160
4.7 AC Voltammetry With Background Subtraction... 161

5. STANDARD HETEROGENEOUS RATE CONSTANTS FOR SOME PORPHYRIN/PORPHYRIN CATION-RADICAL REDOX COUPLES.. 173
5.1 Experimental and Results...................... 173
5.2 Discussion.................................... 177

6. REACTIVITY OF ZINC (II) TETRAPHENYLPORPHYRIN CATIONS TOWARD ANIONIC NUCLEOPHILES........................ 183
6.1 Introduction.................................. 183
6.2 Results and Discussion........................ 189

7. ANODIC VOLTAMMETRY OF MANGANESE[III] TETRAPHENYLPORPHYRIN COMPLEXES 209
7.1 Voltammetry of XMn(III)TPP; X = ClO_4^-, CH_3O^-.. 209
7.2 Voltammetry of XMn(III)TPP; X = Cl^-, $CF_3CO_2^-$...................................... 217
7.3 Voltammetry of (CH_3CO_2)Mn(III)TPP........... 234

CHAPTER PAGE

7.4 Voltammetry of XMn(III)TPP; X = I^-, Br^-...... 249

8. CONCLUDING REMARKS.............................. 253

*****

BIBLIOGRAPHY.. 256

APPENDIX 1. BACKGROUND INFORMATION ON ELECTRODE KINETICS................................. 269

APPENDIX 2. CHRONOCOULOMETRY......................... 276

APPENDIX 3. CYCLIC VOLTAMMETRY....................... 280

APPENDIX 4. THE PROGRAM "THNLAY"...................... 287

LIST OF TABLES

TABLE PAGE

1. Substitution patterns and common names of some etio-type porphyrins.............................. 9

2. Electronic absorption spectra of Mn(III)TPP$^+$ complexes.................................... 40

3. Elemental analysis of Mn(III)TPP$^+$ complexes....... 42

4. Standard Rate Constants for the $Fe(CN)_6^{-3}/Fe(CN)_6^{-4}$ redox couple.................. 172

5. Heterogeneous rate constants for some metalloporphyrin complexes......................... 174

LIST OF FIGURES

FIGURE PAGE

1. Out of plane displacement in manganese porphyrins.................................... 25
2. Energy level ordering of d orbitals in manganese porphyrins.................................... 26
3. (a) Electronic absorption spectra of ClMn(III)TPP.................................... 29
   (b) Electronic absorption spectra of Zn(II)TPP.. 30
4. Saturated calomel reference electrode........... 46
5. Electrochemical cell for voltammetry............ 47
6. Electronic absorption spectra of $(CH_3CO_2)Mn(III)TPP$.................................... 51
7. Thin layer spectroelectrochemical cell.......... 55
8. Rectangular thin layer geometry................. 67
9. Optically transparent thin layer electrode...... 69
10. Radial thin layer geometry...................... 70
11. Solution resistance in radial thin layer electrode.................................... 73
12. Model for potential distribution................ 74
13. Effect of vertical dimension on calculated thin layer voltammograms.................................... 78
14. Comparison of thin layer response at OTTLE and radial thin layer electrodes................ 79

FIGURE PAGE

15. Effect of solution resistance on thin layer response.................................... 80
16. Effect of electrode radius on thin layer response.................................... 81
17. Effect of displacing Luggin capillary............ 82
18. Details of thin layer electrode assembly......... 97
19. Thin layer cyclic voltammetry and potential scanning coulometry of ferrocyanide.............. 91
20. Charge vs concentration for ferrocyanide oxidation at thin layer electrode................ 93
21. Thin layer cyclic voltammetry of ferrocene....... 95
22. Thin layer cyclic voltammetry of Zn(II)TPP....... 97
23. Potential scanning coulometry of Zn(II)TPP....... 98
24. Effect of scan rate on apparent electrolysis charge.. 100
25. Thin layer cyclic voltammetry of I^-.............. 101
26. Charge vs concentration for oxidation of I^-...... 103
27. Thin layer chronocoulometry for oxidation of (ClO_4)Mn(III)TPP................................ 106
28. The Randles equivalent circuit.................... 119
29. The coordinate system in specular reflectance spectroscopy.................................... 128
30. Phase relations in SMACRS........................ 135
31. SMACRS for ferrocyanide........................... 141

FIGURE PAGE

32. Cot ϕ data for ferro-ferricyanide redox couple.................................... 144

33. SMACRS for ClMn(III)TPP.............................. 146

34. SMACRS for DPA.. 147

35. Cot ϕ data for DPA/DPA$^{+\bullet}$redox couple............. 149

36. SMACRS for perylene.................................. 152

37. Electrochemical cell used for SMACRS experiments.................................... 154

38. Instrumentation for SMACRS........................ 155

39. Phase selective ac voltammograms of $(ClO_4)Mn(III)TPP$................................. 163

40. Method-induced error in ac voltammetry with direct background subtraction.................... 168

41. Cyclic voltammetry of Zn(II)TPP.................. 185

42. Reaction paths for $Tl(CF_3CO_2)_3$ oxidation of Zn(II)TPP.. 187

43. Cyclic voltammetry of Zn(II)TPP.................. 190

44. Cyclic voltammetry of Zn(II)TPP in the presence of TMATFA.............................. 193

45. Spectral changes on oxidation of Zn(II)TPP in the presence of TMATFA.......................... 197

46. Thin layer cyclic voltammetry of Zn(II)TPP in the presence of TMATFA.......................... 200

FIGURE PAGE

47. Steady state thin layer voltammetry of Zn(II)TPP in the presence of TMATFA.............. 202

48. Reaction scheme for oxidation of Zn(II)TPP in the presence of TMATFA........................... 205

49. Cyclic voltammetry of Zn(II)TPP in the presence of acetate................................ 206

50. Reaction scheme for oxidized Zn(II)TPP in the presence of acetate................................ 208

51. Cyclic voltammetry of (ClO_4)Mn(III)TPP........... 210

52. Visible spectral changes on oxidation of (ClO_4)Mn(III)TPP................................... 212

53. Near-IR spectral changes on oxidation of (ClO_4)Mn(III)TPP in the presence of H_2O.......... 214

54. Cyclic voltammetry of (ClO_4)Mn(III)TPP in the presence of CH_3OH................................. 215

55. Cyclic voltammetry of (CH_3O)Mn(III)TPP........... 216

56. Cyclic voltammetry of ClMn(III)TPP............... 218

57. Reaction scheme for ClMn(III)TPP and oxidized forms... 222

58. Cyclic ac voltammetry for ClMn(III)TPP........... 224

59. Spectral changes on oxidation of ClMn(III)TPP.... 227

60. Cyclic voltammetry of ClFe(III)TPP............... 228

61. Cyclic voltammetry of (CF_3CO_2)Mn(III)TPP......... 231

FIGURE PAGE

62. Spectral changes on oxidation of $(CF_3CO_2)Mn(III)TPP$ 234

63. Cyclic voltammetry of $(CH_3CO_2)Mn(III)TPP$ in methylene chloride 235

64. Cyclic voltammetry of $(CH_3CO_2)Mn(III)TPP$ in nitrobenzene 238

65. Thin layer cyclic voltammetry of $(CH_3CO_2)Mn(III)TPP$ in dichloroethane 239

66. Reaction scheme for $(CH_3CO_2)Mn(III)TPP$ and oxidized forms 241

67. Visible spectral changes on oxidation of $(CH_3CO_2)Mn(III)TPP$ 243

68. Near-IR spectral changes on oxidation of $(CH_3CO_2)Mn(III)TPP$ 244

69. Cyclic voltammetry of $(CH_3CO_2)Fe(III)TPP$ 246

70. Cyclic voltammetry of IMn(III)TPP 250

71. Cyclic voltammetry of BrMn(III)TPP 252

72. Chronocoulometry of ferrocyanide 279

73. Cyclic voltammetry of $(CF_3CO_2)Mn(III)TPP$ recorded in Y-t mode 284

CHAPTER 1

INTRODUCTION AND BACKGROUND MATERIAL ON THE PORPHYRINS

1.1 Introduction

The literature dealing with various aspects of the chemistry of porphyrins and their metal complexes is vast. Most of the research carried out on these compounds has had as its objective a better understanding of their numerous and diverse biochemical functions. Metalloporphyrins, or the structurally similar metallochlorins, are intimately involved in photosynthesis and respiration. In many organisms, they play key roles in the transport, storage, and activation of dioxygen. Iron-porphyrin-containing proteins are important mediators in the biochemistry of peroxide. It is clear that because of the biochemical significance of the porphyrins, the importance of a clear understanding of their chemistry cannot be overestimated. Two excellent and reasonably current sources of information dealing with the chemistry of porphyrins and metalloporphyrins are the book edited by Smith [1] and the seven volume collection edited by Dolphin [2].

Fuhrhop [3] has noted that the biological role of metalloporphyrins invariably involves some aspect of their redox behaviour. As such, a significant portion of the porphyrin literature treats their redox reactions and several reviews of the subject are available [3-6].

Much of our understanding of the redox behaviour of porphyrins has come from studies utilizing modern voltammetric methods, especially cyclic voltammetry. The latter technique has proven of value in the elucidation of factors affecting redox potentials [7], in studies involving the ligation of species other than the porphyrin ring to the central metal atom [8], and in studies of the heterogeneous charge transfer kinetics of metalloporphyrins [9-11].

More recently, electrochemists have become interested in the possibility of utilizing porphyrins, or the closely related phthalocyanines, as catalysts for the electroreduction of O_2 [12]. The interest arises from the involvement of oxygen in energy conversion/storage systems, i.e. fuel cells. To this end, a number of studies [12] have appeared which treat the electrochemical reduction of O_2 in the presence of soluble metalloporphyrins, or at electrodes modified by either adsorbing or covalently bonding the proposed catalyst to the surface.

A particularly interesting and rapidly growing area of porphyrin chemistry relates to the ability of a number of metalloporphyrins to catalyze the oxidation of hydrocarbons to alcohols, ketones, or epoxides [13-23]. Much of the work has been directed at the development of systems which model the action of cytochrome P-450 [18-21], an iron porphyrin containing protein which displays such catalytic activity in biological systems. Other workers have not overlooked the industrial significance of catalysts for the functionalization of hydrocarbons [16,17].

Of the metalloporphyrins which have been studied with respect to their ability to promote hydrocarbon oxidation, manganese porphyrins perhaps hold the greatest promise. The substrates in most of the studies to date have contained isolated double bonds and may thus be considered activated towards functionalization. Manganese porphyrins, however, have been shown to effect the oxidation of inert alkanes such as cyclohexane [22] and adamantane [20]. For instance, Hill et al. [22] have shown that, in the presence of the powerful oxidant iodosylbenzene, chloro-tetraphenylporphinatomanganese(III) (TPPMnCl) brings about the catalytic conversion of cyclohexane to cyclohexanol and cyclohexyl chloride.

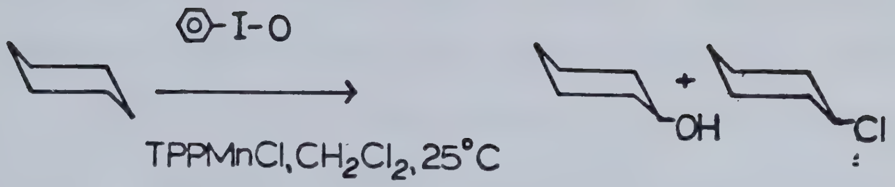

(1)

Such reactions are believed to involve the transfer of an oxygen atom to the substrate from a porphyrin containing high valent manganese, either Mn(IV) [23,24] or Mn(V) [21].

There exists no a priori reason why such high-valent catalytically active species cannot be produced electrochemically. Because of the additional control afforded in electrochemical as opposed to homogeneous reactions [25,26], the prospect of such an accomplishment is particularly attractive from a synthetic viewpoint. In addition, a long-standing problem in electrochemistry is the high overpotential required at the oxygen electrode during the electrolysis of water to H_2 and O_2 [25]. Manganese, in some form, has been shown to play a role in the oxidative decomposition of water during photosynthesis [27], and Mn(IV) porphyrin complexes have been at least partially successful models in this regard [28,30]. The

electrochemical production of such species thus holds some promise for the electrocatalytic oxidation of water.

It was the considerations of the previous paragraph which originally led to the studies undertaken in this work. At the same time, however, it was realized that our understanding of the electrochemical behaviour of metalloporphyrins is far from being complete enough to provide much rationale with which to approach such a problem. The literature dealing with the anodic behaviour of metalloporphyrins is sparse. In the few cases [7,11,35] where manganese porphyrins have been treated, oxidation has been reported to occur at the porphyrin ring, and not the central metal atom. It was proposed, then, to carry out studies of a more fundamental nature directed at characterizing some of the anodic chemistry of manganese porphyrins, and it was hoped that such efforts would contribute to a greater overall understanding of metalloporphyrin redox chemistry.

The stable oxidation state of the metal, i.e. that which is found under aerobic conditions, in manganese and the closely related but biologically more important iron porphyrins, is +3. Since the porphyrin ligand contributes a net charge of -2, a counterion is always present in accordance with the rules of electroneutrality. In poorly coordinating solvents, the counterion is in general bound

to the central metal atom. A prime objective of this work was to elucidate some of the effects which the counterion might exert on the electrochemistry, and in particular, on the anodic voltammetry of metalloporphyrins.

Because the majority of available metalloporphyrins are soluble only in nonaqueous solvents, and so that coordination of the counterion to the central metal atom could be ensured, most of the work has been carried out in solvents of low dielectric constant and donor number. Electrochemical studies in such poorly conducting media are difficult. In addition to problems associated with high solution resistivity, solvent purity is often suspect. Because the work deals largely with anodic electrochemistry, solid electrodes have been used exclusively. These present several disadvantages with respect to the easily renewable and reproducible mercury electrode surface.

The problems associated with the application of electrochemical techniques at solid electrodes and in non-aqueous media have been confronted in this work to some extent, and the first part of this thesis treats the development and application of some methodology which partially alleviates some of the difficulties. The methods were designed specifically with porphyrin electrochemistry in mind, but are applicable in general

and hold great promise for organic and bioelectrochemistry in particular.

1.2 Structure and Nomenclature of Porphyrins and Their Metal Complexes

This section is intended to provide a brief introduction to the chemistry, structure, and nomenclature of porphyrins as they apply to this work. More complete discussions of what follows may be found in reference 1.

The term porphyrin applies to any compound derived by peripheral substitution of the parent compound porphin (I). Porphin itself consists of four pyrrole units linked at their α-positions by methine bridges. Under the classical system of nomenclature, which is still in common use, the β-pyrrole positions are numbered 1-8, while the meso positions, i.e. the methine bridges, are designated by the Greek letters α, β, γ, δ.

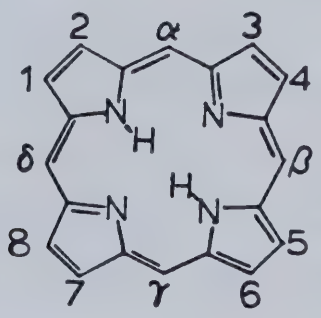

I

Derivatives of porphin containing alkyl substituents at the β-pyrrole positions are commonly referred to as etio-type porphyrins. These have common names formed by attaching a prefix to the word porphyrin. Where different isomers may be formed by interchanging the positions of two or more substituents, a Roman numeral included as a suffix designates a particular isomer. Protoporphyrin IX, for instance, refers to one of the most common naturally occurring porphyrins. Table 1 (adapted from reference 3) provides a listing of prefixes and substitution patterns of some of the etio-type porphyrins most frequently encountered in the literature.

Those porphyrins bearing substituents only at the four methine bridges are referred to as meso-type porphyrins. The four substituents are most commonly derivatives of benzene or pyridine. The parent compound of this family of porphyrins, α-β-γ-δ tetraphenylporphin (II) is commercially available in high purity at relatively low cost. The Greek letters designating the positions of the substituents are commonly neglected in much of the literature and will be in the rest of this work. Where the compound name indicates the presence of four identical substituents, it is understood that these occur at the meso positions unless information to the contrary is provided. Thus tetra-(4-pyridyl)porphin

Table 1

Substitution Patterns and Common Names of Some Etio-type Porphyrins

	Position							
Porphyrin	1	2	3	4	5	6	7	8
Proto-IX	Me	Vi	Me	Vi	Me	Pr	Pr	Me
Deutero-IX	Me	H	Me	H	Me	Pr	Pr	Me
Meso-IX	Me	Et	Me	Et	Me	Pr	Pr	Me
Haemato-IX	Me	ROH	Me	ROH	Me	Pr	Pr	Me
Octaethyl	Et	Et	Et	Et	Et	Et	Et	Et
Etio-I	Me	Et	Me	Et	Me	Et	Me	Et

Me = Methyl

Vi = Vinyl

Pr = Propionic acid

Et = Ethyl

ROH =
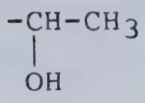
$-\underset{\underset{\displaystyle OH}{|}}{CH}-CH_3$

indicates four pyridine substituents at the meso positions with the pyridine nitrogens four atoms removed from the point of attachment of the pyridine ring to the porphyrin skeleton.

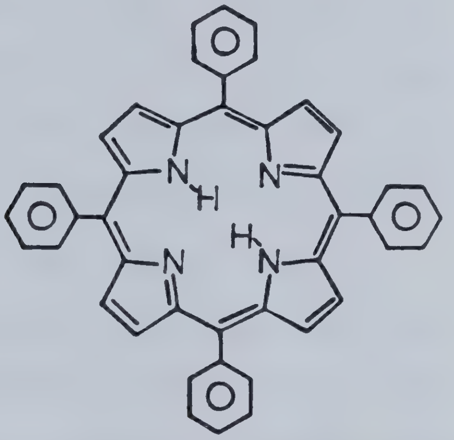

II

The porphin nucleus contains twenty-two π-electrons, but only eighteen of these can be included in any single cyclic conjugation path. The porphyrins are therefore aromatic in accordance with Huckel's 4n + 2 rule. Aromatic substituents in meso-type porphyrins such as tetraphenylporphin (TPP H_2) are in general rotated 60 to 90° [31] with respect to the plane of the porphyrin core due to steric interaction between the ortho-hydrogens of the phenyl substituents and the β-pyrrolic hydrogens of the porphyrin ring. The phenyl groups are therefore excluded from any conjugative interaction with the porphyrin core.

The non-metallated, or free base, porphyrins are amphoteric. They can either consecutively lose or accept two protons. The N-H protons are only very weakly acidic, with pK_a values of the order +16 [32]. This in part accounts for the very slow rates observed in most metal incorporation reactions. On the other hand, both the mono- and di-protonated forms are readily formed with pK_a's in the range 2 to 4 [33].

The porphyrin dianions resulting from the loss of two protons form complexes with metal ions in so-called metal insertion reactions to yield metalloporphyrins. By 1974, successful insertion reactions had been performed with 56 metals or metalloids [34]. These include the alkali metals Li through Cs, the alkaline earths Mg through Ba, all of the transition metals, a number of lanthanides and actinides, all the metals of groups IIIA, IVA, and VA, and a number of metalloids such as B, Si, and As.

The metalloporphyrins often contain metals in unusual stable oxidation states (Os(VI), Ag(II), Mn(III) for instance), and a particularly wide variety of metal coordination environments is available. Buchler [34] has proposed a classification scheme for coordination type based on stoichiometry and stereochemistry, and at least 26 of these coordination types have been observed. The coordination chemistry of metalloporphyrins as it relates to this work will be discussed in subsequent sections.

There are a number of structurally related compounds which are either directly related to the porphyrins through redox reactions, or which have contributed to our understanding of porphyrin redox chemistry through comparative methodology.

The term chlorin (III) refers to the structure obtained on addition of two hydrogen atoms to the β positions of a porphyrin pyrrole unit. The redox chemistry of the chlorins is of singular importance because of their involvement in green plant photosynthesis. The chlorophylls a and b are magnesium-chlorin complexes. Note that although these complexes contain only 20 π-electrons, an eighteen electron inner conjugation path remains and the aromaticity of the ring is undisturbed.

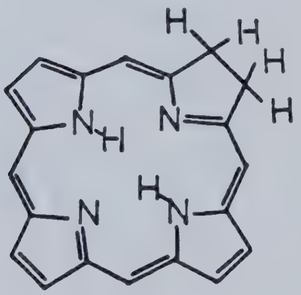

III

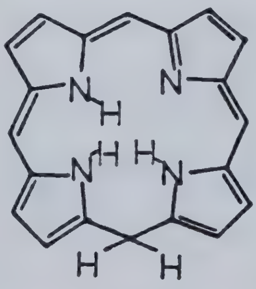

IV

Phlorin (IV), like chlorin, is a dihydroporphyrin. Here, however, hydrogen addition has occurred at one of the pyrrole nitrogens and at a meso-carbon. This results

in the interruption of the cyclic conjugation path, and the phlorins are therefore not aromatic in the same sense as the porphyrins. Iron-phlorin complexes are believed to be intermediates in the catabolism of porphyrins leading to the formation of bile pigments. Other commonly encountered structures where conjugation of the inner macrocyclic ring is interrupted include the dihydroporphyrin porphodimethene (V) and the hexahydro derivative porphyrinogen (VI).

A great deal of work has been done on the redox chemistry of the phthalocyanines (VII) and their metal complexes. Comparisons of the redox chemistry of the porphyrins and the phthalocyanines have provided information concerning how different metal oxidation

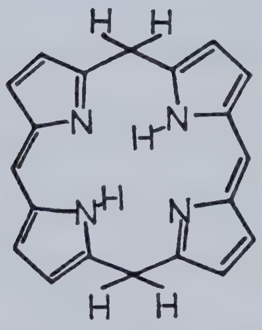

V

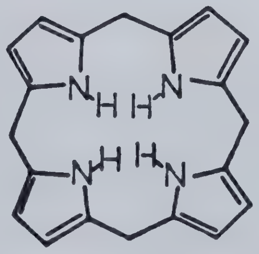

VI

states are stabilized within the ligand cavity [7,34]. The tetrabenzoporphyrins (VIII) are closely related to the phthalocyanines. The phthalocyanines are commercially

important dyestuffs [36] and have implications as catalysts for the electroreduction of O_2 [12].

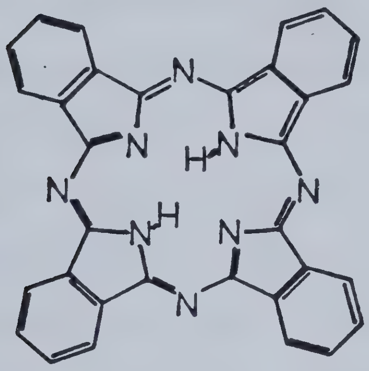

VII

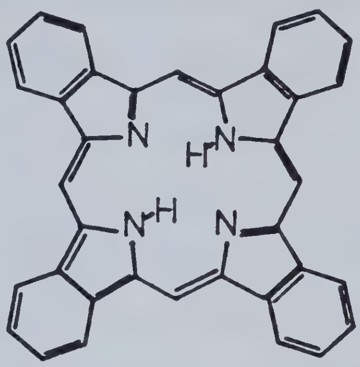

VIII

1.3 Primary Redox Behaviour of Porphyrins and Metalloporphyrins

As previously noted, several reviews [3-6] have appeared concerning this topic. These, and in particular reference 3, are recommended for more detailed information concerning the following discussion.

The free base, or metal-free, porphyrins may be oxidized in successive one-electron steps to yield first a π-radical and then a π-dication. The first process occurs at ca 1 volt vs SCE, depending on the particular

porphyrin, and the second process is generally found at about .3 volts more anodic [3]. While the cation radicals of substituted etio- or meso-type porphyrins are stable for extended periods of time, the cation radical of porphin itself is reported to polymerize rapidly [3]. The stability of the cation radicals may therefore be attributed in part to steric shielding of the porphyrin periphery by the various substituents. In contrast to the cation radicals, the porphyrin π-dications are powerful electrophiles and react rapidly with nucleophiles such as water or methanol [37].

Reduction of free base porphyrins leads to production of, first, an anion radical, generally at potentials ca -1 volt vs SCE. These can be further reduced to dianions at potentials ca .4 volts more cathodic. The reduced species are generally not as stable as the corresponding cationic species, and both the anion-radical and dianion have been observed to abstract protons [38] from solvents such as dimethylformamide (DMF).

The effect of substituents at the porphyrin periphery on the redox potentials may be predicted from the normal arguments concerning inductive effects. Thus, electron-withdrawing groups shift the potentials anodically, while electron-donating substituents have the opposite effect. It has also been noted [3] that the introduction of large

substituents which disturb the planarity of the ring through steric interactions, as is the case with the meso-aryl porphyrins, tends to shift the oxidative and reductive processes of the porphyrin ring to more anodic potentials.

In metalloporphyrins, the effect exerted by the central metal on the potentials of porphyrin ring reductions and oxidations is also believed to be inductive in nature. In the case of the simple +2 metal ions (e.g. Ba^{+2}, Mg^{+2}, Zn^{+2}, Pd^{+2}), plots of voltammetric half-wave potentials for either the first ring reductions or the first ring oxidations vs the Pauling electronegativity of the metal are linear [39]. In the case of +3 or +4 (e.g. Pb(IV), Sn(IV), Sb(III)) metal ions, the effect of the metal on the ring redox potentials is much more pronounced, and no simple correlation between $E_{1/2}$ values and metal property has been found. Assuming that the effect is still largely electrostatic in nature, Fuhrhop et al. [39] have used $E_{1/2}$ values to empirically evaluate a metal inductive parameter h, analogous to Pauling's electronegativities, which may be used to predict the midpoint potential of the various redox reactions associated with the porphyrin ring.

In a number of cases both the central metal atom and the porphyrin ring are capable of participation in charge

transfer reactions. The question of whether a particular charge transfer process is associated with the π-system of the porphyrin ligand or involves a change in oxidation state of the metal ion is an important one. The chemistry of the species produced via an electron transfer can be expected to be very different depending on whether the resultant charge is delocalized through the porphyrin π-system or centered at the metal. Where oxidation is involved, Hoff and Reed have noted [44] that the highest occupied molecular orbitals of the porphyrin ligand do not have the proper symmetry to overlap with any of the metal d orbitals, and the possibility of any sort of resonance hybrid existing where a positive charge is delocalized through metal as well as ligand π-orbitals may therefore be excluded.

The behaviour of the nickel complex of tetraphenylporphyrin (Ni(II)TPP) is especially interesting. In benzonitrile [40,41] this complex undergoes 1-electron electrochemical oxidation to a species whose esr spectrum indicates the presence of high spin Ni(III). On cooling to liquid nitrogen temperatures, this esr spectrum disappears over a matter of hours while a new one characteristic of a π-cation radical appears. In methylene chloride, the temperature dependence is reversed [42]. That is, at room temperature $Ni(II)TPP^{+\bullet}$

is formed while cooling yields Ni(III)TPP. This behaviour illustrates that intramolecular charge transfer between the porphyrin π-system and the metal ion can occur, but the two species are spectrally distinct. The process is best represented as an equilibrium, and not as a resonance process, underscoring the reality of the distinction between metal centered and ring centered oxidation. A similar equilibrium involving intramolecular charge transfer has been observed on oxidation of the iron(II) complex of tetrabenzoporphyrin [43].

During the late 1960's and early 1970's a great deal of attention was directed to the matter of assigning a particular redox process to the porphyrin ring or the central metal atom. In certain cases a simple determination of magnetic moment can provide the criteria for distinction. For instance, the Ag(II) complex of octaethylporphyrin (Ag(II)OEP) contains paramagnetic d^9 Ag with an unpaired electron in a metal orbital. Abstraction of an electron from the metal would result in a diamagnetic d^8 species, whereas removal of an electron from a porphyrin π-orbital would produce a paramagnetic species with two unpaired electrons. In fact, diamagnetic Ag(III)OEP is produced upon 1-electron oxidation of Ag(II)OEP [45].

In cases where an esr signal is observable, this can provide information concerning the nature of the product. The esr spectra of porphyrin π-radicals are typical of organic free radicals and have line widths less than 12 G. Unpaired spin centered at the metal, however, gives rise to linewidths >50 G. It is a general observation that no esr signal is obtained when both the metal and the porphyrin ligand contain unpaired spin density.

Electronic absorbance spectra can be used in many cases to ascertain the nature of the product. The "normal" metalloporphyrin spectrum consists of a very sharp and intense (ε ca 10^5 $M^{-1}cm^{-1}$) band in the 400 nm vicinity (the Soret band), and two sharp but less intense (ε ca 10^4 $M^{-1}cm^{-1}$) bands in the 500-700 nm region (the α and β bands, α indicating the longer wavelength transition). When such a spectrum is observed for the product of a redox reaction, it may be assumed with certainty that no electrons have been added to or removed from the porphyrin ligand [3]. On the other hand, deviations from this type of spectra do not necessarily imply oxidation or reduction of the porphyrin ring. Neither Mn(III) nor Fe(III) porphyrins display a normal metalloporphyrin spectrum.

The spectra of a number of metalloporphyrin π-cation radicals have been reported. These all possess broadened Soret bands of greatly decreased intensity. A broad and generally featureless absorbance extending through the visible and into the near-IR region of the spectrum is found. In certain cases, apparently depending on the ground state symmetry of the π-cation radical [46], a new strong band around 700 nm appears, but the broad visible absorptions are always present. The appearance of such spectral features has often been used to support π-cation radical formulations.

Voltammetric studes of metalloporphyrins in which redox pairs have been unequivocally identified have led to the observation of so-called electrochemical regularities [39] which can be useful in identifying the product of a charge transfer reaction. These are that the first reduction and oxidation of the porphyrin ligand are separated by 2.25 ± 0.15 volts; the removal of a second electron follows the first by an interval of 0.3 ± 0.1 volts; and the addition of a second electron follows the first by 0.4 ± 0.1 volts.

In all but a very few cases application of the above criteria has led to successful identification of the electron transfer site. The most notable disputed case involves the oxidation of ferric porphyrin complexes.

Based on electronic absorbance spectra, electrochemical regularities, and magnetic susceptibility measurements the 1-electron electrochemical oxidations of ClFe(III)TPP [3,39] and of CH_3CO_2Fe(III)TPP [41] had been ascribed to cation radical formation. Other workers favoured an Fe(IV) formulation. This was based on the observation that the pmr shift of the phenyl protons of the μ-oxo dimer $([Fe(III)TPP]_2O)^+$ was less than that expected by comparison with authentic cation radicals such as $Zn(II)TPP^{+\bullet}$ and $Mg(II)TPP^{+\bullet}$ [5,47]. It was also noted that the observed magnetic moment of the oxidized monomers corresponded to a total spin (S = 2) consistent with the presence of high spin d^4 Fe(IV).

The case for cation-radical formation has recently been reargued based on voltammetric behaviour inconsistent with metal oxidation [48], and on the observation of a strong band at ca 1280 cm^{-1}, supposedly diagnostic of meso-tetraarylporphyrin π-cation radicals, in the oxidized products of ClFe(III)TPP and $[Fe(III)TPP]_2O$ [44]. The argument has recently culminated in the appearance of the X-ray structures of oxidized forms of ClFe(III)TPP and ClO_4Fe(III)TPP [49]. The structures of both of these products provide strong evidence for the cation-radical formulation. In addition, the Fe(III) atom of the $[ClFe(III)TPP]^+$ cation was found to lie significantly out

of the plane of the porphyrin nitrogens. This provides a rationalization for the anomalous magnetic moment previously cited for monomer cation radicals, in that the metal $d_{x^2-y^2}$ orbital is now in a position to interact with the porphyrin π-orbitals allowing for anti-ferromagnetic exchange between an unpaired electron on the metal and one associated with the porphyrin. In fact, the magnetic moment of $(ClO_4)_2Fe(III)TPP$, in which the metal was found to lie in the porphyrin plane, was determined to be 6.5 μ_B (S = 3) unequivocally identifying this complex as a porphyrin π-cation radical containing high spin Fe(III). These findings, along with evidence from Mossbauer [50] and NMR [51] measurements, leave little doubt as to the correctness of earlier assumptions that electrochemical oxidation of 5-coordinate Fe(III) porphyrins leads to π-cation radicals.

1.4 Coordination Chemistry of Manganese Porphyrins

The coordination chemistry of manganese porphyrins has been reviewed through 1971 [52]. Most of the early work on manganese porphyrins was carried out because it was felt they might provide models for the manganese dependent evolution of oxygen in green plant photosynthesis. In addition, the abnormal electronic

absorption spectra observed for the Mn(III) porphyrin complexes was supposedly indicative of an unusual electronic structure.

1.4.1 Mn(III) Porphyrins

When Mn(II) salts ($MnX_2 \cdot xH_2O$, X = $CH_3CO_2^-$, Cl^-, etc.) are refluxed with a free base porphyrin under aerobic conditions in a suitable solvent, the corresponding Mn(III) porphyrin complex (XMn(III)P, where P represents the porphyrin ligand) is obtained. The metal insertion reactions do not proceed to any appreciable extent if O_2 is rigorously excluded.

The Mn(III) porphyrins are in general 5-coordinate and contain high spin d^4 manganese. Even coordination of the strong field ligand CN^- does not produce a low spin species [53]. The only known low spin Mn(III) porphyrins are the six-coordinate bis-imidazolate complex $(Im)_2Mn(III)TPP]^-$ [54], and the six-coordinate nitrosyl cyano complex (NO)(CN)Mn(III)TPP [59]. The preference for high spin electronic configurations contrasts sharply with the behaviour of the Fe(III) porphyrins, which may contain either high, low, or intermediate spin iron [55], depending on the nature of the coordination environment.

Several molecular structures [31,53] from X-ray diffraction techniques are now available for Mn(III)

complexes of tetraphenylporphin. In all cases, the manganese atom is displaced from the plane of the porphyrin nitrogens by ca 0.25 Å, as illustrated in Figure 1. The distances shown are taken from an X-ray diffraction study of ClMn(III)TPP [52].

The out of plane distance in the Mn(III) porphyrins is generally just over half of that found in the corresponding high spin Fe(III) complexes. In the iron porphyrins, the metal $d_{x^2-y^2}$ orbital is singly occupied. This is strongly anti-bonding with respect to the occupied sigma orbitals of the porphyrin nitrogens, and the out of plane movement of the metal atom minimizes this unfavourable interaction. In the Mn(III) complexes, however, the $d_{x^2-y^2}$ orbital is unoccupied, and the out of plane position of the metal atom is thought to result from steric interaction between the axial ligand and the porphyrin nitrogens. In ClMn(III)TPP, for instance, the N••Cl distance [31] is nearly equal to the sum of the atomic radii, disallowing closer approach of the chloride to the porphyrin. Interaction between chloride and Mn(III) then draws the metal out of the porphyrin plane.

The out of plane displacement leaves the central metal atom in a distorted square pyramidal coordination environment. Figure 2 illustrates qualitatively the energy level ordering of the individual metal d

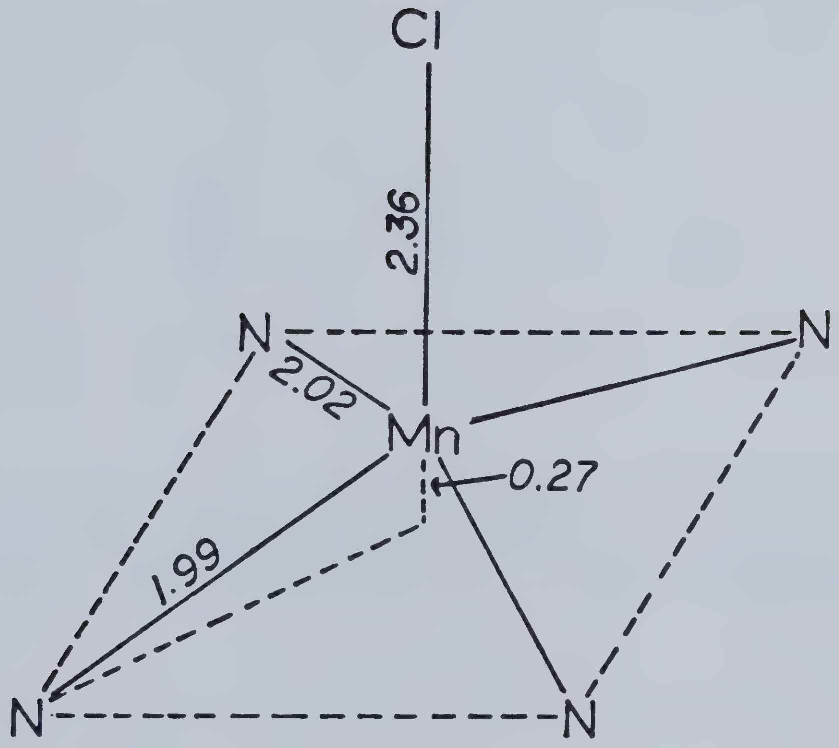
Cl
2.36
N
N
2.02
Mn
0.27
1.99
N
N

Figure 1. Out of plane displacement in ClMn(III)TPP. Bond distances shown are in angstroms.

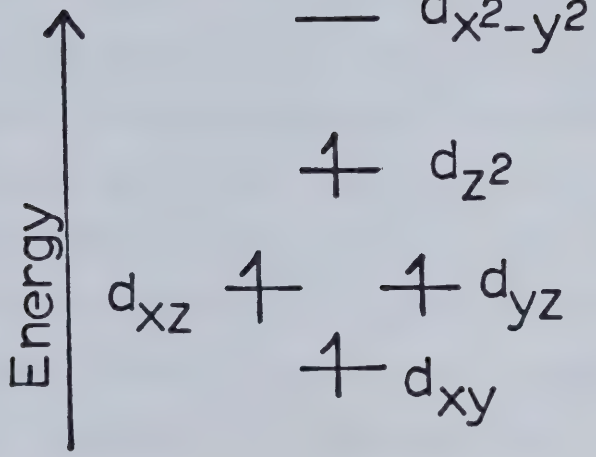
Energy
$d_{x^2-y^2}$
d_{z^2}
d_{xz}
d_{yz}
d_{xy}

Figure 2. Qualitative energy level ordering of d orbitals in 5-coordinate Mn(III) porphyrins. The x and y axes are directed at the porphyrin nitrogens; the z axis is perpendicular to the porphyrin plane.

orbitals. The splitting of the higher energy e_g orbitals is identical to that found in square planar configurations and arises from the same effect. Removal of a ligand on the z-axis results in a lowering of the d_{x^2} orbital energy and an accompanying increase in the energy of the $d_{x^2-y^2}$ orbital. The splitting of the lower energy e_g orbitals, however, is not that which might be expected by analogy to the square planar case where the d_{xz} and d_{yz} orbitals lie lower in energy than the d_{xy} orbital. This is a direct consequence of the out of plane movement of the metal. The d_{xy} orbital, normally lying in the porphyrin plane, interacts less strongly with the porphyrin nitrogens as the metal moves out along the z-axis. Its energy is therefore decreased while the energy of the d_{xz} and d_{yz} orbitals is increased, in accordance with the preservation of an energy barycenter. This orbital scheme is commonly applied to both Fe and Mn porphyrins to predict ligand field effects.

X-ray studies have also provided information concerning the mode of bonding between the metal and counterion. For instance, the Mn-Cl bond distance in ClMn(III)TPP is equal to the sum of the ionic radii. In ClFe(III)TPP, however, the Fe-Cl distance is considerably shorter, and the decrease observed cannot be accounted for by the increase in nuclear charge in going from Mn(III) to

Fe(III) [31]. The axial bonding (i.e. that involving ligands situated on an axis through the metal atom and perpendicular to the porphyrin plane) in Mn(III) porphyrins is in general found to be weaker than in their Fe(III) analogues, and is believed to be largely electrostatic in nature. On the other hand, Mn(III) bonds more strongly to the porphyrin nitrogens than does Fe(III).

As has been noted, Mn(III) porphyrins display abnormal electronic spectra. The distinguishing feature is that the intense Soret band of the normal metalloporphyrin spectrum is split into two bands. Boucher [52] has suggested that the anomolous behaviour results from bonding π-back between the metal e_g ($d_{xz,yz}$) orbitals and the antibonding π* orbitals of the porphyrin ligand. The singularity of Mn(III) in this respect is not understood, however. Figure 3 illustrates the visible spectra of ClMn(III)TPP, and, for comparison, that of Zn(II)TPP (taken from this work), which displays a normal metalloporphyrin spectrum. The numbering of the bands for the manganese complex follows the system introduced by Boucher [52], and is in common use in the literature dealing with manganese porphyrins. The term "Soret", as applied to manganese porphyrins in this work, will refer to band V.

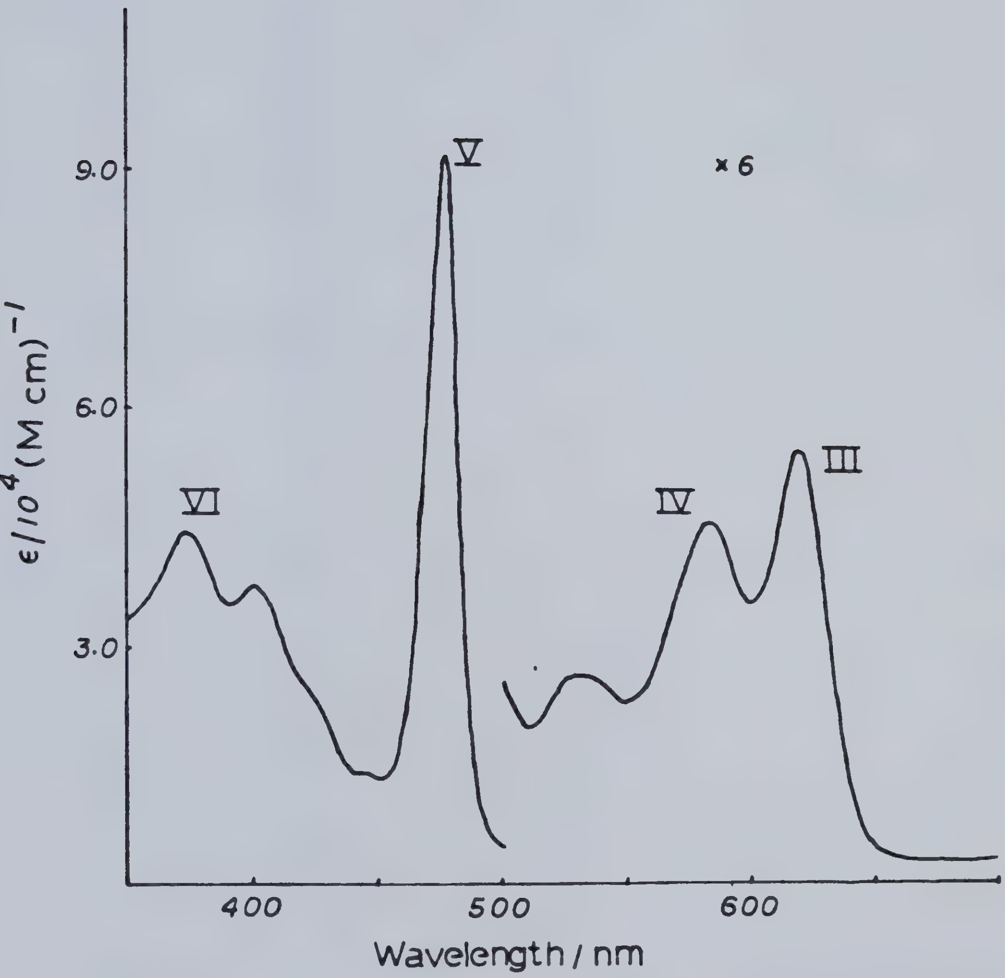

Figure 3a. Electronic absorption spectrum of ClMn(III)TPP in $C_2H_4Cl_2$.

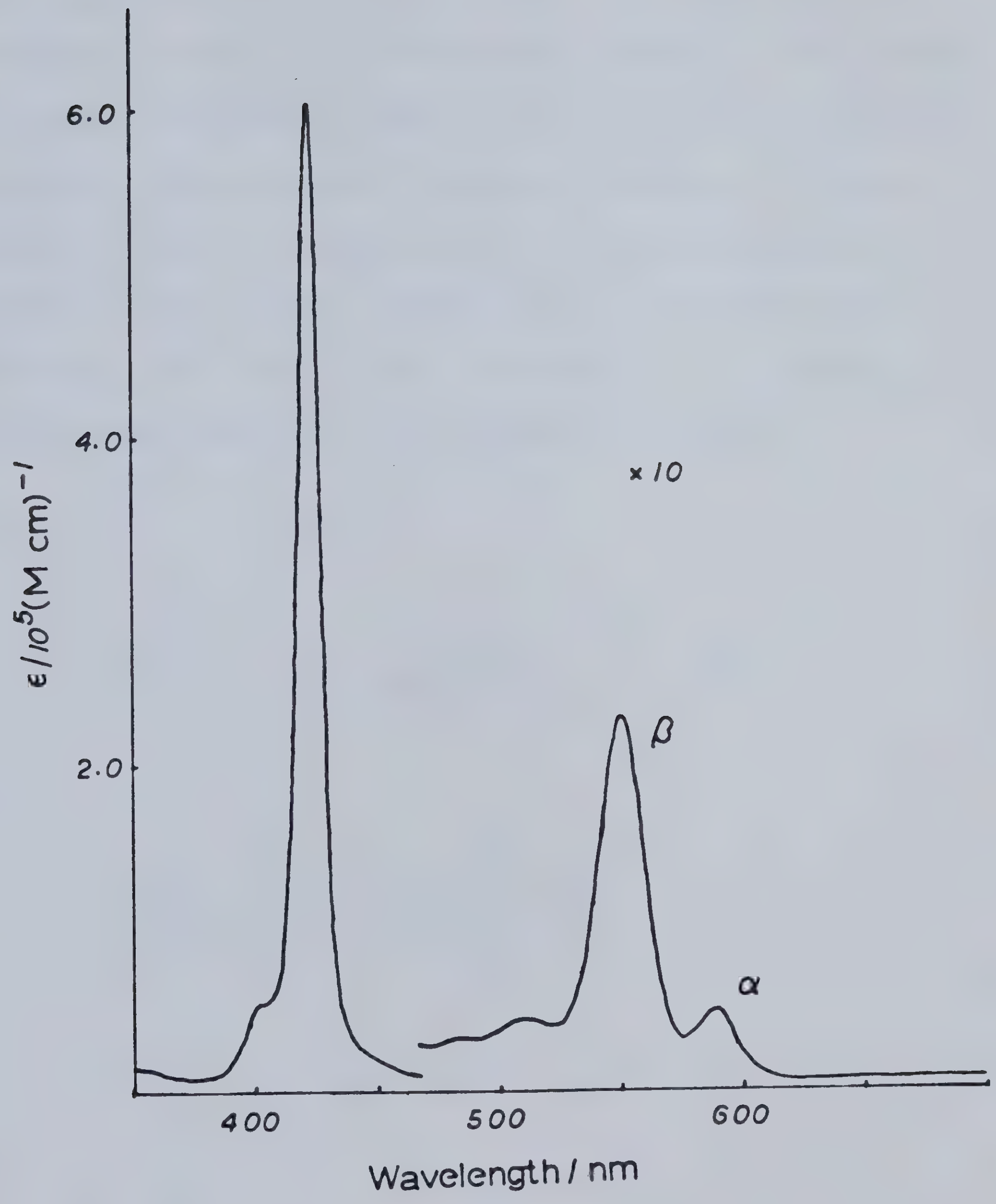

Figure 3b. Electronic absorption spectrum of Zn(II)TPP in $C_2H_4Cl_2$.

In non-bonding solvents such as CH_2Cl_2, the spectra of manganese porphyrins are highly dependent on the counterion, while in coordinating solvents like pyridine or dimethylsulfoxide (DMSO) no dependence on counterion is observed. This has been taken as evidence (52) that the counterion remains coordinated to the manganese in solvents of low donor number, but is replaced according to equilibria (2) and (3) (X = counterion, S = solvent, and the ellipse represents the porphyrin ligand).

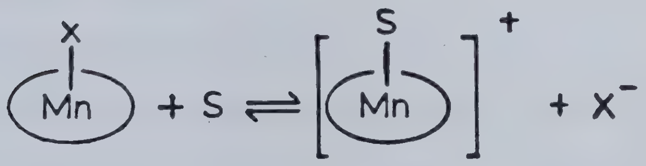

(2)

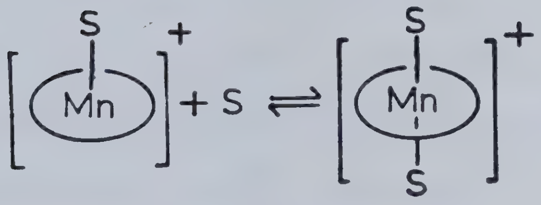

(3)

That equilibrium (1) involves substitution of, and not addition trans to, the counterion has been determined by polarographically monitoring the free chloride concentration while titrating dichloroethane solutions of

ClMn(III)TPP with donor molecules, S, such as pyridine or DMSO [35].

1.4.2 Mn(II) Porphyrins

The Mn(II) porphyrin complexes may be prepared by electrochemical reduction at ca -0.1 V vs SCE [56], or by chemical reduction with a variety of reductants [56,57]. In the presence of O_2, and at room temperature, these revert back to as yet unidentified Mn(III) species [58,60] while at low temperatures reversible binding of dioxygen has been observed [61].

Mn(II) porphyrins share the preference of their oxidized redox partners for high spin configurations. Here, however, the $d_{x^2-y^2}$ orbital, directed at the porphyrin nitrogens, is occupied resulting in a substantially increased out of plane displacement of the metal atom in 5-coordinate Mn(II) porphyrins relative to the 5-coordinate Mn(III) species. In the complex (N-MeIm)Mn(II)TPP (N-MeIM = N-methylimidazole), for instance, the out of plane distance of the Mn(II) ion is 0.56 Å [57]. In the 4-coordinate species Mn(II)TPP, this distance is reduced to 0.14 Å, underscoring the importance of axial ligation in determining the position of the metal within the porphyrin cavity. No examples of 6-coordinate Mn(II) porphyrins are known.

Somewhat surprisingly, the Mn(II) porphyrins possess normal metalloporphyrin electronic absorption spectra with an intense, unsplit Soret band at ca 400 nm. This apparently indicates decreased interaction between the porphyrin π^* orbitals and the metal atom.

1.4.3 Mn(IV) and Mn(V) Porphyrins

As already noted, the higher valent manganese porphyrin complexes are of special interest because of their potential usefulness as catalysts for hydrocarbon and water oxidation. Loach and Calvin [62] were the first to tentatively identify a Mn(IV) species. A product suggested to be $(OH)_2Mn(IV)Hpor$ (Hpor = Hematoporphyrin dianion) was observed upon 1-electron sodium hypochlorite oxidation of (OH)Mn(III)Hpor at pH > 9 in ethanol-water mixtures. As has been noted by Harriman [63] and Boucher [52], however, the evidence for Mn(IV) is not altogether compelling, and the electronic spectrum reported is more consistent with a cation radical formulation. The (OH)Mn(III)Hpor/NaOCl system does, however, bring about the oxidative cleavage of a number of ethers [64], and evidence has been presented that the midpoint potential of the associated redox couple at pH < 9 lies above that for the oxidation of water [30,65].

More convincing evidence for the existence of high valent manganese porphyrins has come from the reactions of XMn(III)TPP (X = Cl^-, Br^-, N_3^-) with iodosylbenzene in nonaqueous solvents [20,22]. The spectra of species isolated from such reaction mixtures are not indicative of cation radical formation and contain an intense, though somewhat broadened, Soret band at 415 nm.

Because iodosylbenzene contains two oxidizing equivalents, the resulting species were originally believed to contain Mn(V), in accordance with reaction (4).

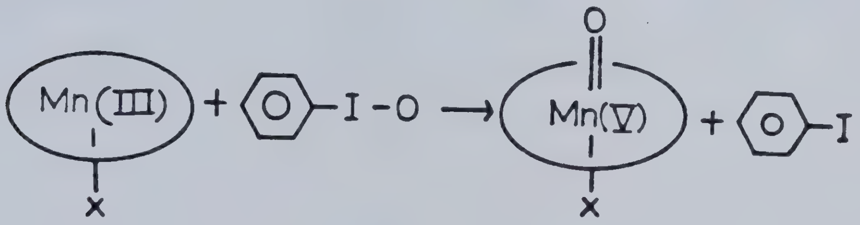

(4)

Apparently identical electronic spectra have been obtained, however, on reaction of Mn(II)TPP with iodosylbenzene [24], and with O_2 [18]. (The latter system is catalytically active towards hydrocarbon oxidation.) The implication in these studies is that the product contains Mn(IV). Hill and Schardt [66] have recently reported the X-ray characterization of a μ-oxobridged Mn(IV) dimeric species $[N_3Mn(IV)TPP]_2O$ prepared by

reaction of iodosylbenzene and $N_3Mn(III)TPP$, and species such as this might resolve the apparent anomolies. In none of the iodosylbenzene reactions has the reaction stoichiometry been determined.

Irradiation of $N_3Mn(III)TMP$ (TMP = tetramesitylporphin dianion), reaction (5) [67], and hypochlorite oxidation of $(CH_3O)Mn(III)TTP$ (TTP = tetra(p-tolyl)porphin dianion) in the presence of ammonia [68] have very recently led to the isolation of the corresponding porphyrin complexes described as containing Mn(V), and which contain a Mn≡N triple bond. The nitrido Mn(V) porphyrins are exceptionally stable, and are reported to resist reduction by sodium anthracenide [68].

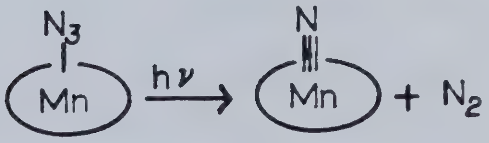

(5)

CHAPTER 2

EXPERIMENTAL

2.1 Preparation of Compounds

2.1.1 Zn(II)TPP

This was prepared after the method recommended by Adler et al. [69]. Zinc acetate was first prepared by refluxing 200 mL of glacial acetic acid over zinc dust for ~2 h. The mixture was filtered to remove unreacted zinc. After concentrating the filtrate to ca 50 mL and cooling, 3 g of white crystalline material were obtained.

One g of the zinc acetate so prepared was added to 400 mL of DMF containing 1 g of tetraphenylporphin (Aldrich) and the resulting mixture was refluxed for 2 h. The solvent was then removed by evaporation on a steam bath, and the resulting solid residue was washed with water. After drying, this was taken up in chloroform and chromatographed on an alumina column. Unreacted $TPPH_2$ eluted first as a sharp purple band closely following the solvent ($CHCl_3$) front. This was followed by a red band containing Zn(II)TPP. A blue band (product not

characterized) eluted at much later times. Addition of CH_3OH to the $CHCl_3$ fraction containing Zn(II)TPP caused the metalloporphyrin to precipitate. This was collected by filtration and dried in vacuo overnight at 70°C. The uv-vis absorption spectra and the cyclic voltammetric half-wave potentials of the product agree with those reported in the literature for Zn(II)TPP [70].

2.1.2 (CH_3CO_2)Mn(III)TPP

This, again, was prepared after Adler's DMF method [69]. One g of $Mn(CH_3CO_2)_2 \cdot 4H_2O$ was added to 250 mL of refluxing DMF containing 2.5 g of $TPPH_2$. The reaction was followed to completion (~30 min) by thin layer chromatography on alumina, using chloroform as solvent, by watching for the disappearance of the purple spot at the solvent front due to $TPPH_2$. The solvent was then evaporated on a steam bath. (Adler has recommended the addition of an excess of water to precipitate the metalloporphyrins formed. That procedure has worked well in this laboratory with zinc and iron porphyrins, but with manganese it results in a colloidal dispersion from which product recovery by filtration requires several days. Addition of a large excess of $NaCH_3CO_2$, or heating, is only partially successful in bringing about coagulation.)

After washing with water, the solid residue was extracted into methanol using Soxhlet apparatus. ($TPPH_2$ is totally insoluble in methanol, and most of its metal complexes, excluding manganese, are only very slightly soluble.) The methanol was then removed by evaporation and the resulting product was recrystallized from glacial acetic acid containing 20% (by volume) acetic anhydride. The product was dried overnight in vacuo at 90°C. The resulting dark green crystals displayed uv-vis absorption spectra and voltammetric behaviour identical to those of authentic samples of $(CH_3CO_2)Mn(III)TPP$ obtained from Porphyrin Products Inc., Logan, Utah.

2.1.3 XMn(III)TPP; X = Cl^-, Br^-, I^-, ClO_4^-, $CF_3CO_2^-$

The strategy developed here for the preparation of these compounds is based on simple acid-base chemistry. Acetic acid is a weak acid, and acetate ion should therefore be displaced by X^- in acidic media provided HX is a stronger acid.

Two hundred mg of $(CH_3CO_2)Mn(III)TPP$ were dissolved in 150 mL of methanol. To this solution, 3-4 mL of an aqueous solution 1 M in the desired acid, HX, were added. After stirring for a few minutes, 350 mL of H_2O were added dropwise to facilitate precipitation of the product. (Rapid addition of H_2O should be avoided, as the

resulting precipitate is too fine to be conveniently collected by filtration.) The product was recovered by filtration and washed with water. The recovery is essentially quantitative as judged by the lack of colour in the filtrate. The whole procedure was repeated a second time to ensure complete replacement of the acetate ion, and the products were dried overnight in vacuo at 90°C. (The second acid treatment is apparently not necessary as it produces no further changes in the visible absorption spectra of the complexes.)

Addition of HF to methanol solutions of $(CH_3CO_2)Mn(III)TPP$ resulted in immediate formation of a green precipitate which proved to be insoluble in all common solvents. Similar observations have been made by Kelly and Kadish [35] in their attempts to isolate FMn(III)TPP from aqueous KF solutions. Because of its insolubility, the product was not studied further.

That acetate is replaced by this method is verified by the changes that occur in the visible absorption spectra (Table 2), by the very different voltammetric behaviour observed for the various compounds, and by the absence of acetate C-H (2900 cm^{-1}) and C=O (1624 cm^{-1}) stretching vibrations observed in the KBr disc IR spectrum of $(CH_3CO_2)Mn(III)TPP$. The trifluoroacetate and perchlorate complexes possess strong IR absorptions at

Table 2

λ_{max}(log ε)

X	III	IV	V	VI
$CH_3CO_2^-$	606(3.8)	568(3.9)	469(5.1)	371(4.6)
$CF_3CO_2^-$	608(4.0)	573(4.1)	474(5.0)	381(4.7)
Cl^-	619(4.0)	583(3.9)	478(5.0)	374(4.7)
Br^-	623(4.0)	587(3.9)	484(4.9)	379(4.8)
I^-	636(4.0)	601(3.8)	498(4.7)	389(4.9)
ClO_4^-	606(3.9)	569(4.0)	481(4.6)	389(4.8)
CH_3O^-	614(~3.9)	577(~3.9)	471(~4.8)	374(~4.6)

1700 cm^{-1} (ν, C=O) and 1120 cm^{-1} (ν, ClO_4) respectively, verifying the presence of the desired anion. All products were further characterized by elemental analysis (Table 3). For the halides [71] and the perchlorate complex [35,54], the position of the uv-vis absorption maxima are in excellent agreement with those reported in the literature. The trifluoroacetate complex has not been previously characterized. Thin layer chromatography on alumina with $CHCl_3$ as solvent gives only a single spot for all compounds, indicating no demetallation or decomposition of the porphyrin has occurred.

2.1.4 (CH_3O)Mn(III)TPP

Methanol was first refluxed over Mg turnings for 6 h in order to remove water and then distilled. To 400 mL of the "anhydrous" product were added 0.5 g of (CH_3CO_2)Mn(III)TPP and 0.2 g of anhydrous sodium methoxide. The resulting mixture was then concentrated to ~70 mL by heating and passing a stream of dry argon over the solution. The mixture was cooled and allowed to stand overnight, yielding dark green crystals. These were collected by filtration and dried in vacuo at 80°C.

That acetate ion had been replaced was verified by the changes in the electronic absorption spectra (Table 2), and the absence of the 1624 cm^{-1} band in the KBr disc

Table 3

Elemental Analysis of Mn(III)TPP$^+$ Complexes

	%C		%H		%N		% Other	
X	Calc'd	Found	Calc'd	Found	Calc'd	Found	Calc'd	Found
$CH_3CO_2^-$	76.0	77.2	4.30	4.70	7.71	7.3	O, 4.40	4.48
Cl^-	75.2	75.3	4.01	4.03	7.97	8.03	Cl, 5.04	5.2
Br^-	70.7	69.3	3.77	3.76	7.49	7.27		
I^-	66.5	66.5	3.55	3.57	7.05	6.93		
$CF_3CO_2^-$	70.8	70.7	3.61	3.58	7.18	7.13		
ClO_4^-	68.9	67	3.68	3.54	7.30	7.1		
CH_3O^-	77.4	75.3	4.47	4.32	8.02	7.56		

IR spectrum of the product. Methoxide complexes of metalloporphyrins have been reported to possess IR absorptions in the region 1000 to 1100 cm^{-1} [72]. All of the manganese porphyrins prepared here display sharp intense bands at 1070 cm^{-1}. This band in the methoxide complex is considerably broader than in the other complexes, and a shoulder at 1060 cm^{-1} may be due to the methoxide C-O stretching vibration. A weak band at 2900 cm^{-1} indicates the presence of non-aromatic C-H.

The mass spectrum of the compound displays a relatively intense peak at m/e = 31 (consistent with CH_3O^+) which is not present in the mass spectra of the other complexes reported. This is three times more intense than a peak observed at m/e = 32, suggesting that the peak at m/e = 31 arises from methoxide, and not methanol. (The ratio of the peak intensity at 31 mass units to that at 32 is reported as 1.6 in the mass spectrum of MeOH [73].)

Thin layer chromatography of the complex on silica gel with $CHCl_3$ as solvent displays a purple spot at the solvent front ($TPPH_2$), a faint yellow spot eluting at later times, and a dark green immobile spot due to the metal-porphyrin complex. Clearly some decomposition of the manganese porphyrin has occurred. Boucher [74] has also observed decomposition of manganese porphyrins when

isolating them from strongly basic solutions. The purity of the compound prepared here was estimated at 90-95% by comparing the absorbance of band V of the electronic spectra observed in CH_3OH containing 0.1 M HCl to that observed for ClMn(III)TPP in the same solvent mixture. (The absorption maxima of both solutions occur at identical wavelength.)

2.1.5 $(Et_4N^+)(CH_3CO_2^-)$, $(Me_4N^+)(CF_3CO_2^-)$

Tetraethylammonium acetate and tetramethylammonium trifluoroacetate were prepared by the method described by Goering et al. [75] for the preparation of tetramethylammonium acetate. Three mL of glacial acetic acid were titrated with a 10% aqueous solution of tetraethylammonium hydroxide until neutral to bromothymol blue. The water was then removed in vacuo at 60°C and the resulting solid residue was recrystallized from acetone. The product was then dried again at 50°C in vacuo. Tetramethylammonium trifluoroacetate was prepared in an identical manner by titration of trifluoroacetic acid with 10% aqueous tetramethylammonium hydroxide. The presence of the desired anions was verified by the appearance of the appropriate band in the KBr disc IR spectra of the products (CF_3CO_2, ν C=O at 1660 cm^{-1}; CH_3CO_2, ν C=O at 1550 cm^{-1}).

2.2 Electrochemical Experiments

2.2.1 Reference Electrodes

A saturated calomel electrode (SCE) was used to provide a reference potential for the majority of the voltammetric experiments performed. The details of its construction are shown in Figure 4. The calomel paste was prepared according to Adams [76]. A few drops of Hg were added to a mortar containing mercurous chloride and ground until the surface of the Hg_2Cl_2 was uniformly gray. Just enough saturated aqueous KCl was then added to provide a thick paste on further grinding. The SCE was stored in a saturated KCl solution when not in use.

A Ag/Ag^+ reference electrode was used in some of the experiments where acetonitrile was the solvent. This was of identical construction except that the calomel paste and Hg contact were replaced by a silver wire. The filling solution in this case was acetonitrile containing 0.1 M tetrabutylammonium perchlorate and 0.01 M $AgNO_3$.

2.2.2 Electrochemical Cell for Voltammetric Experiments

The design of the cell used for chronocoulometry, cyclic voltammetry, and alternating current voltammetry is illustrated in Figure 5. This is a conventional three electrode configuration. The working electrode consisted

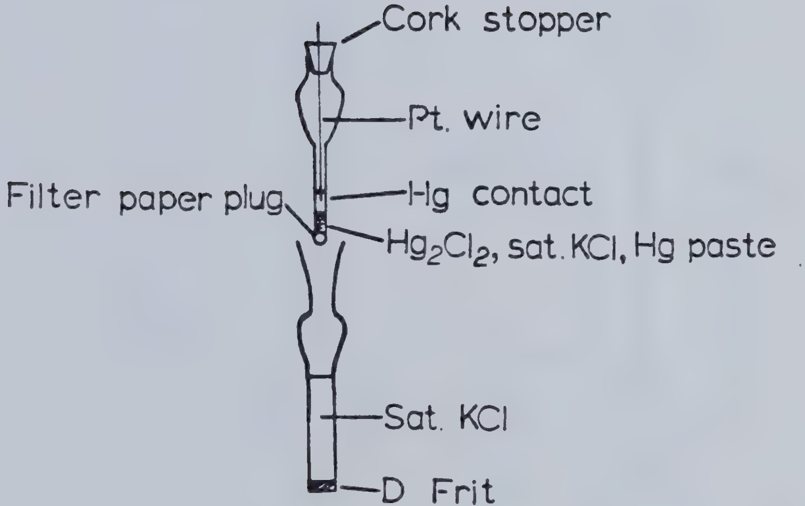
Cork stopper
Pt. wire
Filter paper plug
Hg contact
Hg_2Cl_2, sat. KCl, Hg paste
Sat. KCl
D Frit

Figure 4. Construction of saturated calomel reference electrode.

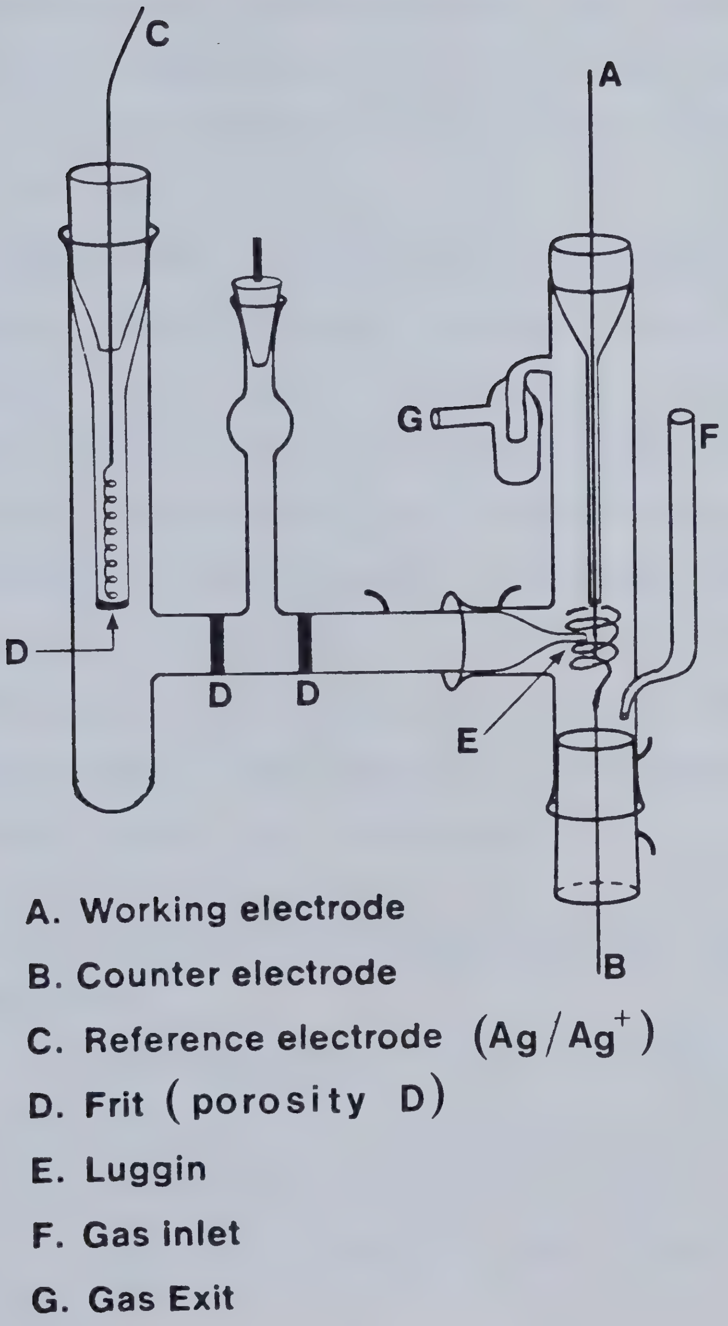

C
A
G
F
D
D
D
E
B
A. Working electrode
B. Counter electrode
C. Reference electrode (Ag/Ag$^+$)
D. Frit (porosity D)
E. Luggin
F. Gas inlet
G. Gas Exit

Figure 5. Electrochemical cell used for voltammetric experiments.

of a platinum wire 7 mm in length and 1 mm in diameter. This was surrounded by a platinum wire counter electrode formed into a helical configuration. The reference potential was sensed at the tip of a Luggin capillary (o.d. - 1.5 mm) positioned 2-3 mm from the surface of the working electrode.

A glassy carbon working electrode was used in some experiments. This consisted of a glassy carbon disc 3 mm in diameter fitted into a 3 mm i.d. glass tube and sealed with epoxy. The surface of the glassy carbon disc was polished to a mirror finish on a felt polishing pad with 0.5 μm alumina polishing powder. Electrical contact to the carbon disc was achieved via a small quantity of Hg inside the glass tube and situated on top of the carbon disc. Connection to the potentiostat was achieved via a copper wire inserted into the Hg pool.

2.2.3 Solvents, Supporting Electrolytes and Other Reagents

Tetra(n-butyl)ammonium perchlorate (TBAP) served as supporting electrolyte for all nonaqueous experiments. This was used as received from either Fluka or Southwestern Analytical Chemicals after drying in a vacuum oven at 40°C.

The majority of the porphyrin voltammetric experiments were carried out in either dichloromethane or 1,2-dichloroethane. No difference in the electrochemical behaviour of any of the species investigated was noted in changing from one of these solvents to the other. CH_2Cl_2 was found to be preferable in terms of the simplicity of the purification procedure required to achieve satisfactory residual current levels in voltammetric experiments, but its volatility makes it too difficult to use in experiments where the concentration of electroactive species must be accurately known, and in these cases $C_2H_4Cl_2$ has been found to be a satisfactory replacement. The solubility of some of the porphyrins investigated is considerably less in dichloroethane than in dichloromethane, however.

Dichloromethane was distilled from CaH_2, retaining the middle 60%. This was stored in the dark and passed through a column of activated basic alumina (Woelm Super) immediately prior to use. Dichloroethane was first extracted with an equal volume of cold concentrated H_2SO_4. This was followed by extraction with 10 equal volume portions of 5% aqueous NaOH [77]. This was then dried over anhydrous Na_2SO_4, followed by fractional distillation from CaH_2. The product was stored in the dark and passed through a basic alumina column prior to use.

Chloride ion appears as a common contaminant in chlorocarbon solvents. The manganese porphyrin complexes described here provide a very convenient means of assessing the extent of this contamination at very low levels. Figure 6 illustrates the electronic absorption spectrum of 9.07×10^{-6} M (CH_3CO_2)Mn(III)TPP obtained in $C_2H_4Cl_2$ purified according to the above procedure (solid line) and of 1.07×10^{-5} M (CH_3CO_2)Mn(III)TPP in $C_2H_4Cl_2$ taken directly from the reagent bottle. In the non-purified solvent the spectrum obtained is identical to that of ClMn(III)TPP, indicating a Cl^- concentration of greater than 10^{-5} M. It is interesting to note that the manufacturers specifications list Cl^- as not detectable for this particular solvent. The length of time which the product had been in storage before being received in this laboratory, however, is not known.

Based on the visible absorption spectra of either the acetate or perchlorate manganese porphyrins, extraction with 5% aqueous NaOH, with 0.1 M $AgNO_3$, or simply shaking with basic alumina have all been found to be effective at reducing chloride to below micromolar levels in $CHCl_3$, CH_2Cl_2, and $C_2H_4Cl_2$. Distillation from CaH_2 does not significantly reduce the chloride concentration. Omission of the sulfuric acid extraction in the purification of dichloroethane results in unsatisfactory voltammetric

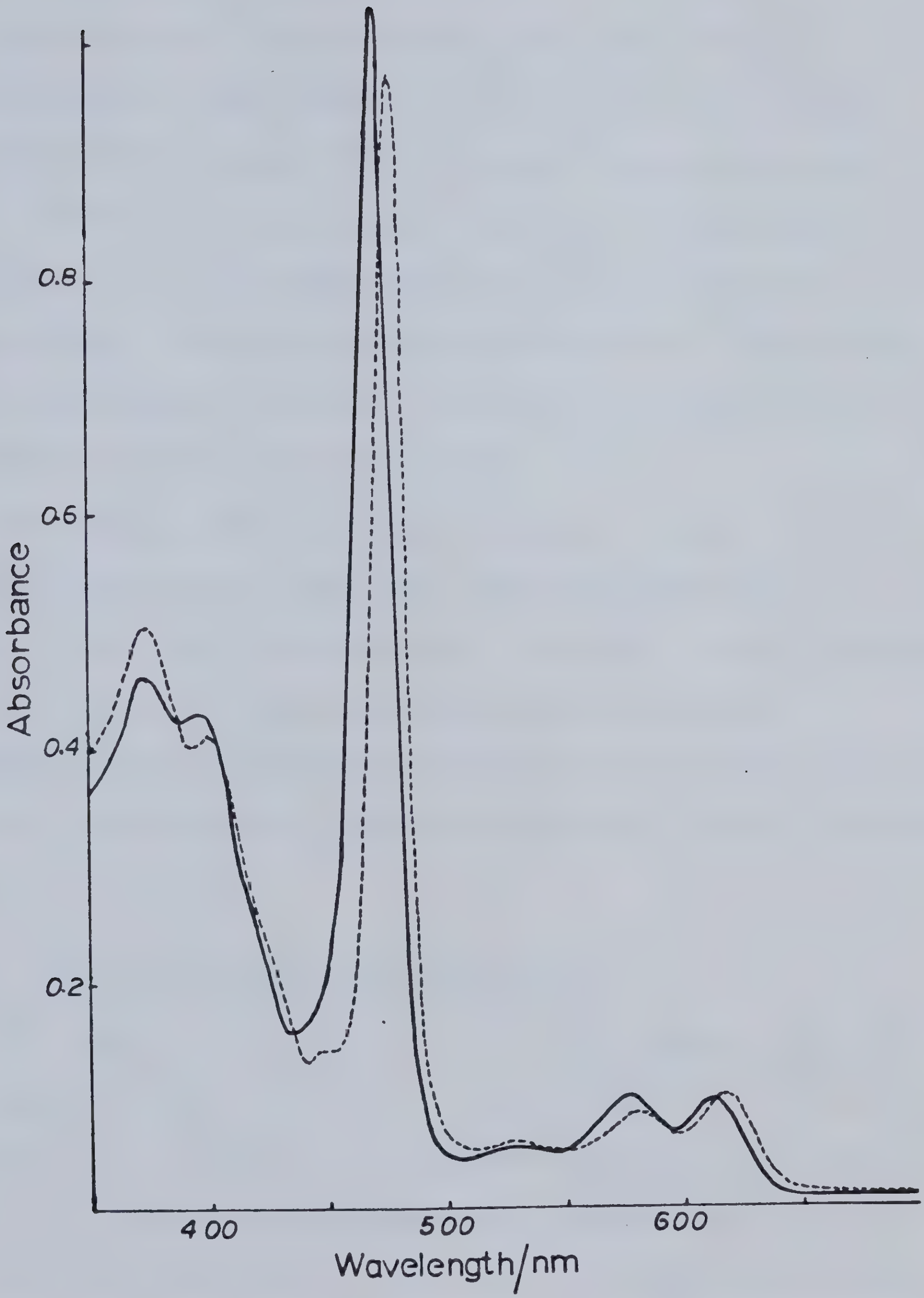

Figure 6. Electronic absorption spectra of $(CH_3CO_2)Mn(III)TPP$ in purified (solid line) and non-purified (dashed line) dichloroethane.

residual currents, and a small voltammetric wave at ca 0.8 volts vs SCE is observed.

Acetonitrile (Caledon HPLC grade) was used in electrochemical experiments after shaking with neutral alumina (Woelm Super). Nitrobenzene was fractionally distilled from BaO at reduced pressure (100 mM Hg) and stored over 4 Å molecular seives. Nitromethane was distilled at 100 mM Hg and stored over molecular seives. Water was triply distilled. Dimethylsulfoxide (Burdick and Jackson) was used as received.

All other reagents, with the exception of 9,10-diphenylanthracene, which was recrystallized from acetonitrile, were reagent grade and used without further purification. All solutions for electrochemical experiments were outgassed by bubbling argon gas, passed through a drying tube packed with calcium hydride, through them for ~5 min.

2.2.4 Electrochemical Instrumentation

The potentiostat used for all experiments was a Hi-Tek type DT-2101. This unit incorporates its own current follower, and facility for positive feedback compensation of solution resistance between the Luggin capillary and the working electrode is provided. In experiments where this was used, the current follower output was monitored

on an oscilloscope and the amount of feedback was increased until the potentiostat was driven into oscillation. This setting was then decreased until stable operation could just be maintained. This method of compensation is in common use [78] and appears to be the only method which has been employed by workers in the field of porphyrin electrochemistry [6].

The applied potential waveforms for dc voltammetric experiments were derived from a Hi-Tek model PPR1 waveform generator, the output of which was taken directly to one of the adder inputs of the potentiostat. In ac voltammetric experiments, the sinusoidal output from a Global Associates oscillator was taken to the second adder input of the potentiostat. The output of the potentiostat's current follower was then taken to the input of either a Bentham model 223 or a PAR model HR-8 lock-in amplifier.

All voltammetric traces were recorded on a Hewlett-Packard model 2045-A X-Y-T recorder.

The integrator used in chronocoulometric and thin layer coulometric experiments was a conventional operational amplifier based design constructed and calibrated in this laboratory by Dr. B. Stanley Pons.

2.2.5 Transmission Spectroelectrochemistry

The cell used for observation of electronic absorption spectra as a function of applied potential is illustrated in Figure 7. This consisted of two quartz plates (25 × 40 mm) fused together at their longest edges such that the inner faces of the plates were separated by 0.5 mm. A platinum gauze (3 mm × 40 mm) working electrode and two platinum wire counter electrodes, situated parallel to and on either side of the working electrode, could be slipped inside the quartz cell. Two rectangular strips of filter paper were cut prior to each experiment and slipped into the cell along either side of the working electrode. This served to prevent diffusion of electroactive species between the counter and working electrodes, and to prevent them from coming into direct electrical contact. It will hopefully become obvious during the discussion on thin layer techniques that this particular cell design allows much improved control of the potential applied to the working electrode than do more conventional optically transparent thin layer electrodes. It does not, however, allow coulometric experiments to be performed. The cell is filled with solution by capillary action and the precise volume of solution in contact with the working electrode cannot be assumed to remain constant between experiments.

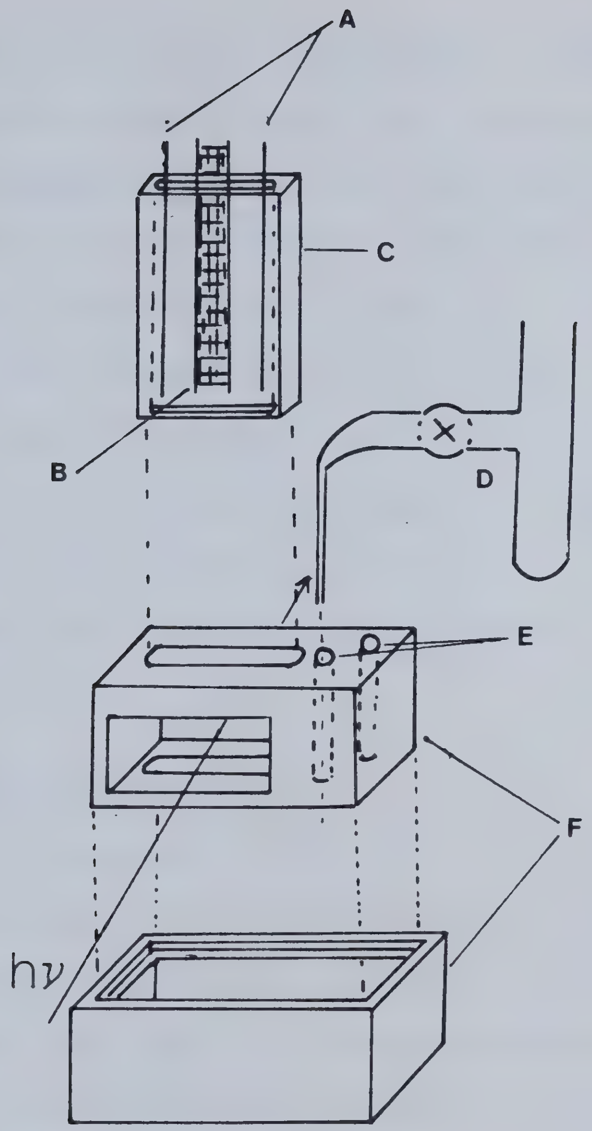

Figure 55. Thin layer optical cell:

A. Pt wire counter electrodes
B. Pt gauze working electrode
C. Fused quartz plates
D. Reference electrode compartment and Luggin capillary assembly
E. Ports for sample injection and Luggin capillary
F. Teflon solution boat and cover

A Teflon vessel was constructed to contain the filling solution and to allow for positioning of the electrode assembly. The quartz cell and Teflon vessel were assembled and positioned in the sample compartment of a Cary model 14 spectrometer such that the working electrode was directly in the path of the optical beam. The sample compartment was then closed and flushed with dry argon. The solution was degassed external to the spectrometer and injected into the Teflon vessel by means of a syringe and a length of polyethylene (1 mm o.d.) tubing.

2.2.6 Other Experiments

A brief introduction to the theory of electrode kinetics, as well as the techniques of cyclic voltammetry and chronocoulometry, are included in an Appendices 1-3. As the thin layer and ac voltammetric techniques used have been developed in this work, these will be discussed in detail in the body of the thesis.

Elemental analysis and vapour phase osmometry were performed by the Microanalytical services personnel at the University of Alberta. Mass and IR spectra were recorded with AEI MS12 and Nicolet 7000 series spectrometers, respectively, by the spectral services personnel at the University of Alberta. Routine IR spectra were recorded with a Perkin-Elmer 337 grating instrument.

CHAPTER 3

VOLTAMMETRY AND COULOMETRY AT IMMERSED THIN LAYER ELECTRODES

3.1 Introduction

Before any attempt can be made to quantitatively analyze a voltammetric wave, or any inference concerning the nature of the product of a heterogeneous charge transfer process can be drawn, the number of electrons, n, associated with the underlying redox process must be known. A number of voltammetric criteria [78] can be applied to this end provided that the associated charge transfer process is reversible: i.e., no homogeneous reactions are coupled to the heterogeneous charge transfer, and the standard heterogeneous rate constant, k_s, is large enough that the Nernst equation can be used to calculate the concentrations of the two forms of the redox couple. If this is not the case, then some method other than the application of standard voltammetric criteria must be used. This is most often controlled potential coulometry [79].

Controlled potential coulometry involves measurement of the charge required to completely convert an electroactive species to whatever product, or products, may be stable at some particular constant applied potential. Application of Faraday's laws in conjunction with knowledge of the quantity of electroactive species present then allows calculation of the number of electrons passed per molecule of reactant.

The procedure employed in controlled potential coulometry generally involves applying a constant potential to the working electrode and allowing current to flow until it has decayed to within a few percent of its initial value, or until no further decay of the current with time is observed. The total charge passed during this time is then assumed to correspond to that required for complete electrolysis. In most conventional coulometric cell designs, such an experiment requires several hours to complete, and the precision with which n-values may be determined is often not good. The procedure is especially disadvantageous when working with organic systems where solvents or electroactive species are difficult to purify or are available in limited quantity. When working at potentials near the anodic or cathodic limits of the solvent, or when the electrolysis products are of limited stability, the current may never

decay to background levels. Under such circumstances it is extremely difficult to be objective in determining an electrolysis endpoint. The poor potential distribution across the working electrode surface which is encountered in many coulometric cell designs is particularly pronounced when working in nonaqueous solvents, and may prohibit the determination of n for a particular voltammetric wave when this is not well separated in potential from other voltammetric processes.

In aqueous systems, thin layer electrochemistry [80] offers a very attractive alternative to controlled potential coulometry for n-value measurement. Here, a very small volume of solution is confined to a thin layer (2-50 μm) next to the electrode surface. Complete electrolysis of the electroactive species can then be achieved in very short time periods (ca 1 sec). Diffusion of electroactive species within the thin layer may often be ignored in theoretical treatments, and the resulting equations are especially simple and easy to interpret. The peak currents in thin layer voltammetry theoretically occur at the formal redox potential, and this fact, in conjunction with the absence of diffusion of electroactive material from the bulk solution, results in greater resolution of poorly separated waves than can be achieved in diffusion-controlled experiments such as cyclic

voltammetry. (The shape of the thin layer voltammetric wave will be shown to be identical to that obtained in ac voltammetry, the latter technique being noted for its ability to resolve closely spaced charge transfer processes [81].) The short time required for complete electrolysis makes thin layer techniques particularly powerful for the determination of the stoichiometry of complex electrode reactions.

Thin layer electrodes in general suffer from problems associated with uneven potential distribution across the electrode surface [84]. This arises from the high resistance presented to the flow of current through thin layers of solution with small cross-sectional areas. Even in highly conductive aqueous media, the potential distribution is such that agreement between theory and experiment is seldom excellent. As a result, examples of the application of thin layer techniques to the determination of, for instance, heterogeneous kinetic parameters are rare. Cells have been designed utilizing conductive membranes [82] to provide a uniform current path between the counter and working electrodes, and these alleviate, to a large extent, the problem of uneven potential distribution. These are difficult to construct, however, and have not found common usage.

In nonaqueous solvent/electrolyte systems, solution resistivities as high as 3000 ohm-cm [83] may be encountered. The resulting potential distribution problems are particularly severe, and it has been suggested [84] that implementation of thin layer methodology, even in solvents of relatively high dielectric constant, such as acetonitrile or dimethylformamide, would be difficult. It is precisely in such poorly conducting media that the advantages of thin layer methodology would be most beneficial, however.

In this chapter the application of thin layer voltammetry and coulometry in non-aqueous media is considered. The discussion is centered around immersed thin layer electrodes, i.e. those in which the edges of the thin layer cavity are immersed in bulk solution, since a greater cross sectional area is available for the flow of current, and the resulting potential distribution is therefore less severe [85]. Such cell designs always suffer to some extent from diffusion of electroactive material from the bulk solution into the thin layer cavity, but it will be demonstrated experimentally that this does not seriously affect the usefulness of the results.

3.2 Linear Sweep Voltammetry at Thin Layer Electrodes

The theory and application of thin layer voltammetric methods has been reviewed in detail [80]. The most commonly used technique is that of linear sweep voltammetry. Here, a linearly increasing potential is applied to the working electrode and the resulting current is recorded as a function of the applied potential. In the cyclic version of this technique, the direction of the potential scan is reversed once some predefined switching potential is reached, and recording of the current is continued while the potential is linearly scanned back to its initial value.

If the thickness of the thin layer of solution next to the working electrode is sufficiently small, and if the rate, $dE/dt = \nu$, at which the applied potential is varied is sufficiently slow, then all species may be considered to be uniformly distributed throughout the thin layer cavity. Given the generalized electrode reaction

$$\mathrm{Ox} + ne^- \rightleftarrows \mathrm{Red}$$

and the above conditions, the current resulting as the potential is scanned from a value where one form of the redox couple predominates to a point where the other form is favoured is given by

$$i = nFV(d\,C_{Ox}/dt) \tag{3-1}$$

where V is the volume of the thin layer. (The sign convention adopted here is that of the Stockholm convention [86]. Anodic currents are taken as positive and result from the application of increasingly positive potentials.) If the electrode reaction is reversible then the relative concentrations of oxidant and reductant are given by the Nernst equation,

$$E = E° + \frac{RT}{nF}\ln(C_{Ox}/C_{Red}) \tag{3-2}$$

which, in conjunction with the requirement of stoichiometry

$$C^{\circ}_{Ox} = C_{Ox} + C_{Red}$$

leads to

$$C_{Ox} = C^{\circ}_{Ox}[1-[1+\exp(\frac{nF}{RT}(E-E°))]^{-1}] \tag{3-3}$$

Differentiation of equation 3-3 with respect to time and substitution into equation 3-1 gives

$$i = \frac{(nF)^2 V\nu C^0_{Ox} \exp[(nF/RT)(E-E^0)]}{RT[1 + \exp[(nF/RT)(E-E^0)]^2} \qquad (3-4)$$

as first derived by Hubbard and Anson [87]. This equation describes a Gaussian shaped curve with the peak current occurring at E° and given by

$$i_p = \frac{(nF)^2 V\nu C^0_{Ox}}{4RT} \qquad (3-5)$$

The second order dependence of the peak current on the number of electrons makes equation 3-5 particularly attractive for n-value determination.

A voltammetric criterion allowing for the determination of n without prior knowledge of C_{Ox} or V may be readily derived. One-half of the peak current is given by

$$i_p/2 = \frac{(nF)^2 V\nu C_{Ox}}{8RT}$$

Substitution of this current into equation 3-4 and solving for (E-E°) leads to the quadratic expression

$$a^2 - 6a + 1 = 0$$

where

$$a = \exp[(nF/RT)(E-E°)]$$

At 25°C this gives

$$E-E° = \frac{\pm 45}{n}\ \text{mV} \qquad (3\text{-}6)$$

The width of the peak at half-height is therefore given by

$$\Delta E_{.5h} = \frac{90}{n}\ \text{mV} \qquad (3\text{-}7)$$

This result has apparently not appeared in the literature, but should provide a rapid and convenient means for estimating n. (The same expression for the width at half-height and the same second order dependence of the peak height on n apply to the reversible ac voltammetric wave [88].)

More rigorous derivations of the linear sweep thin layer voltammetric response, taking into account the diffusion of electroactive species within the thin layer cavity, have appeared [87]. The resulting equations are cumbersome and have not found common use. Provided the thin layer thickness is of the order of 10 μm or less, the results of this treatment do not differ significantly from the predictions of equation 3-4 when the potential sweep

rate is 10 mV/s or less. The effects of solution resistance, and the resulting uneven potential distribution, on the linear sweep voltammetric response have not previously been considered in any type of quantitative manner. Experimentally, however, some degree of asymmetry in the peaks is always observed, and anodic peak potentials are displaced to anodic values while the reverse is observed for cathodic peaks.

3.3 Effects of Solution Resistance on the Thin Layer Voltammetric Response

The model used here to describe the potential distribution in thin layer cells was first used by Goldberg et al. to describe resistive effects in combined esr-electrochemical cells [89], and in thin layer cells [84], during current and potential step experiments. It has not, however, been used to describe resistive effects during potential sweep experiments, or to predict the extent to which cell geometry might determine the magnitude of such effects.

Two types of cell geometry will be considered here. The first, Figure 8, consists of a square or rectangular metallic electrode surface placed in a plane parallel to an insulating surface. The two surfaces are separated by a distance l, equal to the thickness of the thin layer

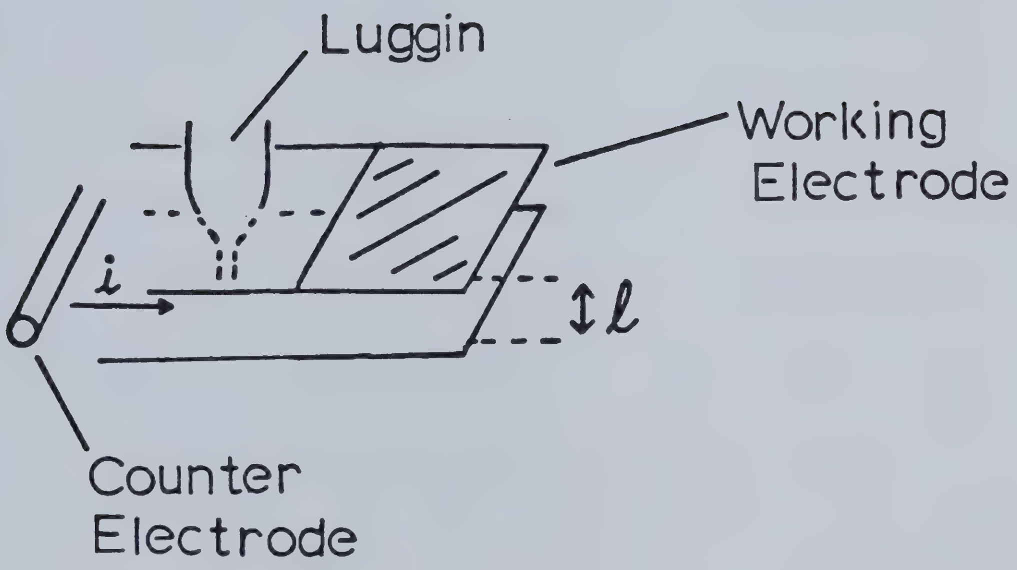
Luggin
Working Electrode
i
ℓ
Counter Electrode

Figure 8. Geometry of rectangular thin layer electrode.

cavity. Three of the edges of the electrode are considered insulating, and the fourth edge is equidistant from a secondary electrode placed within the cavity such that uniform parallel current flow between the secondary electrode and the exposed edge of the working electrode may be assumed. The working electrode potential is sensed via a Luggin capillary placed between the secondary and working electrodes. This geometry corresponds to that found in optically transparent thin layer electrodes (OTTLE's), where the working electrode, generally a platinum or gold mini-grid, Figure 9, is transparent to the passage of light.

The second geometry, Figure 10, corresponds to the type of immersed thin layer electrode first used by Oglesby et al. [85]. The working electrode surface is a planar disc, and a radially uniform current path is provided between the edges of the disc and a secondary electrode arranged concentric to the disc.

The model used to discuss the potential distribution across the working electrode considers that the thin layer cavity next to the working electrode may be divided into a number of volume increments, each successive increment being displaced a distance dx from the capillary tip. As the volume increments lie at successively greater distances from the Luggin, successively greater solution

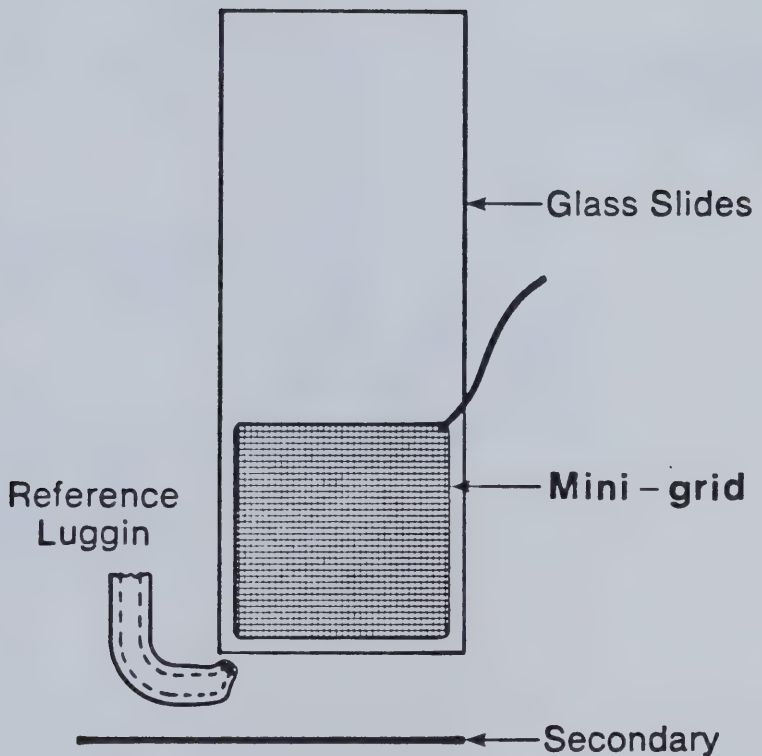
Glass Slides
Mini - grid
Reference Luggin
Secondary

Figure 9. Optically transparent thin layer electrode.

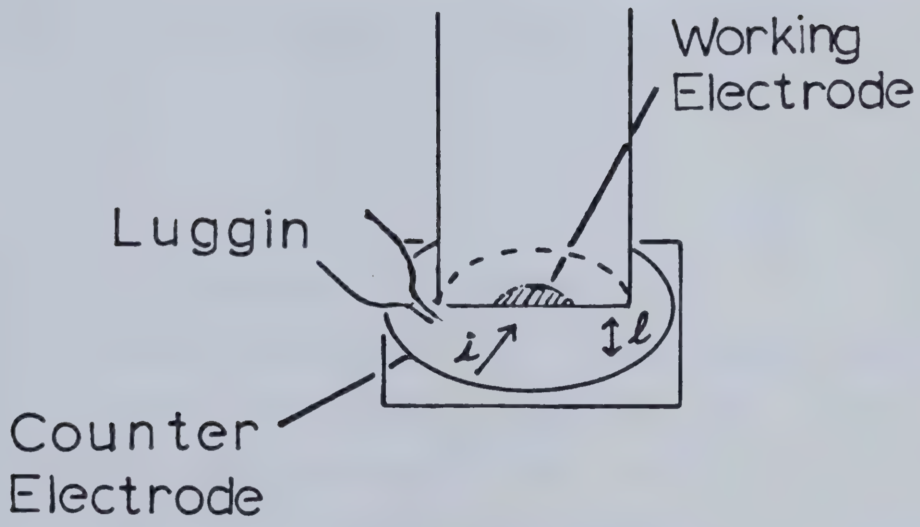
Working
Electrode
Luggin
Counter
Electrode
i
ℓ

Figure 10. Concentric radial thin layer electrode geometry.

resistances are presented to the current flowing into each increment. In the OTTLE geometry, the volume of each increment is constant, and given by wldx, where w is the length of the exposed edge of the working electrode. The individual resistances separating the volume increments are also constant, and may be calculated from

$$R_i = \rho \, dx/lw \qquad (3\text{-}8)$$

where ρ is the specific resistivity of the solvent/electrolyte system. The uncompensated resistance, $R_u = R_1$, between the Luggin tip and the first volume increment is given by equation 3-8 where dx is now the distance between the Luggin and the edge of the working electrode.

In the concentric radial geometry, the volume of each increment is that contained between two concentric cylinders of radii r and r-dr, and may be calculated from

$$V_i = \pi \, l(2r_i dr - dr^2) \qquad (3\text{-}9)$$

where r_i is the outer radius of V_i. As the radii of the volume increments decreases, so does the cross-sectional area available for the flow of current. The resistance increments between successive volumes therefore must

increase as the radii of the volume increments decrease. The resistances can be calculated with reference to Figure 11. If the difference dr between the radii, r_i and r_{i-1}, of two cylinders is infinitesimal, then the resistance to current flow between the two cylinders is given by

$$R = \rho dr/2\pi rl$$

If dr is no longer required to be infinitesimal, then the resistance between the two cylinders will be given by

$$R_i = \int_{r_i}^{r_{i-1}} \frac{\rho dr}{2\pi rl}$$

or

$$R_i = (\rho/2\pi l)\ \ln(r_{i-1}/r_i) \qquad (3\text{-}10)$$

The effective potential at each of the volume elements may be calculated once the volumes of the individual elements and the resistances between them are known. With reference to Figure 12, depicting the case for the radial concentric cell geometry, suppose that the total current flowing into the thin layer cavity is i_t. If the applied potential, i.e. that appearing at the Luggin tip, is E_{app}, then the potential appearing at the first volume increment is given by

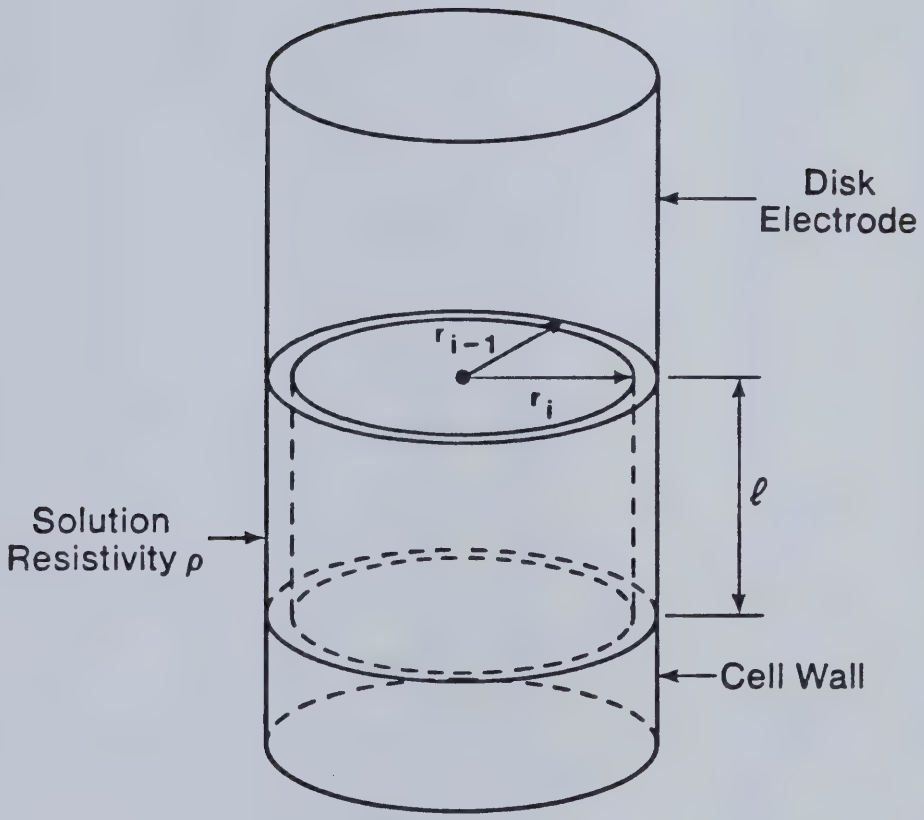
Disk Electrode
r_{i-1}
r_i
ℓ
Solution Resistivity ρ
Cell Wall

Figure 11. Solution resistance in concentric radial thin layer electrodes.

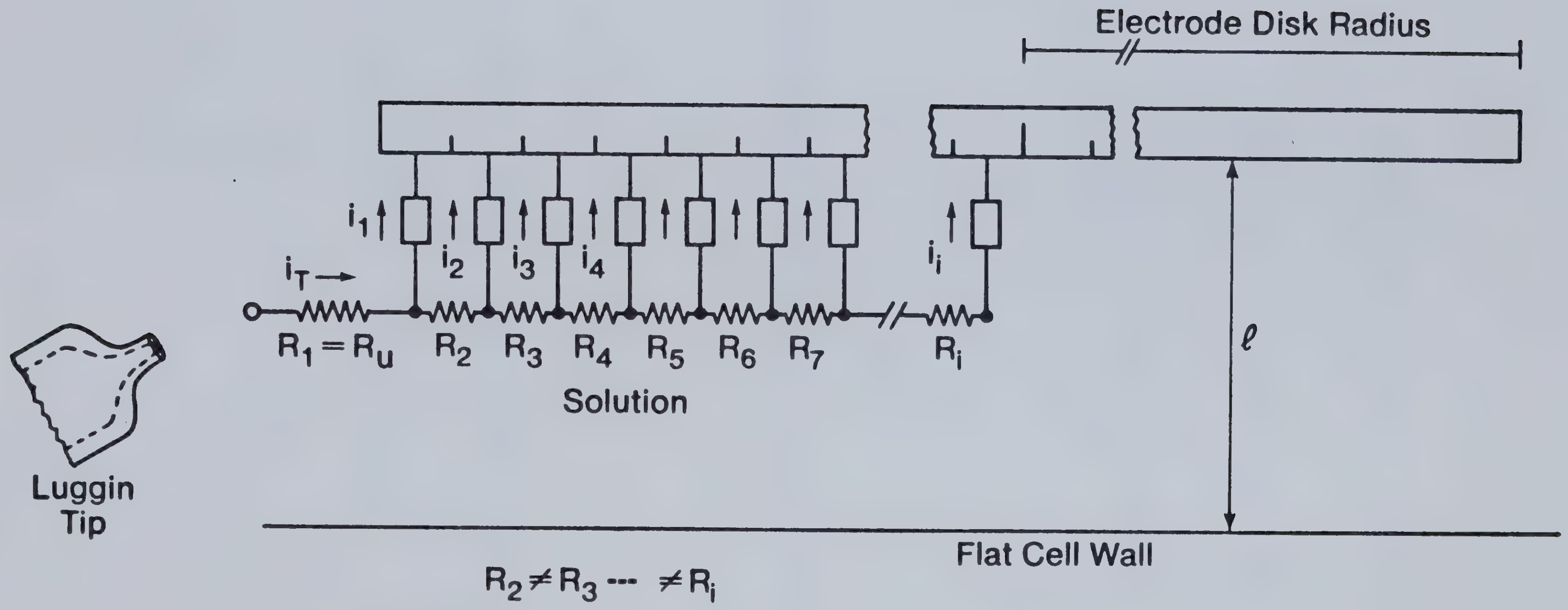

Electrode Disk Radius
i_1
i_2
i_3
i_4
i_i
i_T
$R_1 = R_u$
R_2
R_3
R_4
R_5
R_6
R_7
R_i
ℓ
Solution
Luggin Tip
Flat Cell Wall
$R_2 \neq R_3 \cdots \neq R_i$

Figure 12. Model for the potential distribution at thin layer electrodes.

$$E_1 = E_{app} - i_t R_1 \tag{3-11}$$

The current, i_1, flowing into the first volume element may now be calculated from equation 3-4 by setting $V = V_1$ and $E = E_1$. Now, if n volume elements are assumed, the current flowing through R_2 is given by

$$i_t - i_1 = \sum_{j=2}^{n} i_j$$

and the potential appearing at the second volume increment is

$$E_2 = E_1 - R_2 \sum_{i=2}^{n} i_i$$

With knowledge of E_2 and V_2, the current i_2 is obtained, and so on until all of the individual potentials and currents have been obtained. Noting that

$$\sum_{j=1}^{n} i_j = i_t - \sum_{j=1}^{i-1} i_j \tag{3-12}$$

the equation

$$E_i = E_{i-1} - R_i\left(i_t - \sum_{j=1}^{i-1} i_j\right) \tag{3-13}$$

may be applied generally to determine the potential distribution in thin layer cells.

An iterative procedure based on equation 3-13 has been developed here to allow numerical calculation of thin layer voltammograms. Equation 3-4 is used to provide an initial estimate, i_t, of the total current flowing to the thin layer electrode. Equation 3-13 is then used as described above to calculate the potentials and currents associated with the individual volume elements. If the initial estimate agrees within 0.1% of the sum of the individual currents, it is assumed to be correct. If it does not, a new estimate is calculated according to

$$i_t' = i_t - C$$

where C is a small value of appropriate sign calculated within the program on the basis of the difference between the initial estimate and the sum of the individual currents. The procedure is then repeated until the desired degree of convergence is obtained.

The iteration was programmed in Fortran and tested on the Amdahl V-107 computer at the University of Alberta. The program was then translated into Pascal and run on a Three Rivers mini-computer. This computer had been

interfaced to a Bascomb-Turner digital X-Y recorder so that the resulting curves could be plotted directly. A Fortran version of the program used is included in appendix 4. In general, twenty volume increments were assumed for the calculations. In no case, however, was a significant difference in the results observed upon decreasing the number of elements to 10.

The program has been used to predict the effects of various parameters on the resistance induced asymmetry of the thin layer voltammetric waves. The results are presented in Figures 13 to 17. All of the curves are anodic, and the potential is scanned from left to right. The potential scan rate assumed in all cases is 5 mV/s, the thickness of the thin layer is 10 μm, and the concentration of electroactive species is 1 mM. Other parameters are listed in the figures as follows: dref is the distance between the Luggin tip and the edge of the working electrode, ρ is the solution resistivity, r is the radius of the working electrode in the concentric radial configuration, and w and h are the width and length of the working electrode in the OTTLE configuration, w being considered parallel to the secondary electrode. In all of the figures the central curve, marked a, is that calculated directly from equation 3-4 assuming zero solution resistance. For purposes of comparison and clarity, all other curves are normalized to this one.

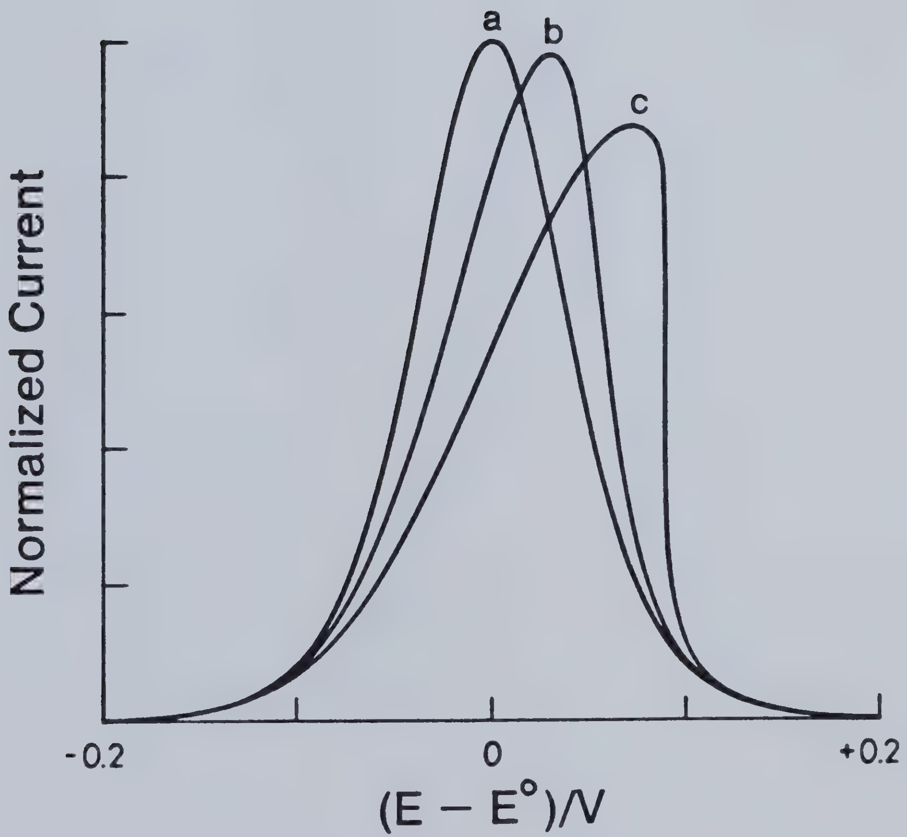

Figure 13. Effect of increasing vertical dimension of the working electrode in the OTTLE configuration: ρ = 250 Ω-cm; dref = .1 cm; w = .354 cm;

(a) theoretical response with $\rho = 0$
(b) h = .177 cm
(c) h = .354 cm

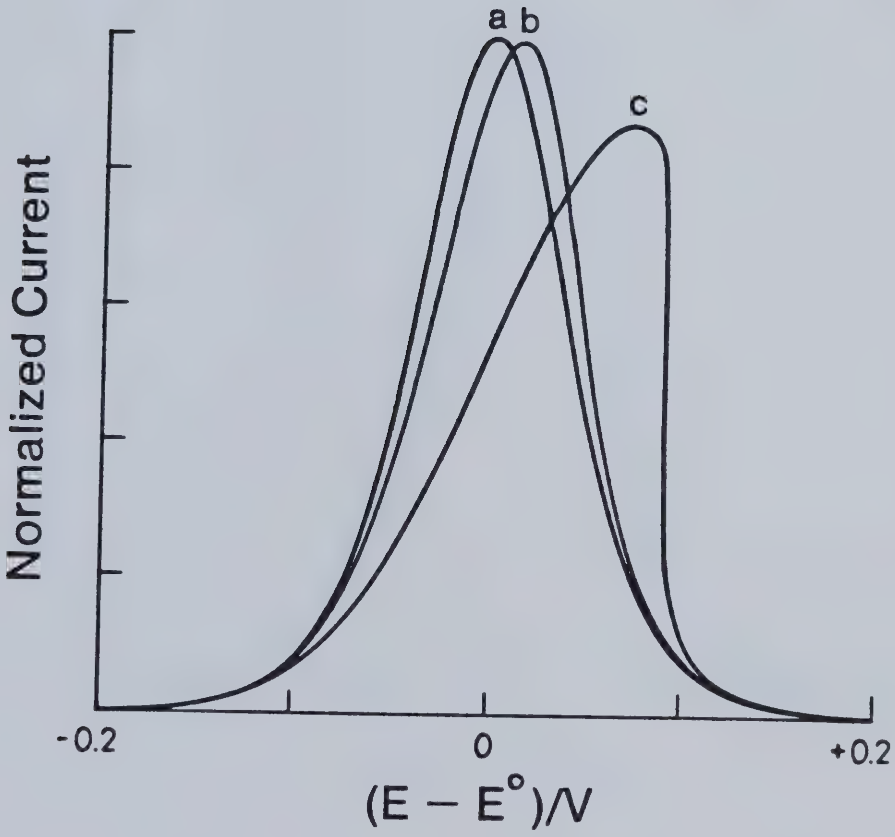

Figure 14. Comparison of resistive effects on calculated voltammograms at OTTLE (c) and radial (b) thin layer electrodes of equal area: ρ = 250 Ω cm; dref = .1 cm.

(a) theoretical response with ρ = 0
(b) r = .2 cm
(c) h = w = .354 cm

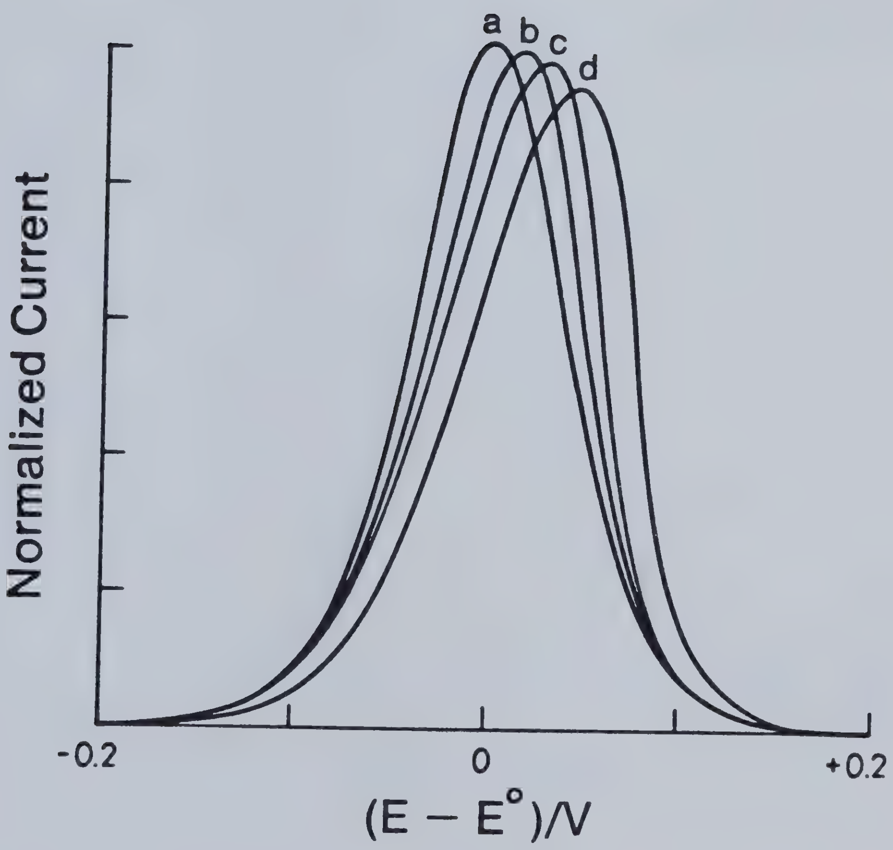

Figure 15. Effect of solution resistance on calculated voltammograms at radial thin layer electrode: r = .4 cm; dref = .1 cm

(a) theoretical response with $\rho = 0$
(b) $\rho = 100$ Ω-cm
(c) $\rho = 200$ Ω-cm
(d) $\rho = 300$ Ω-cm

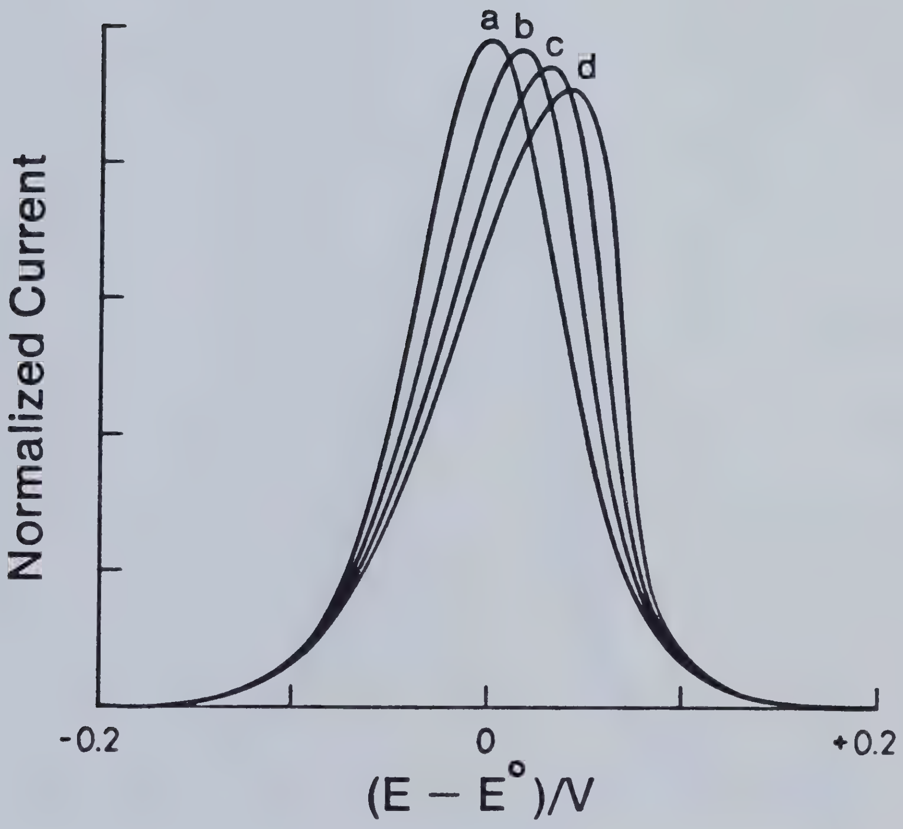

Figure 16. Effect of electrode radius on calculated voltammograms at radial thin layer electrode:
ρ = 250 Ω-cm; dref = .1 cm.
(a) theoretical response with ρ = 0
(b) r = .2 cm
(c) r = .3 cm
(d) r = .4 cm

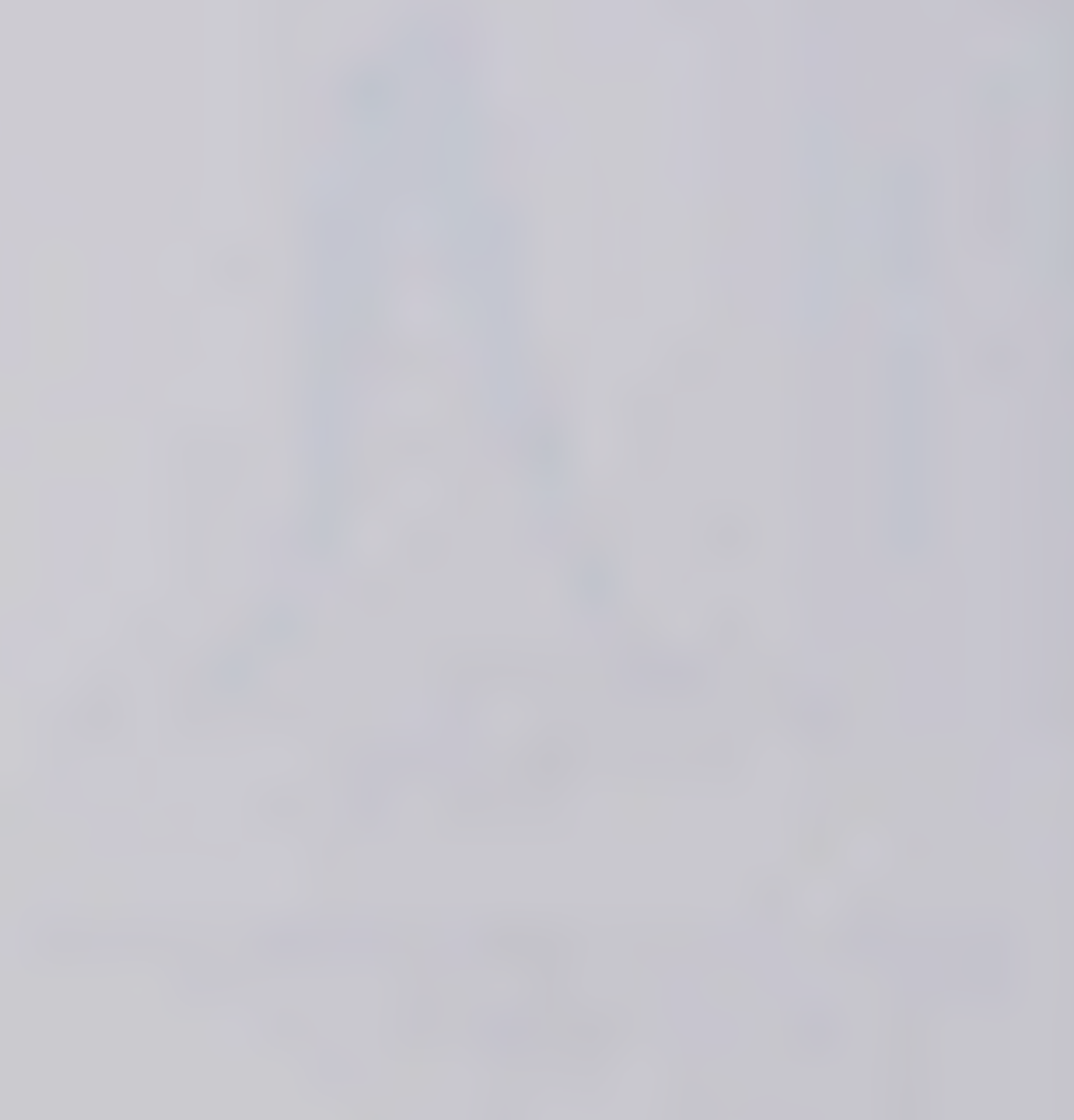

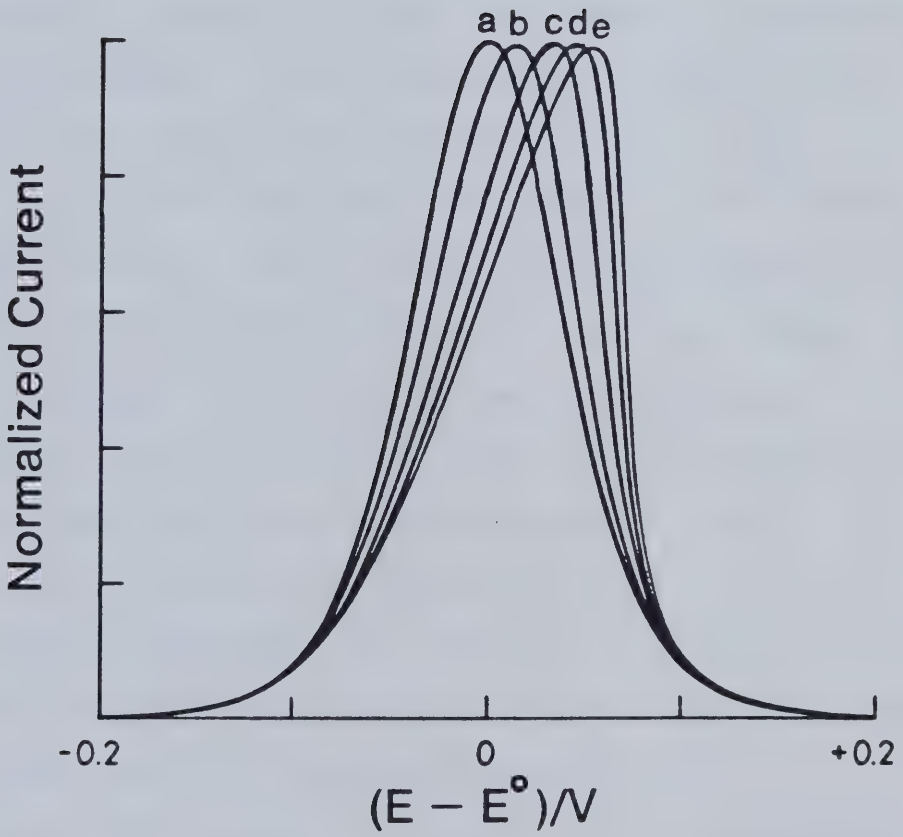

Figure 17. Effect of displacing Luggin capillary on calculated thin layer voltammograms at radial thin layer electrode: ρ = 250 Ω-cm; r = .2 cm.

(a) theoretical response with ρ = 0
(b) dref = .1 cm
(c) dref = .5 cm
(d) dref = 1.0 cm
(e) dref = 1.5 cm

Figure 13 illustrates some results calculated for the OTTLE configuration. The solution resistance used here, $\rho = 250$ ohm-cm, corresponds roughly to that expected [83] for the commonly used solvent/electrolyte system CH_3CN/0.1 M TBAP. The resistive potential drops in this case occur along the dimension h, and this parameter therefore determines the degree to which the curves are affected by ohmic polarization. The dimension h in Figure 13c is 0.354 cm, and is much less than that used in most conventional OTTLE designs. The effect of the solution resistance can be reduced dramatically by decreasing h, as in Figure 13b, where this dimension has been halved. The same effect can be achieved by using two counter electrodes placed parallel to and at equal distances from opposite edges of the working electrode. These considerations led to the design of the spectroelectrochemical cell discussed in Chapter 2. A similar design has been employed by Goldberg et al. [90] in combined esr-electrochemical experiments.

Figure 14 compares the results of the calculation for the OTTLE configuration with those obtained for a radial concentric geometry where the area of the two working electrodes, and all other parameters, are identical. This figure clearly illustrates the superiority of the radial configuration. In comparing Figures 13b and 14b, it is

evident that the radial configuration should provide better results than an OTTLE cell of half the working electrode area. Geometry is clearly an extremely important factor in thin layer electrochemical cell design.

Figures 15 and 16 illustrate the effects of varying the solution resistivity and the electrode radius, respectively, for the radial configuration. In comparing the two figures it is evident that, at least for radii in the 2 to 4 mm range and solution resistivities in the 300 ohm-cm vicinity, decreasing the electrode radius by 1 mm has very nearly the same effect as decreasing the solution resistivity by 100 ohm-cm. Thus, when forced to work in highly resistive media, smaller electrodes should give better results. It should be noted, however, that diffusion of electroactive material into the thin layer cavity, which has been ignored in these calculations, will become more important as the electrode radius is decreased. There will therefore be a limit, dictated largely by the ratio of the electrode area to the thickness of the thin layer cavity, to how small a practical electrode may be made.

Figure 17 illustrates the effects of displacing the Luggin tip to greater distances from the edge of the working electrode. The magnitude of the uncompensated

resistance, R_u, apparently has little effect on the magnitude of the peak currents, but does introduce substantial asymmetry into the voltammetric waves. Placement of the Luggin capillary is an important consideration in the design of any electrochemical cell.

The program predicts that the thickness of the thin layer cavity has no effect on the normalized current-voltage curves. This result is readily predictable. While the individual resistance increments decrease in direct proportion to an increase in the thin layer thickness, the individual volumes, and hence the currents, increase. The individual iR potential drops across the working electrode therefore remain constant, and the potential distribution is unaffected.

The effect of other factors which affect the magnitude of the current, but not the resistance increments, can be readily predicted. Hence, an increase in either the sweep rate, ν, or the concentration of electroactive species will result in an increase in current, and a corresponding deterioration in the quality of the voltammograms will be observed.

3.4 Experimental

A thin layer cell was constructed using the radial concentric configuration, and its performance evaluated in a variety of solvent-electrolyte systems. Two electrodes were tested. The first consisted of a planar glassy carbon disc, ca 3 mm in diameter, sealed with epoxy into a glass tube. The second consisted of a 1.5 mm diameter Pt wire press fitted into the end of a Teflon tube such that the tip of the wire was flush with the lower surface of the tube. The wire was offset in the tube, allowing for closer proximity of the Luggin tip and the edge of the working electrode. The experimental arrangement, including a detail of the offset platinum button electrode, is illustrated in Figure 18. The secondary electrode used was a platinum wire formed into a circle concentric with the working electrode circumference.

Both electrodes were machined flush to the lower surface of the Teflon mounting block by inserting the electrode into the block, tightening the securing screw, and working the lower surface of the assembly across a piece of 600 wet and dry sandpaper placed on top of a piece of heavy plate glass. This was followed by polishing with 0.05 μm alumina on a soft polishing felt, mounted on plate glass, until the working electrode exhibited a mirror-like finish.

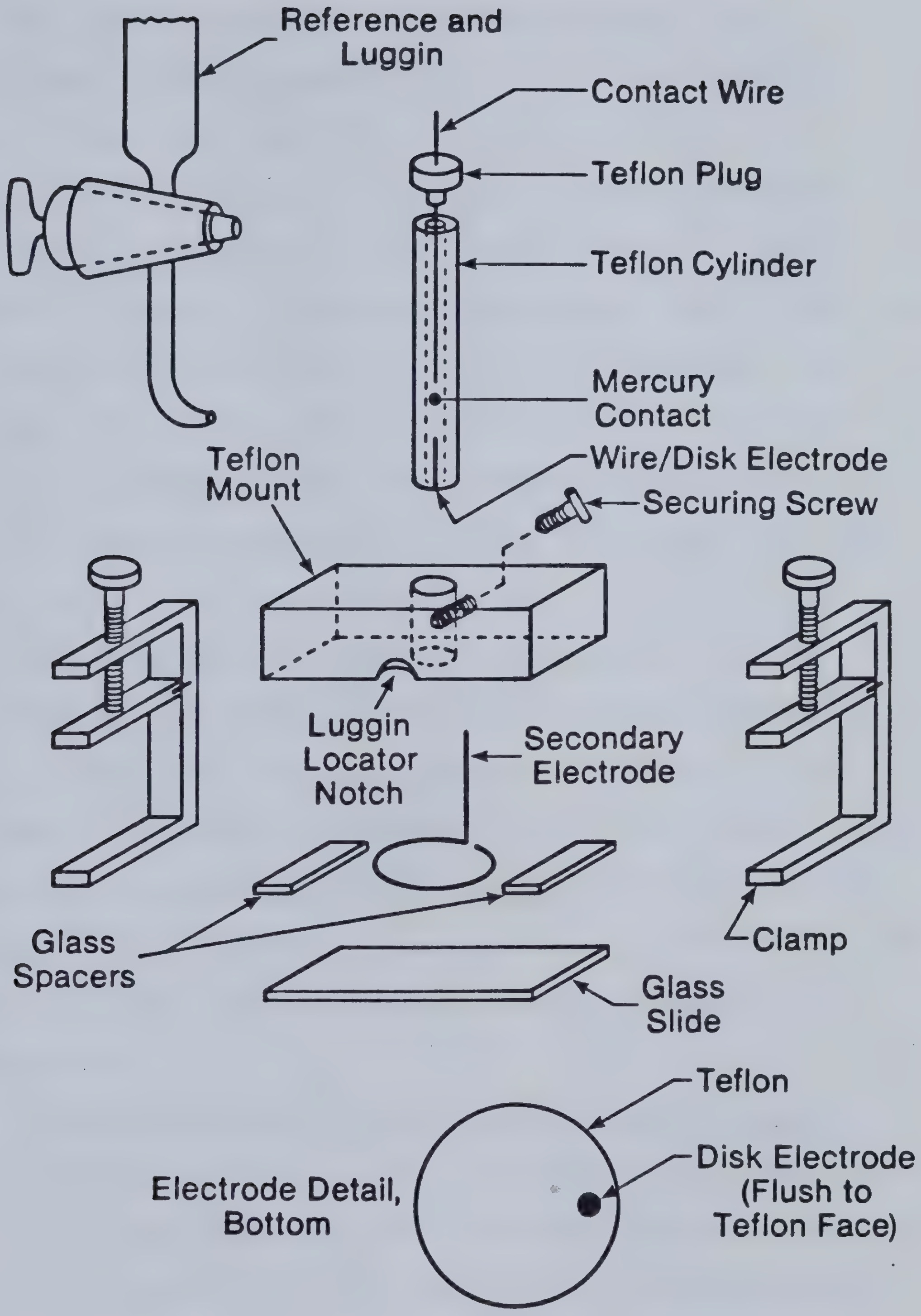
Reference and Luggin
Contact Wire
Teflon Plug
Teflon Cylinder
Mercury Contact
Wire/Disk Electrode
Teflon Mount
Securing Screw
Luggin Locator Notch
Secondary Electrode
Glass Spacers
Clamp
Glass Slide
Teflon
Electrode Detail, Bottom
Disk Electrode (Flush to Teflon Face)

Figure 18. Details of thin layer electrode assembly.

The Teflon mount and electrode assembly was positioned above the surface of a microscope slide by means of two glass spacers cut from a second glass slide. The spacers and slide were fixed to the bottom of the Teflon mount with the aid of two laboratory pinch clamps. A piece of glassine powder paper (Eli Lilly) was then placed between the surface of the microscope slide and the working electrode, and the electrode was then pushed, as firmly as possible without breaking the glass, onto it. After tightening the securing screw, the powder paper could be pulled out of the thin layer cavity, providing adequate polishing of the working electrode surface had been accomplished. The entire assembly was then lowered into a beaker containing the solution of interest. In order to exclude contamination by O_2 or H_2O, experiments were carried out in a polyethylene glove bag flushed with dry argon. A glass cover was placed over the beaker in order to help prevent solution losses from evaporation.

The thickness of the thin layer cavity was found to vary between 5 and 15 μm, as calculated on the basis of the charge required to completely electrolyze a known quantity of material within the cavity. Once a suitable thin layer thickness was attained (<10 μm to minimize diffusion into the cavity), the assembly could be used

repetitively provided repositioning of the working electrode had not occurred. Rinsing of the electrode cavity was achieved by directing a rapid stream of fresh solution at the edge of the working electrode from the tip of a disposable pipet inserted into the Luggin locator notch. Ten such rinsings were always found to produce reproducible results.

The Hi-Tek potentiostat was found to be particularly unstable when used with this cell assembly, and frequently drifted into oscillation during the course of an experiment. This problem was rectified by the inclusion of a 100 pF capacitor, shunting the reference and secondary electrodes, in the experimental hook-up. The use of such stabilizing capacitors is common [83]. Because the level of the currents measured was exceptionally small, a Bentham model 210E current follower, capable of measuring currents in the pA to μA range, was used instead of the current follower incorporated into the potentiostat. In coulometric experiments, a conventional operational amplifier based integrator, constructed in this laboratory, was used to monitor the charge passed. Positive feedback compensation of iR_u was not employed in any of the thin layer experiments.

3.5 Results and Discussion

Figure 19a presents a cyclic voltammogram obtained in 1 M aqueous KCl containing 1 mM $K_4Fe(CN)_6$ at the glassy carbon thin layer electrode. The $Fe(CN)_6^{-3}/Fe(CN)_6^{-4}$ redox couple is known to be a reversible one-electron system (Chapter 4). The small difference in the anodic and cathodic peak potentials, $\Delta E_p = 30$ mV, corresponds to near ideal thin layer behaviour, and the width of the forward peak at half-height is 105 mV, in good agreement with the 90 mV prediction of equation 3-7 for a reversible one-electron process. The formal potential of the redox couple was estimated as the average of the forward and reverse peak potentials, and is identical to the value of 0.219 volts vs SCE obtained for the half-wave potential by conventional cyclic voltammetry under the same conditions.

Figure 19b illustrates the charge passed as a function of potential as recorded during the anodic sweep of Figure 19a. Potential scanning coulometry at thin layer electrodes has been used previously [91], but the method of defining the endpoint was not discussed. In general, three essentially linear regions are observed in the coulometric wave. The slowly rising region at the foot of the wave is due to integration of the residual charging current, while that at potentials well past the formal potential of the redox couple represents, to a

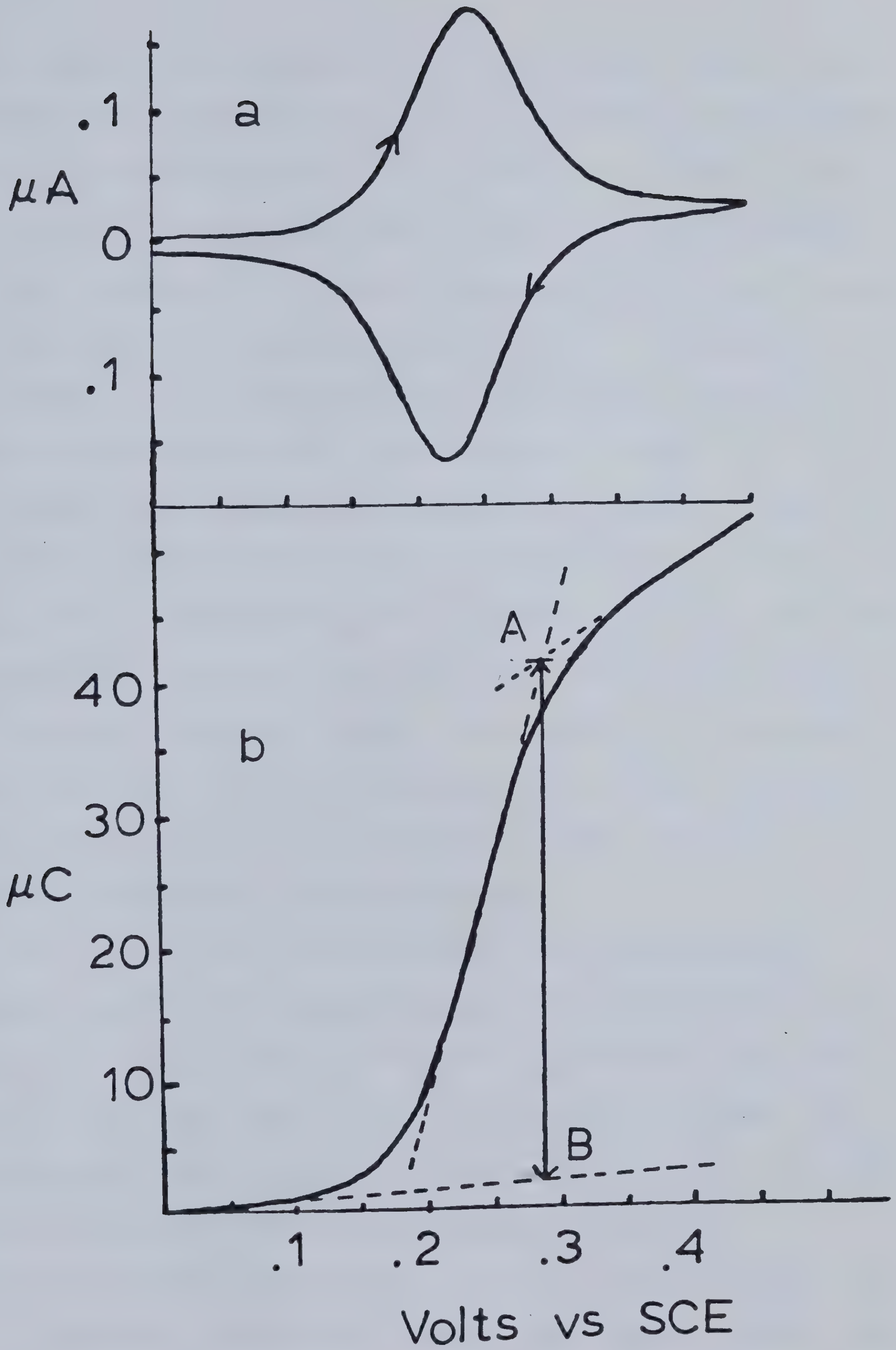

Figure 19. (a) Cyclic voltammogram of 1 mM $K_4Fe(CN)_6$ at glassy carbon thin layer electrode in 1 M aq. KCl, ν = 5 mV/s. (b) Charge vs potential recorded during forward sweep of voltammogram in (a).

large extent, the diffusion of electroactive species into the thin layer cavity from the bulk solution. The rapidly rising portion in between the two extremes is due to the electrolysis of the electroactive species trapped within the thin layer next to the working electrode. The charge corresponding to complete electrolysis of the analyte has been taken as that lying between the points A and B in Figure 19b as obtained by the indicated linear extrapolations. Figure 20 illustrates a plot of charge vs concentration for the oxidation of ferrocyanide ion in 1 M aqueous KCl as obtained by this method. Although the data is admittedly somewhat limited, the linearity of the plot and the zero intercept suggest the validity of the method used. The four points all lie within 3% of the indicated line. This precision is in excess of that usually required for n-value determinations.

While the glassy carbon electrode is apparently adequate for use in aqueous systems, its performance in nonaqueous systems was not deemed satisfactory. For the oxidation of Zn(II)TPP in dichloroethane solutions, the forward and reverse peaks were separated in excess of 250 mV even when very low sweep rates were used, and resolution between successive electron transfer steps was not as complete as had been hoped. For these reasons, the platinum thin layer electrode, as already described, was

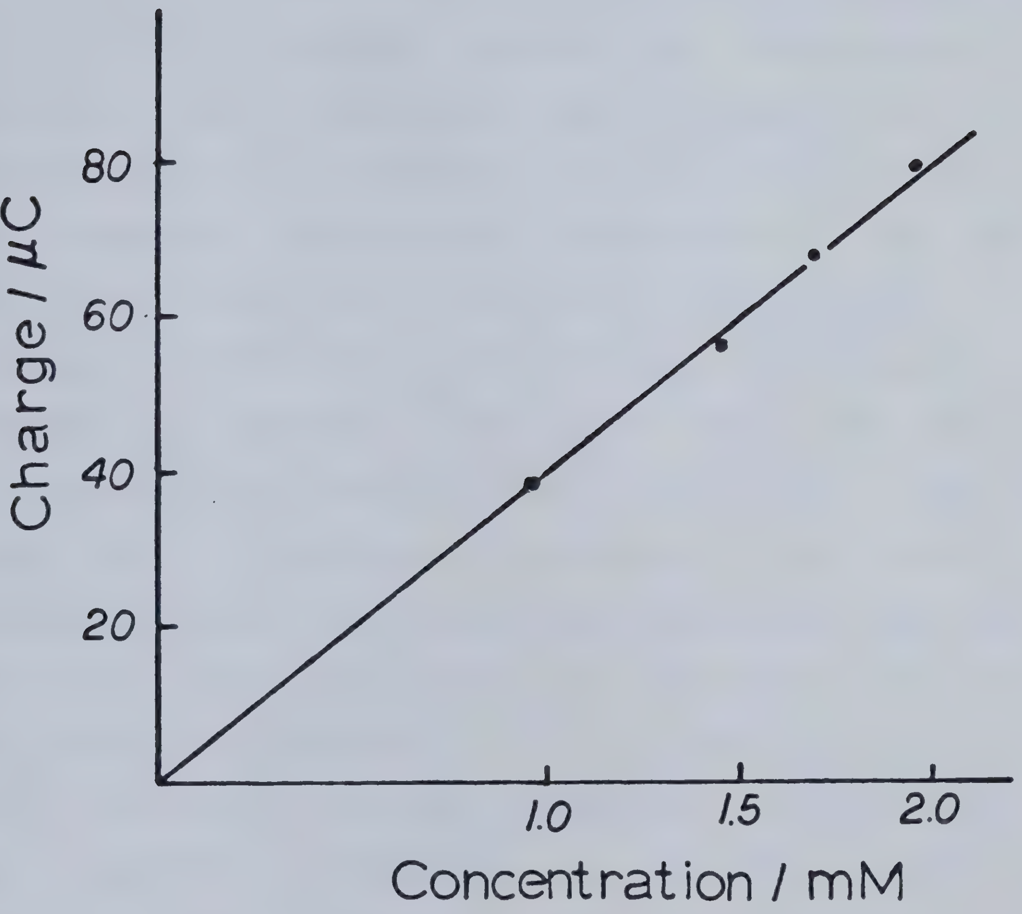

Figure 20. Charge vs concentration for 1 M aq. KCl solutions of $K_4Fe(CN)_6$ as determined by potential scanning coulometry at the glassy carbon thin layer electrode. Sweep rate employed was 5 mV/s.

constructed on the basis of predictions that the smaller electrode radius would improve the performance of the thin layer cell.

Figure 21 illustrates thin layer cyclic voltammograms at the platinum electrode obtained for 1 mM ferrocene in CH_3CN/0.1 M TBAP at potential sweep rates of 10, 100, and 200 mV/s. At potential sweep rates of 10 mV/s or less, the forward and reverse peaks are separated by less than 50 mV. At a sweep rate of 100 mV/s, the peaks are separated by 120 mV, while at 200 mV/s, a 210 mV peak separation is observed. These latter sweep rates are far in excess of those commonly used. The ability to vary the sweep rate is an important consideration in work where qualitative mechanistic diagnosis of electrode reactions is sought, and is responsible to a large extent for the popularity of conventional cyclic voltammetry. In at least some cases, thin layer techniques should be even more powerful in this regard. Some indication of this has appeared in the literature [92-94], and should be apparent in subsequent chapters of this thesis.

It will be noticed, with reference to Figure 21, that the voltammograms obtained at higher sweep rates, although exhibiting a greater degree of asymmetry, are in fact better defined against the background. This is due to the fact that currents associated with diffusion from the

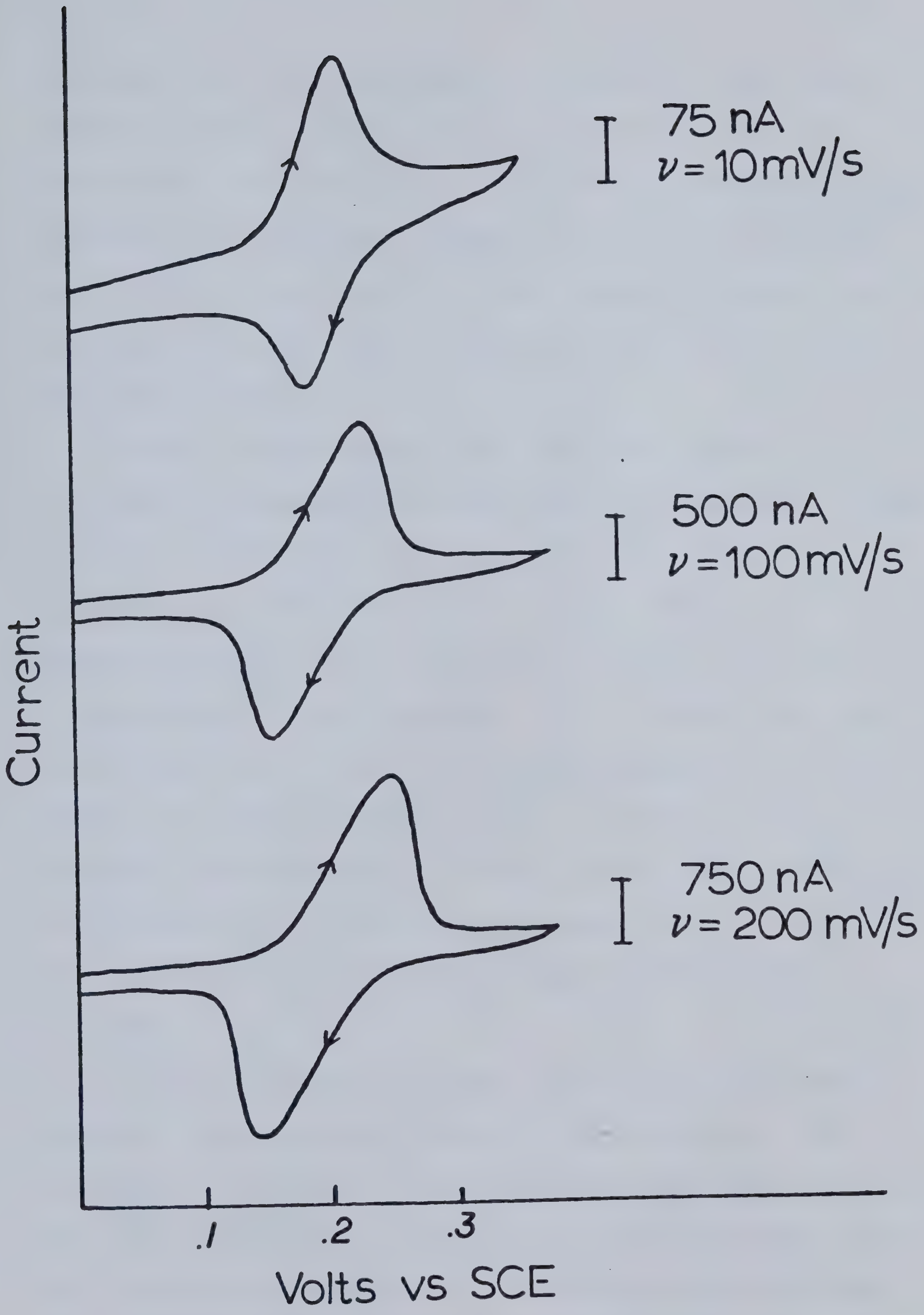

Figure 21. Cyclic voltammograms of 1 mM ferrocene at Pt thin layer electrode in CH_3CN(.1 M TBAP).

solution bulk are independent of potential scan rate, while the peak currents increase with scan rate, as indicated by equation 3-4. The greater influence of bulk diffusion at electrodes of smaller radius, as earlier predicted, is manifested in the increased current observed at potentials past the forward peak in the lower sweep rate voltammograms.

Figure 22 illustrates the thin layer cyclic voltammetric behaviour of Zn(II)TPP in $C_2H_4Cl_2$/0.2 M TBAP at anodic potentials. The two successive anodic waves correspond to formation of the cation radical and dication, respectively, while the cathodic waves are due to reduction of these species. At low sweep rates near ideal behaviour is observed for this system. At 3 mV/s forward and reverse peaks for the individual redox processes are separated by 30 mV and the peak widths at half-height are 110 mV. Even at sweep rates as high as 100 mV/s successive redox processes are completely resolved.

Figure 23 presents charge versus potential plots recorded during anodic sweeps for this system. The coulometric waves were recorded at various sweep rates and have been successively displaced by 200 mV in the figure for purposes of clarity. It is evident that the waves become much better defined as the sweep rate is increased,

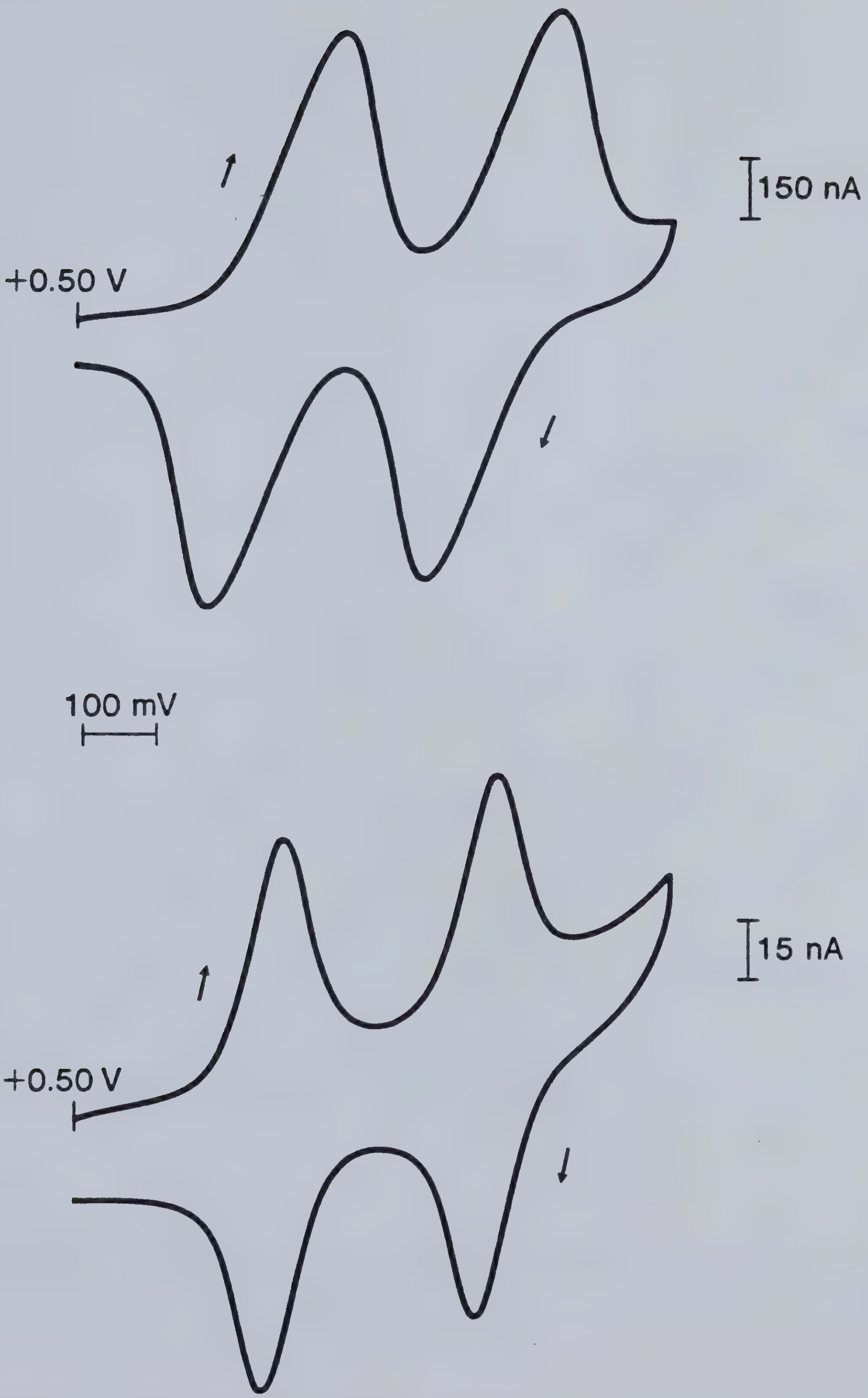

Figure 22. Cyclic voltammograms of 1 mM Zn(II)TPP at Pt electrode in $C_2H_4Cl_2$(.2 M TBAP). Upper curve, ν = 100 mV/s; lower curve, ν = 5mV/s.

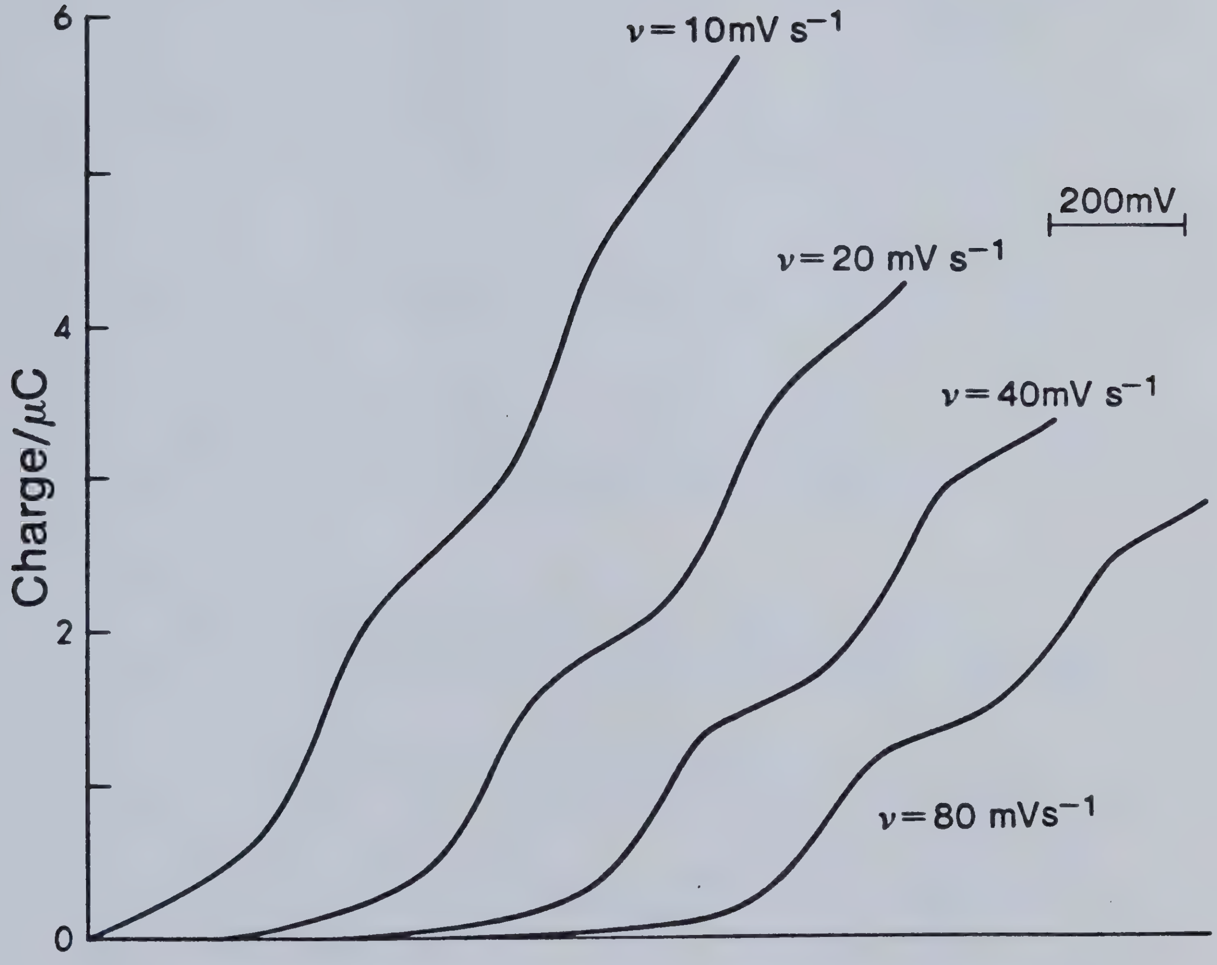

Figure 23. Potential scanning coulometry for 1 mM Zn(II)TPP at Pt thin layer electrode in $C_2H_4Cl_2$(.2 M TBAP) as recorded at various sweep rates.

and the electrolysis endpoints are therefore more easily determined.

Figure 24 illustrates the apparent charge required for complete electrolysis in the first anodic wave plotted as a function of potential sweep rate. The endpoints were determined by the method previously outlined in Figure 19b. At lower sweep rates there is a trend to higher values. This can be ascribed to the longer time period available for diffusion of reactant into the thin layer cavity during the course of the experiment. At sweep rates greater than 20 mV/s, a constant value is obtained, and higher sweep rates are therefore recommended for coulometric work.

Figure 25 illustrates the thin layer cyclic voltammetric behaviour observed at the platinum electrode for the oxidation of tetra(n-butyl)ammonium iodide in CH_3CN/0.1 M TBAP. The successive anodic waves correspond to the oxidation of I^- and I_3^-, respectively, while the cathodic waves represent the reduction of I_2 and I_3^-. The pertinent equilibria, as indicated by Popov and Geske [95], are

$$3I^- - 2e^- \rightleftarrows I_3^- \qquad (3\text{-}14)$$

and

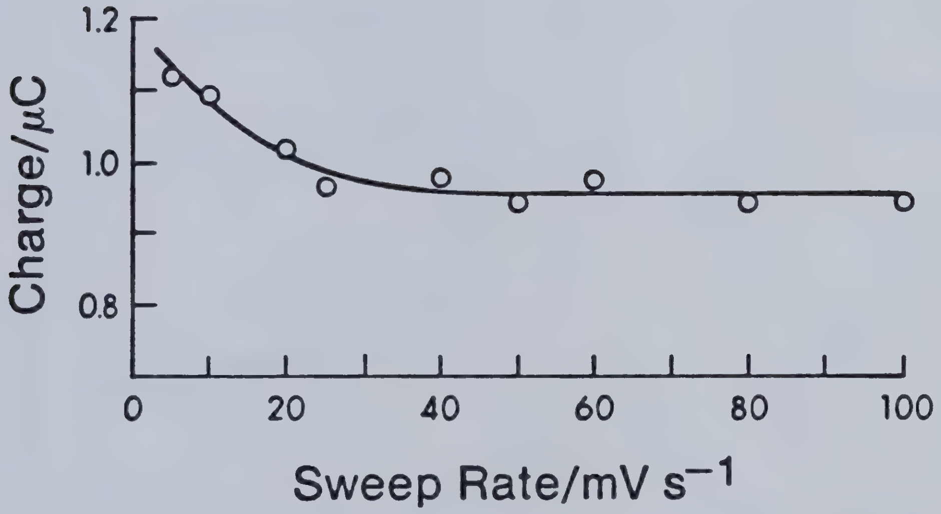

Figure 24. Apparent charge required for complete 1-electron oxidation of 1 mM Zn(II)TPP in $C_2H_4Cl_2$(.2 M TBAP) as determined by potential scanning coulometry at Pt thin layer electrode at various sweep rates.

Figure 25. Cyclic voltammogram of 2 mM I^- in CH_3CN(.1 TBAP) at Pt thin layer electrode.

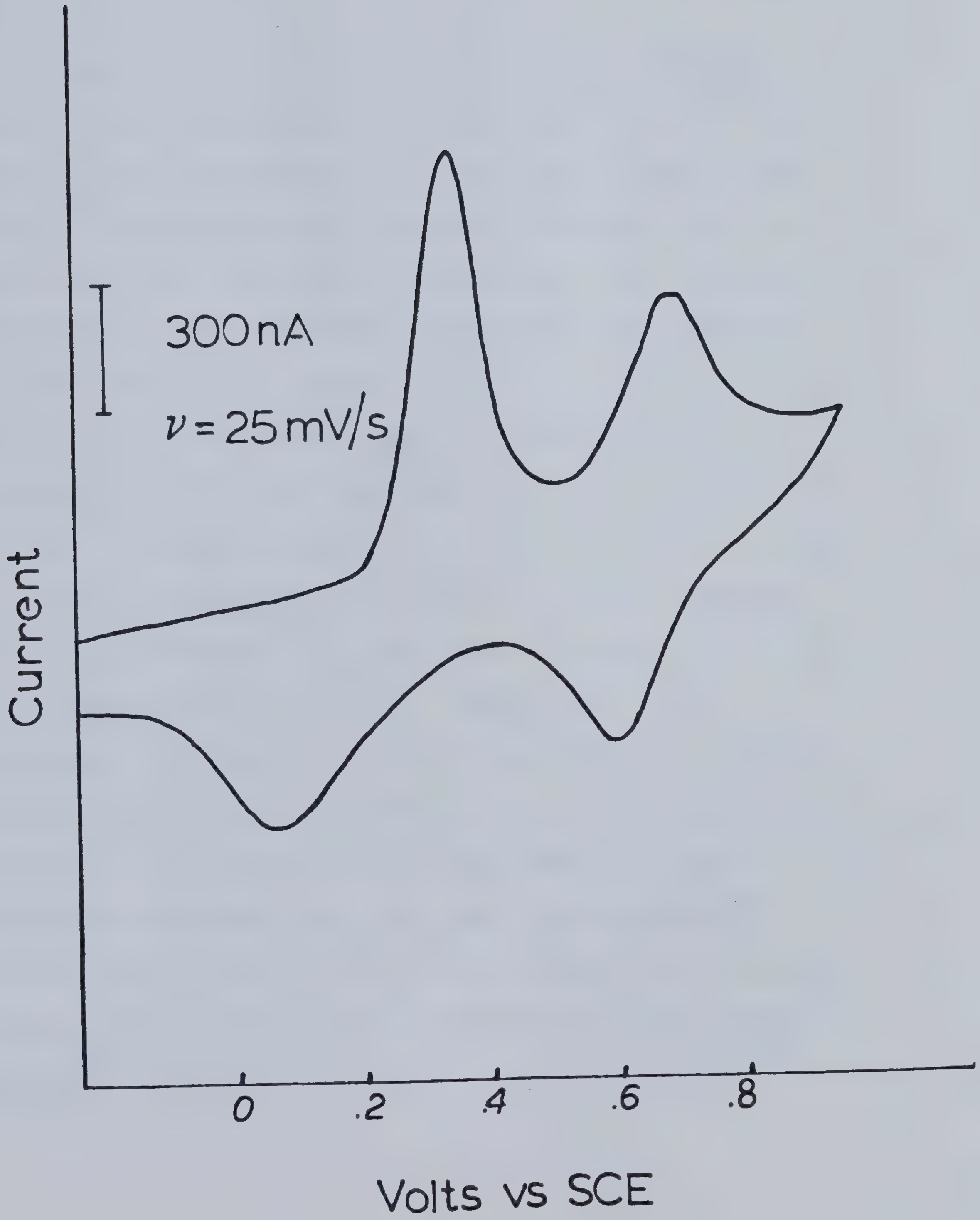

$$2I_3^- - 2e^- \rightleftarrows 3I_2 \qquad (3\text{-}15)$$

Figure 26 is a plot of the charge required for complete conversion of the I^- within the cavity to I_3^-, as determined by the methods described here. Again, the linearity of the plot and the zero intercept serve to demonstrate the validity of the method. The precision indicated by this experiment is ±5% absolute deviation.

The ratio of the charge associated with the second oxidation in Figure 25 to that for the first was determined as 0.50 when the sweep rate was 25 mV/s, and 0.46 when the sweep rate was 100 mV/s. The former value is in better agreement with the ration of 1/2 expected from the stoichiometry of reactions 3-14 and 3-15. The lower value obtained at higher sweep rates is not understood. The ratio of the charge associated with the second oxidation of Zn(II)TPP to that of the first was observed to be independent of sweep rate. It must therefore be assumed that the sweep rate dependence observed here is due to some unknown factor in the anodic chemistry of I^-, rather than a problem with the method employed.

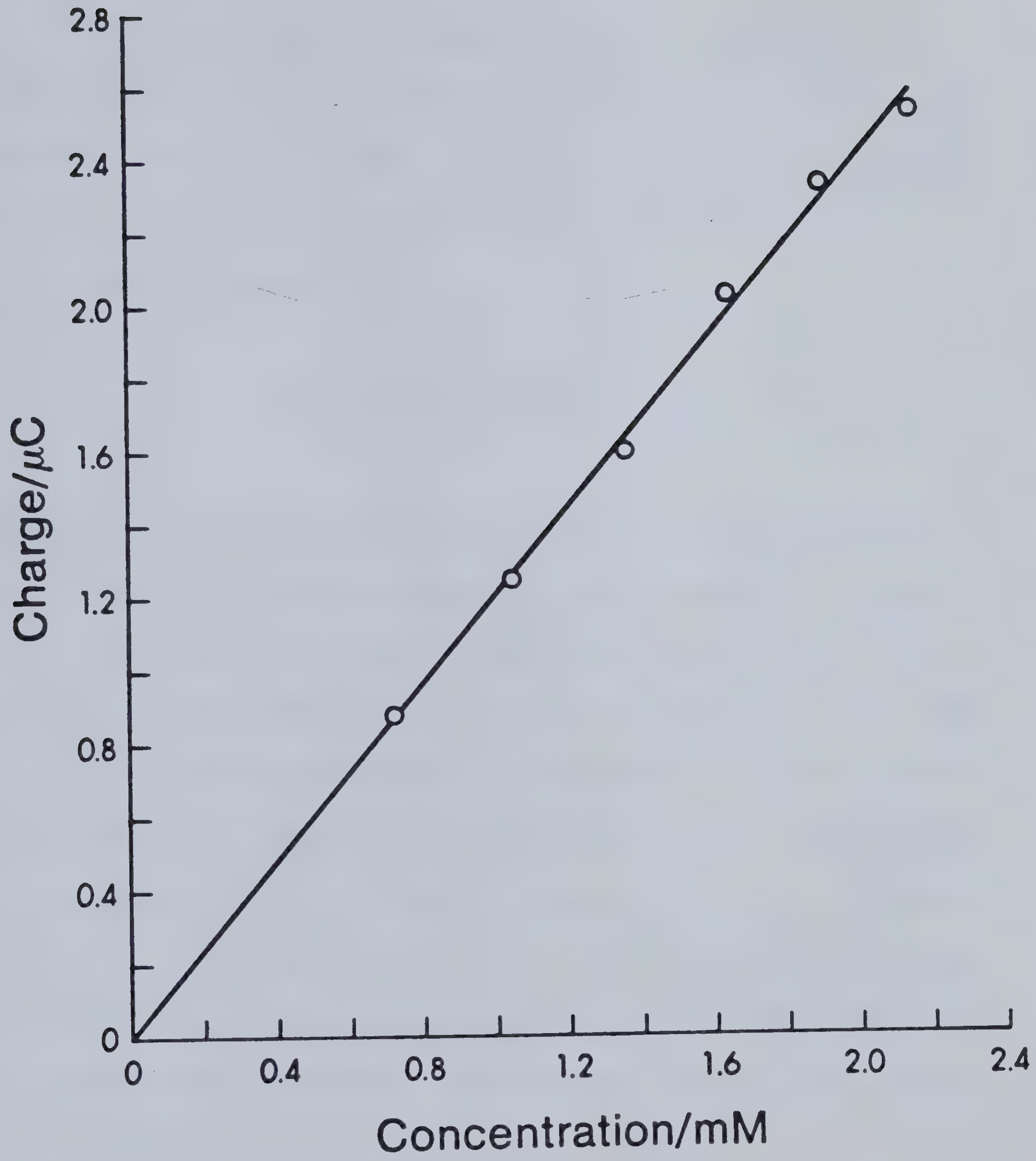

Figure 26. Charge vs concentration for first oxidation of I^- in CH_3CN(.1 M TBAP) as determined by potential scanning coulometry at Pt thin layer electrode.

3.6 Chronocoulometry at Immersed Thin Layer Electrodes

In conventional voltammetric cells, when the electrode potential is suddenly pulsed to a value where a Faradaic electron transfer process occurs at a diffusion controlled rate, the charge vs time behaviour [96], at later times, is given by

$$Q = \frac{2nFAD^{1/2}C^{*}t^{1/2}}{\pi^{1/2}} + Q_{DL} \qquad (3\text{-}16)$$

where Q is the total charge passed, D is the diffusion coefficient of the electroactive species and C* is its bulk concentration. Q_{DL} is the charge associated with charging of the double layer and A is the electrode area.

If the same experiment is carried out at an immersed thin layer electrode, the charge recorded at times after that corresponding to complete electrolysis of the species within the thin layer cavity will be dictated solely by diffusion into the cavity. By analogy to equation 3-16, the charge-time transient obtained at later times should follow an equation of the form

$$Q = \frac{2nFA'D^{1/2}C^{*}t^{1/2}}{\pi^{1/2}} + Q' \qquad (3\text{-}17)$$

where A' is the exposed surface area of the cylinder contained between the working electrode surface and the glass insulator, and Q' is a constant dictated by the length of time required for complete electrolysis of the species within the thin layer cavity. A plot of Q vs $t^{1/2}$ should therefore exhibit a linear region at later times. The line should be displaced along the Q axis by some amount allowing the determination of n and A', and its slope should then allow the determination of D. The parameters n and D should therefore be available from a single experiment. In most other voltammetric techniques, cyclic voltammetry and chronoamperometry, for instance, only the product $nD^{1/2}$, or $n^{3/2}D^{1/2}$ is available.

Figure 27 presents a Q vs $t^{1/2}$ plot obtained for the one-electron oxidation of $(ClO_4)Mn(III)TPP$ in $C_2H_4Cl_2$/.2 M TBAP at the platinum thin layer electrode. The background charge was obtained in a separate experiment in the absence of electroactive species and was subtracted from the data. The predicted linear behaviour is indeed observed at later times. The charge indicated at point A in the figure is 4% less than that indicated by potential scanning coulometry as corresponding to complete electrolysis of the species within the thin layer cavity. Experimental evaluation of the applicability of the proposed method to the simultaneous determination of

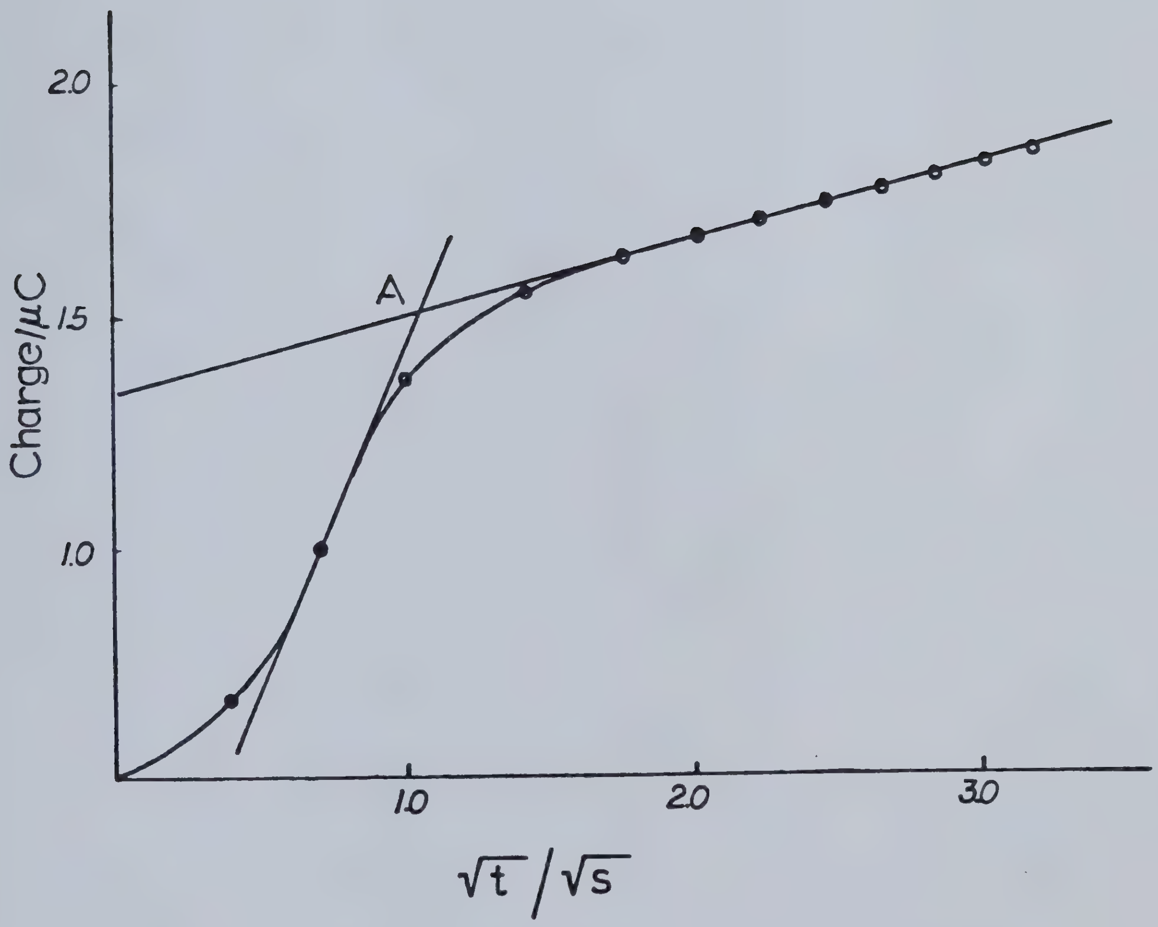

Figure 27. Charge vs $t^{\frac{1}{2}}$ for 1-electron oxidation of $(ClO_4)Mn(III)TPP$ in $C_2H_4Cl_2$(.2 M TBAP) at Pt thin layer electrode under potential step conditions.

n-values and diffusion coefficients has been reserved for a later project.

CHAPTER 4

ALTERNATING CURRENT METHODS

4.1 Introduction

As noted in Chapter 1, there has been considerable interest in the determination of heterogeneous rate constants for metalloporphyrins in hopes that such data might profit our understanding of the electron transfer process in metalloporphyrin containing enzymes. A number of factors [11], such as metal position in the porphyrin plane, changes in spin state accompanying metal oxidation or reduction, and solvation effects, have been suggested to play important roles in determining the rate at which a particular porphyrin undergoes electron transfer. Attempts at correlating metalloporphyrin heterogeneous electron transfer rate constants with such factors have not been very successful to date, however. It is evident that much more data is required before an overall picture of the important factors governing metalloporphyrin electron transfer mechanisms can be developed.

Cyclic voltammetry appears to be the only method which has been applied to the determination of

heterogeneous electron transfer rate parameters in metalloporphyrins. Although this technique is extremely powerful for qualitative diagnosis of electrode reactions, especially when these are coupled to homogeneous reactions, it is generally not noted by electrochemists to be particularly accurate or precise when applied to the determination of heterogeneous rate parameters [78], especially when the associated rate constant is large.

When the difference in the peak potentials obtained on the forward and reverse peaks is greater than the theoretical value of 59/n mV predicted for a reversible electron transfer, the value obtained can be compared with numerically computed working curves (see appendix 3) which provide for determination of the standard heterogeneous rate constant k_s. The value of the peak separation, ΔE_p, increases with the potential scan rate, ν. For maximum reliability in the results, ν should be chosen so that ΔE_p is in the vicinity of 100 mV [11].

The problems associated with this method are several [98]. Firstly, the peaks obtained are not sharp, and precise determination of their position is difficult. Secondly, they are distorted from their theoretical shape by the presence of the background current due to charging of the double layer capacitance. This is particularly important when higher sweep rates must be used, since the

faradaic peak currents increase as $\nu^{1/2}$, while the background current increases, in the absence of uncompensated resistance, as ν. Thirdly, but probably most importantly, the applied potential will differ from the true potential across the solution-electrode interphase by an amount iR_u, where i is the current, and R_u is the uncompensated resistance between the edge of the working electrode and the tip of the Luggin capillary.

Uncompensated resistance is particularly serious when high currents resulting from, for instance, the use of rapid scan rates, are encountered, or when work is carried out in highly resistive media, as is generally the case for metalloporphyrin studies. As pointed out in Chapter 2, most porphyrin chemists have employed electronic positive feedback compensation to minimize the problem. The method used to adjust the amount of feedback, i.e. adjustment to the limit of potentiostat stability, is less than satisfactory for precise, accurate work, however. The degree of compensation attained by this method will in fact be dependent on the electronic transfer functions of both the potentiostat and the electrochemical cell [97]. In this laboratory, it has been found that the method, as employed with the extremely high gain Hi-Tek potentiostat, may leave as much as 100 ohms of uncompensated resistance remaining. Bewick has noted [98] that, in some cases, it

is possible to overcompensate by this method. The procedure recommended by Britz [97] for handling resistance problems is to use whatever means available to minimize the uncompensated resistance, to measure that remaining, and to correct mathematically the results for its presence. That philosophy has been adopted for most of the work here.

Because of the problems inherent in the application of cyclic voltammetry to the determination of heterogeneous electron transfer parameters, the development and applicability of other methodology appropriate to porphyrin electrochemistry has been considered here. In particular, the application of alternating current methods has been dealt with.

Alternating current techniques [81,88] have long been recognized as methods of choice for the quantitative characterization of electrode processes. More recently, with the advent of linear sweep cyclic ac voltammetry [99,100], it has been shown that ac methods can retain at least as much, and often more, qualitative diagnostic information as the more popular technique of cyclic voltammetry.

4.2 Background to AC Voltammetry

In the ac voltammetric experiment, a linear potential sweep is applied to the working electrode. In cyclic versions, the direction of the sweep is reversed at some predetermined switching potential, as in conventional cyclic voltammetry. Superimposed on this slowly varying dc potential program is a small amplitude sinusoidal potential perturbation. The resulting current contains both a dc component, which is identical to that obtained in conventional voltammetry, and an ac component, associated with the sinusoidal potential perturbation. Appropriate instrumentation is then used to extract only the alternating contribution to the overall current response. Where tuned amplification is employed, the magnitude of the alternating current response of the same frequency as the applied potential modulation is plotted as a function of the applied dc potential. Where phase sensitive detection is used, the magnitude of the ac response of the same frequency as, and exhibiting some preselected phase shift with respect to, the potential modulation is determined.

The derivation of the current response to such an applied potential program is not trivial, and will not be attempted here. Particularly informative accounts of the details have been given by Smith [88], Sluyters and

Sluyters-Rehbach [101], and by Macdonald and McKubre [102]. It is constructive, however, to consider some of the assumptions involved.

It is generally assumed that the mean concentrations of the electroactive species at some distance out in the solution are fixed by the dc potential program. The ac potential program then results in small fluctuations of the concentrations next to the electrode surface about the mean. Physically, the assumption implies that the diffusion layer thickness associated with dc events is much greater than that associated with the ac process. Experimentally, the requirement is that the dc potential scan rate is much less than the product of the frequency and amplitude of the ac potential perturbation. Bond et al. have suggested [103], on the basis of extensive numerical calculations, that provided $f\Delta E > 1.6\ \nu$, where f is the ac frequency, ΔE is the potential modulation amplitude, and ν is the dc potential scan rate, then the assumption introduces no significant discrepancy between theory and experiment.

The second major assumption involves the magnitude of the applied sinusoidal potential. The derivation of practical expressions for the ac voltammetric response requires that a linear relationship exist between the faradaic current and the applied potential. The equations

of electrode kinetics, however, predict that the current is exponentially dependent on the potential (Appendix 1). In order that these exponential functions may be approximated as linear relations, the magnitude of the applied potential perturbation must be very small. Smith [88] has suggested that the assumption of small amplitude perturbation is accurate for applied sinusoidal potentials of up to 8 mV peak to peak, and for many systems does not introduce significant discrepancy between theory and experiment for modulation amplitudes of up to 20 mV. It should be noted that the non-linear relationships between the faradaic current and applied potential give rise to the presence of second and higher harmonic components in the ac response, and these, as well as the fundamental harmonic component of the current, can provide information about the electrode processes.

The fundamental harmonic ac voltammetric response may be represented [88] as the product of several functions by

$$I(\omega t) = I_{rev}F(t)G(\omega)\sin(\omega t + \phi) \qquad (4\text{-}1)$$

The function I_{rev} represents the amplitude of the faradaic alternating current for the completely reversible electrode process,

$$\mathrm{Ox} + ne^- \rightleftarrows \mathrm{Red} \qquad (4\text{-}2)$$

and is given by

$$I_{rev} = \frac{n^2F^2AC^*_{Ox}(\omega D_{Ox})^{1/2}\Delta E}{4RT\ \cosh^2(j/2)} \qquad (4\text{-}3)$$

Here, A is the electrode area, C^*_{Ox} is the bulk concentration of Ox, ω is the frequency of the applied modulation (in rad/s), ΔE is the amplitude of the potential perturbation, D_{Ox} is the diffusion coefficient of Ox, and j is given by

$$j = nF(E_{dc} - E^r_{1/2})/RT \qquad (4\text{-}4)$$

where E_{dc} is the potential associated with the linear sweep potential program, and $E^r_{1/2}$ is the reversible voltammetric half-wave potential. This differs from E°, the standard potential of the redox couple, according to

$$E^r_{1/2} = E^0 - \frac{RT}{nF}\ln[(f_R/f_{Ox})(D_{Ox}/D_R)^{1/2}] \qquad (4\text{-}5)$$

Here, f_R and f_{Ox} are the activity coefficients of Red and Ox, respectively, and D_{Ox} and D_R are the appropriate diffusion coefficients.

The function, I_{rev}, describes a bell shaped peak symmetrical about $E^r_{1/2}$. The bell shape arises from the inverse $\cosh^2$ dependence of the current amplitude on potential. I_{rev} describes the response obtained for a perfectly reversible system. The peak width at half-height is given, in this case, by 90/n mV.

The function F(t) represents a correction to the amplitude of the reversible alternating current arising from irreversibility of the dc electrode processes, and is given by

$$F(t) = (1+\exp(-j))\left(\alpha C_{Ox}+(D_R/D_{Ox})^{1/2}\beta\exp(j)C_R\right)/C^*_{Ox} \quad (4\text{-}6)$$

Here, C_{Ox} and C_R are the surface concentrations of the electroactive species, α is the charge transfer coefficient, and $\beta = 1-\alpha$. Where the surface concentrations can be predicted by the Nernst equation, F(t) does not differ from unity. For the simple quasi-reversible electrode reaction, F(t) = 1 can be achieved by selecting the dc potential scan rate slow enough. Deviations of F(t) from unity result in a separation of the forward and reverse peaks during cyclic ac voltammetric experiments.

The function, $G(\omega)$, represents a correction to the current amplitude arising from irreversibility of the electrode process in the ac time scale, and is given by

$$G(\omega) = \{2/[1 + (1 + (\frac{2\omega}{\lambda})^{1/2})^2]\}^{1/2} \qquad (4\text{-}7)$$

The parameter λ is given by

$$\lambda = k_s(\exp(-\alpha j) + \exp(\beta j))/D^{1/2} \qquad (4\text{-}8)$$

where k_s is the standard heterogeneous rate constant, and

$$D = D_{Ox}^{\beta} D_R^{\alpha} \qquad (4\text{-}9)$$

This function is much more sensitive to slow charge transfer kinetics than the corresponding dc function F(t), and for most electrode processes will equal unity only at very small ω.

The phase angle, ϕ, between the fundamental harmonic current and the applied potential, is given by

$$\cot \phi = 1 + \frac{(2\omega)^{1/2}}{\lambda} \qquad (4\text{-}10)$$

If measurements of the phase angle are made at $E_{dc} = E^r_{1/2}$, then $j = 0$, and $\lambda = 2k_s/D^{1/2}$. The phase angle is then given by

$$\cot \phi = 1 + (D/2)^{1/2}\omega^{1/2}/k_s \qquad (4\text{-}11)$$

Equation 4-11 frequently provides the basis for determination of k_s when ac techniques are employed. Note that in the limits $k_s \rightarrow \infty$, or $\omega \rightarrow 0$, i.e. when the rate of electron transfer is controlled solely by bulk diffusion, cot ϕ is unity (i.e. $\phi = 45°$).

AC techniques suffer, as do all techniques where current is measured, from the presence of uncompensated solution resistance and double-layer capacitance. Just as they are more sensitive to heterogeneous rate parameters, they are also more sensitive to the presence of extraneous background currents.

The extraction of the faradaic component of the total alternating current during an ac voltammetric experiment generally relies on the assumption that the electrode-solution interphase may be represented by an equivalent electronic circuit. Where the faradaic process is a simple charge transfer uncomplicated by coupled homogeneous reactions or physical processes such as adsorption of electroactive species accompanying the electron transfer step, the Randles equivalent circuit [104], Figure 28, is assumed. Here the total current, I_t, is the sum of the faradaic current, I_f, and the capacitive current, I_c. R_u represents the uncompensated solution resistance and C_{DL} is the double layer capacitance. These

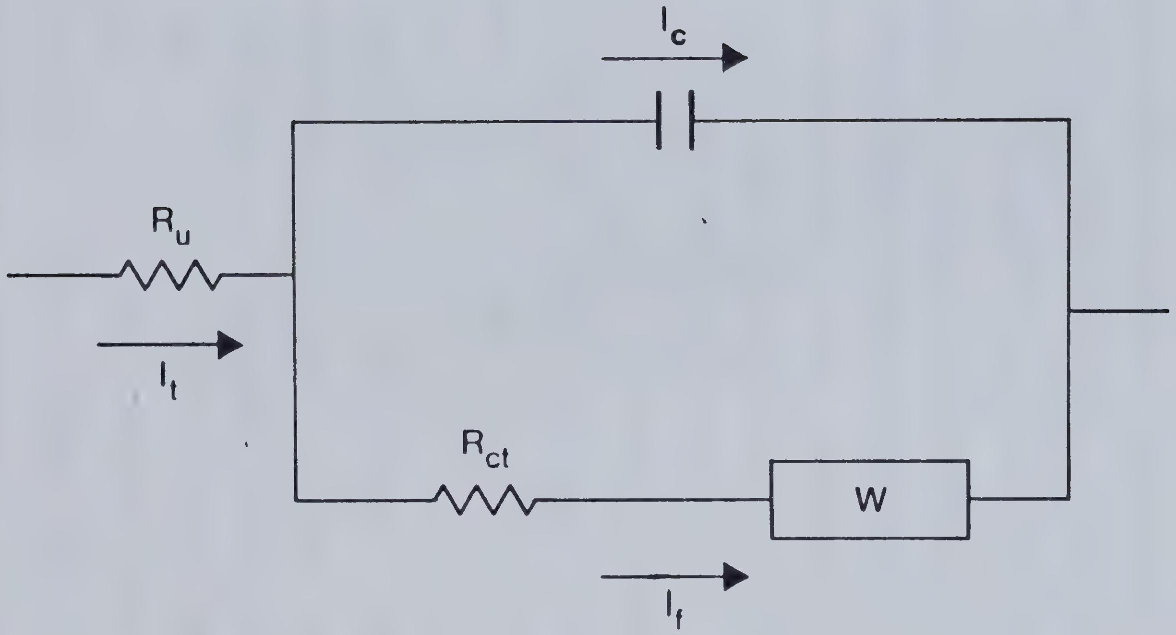
I_c
R_u
I_t
R_{ct}
W
I_f

Figure 28. The Randles equivalent circuit.

are generally determined in the absence of any electroactive species. The faradaic current flowing in the lower branch of the circuit can then be extracted from I_t by appropriate vector subtraction techniques [88]. R_{CT}, the charge transfer resistance, represents the resistance presented to faradaic current flow due to finite k_s, and W, the Warburg impedance, is a generalized frequency-dependent impedance representing resistance to mass transfer between the electrode surface and solution bulk. Once the alternating current component I_f has been determined it may be analyzed according to the ac voltammetric expressions already presented.

The method of subtracting I_c from I_t requires that the value of C_{DL} measured in the absence of faradaic current is the same in its presence. There is some question that this is the case [105]. A second problem concerns the applicability of the Randles circuit to solid electrodes. Some frequency dispersion (i.e. non-ideal behaviour) of the electrode impedance in the absence of electroactive species is very often observed in ac work at solid electrodes. This has been suggested to arise from the effects of surface roughness [106]. Other workers [107] have noted that the Hg electrode is not free from such effects and have suggested an incomplete understanding of the nature of the electrical double-layer

as being responsible for the theory-experiment discrepancies. It should also be noted that the direction of the frequency dispersion is consistent with the presence of electroactive impurities, and it is often difficult to assess to what extent this may play a role. A number of other factors related to experimental design, such as shielding of the working electrode by the Luggin capillary [101], or the presence of stray impedances within the electrochemical cell [108], may also contribute to the frequency dispersions.

Whatever the cause of the non-idealities, it is important to be able to make measurements of heterogeneous rate parameters at solid electrodes, and such measurements are frequently made. It is also important to realize that the non-idealities do not result from the methodology employed. They are due to real physical-chemical phenomena, and it cannot be assumed that they do not affect data obtained by methods other than ac techniques. It is simply easier to ignore their presence when less sensitive techniques are employed. In addition, the mathematical tractability of the ac experiment often makes it possible to evaluate the extent to which non-ideal behaviour affects the faradaic response. These considerations, and others, have led Macdonald and McKubre [102] to the conclusion that techniques based on concepts

of electrode impedance represent the most generally applicable approach to the study of electrode processes.

It would clearly be advantageous if the faradaic component of the total alternating current could be obtained without requiring knowledge of the processes which give rise to the additional currents. Some methodology which allows this has been developed here.

4.3 Spectroscopic Determination of the AC Voltammetric Response

The electrochemical literature of the past decade reveals an increasing interest in the spectroscopic monitoring of electrode reactions [109]. Although a large number of spectroscopic methods have been utilized to advantage, UV-visible absorption spectroscopy has been the most extensively exploited. One of the most important advantages of measuring the change in absorbance resulting from an electrode reaction, as opposed to measurement of the resulting current, is the additional selectivity afforded by including wavelength as an experimental variable.

UV-visible absorption spectroelectrochemistry as carried out either at optically transparent electrodes (OTE's) [110,111] or in reflectance experiments at conventional solid planar electrodes [112-117] has been

used to great advantage in the spectroscopic characterization of primary and secondary products of electrode reactions, and in mechanistic studies of homogeneous reactions coupled to an electrode reaction (see, for example, references [113-117]). Recently, Bancroft et al. [118] have extended chronocoulometric theory to spectroscopic observation at OTE's to yield a method for the determination of heterogeneous charge transfer parameters. These authors note that the additional selectivity afforded by spectroscopic determination of the electrochemical response is particularly advantageous when dealing with solvents or redox species which are difficult to purify. The absence of double layer charging contribution to the observed signals is also a distinct advantage.

Spectroscopic monitoring of porphyrin electrode reactions is particularly attractive as these species have very large molar absorptivities, and extremely good signal to noise ratios should be obtainable. This should allow electrode kinetic studies to be carried out at very low concentrations. As most metalloporphyrins are only sparingly soluble in a variety of solvents, this should, in turn, allow such studies to be carried out in a wider variety of solvents than has previously been possible.

When an alternating current results from alternate formation and removal of one form of a redox couple at the surface of an electrode surface, the intensity of a beam of light either transmitted through or reflected from the surface of the electrode will vary in accordance with the alternation of the relative concentrations of the two forms of the redox couple, provided that they have different molar absorptivities at the wavelength of the radiation. This alternation of light intensity has already been exploited in the technique of modulated specular reflectance spectroscopy (MSRS) [112-117]. In MSRS, a typically large amplitude periodic square wave potential is applied to the electrode such that first one and then the other form of a redox couple predominate periodically at the surface of an electrode. A phase sensitive detector (PSD) is used to monitor the variation in intensity of a light beam reflected from the surface of the electrode and the PSD output plotted vs wavelength provides a difference spectrum of the oxidized and reduced forms of the electroactive species. Although this technique has been used to provide qualitative support for proposed reaction mechanisms at surfaces [112] and in the diffusion layer [113-117], no example of its use in a quantitative manner exists.

It is shown here that if a small amplitude sinusoidal perturbation is superimposed on a slowly varying cyclic potential ramp applied to an electrode, the output of a PSD monitoring a light beam reflected from the electrode surface mirrors the charging current corrected ac voltammetric response. Sinusoidally modulated ac reflectance spectroscopy (SMACRS) is implemented with the same instrumentation [116] as previously used in MSRS and retains both the qualitative and quantitative utility of linear sweep ac voltammetry in conjunction with the advantages of spectroscopic observation.

As mentioned above, UV-vis absorption spectroelectrochemistry can be carried out by measurement of the intensity of a light beam either transmitted through or reflected from an electrode. Although what follows is equally applicable, in principle, to OTE's, the reflectance experiment has several important advantages. First, the intensity of a light beam transmitted through an OTE may be considerably reduced relative to that reflected from the corresponding solid electrode. Second, OTE's formed by deposition of a thin conducting film on a transparent substrate often have high resistances which may not be compensated for by positioning the Luggin capillary close to the electrode surface and can lead to uneven current distribution across the electrode

surface. Third, because in the reflectance experiment the light beam passes through the double layer twice at some angle from a normal to the electrode surface, it encounters a greater number of the species of interest. The reflectance technique is thus inherently more sensitive. Fourth, since the secondary electrode must not obstruct the light path, it is not possible in a transmission experiment to arrange the working electrode such that all points on its surface are equidistant from the counter electrode. The resulting potential distribution across the electrode surface may be particularly undesirable when working in non-aqueous electrolyte solutions or at optically transparent thin layer electrodes. For these reasons the discussion is confined to measurement of the ac response by reflectance spectroscopy.

Winograd et al. have shown [119] that for the electrode process with no homogeneous complications

$$\mathrm{Ox} + ne^- \rightleftarrows \mathrm{Red}$$

the absorbance-time profile measured at an OTE at a wavelength where only the reduced species absorbs is given by

$$A(t) = \frac{\varepsilon_R}{nFA} \int_0^t i(t)\, dt \qquad (4\text{-}12)$$

where A(t) is the absorbance, ε_R is the molar extinction coefficient of the reduced species, and other notation is conventional. If both the oxidized and reduced forms of the electroactive species absorb at the wavelength of the incident radiation, then

$$A(t) = \frac{\Delta\varepsilon}{nFA} \int_0^t i(t)\, dt \qquad (4\text{-}13)$$

where $\Delta\varepsilon = \varepsilon_R - \varepsilon_{Ox}$ is the difference in molar absorptivities of the two forms of the redox couple. Note that this equation assumes that a second identical electrochemical cell, but to which no potential program is applied, is placed in the reference compartment of the spectrometer. Otherwise, a constant must be added to the right hand side of the equation.

Where the light beam is reflected from the surface of the electrode, this result must be corrected for the fact that the light passes through the double layer twice. The coordinate system used in electro-reflectance studies is illustrated in Figure 29.

For a light beam reflecting off a planar electrode, the absorbance-time profile is obtained by integrating the number of absorbing species along the path of the light

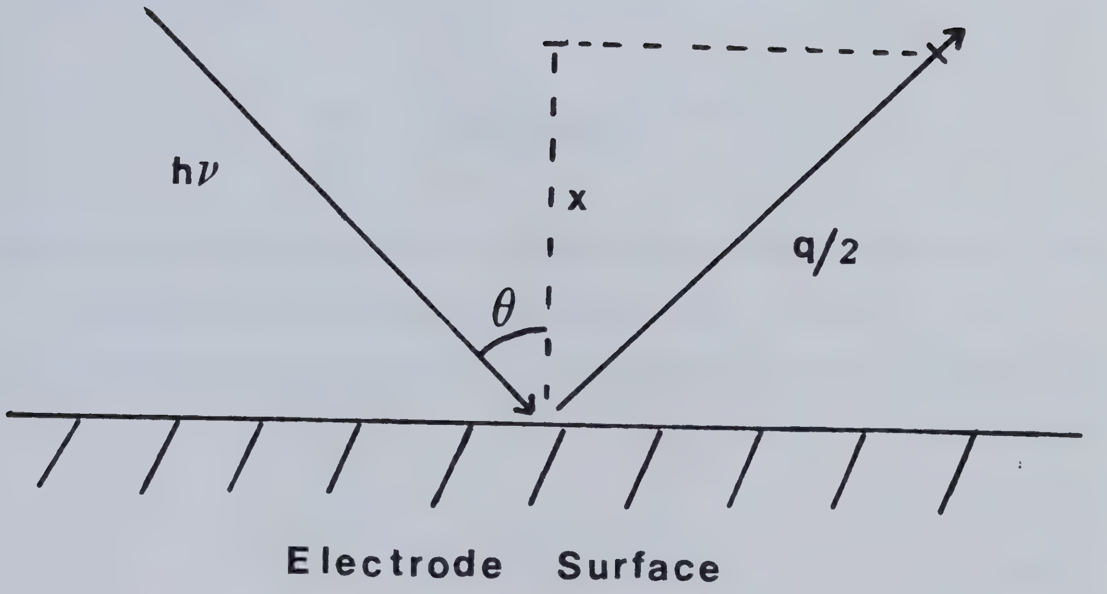
hν
x
θ
q/2
Electrode Surface

Figure 29. The coordinate system used in combined electrochemical specular reflectance spectroscopy experiments.

beam. The integration coordinate assumed in the derivation of equation 4-13 is parallel to x in the figure. In reflectance spectroscopy, the integration coordinate lies along q. Since

$$q = \frac{2x}{\cos\theta} \qquad (4\text{-}14)$$

the right hand side of equation 4-13 must be multiplied by $2/\cos\theta$ to give

$$A(t) = \frac{2\Delta\varepsilon}{nFA\ \cos\theta} \int_0^t i(t)\ dt \qquad (4\text{-}15)$$

where θ is the reflectance angle illustrated in Figure 29.

When single beam spectrometers are used in reflectance experiments, the parameter generally measured is

$$\frac{\Delta R}{R} = \frac{R(t) - R(0)}{R(0)} \qquad (4\text{-}16)$$

where R(t) is the intensity of a reflected light beam at some time t, and R(0) is its intensity at t = 0.

Since

$$\frac{R(t)}{R(0)} = 1 + \frac{\Delta R}{R} \qquad (4\text{-}17)$$

and, from the definition of absorbance,

$$A(t) = -\log \frac{R(t)}{R(0)} \qquad (4\text{-}18)$$

it follows that

$$\ln\left(1 + \frac{\Delta R}{R}\right) = -\frac{4.606\ \Delta\varepsilon}{nFA\ \cos\theta} \int_0^t i(t)\ dt \qquad (4\text{-}19)$$

This result is general provided no homogeneous complications exist, and the derivation of the spectroscopic response to a particular potential perturbation is simply a matter of performing the appropriate integration. When $\Delta R/R$ is small (values greater than 10^{-3} have only very rarely been observed) then equation 4-19 can be linearized to give

$$\frac{-\Delta R}{R} = \frac{4.606\ \Delta\varepsilon}{nFA\ \cos\theta} \int_0^t i(t)\ dt \qquad (4\text{-}20)$$

Now, when a potential program identical to that used in ac voltammetry is applied to the working electrode, the concurrent specular reflectance response, as detectable either by phase sensitive detection or tuned amplification, is given by substituting equation 4-1 into equation 4-20 leaving

$$-R(\omega t) = \frac{4.606\ \Delta\varepsilon}{nFA\ \cos\theta}\ I_{rev}F(t)G(\omega) \int_0^t \sin(\omega t + \phi)\ dt \qquad (4\text{-}21)$$

where, for simplicity, the normalized parameter

$$R(\omega t) = \frac{\Delta R}{R}(\omega t)$$

has been defined as the fundamental harmonic of the alternating component of the reflectance response. It is important to note that the function F(t), which expresses a time dependence of the amplitude of the sinusoidal response imposed by dc processes, can be considered constant with respect to the ac time scale, and hence does not enter into the integration. Carrying out the integration and cancelling terms gives

$$R(\omega t) = R_{rev}\ F(t)\ G(\omega)\ \cos(\omega t + \phi) \qquad (4\text{-}22)$$

where

$$R_{rev} = \frac{4.606\ \Delta\varepsilon nF\Delta E\ C^*_{Ox}D^{1/2}_{Ox}}{\omega^{1/2}\cos\theta\left(4RT\ \cosh^2(j/2)\right)} \qquad (4\text{-}23)$$

Comparison of these expressions with the analogous expressions for the alternating current reveals that the alternating reflectance is phase-shifted 90° from the faradaic current. Thus the phase angle ϕ is readily

accessible. Also, it will be noted that while the alternating current increases with the square root of the frequency, the reflectance decreases.

Since it is desirable to obtain measurements at relatively high frequencies, the measurement of reflectance may appear to be disadvantageous with respect to measurement of the current. However, as will be illustrated later, the current associated with charging of the double layer capacitance does not, in general, contribute to the spectral response. When the current is measured the contribution from charging of the double layer capacitance increases, in the absence of uncompensated resistance, linearly with the frequency. The ratio of faradaic to background current thus also decreases as $\omega^{1/2}$ increases. The absence of charging current in the spectral response implies that the smaller signals obtained at higher frequencies may not be as serious a problem as might first be expected.

The ratio of the magnitude of the fundamental harmonic current to the corresponding reflectance parameter is given by

$$\frac{|I(\omega t)|}{|R(\omega t)|} = \frac{nFA\omega\cos\theta}{4.606\ \Delta\varepsilon} \qquad (4\text{-}24)$$

This relation may prove to be of value in the determination of n-values or extinction coefficients. Unlike most voltammetric criteria, its application does not require that the charge transfer process is reversible. More importantly, however, it shows that at any given frequency, the alternating reflectance is just a multiple of the corresponding alternating current. Hence all previously derived qualitative and quantitative aspects of the ac voltammetric response (e.g. peak width at half-height, peak separation and cross-over potential in cyclic ac voltammetry) apply equally well to the SMACRS experiment.

In general, three approaches are possible for the extraction of heterogeneous kinetic parameters from ac voltammetric data and hence from alternating reflectance data. A computer fit of $R(\omega t)$ vs $\omega^{1/2}$ may be used to evaluate the various parameters in equation 4-22 [101]. The peak separation as a function of sweep rate may be used in conjunction with working curves for the determination of the heterogeneous rate constant k_s, as in cyclic ac voltammetry [99]. The frequency dependence of the phase angle, ϕ, may be used to evaluate k_s and α, the charge transfer coefficient [88]. For several reasons, we have concentrated our efforts on the measurement of phase angles for the determination of heterogeneous kinetics.

First, they are readily accessible to PSD techniques. In addition, they do not require the computation of working curves for the determination of heterogeneous rate constants. Most importantly, Smith has shown [88] that phase angle data is not significantly affected by the magnitude of the modulation voltage, ΔE, for values up to 20 mV, provided $k_s > 10^{-2}$ cm/s. The ability to use larger modulations can be particularly important in spectroelectrochemical studies where $\Delta\varepsilon$ is small.

The various phase relations in the SMACRS experiment are best discussed in terms of a phasor diagram, as in Figure 30. For the purposes of the following discussion, phasor, or vector, quantities will be denoted by an asterisk appearing as a superscript to indicate that the mathematical operations involved are vector operations, while the absence of an asterisk indicates that only the magnitude of the indicated phasor is involved in the operations.

The direction of the phasor ΔE^*_{app}, representing the applied sinusoidal potential perturbation, is used to define the coordinate system in Figure 30. The total current I^*_t in general leads ΔE^*_{app} by some phase angle ϕ_m. In the figure, the applicability of the Randles circuit has been assumed in that I^*_t is represented as the sum of the faradaic current, I^*_f, and a purely capacitive

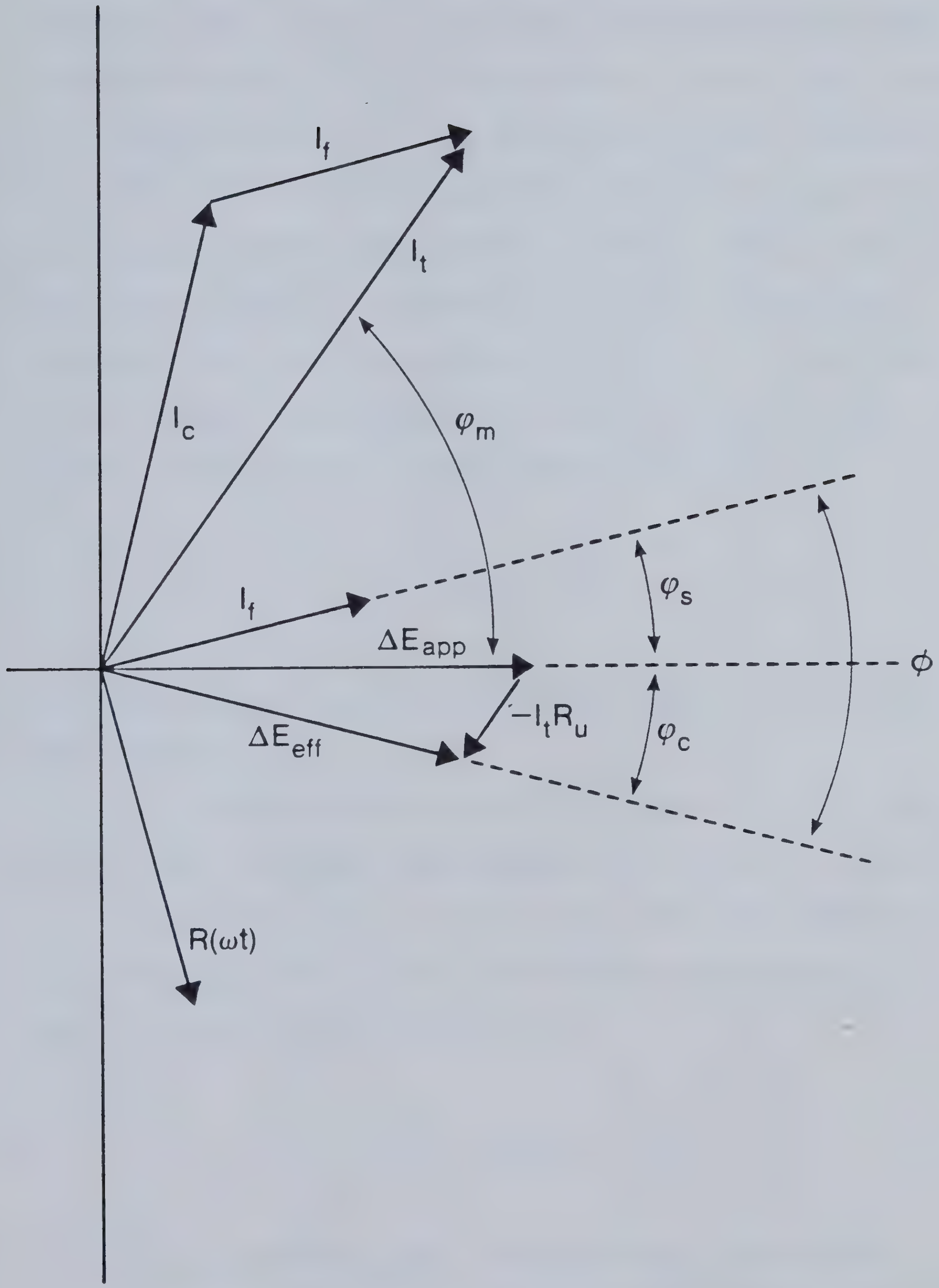
I_f
I_t
I_c
φ_m
I_f
φ_s
ΔE_{app}
ϕ
$-I_tR_u$
ΔE_{eff}
φ_c
$R(\omega t)$

Figure 30. Phase relations in the SMACRS experiment.

component, I_c^*. This is not a necessary assumption, however, and the nature of other components appearing in conjunction with I_f^* is irrelevant as long as they do not contribute directly to the observed spectral response.

The phasor $R^*(\omega t)$ lags I_f^* by 90°, and the phase angle, ϕ_s, between the faradaic current and the applied modulation voltage is therefore readily determinable through phase sensitive detection of the in-phase and 90° out of phase, or quadrature, components of the SMACRS response, R' and R", respectively. In this case

$$\cot \phi_s = \frac{R''}{R'} \tag{4-25}$$

The phase angle ϕ_s is not directly measurable by other methodology.

If the uncompensated solution resistance, R_u, is zero, then no other measurements are necessary, since ϕ_s = ϕ in this case. If R_u is not zero, then the effective voltage across the electrode/solution interphase will differ from ΔE^*_{app} according to

$$\Delta E^*_{eff} = \Delta E^*_{app} - I^*_t R_u \tag{4-26}$$

and is thus phase-shifted through some phase angle, ϕ_c, from ΔE^*_{app}, as noted in the Figure. In this case, the phase angle, ϕ, required for kinetic analysis is given by

$$\phi = \phi_s + \phi_c \qquad (4\text{-}27)$$

The phase angle ϕ_c is readily determined if the magnitude of the total current, I_t, and its phase angle ϕ_m, with respect to ΔE^*_{app} are known. In this case, Smith [88] has given

$$\sin \phi_c = \frac{I_t R_u \sin \phi_m}{\left(\Delta E^2_{app} + (I_t R_u)^2 - 2\Delta E_{app} I_t R_u \cos \phi_m\right)^{1/2}} \qquad (4\text{-}28)$$

This equation makes no assumptions concerning the nature of the components giving rise to I^*_t. The values I_t and ϕ_m may be determined through phase sensitive detection of the in-phase and quadrature components, I'_t and I''_t, of I^*_t, since

$$I_t = (I'^2_t + I''^2_t)^{1/2} \qquad (4\text{-}29$$

and

$$\tan \phi_m = I''_t / I'_t \qquad (4\text{-}30)$$

The value of R_u may be determined by stepping the dc potential out of the electroactive region and determining I^*_t. In this case the interphase may be treated as a

resistor, R_u, and capacitor, C_{DL}, in series, for which [120]

$$\tan \phi_m = 1/\omega C_{DL} R_u \tag{4-31}$$

and

$$\frac{\Delta E_{app}}{I_t} = \left(R_u^2 + (1/\omega C_{DL})^2\right)^{1/2} \tag{4-32}$$

Solving equation 4-31 for ωC_{DL} in terms of R_u and $\tan \phi_m$, and substituting into equation 4-32 leads to

$$R_u = \frac{\Delta E_{app}}{I_t} \cos \phi_m \tag{4-33}$$

The use of equation 4-33 is tantamount to equating the in-phase component of the electrode impedance to the uncompensated resistance. As such, it is common practise [97] to base the calculations on data taken at as high a frequency as is permitted by the instrumentation, as values of R_u obtained at lower frequencies will tend to be high due to contributions from trace faradaic impurities, or from non-ideal behaviour of the double layer capacitance. To the extent that the double layer does include a capacitive component, albeit a frequency dependent one, all other components in the equivalent

circuit will effectively short out at high frequencies, except R_u. The apparent value of R_u obtained from equation 4-33 will therefore converge to the true value as the frequency is increased [101]. It has been found in this laboratory that the values obtained are constant within a few percent at frequencies between 2 kHz and 10 kHz and, in exceptionally clean systems where the residual current is particularly low, consistent values have been obtained at frequencies as low as 400 Hz.

4.4 Results and Discussion

The choice of an experimental system with which to evaluate any method purporting to facilitate the determination of heterogeneous electron transfer rate parameters is a difficult one to make. The values reported for systems which have been studied by different workers are frequently at variance. The system chosen here was the $Fe(CN)_6^{3-}/Fe(CN)_6^{-4}$ redox couple in 1 M aqueous KCl. Although the standard rate constant for this couple is now known to be highly dependent on the conditions under which it is obtained [121,122], a number of workers [122-124] have reported values consistent with k_s = 0.9 cm/s at Pt when obtained using mM or greater concentrations of the electroactive species in 1 M KCl.

Figure 31 presents the SMACRS response obtained during a cyclic ac voltammetric experiment in 1 M aqueous KCl containing 10 mM $K_4Fe(CN)_6$ at a platinum electrode. The wavelength of the beam monitored was 420 nm, the absorption maximum for the $Fe(CN)_6{}^{3-}$ ion. At low sweep rates, Figure 31a, the forward and reverse sweeps coincide, indicating reversibility of the charge transfer process on the dc time scale. The peak potential here is 0.219 V vs SCE, and agrees with the voltammetric half-wave potential as estimated from cyclic voltammetry in the same electrochemical cell. This peak potential is independent of the modulation frequency employed. The peak width at half-height is 94 mV, in excellent agreement with the theoretical value of 90/n mV expected for a reversible one-electron transfer.

At higher sweep rates, Figure 31b, the forward and reverse peaks are observed to separate, indicating non-Nernstian dc behaviour in accordance with the theory of cyclic ac voltammetry. The crossover potential, at which the forward and reverse peaks coincide, has been shown [99] to occur at

$$E_{CO} = E^{r}_{1/2} + \frac{RT}{nF} \ln \frac{\alpha}{1-\alpha} \qquad (4-34)$$

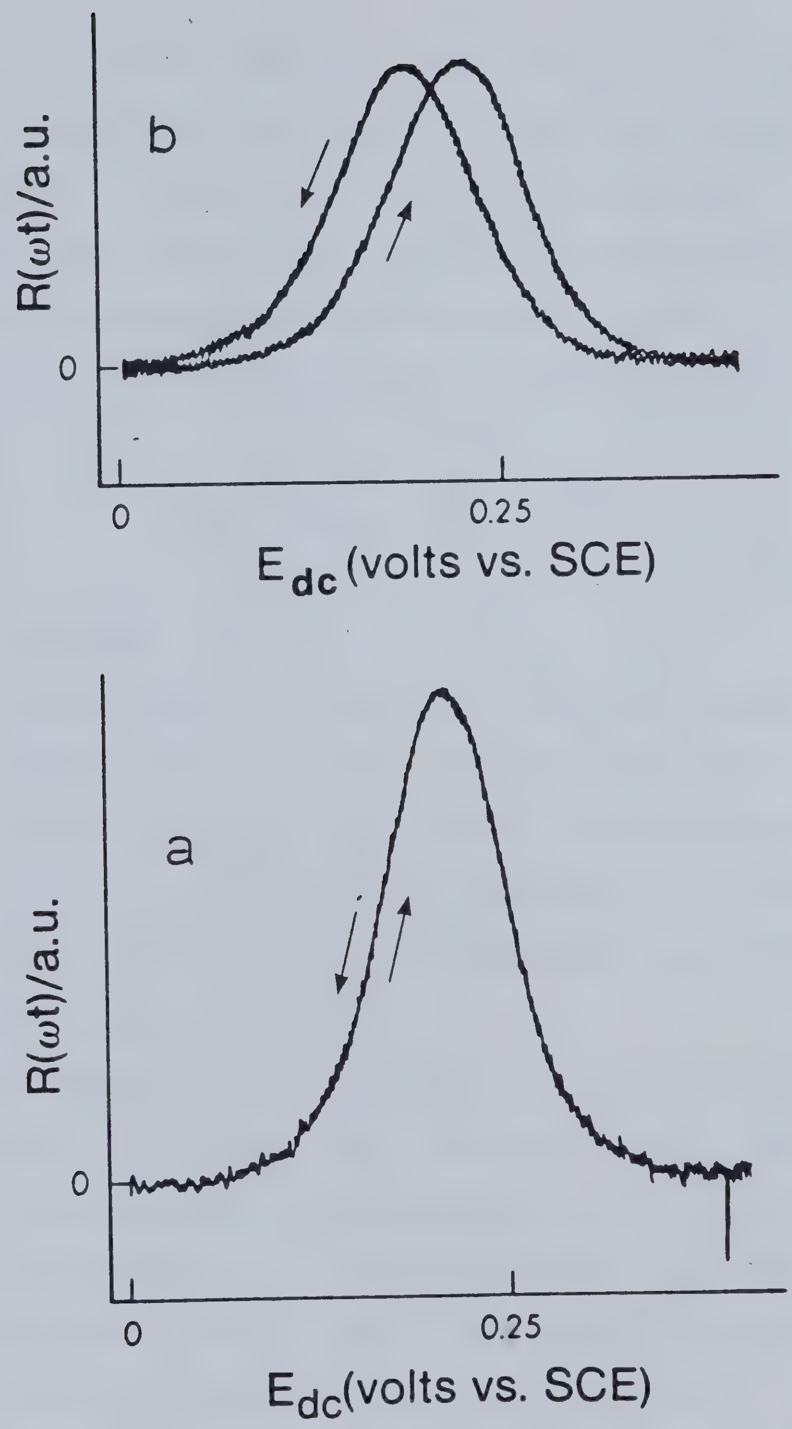

Figure 31. R(ω t) vs potential for 10 mM $K_4Fe(CN)_6$ in 1 M aq. KCl; $\lambda = 420$ nm; $\Delta E_{app} = 18$ mV; (a) $\omega/2\pi = 43.9$ Hz, $\nu = 2$ mV/s; (b) $\omega/2\pi = 75.0$ Hz, $\nu = 200$ mV/s.

In Figure 31b, this point is identical to the low scan rate peak potential, and indicates that the charge transfer coefficient, α, for this system is equal to 0.5. This may also be inferred from the frequency independence of the low scan rate peak potential, as Smith as shown [88] that this reaches a limiting value of

$$\underset{\omega\to\infty}{E_p} = E^r_{1/2} + \frac{RT}{nF} \ln \frac{1-\alpha}{\alpha} \qquad (4\text{-}35)$$

at high frequency.

It will be noted that the base lines of Figure 31 are flat and correspond to electrical zero. This is in contrast to the non-zero curved base lines arising from charging current contribution to the responses generally obtained with conventional ac voltammetric methods (see, for example, reference [99]).

Phase angle data were collected by first stepping the dc potential to the half-wave potential of the redox couple. After waiting a few seconds for the system to stabilize, the output of a PSD monitoring that component of the spectral response which was in phase with the applied potential modulation was recorded for ca 3 seconds with a recorder operating in the Y-t mode. This was followed by 3 s recordings of the quadrature component of the spectral response, and of the in-phase and quadrature

components of the current. After recording of the currents, the spectral components were measured again to ensure that no time dependence of the magnitude or phase of the signal existed. This sequence was repeated a minimum of 6 times at each frequency investigated, and the medians of the values obtained were used in calculating the various phase relations indicated in equations 4-25, and 4-27 to 4-30.

A plot of cot ϕ vs $\omega^{1/2}$ (lower trace) so obtained for the ferro-ferricyanide redox couple is illustrated in Figure 32. The plot is linear with the vertical intercept at unity, in accordance with equation 4-11. From equation 4-11 and the individual cot ϕ values, a value for the heterogeneous rate constant of $k_s = 0.096 \pm 0.008$ cm/s was obtained, in excellent agreement with the value 0.09 expected from the literature (vide supra). The upper trace in Figure 32 corresponds to values of cot ϕ_s obtained before correction for the effects of uncompensated resistance.

The value of R_u used in equation 4-28 to calculate the cot ϕ data of Figure 32 was only 2.3 ohms. It is apparent that, even with this small uncompensated resistance, the magnitude of the phase angle correction, ϕ_c, is large, particularly at higher frequencies. This is largely due to greater currents resulting from the use of

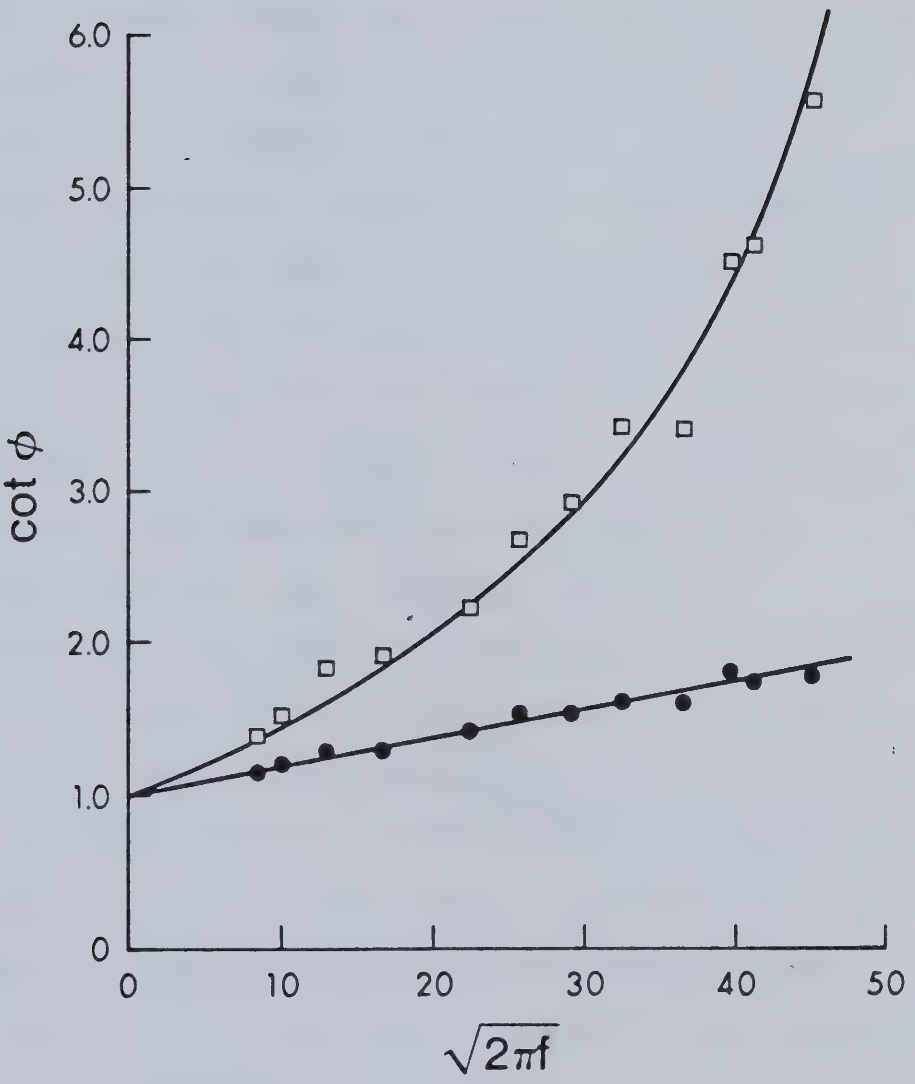

Figure 32. Cot ϕ data for ferro-ferricyanide system as obtained by SMACRS at E_{dc} = .219 V vs SCE, other parameters as in Fig. 31. Lower trace is corrected for R_u = 2.3 Ω .

10 mM concentrations and 18 mV modulation voltages. These conditions were desirable in this case because of the small value of $\Delta\varepsilon$ associated with the ferro-ferricyanide system ($\Delta\varepsilon$ = 1020 at 420 nm) [14]. For many systems of interest, however, $\Delta\varepsilon$ will be larger than this, and the concentration of electroactive species and modulation amplitudes may be reduced accordingly. Figure 33 illustrates SMACRS data obtained at cathodic potentials in DMSO/0.1 M TBAP containing 10^{-5} M ClMn(III)TPP. The change in molar absorptivity, $\Delta\varepsilon$, associated with the redox couple $(\mathrm{Mn(III)TPP})^{+}/(\mathrm{Mn(II)TPP})$ in this solvent is approximately 8×10^{4} in this solvent, and good signal to noise ratios were obtained with 8 mV peak to peak modulation voltages, even at these very low concentrations. A cyclic voltammogram obtained in the same solution is also indicated in the figure. The cathodic and anodic peaks associated with the Mn(II)/Mn(III) couple are barely discernible against the background current. Comparison of the SMACRS and cyclic voltammetric responses adequately demonstrates the sensitivity of the former technique when large changes in molar absorptivity are involved.

Figure 34a illustrates a cyclic voltammogram for the $\mathrm{DPA/DPA^{+\bullet}}$ redox couple (DPA = 9,10-diphenylanthracene) in CH_3CN/0.1 M TBAP. The peaks labelled 1 and 2 are due to

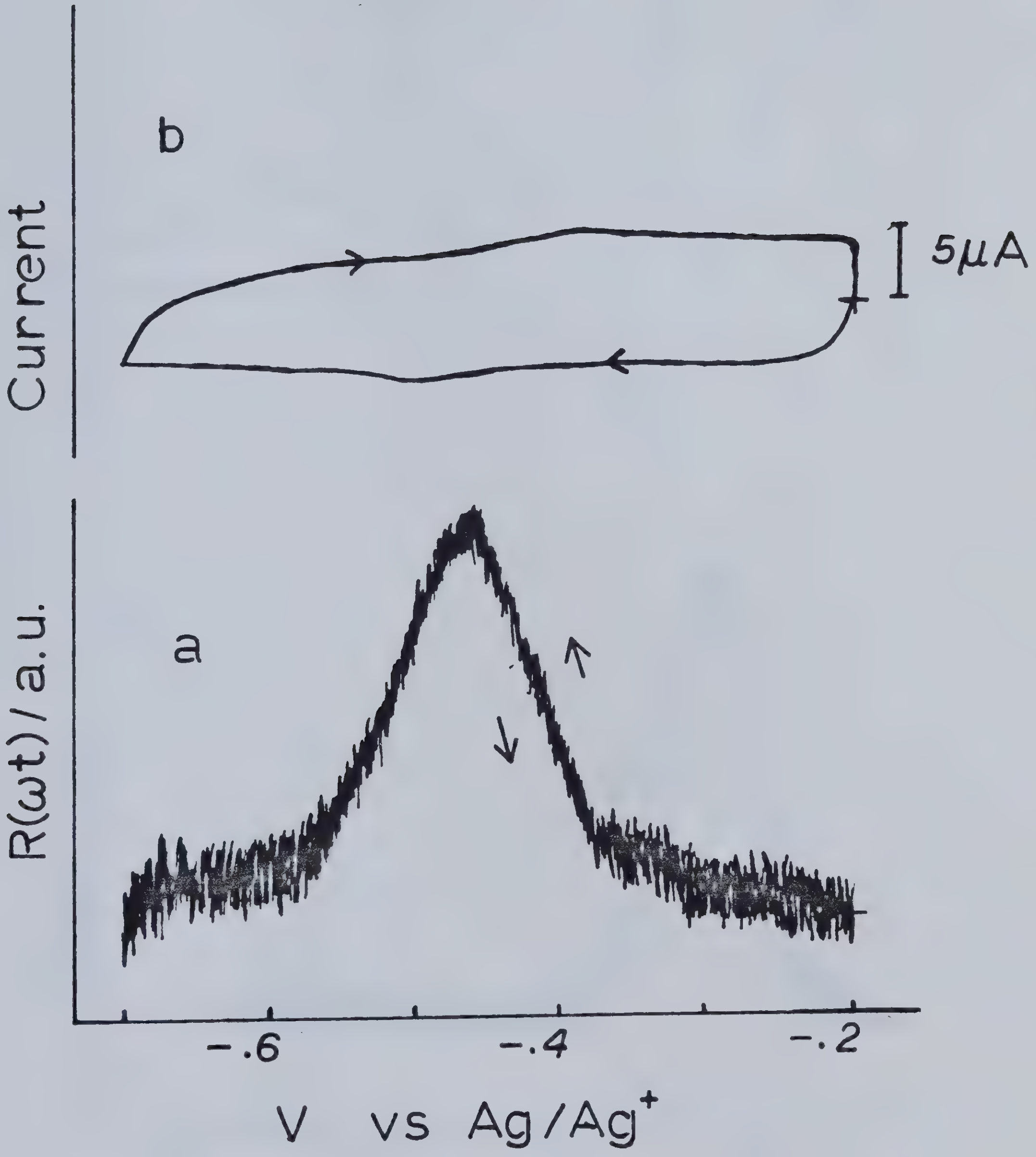

Figure 33. (a) R(ωt) vs potential (Volts vs Ag/Ag$^+$ (.01 M, DMSO)) for 1 x 10^{-5} M ClMn(III)TPP in DMSO (.1 M TBAP); λ = 446 nm; ω/2π = 44Hz; ΔE = 8mV; ν = 5 mV/s. (b) Cyclic voltammogram of the same system; ν = 50 mV/s.

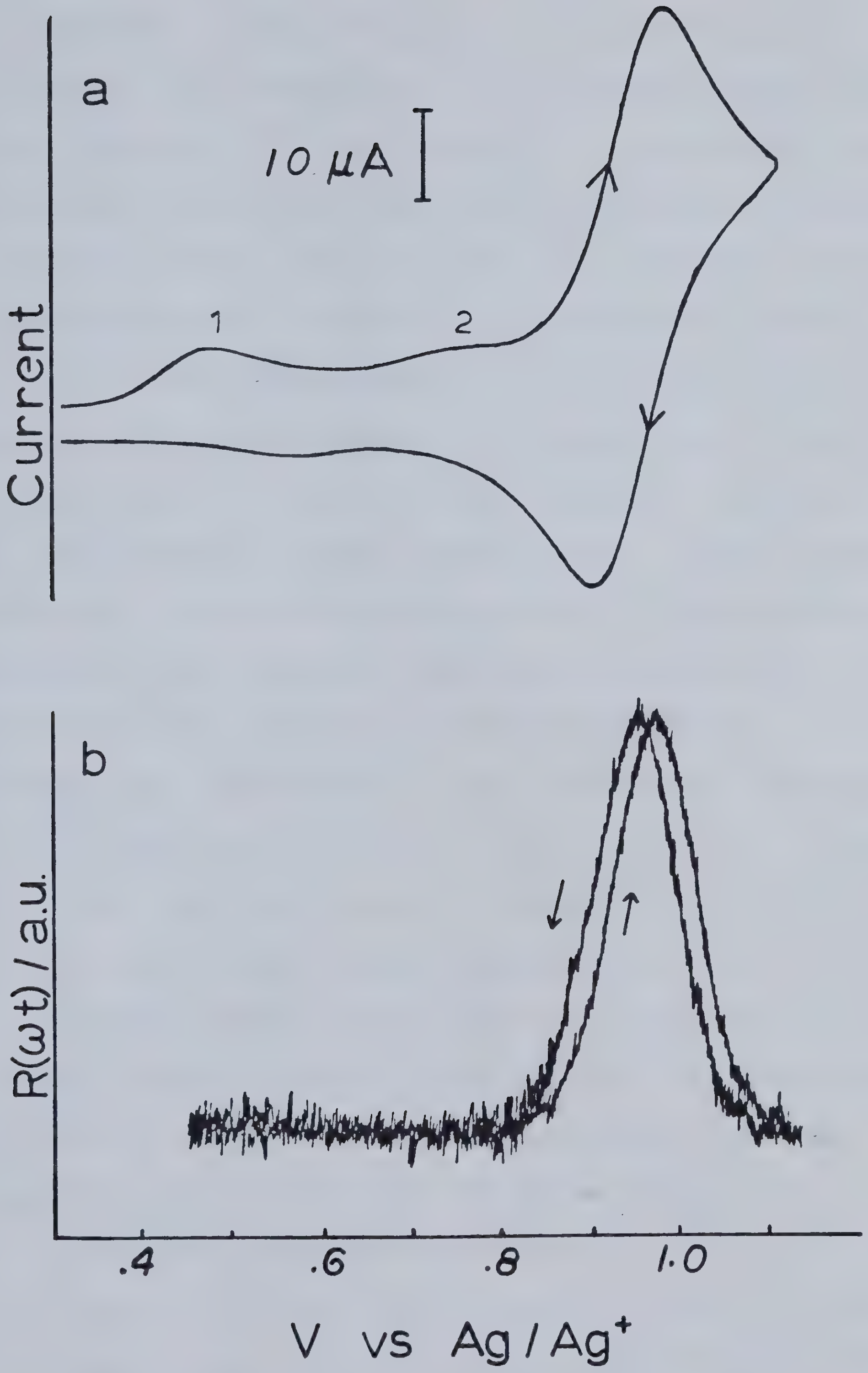

Figure 34. (a) Cyclic voltammogram of 1 mM DPA in CH_3CN(.1 M TBAP); ν = 100 mV/s. (b) R(ω t) vs potential recorded in the same system; λ = 595 nm; ΔE = 10 mV; $\omega/2\pi$ = 70 Hz, ν = 100 mV/s.

the presence of some impurity in the system. Their presence is not observable in the SMACRS response (Figure 34b) recorded at 595 nm, however. It is obvious that the additional selectivity afforded by spectroelectrochemical technology can be important from the viewpoint of analysis involving complex mixtures of electroactive species.

As further confirmation of the applicability of the method to the determination of heterogeneous electron transfer kinetics, a phase angle analysis was performed for the DPA/DPA$^{+\bullet}$ couple (this time in a clean system). Figure 35 illustrates the cot ϕ vs $\omega^{1/2}$ data obtained. The upper trace (squares) corresponds to the cot ϕ_s values obtained before correction for the effects of uncompensated resistance. The lower traces correspond to cot ϕ values obtained after correction for the presence of 19.4 ohms (circles), as was actually measured for this system, and 25 ohms uncompensated resistance.

Several points can be made with reference to this figure. First, although the value of 19.4 ohms used in calculating the center trace is nearly an order of magnitude greater than the 2.3 ohm value used in correcting the ferro-ferricyanide data of Figure 32, the magnitude of the phase angle correction is no greater. This results from the use of lower concentrations for the DPA system (1 mM) as opposed to the ferrocyanide system

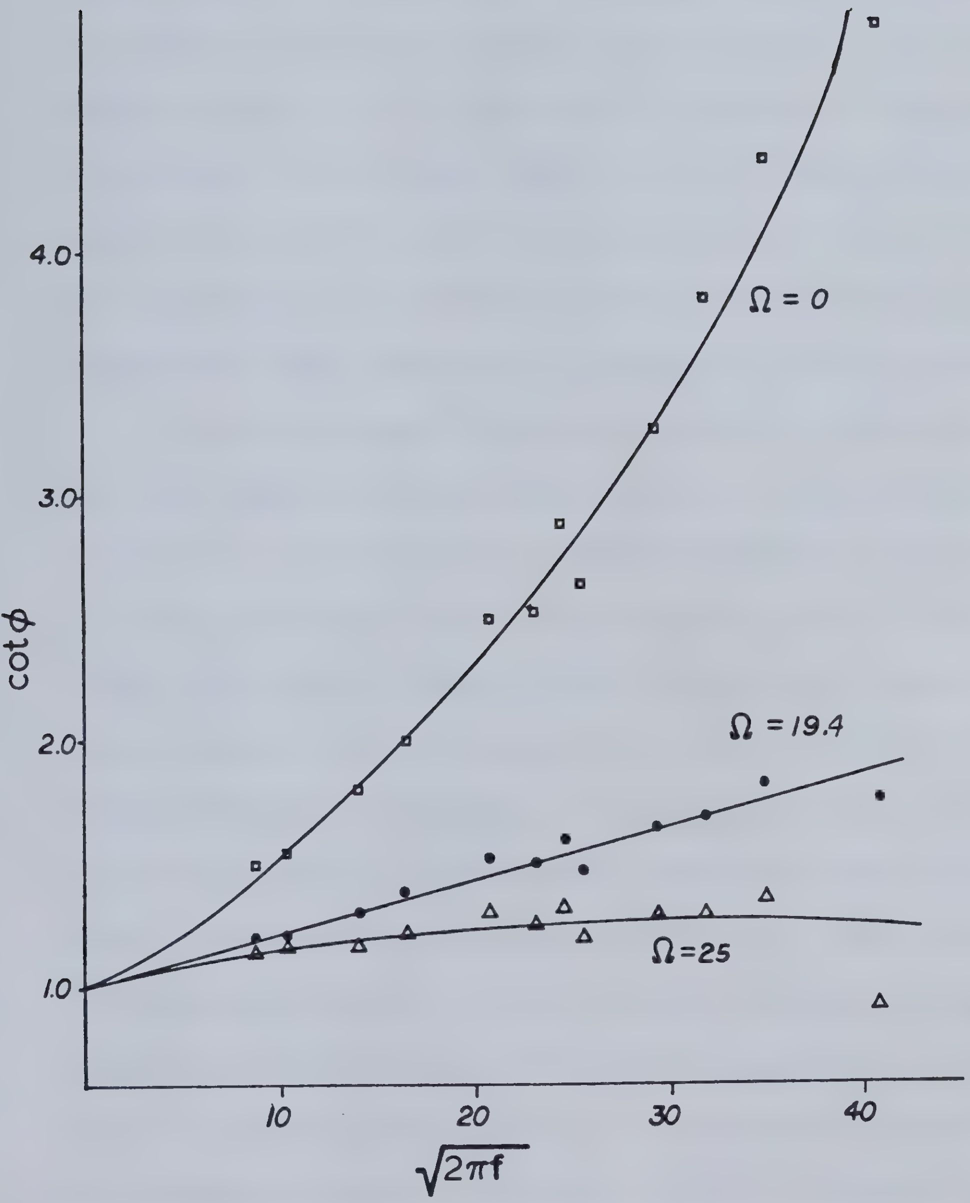

Figure 35. Cot φ data for DPA/DPA$^{+\cdot}$ as determined at E_{dc} = .94 Volts vs Ag/Ag^{+}(.01 M, CH_3CN); other parameters as in Figure 34b.

(10 mM). Second, in comparing the centre and lower traces of Figure 35, it is apparent that the linearity of the resulting plot, and the correspondence of the vertical intercept to unity, serve as sensitive indicators of the reliability of the R_u value used in making the phase angle corrections. It is feasible to develop a computer program to correct phase angle data using a value of R_u which is selected such that the least squares intercept is unity, or the deviations from linearity are minimized, and thus circumvent the necessity of measuring this parameter.

The phase angle data were used to calculate a value for the heterogeneous rate constant of the $DPA/DPA^{+\bullet}$ couple in accordance with equation 4-11. Assuming a value for the diffusion coefficient of $D = 1.97 \times 10^{-5}$ cm^2/s [125], the value obtained was 0.14 ± 0.01 cm/s. This value is an order of magnitude less than the value of 1.6 cm/s obtained in $CH_3CN/0.1$ M $(CH_3CH_2)_4N^+ClO_4^-$ by Peover and White [126]. Their value, however, was obtained by high speed cyclic voltammetry, and has been criticized by Koizumi and Aoyagui. These latter authors reported a rate constant for the $Per/Per^{+\bullet}$ (Per = perylene) couple of 0.7 cm/s in $C_6H_5NO_2/0.4$ M TBAP as obtained by the double galvonostatic pulse technique [127], a method more suitable for determining rate constants of this order of magnitude.

Attempts to apply SMACRS to the determination of k_s for the Per/Per$^{+\bullet}$ redox couple under the conditions reported by Koijumi and Aoyagui have been unsuccessful to date. The values of cot ϕ obtained did not differ significantly from unity at frequencies up to 500 Hz. The signals obtained at frequencies higher than this were too small to allow accurate determination of the associated phase angle. It is noteworthy, however, that while the forward and reverse peaks for the DPA/DPA$^{+\bullet}$ couple begin to separate at dc potential sweep rates as low as 100 mV/s, no separation of the forward and reverse peaks for the Per/Per$^{+\bullet}$ system is observed at sweep rates of up to 700 mV/s. Since the peak separation in cyclic ac voltammetry increases as the rate constant decreases, this clearly indicates that k_s for the Per/Per$^{+\bullet}$ couple is considerably greater than that for the DPA/DPA$^{+\bullet}$ couple, and adds some credibility to the value reported here for DPA. The SMACRS response obtained for the Per/Per$^{+\bullet}$ couple at 700 mV/s and 700 Hz is presented in Figure 36. Because of the very small signals obtained at this frequency, the output of the PSD was fed into a Hi-Tek type AA-1 signal averager, and the data presented is the result of 64 repetitive scans.

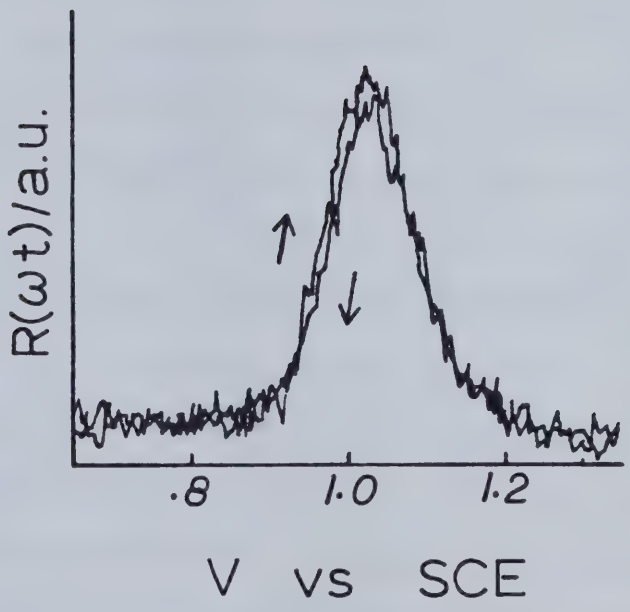

Figure 36. R(ω t) vs potential for 1 mM perylene in $C_6H_5NO_2$(.4 M TBAP); λ = 590 nm; Δ E = 10 mV; ω/2π = 700 Hz; ν = 700 mV/s.

4.5 Electrochemical Cell and Instrumentation for SMACRS

The cell used in this work was a conventional design used previously in MSRS [113], and is illustrated in Figure 37. The working electrode was a 7 mm o.d. Pt disc silver-soldered onto a brass shaft and heat shrunk into a Kel-F tube. The electrode surface was machined flat and polished to a mirror finish on 0.03 μm polishing alumina. The counter electrode consisted of a piece of Pt foil welded to a Pt wire sealed in glass. Light from a 200 watt Hg-Xe arc lamp could be focussed at a 45° angle onto the surface of the working electrode through a quartz window incorporated into the body of the cell. This was then reflected to a photomultiplier tube through a second quartz window positioned 90° from the first.

The instrumental arrangement is essentially identical to that used commonly in MSRS studies, and is pictured in Figure 38. All of the components are commercially available. The heart of the instrument is the photomultiplier tube (PMT), in this case an RCA 31000 M. This provides an output current, C, linearly related to the intensity, R(t), of the reflected light beam impinging upon it. For monochromatic light, one can write

$$C = A(\lambda, V_s)\ R(t) \qquad (4\text{-}36)$$

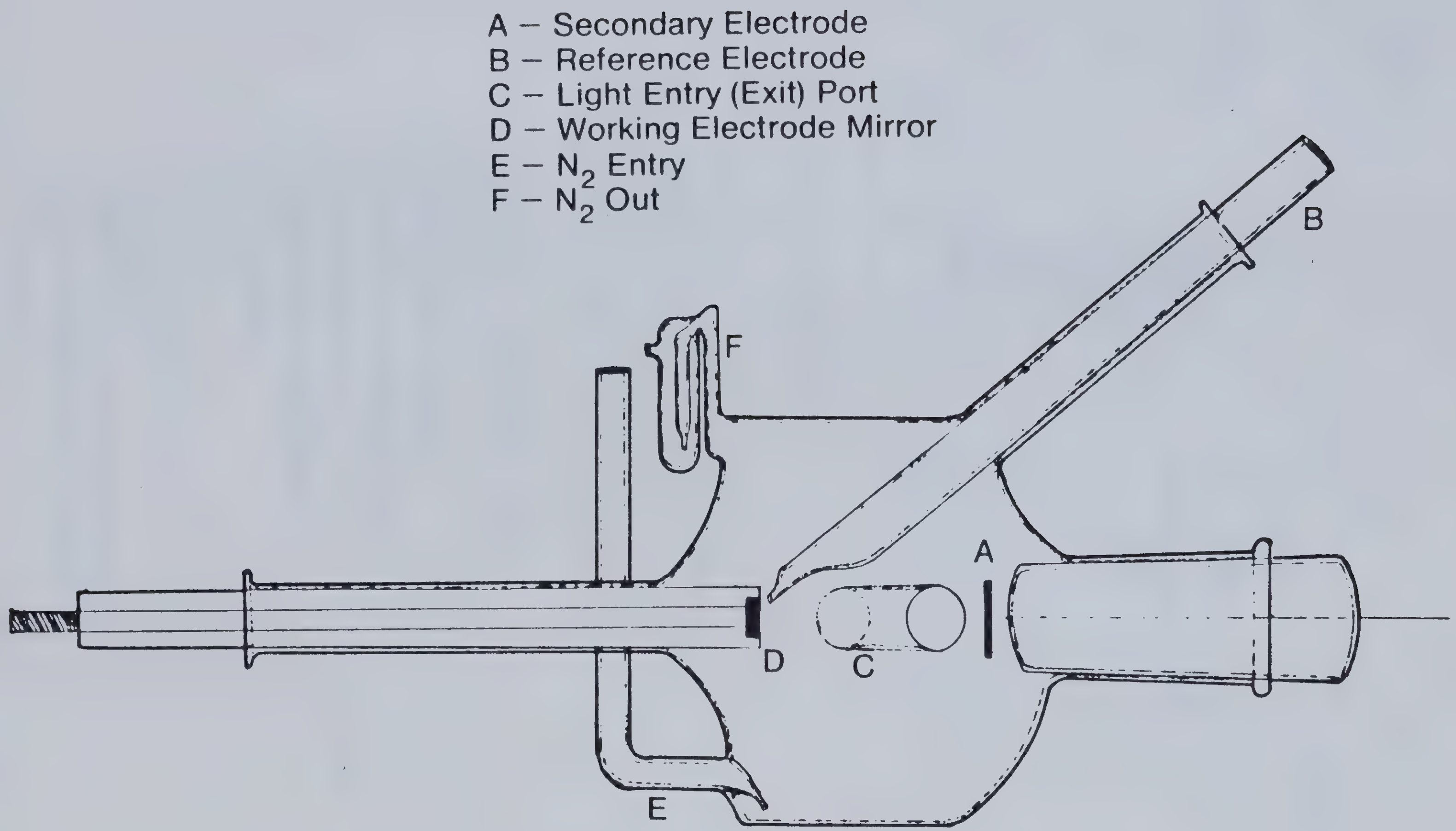
A — Secondary Electrode
B — Reference Electrode
C — Light Entry (Exit) Port
D — Working Electrode Mirror
E — N_2 Entry
F — N_2 Out
B
F
A
D
C
E

Figure 37. Electrochemical cell for SMACRS experiments.

Instrumentation for SMACRS

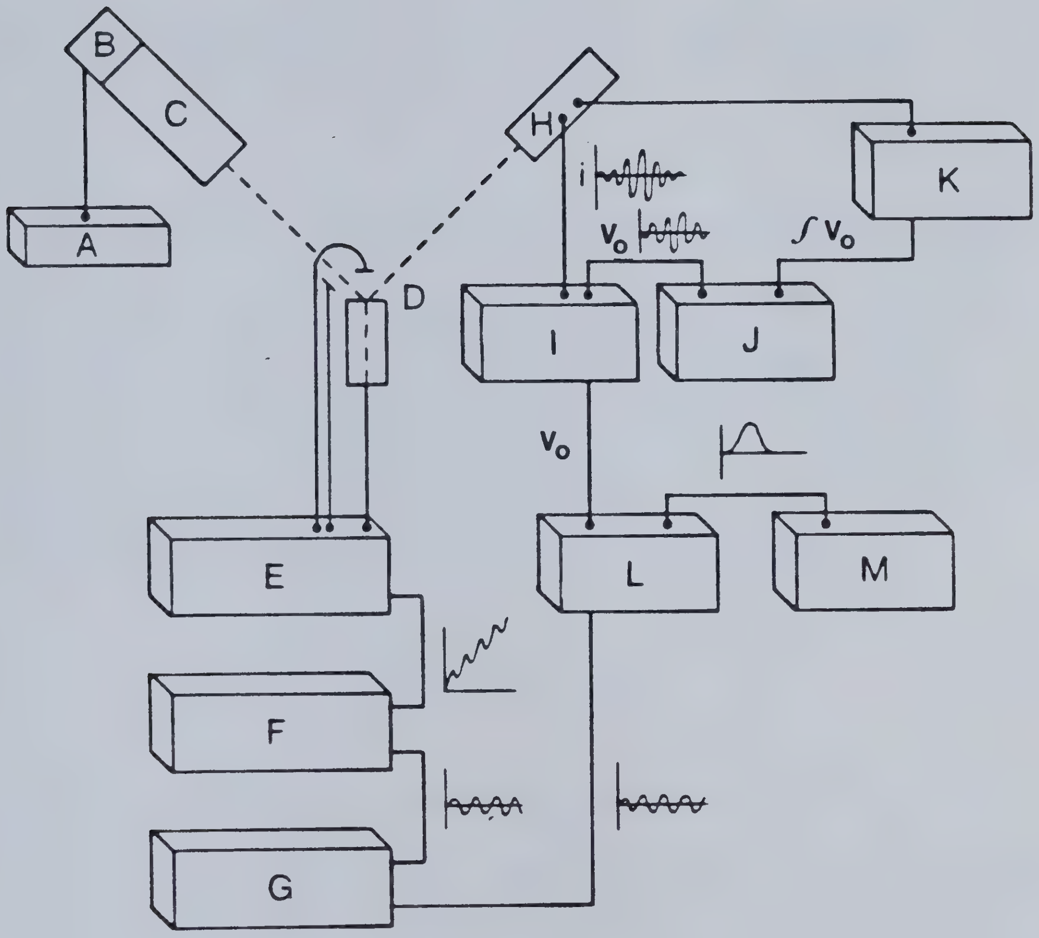

- A. Power supply for lamp.
- B. Lamp
- C. Monochromator
- D. Electrochemical cell
- E. Potentiostat
- F. Waveform generator
- G. Oscillator
- H. PMT
- I. Current follower
- J. Integrator
- K. PMT high voltage source
- L. Lock-in Amplifier / PSD
- M. Recorder

Figure 38. Instrumentation for SMACRS experiments.

where A is the gain of the PMT, λ is the wavelength of the incident radiation, and V_s is the high-voltage supplied to the PMT.

In order that the current, C, may be amplified and converted to a voltage for recording purposes, the signal C is taken to the input of a current follower. The Bentham model 210E current follower used in this work includes a summing network such that a constant offset voltage may be added to the output, according to

$$V_o = SC + V_{off} \qquad (4\text{-}37)$$

where V_o is the output voltage provided by the current follower, S is the current amplification factor, and V_{off} is whatever constant offset voltage may be selected for the purpose at hand.

Now, at the beginning of an experiment, before any potential has been applied to the working electrode, the intensity of the light reaching the PMT is R(0) and the current follower output is given by

$$V_o = SA(\lambda,V_s)\ R(0) + V_{off} \qquad (4\text{-}38)$$

The voltage offset is then adjusted so that this signal is zero according to

$$V_{off} = -SA(\lambda,V_s)\ R(0) \qquad (4\text{-}39)$$

At some later time, t, when a voltage has been applied to the working electrode and a concomitant change in the intensity of the light reaching the PMT has occurred, the current follower output will be

$$V_o = SA(\lambda,V_s)\ R(t) - SA(\lambda,V_s)\ R(0) \qquad (4\text{-}40)$$

Division of this result by equation 4-39 and cancelling terms gives

$$\frac{-V_o}{V_{off}} = \frac{R(t) - R(0)}{R(0)}$$

or

$$-V_o = V_{off}\ \frac{\Delta R}{R} \qquad (4\text{-}41)$$

The provision to offset the current follower output thus allows direct measurement of the parameter $\Delta R/R$.

In order that reliable measurements of $\Delta R/R$ may be made throughout the course of an experiment, the identity

defined by equation 4-39 must be maintained. In general, however, R(0) will vary due to, for instance, a buildup of absorbing species associated with the dc portion of the experiment, and a compensating adjustment in the gain, $A(\lambda,V_s)$, of the PMT must be made by varying the value of the high-voltage, V_s, supplied to it. This is tantamount to requiring that no dc component of V_o exists.

The high voltage supplied by the PMT power supply, in this case a Bentham model 219, is determined by the value of an input control voltage, V_c. The control voltage, in turn, is obtained by integrating the output voltage of the current follower according to

$$V_c = \frac{-1}{RC} \int_0^t V_o \, dt \qquad (4\text{-}42)$$

The integrator acts, essentially, as a low pass filter, and periodic components of frequency f >> 1/RC will have negligible influence on V_c. The integration time constant, RC, used in this work was 3 seconds.

Any dc component of V_o, however, will directly influence V_c and a compensating adjustment in the voltage supplied to the PMT will be made such that the dc level associated with V_o is effectively controlled at zero.

The current follower output, V_o, was taken simultaneously to an analogue integrator, providing the

feedback control voltage V_c, and to the input of a PSD. The PSD allows determination of the in-phase and quadrature components of periodic input signals. For a sinusoidal input voltage, V_o, the PSD output is given by

$$V_{PSD} = S\ V_o \cos \phi \qquad (4\text{-}43)$$

where S is the amplification factor and ϕ is the phase angle between V_o and some reference signal supplied to the PSD. The reference signal in this work was derived from the oscillator supplying ΔE^*_{app} to the adder input of the potentiostat. Zero phase difference between this signal and that appearing at the reference electrode was measured at frequencies up to 5 kHz, verifying that no phase shift was introduced by the potentiostat. The PSD includes a phase shifter capable of internally shifting the reference signal by 90°, thereby allowing the determination of both the in-phase and quadrature components of the input signal.

All commercially available PSD's include a low pass filter to remove high-frequency noise from the output signal. Some care must be exercised in selecting the time constant associated with this filter, as too long a setting can result in attenuation of the signal and introduce artificial separation of the forward and reverse

peaks. In practise the time constant may be adjusted by decreasing it to a point where further change does not affect the SMACRS response obtained. This setting must be re-evaluated when either the frequency or dc scan rate of the applied potential program is changed.

4.6 AC Voltammetry With Background Correction

Although it is felt that the applicability of SMACRS to the study of electrode kinetics has been adequately verified, the experiment, in its present state, requires an inordinate amount of time. Each one of the cot ϕ points in Figures 32 and 35 is the result of 6 or more independent determinations of the in-phase and quadrature components of the SMACRS response, and three independent measurements of the analogous current components. Accounting, in addition, for the measurement of the frequency and the applied modulation voltage, each point thus represents twenty or more separate measurements. The method is amenable to computer acquisition of data, and more modern PSD's allow the simultaneous determination of both the in-phase and quadrature signal components. McCreary [128] has shown that by increasing the angle of incidence, θ, of the light beam, signal to noise improvements of up to 200 times can be achieved in specular reflectance experiments. It is expected that in

the future, both the time requirements and precision of the method will be greatly improved upon. In the meantime, however, some alternative methodology has been considered.

4.7 AC Voltammetry With Background Subtraction

If all other current components except those associated with the faradaic process of interest could be subtracted from the total current, that remaining would be subject to phase angle analysis through the same procedures as already discussed for SMACRS. Subtraction of the background current as obtained either by its measurement in the absence of the electroactive species of interest, or by baseline extrapolation, is commonly employed in potentiostatic techniques such as chronoamperometry and cyclic voltammetry. Unless the uncompensated resistance is zero, however, the method is not strictly valid, and has not been applied to kinetic analysis based on impedance methods. The problem is that the potential across the electrode/solution interphase is different in the presence of a faradaic current than in its absence by virtue of the $I_f^*R_u$ potential drop. Hence, the background current cannot be expected to be unaffected by the presence of the faradaic process. In conventional ac methods, the solution has been to calculate the

background current on the basis of the value of the double layer capacitance measured in the absence of the electroactive species, as previously noted. In this section, the feasibility of directly subtracting the background currents is considered from the viewpoint that, given the questions concerning calculation of the background current, especially at solid electrodes, the resulting method may be just as valid.

The proposed method is to estimate the in-phase and quadrature components, I_f' and I_f'', of the faradaic current by a simple baseline extrapolation in the appropriate phase selective linear sweep voltammograms. Typical voltammograms obtained in-phase and 90° out of phase from the applied potential modulation illustrating the extrapolation procedure are presented in Figure 39. The data were obtained during an anodic sweep in $C_2H_4Cl_2$/0.2 M TBAP containing 8.2×10^{-4} M (ClO_4)Mn(III)TPP, and the peaks correspond to the (ClO_4)Mn(III)TPP/(ClO_4)Mn(III)TPP$^{+\bullet}$ redox couple. Note that in this particular solvent system the baselines are exceptionally flat, and the extrapolation can therefore be made with a minimum of subjectivity.

Once I_f' and I_f'' have been estimated, the phase angle ϕ_s may be calculated from

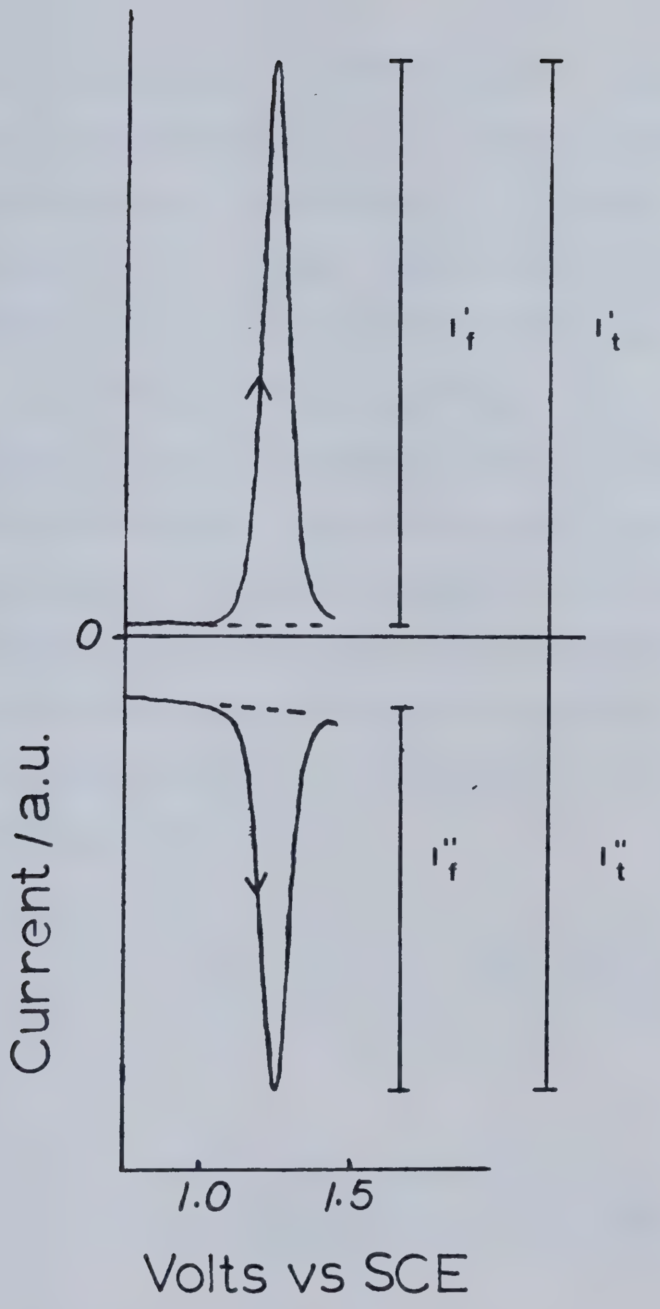

Figure 39. In-phase (upper trace) and quadrature ac voltammograms for 0.8 mM $(ClO_4)Mn(III)TPP$ in $C_2H_4Cl_2$(.2 M TBAP); $\nu = 5$ mV/s; $\omega/2\pi = 21$ Hz, $\Delta E = 6$ mV

$$\tan \phi_s = I_f''/I_f' \qquad (4\text{-}44)$$

Since I_t' and I_t'' are also available from the voltammograms, if R_u is determined by the method already outlined, then the phase angle correction, ϕ_c, may be determined through equation 4-28. Hence, the standard electron transfer rate constant may be obtained via equations 4-27 and 4-11.

A feeling for the magnitude of the error involved as a result of the assumption that the background current is unaffected by the presence of the faradaic current may be obtained in the following way. If one assumes the applicability of the Randles' equivalent circuit, then, following Sluyters and Sluyters-Rehbach [101], the in-phase and quadrature components of the total electrode impedance are given by

$$Z' = R_u + \frac{\theta + \sigma\omega^{-1/2}}{(\sigma\omega^{1/2}C_{DL}+1)^2 + \omega^2 C_{DL}^2(\theta+\sigma\omega^{-1/2})^2} \qquad (4\text{-}45)$$

and

$$Z' = \frac{\omega C_{DL}(\theta+\sigma\omega^{-1/2})^2 + \sigma^2 C_{DL} + \sigma\omega^{-1/2}}{(\sigma\omega^{1/2}C_{DL}+1)^2 + \omega^2 C_{DL}^2(\theta+\sigma\omega^{-1/2})^2} \qquad (4\text{-}46)$$

respectively. Here, θ is the charge transfer resistance, given by

$$\theta = \frac{2RT}{n^2F^2Ak_sC^*_{Ox}} \tag{4-47}$$

and σ, the Warburg coefficient, is given by

$$\sigma = \frac{2\sqrt{2}\ RT}{n^2F^2AC^*_{Ox}D^{1/2}} \tag{4-48}$$

These expressions for σ and θ assume that $E_{dc} = E^r_{1/2}$, and that $D_{Ox} = D_R = D$. If the value of k_s and D for a particular system can be estimated, and if estimates of the electrode area and the double capacitance can be obtained, then Z' and Z" can be calculated. The magnitude of the total electrode impedance is given by

$$Z = (Z'^2 + Z''^2)^{1/2} \tag{4-49}$$

and the associated phase angle, ϕ_m, is given by

$$\tan \phi_m = Z''/Z' \tag{4-50}$$

The in-phase and quadrature components of the total current are given by

$$I_t = \Delta E_{app}/Z \tag{4-51}$$

$$I_t' = I_t \cos \phi_m \tag{4-52}$$

and

$$I_t'' = I_t \sin \phi_m \qquad (4\text{-}53)$$

The electrode impedance in the absence of electroactive species is similarly determined since, in this case,

$$Z_b' = R_u \qquad (4\text{-}54)$$

and

$$Z_b'' = 1/\omega C_{DL} \qquad (4\text{-}55)$$

and the in-phase and quadrature components, I_b' and I_b'', of the background current can be calculated in a manner analogous to that used for the total currents. The faradaic components, I_f' and I_f'', can be obtained by

$$I_f' = I_t' - I_b' \qquad (4\text{-}56)$$

and

$$I_f'' = I_t'' - I_b'' \qquad (4\text{-}57)$$

and the phase angles ϕ_c and ϕ_s are then available as already described (eqns 4-44 and 4-28), and an apparent rate constant, in theory identical to that which would be obtained by the proposed method of background correction, can be calculated. Comparison of this value with that used in the original calculation of the charge transfer resistance therefore provides an estimate of the error associated with the method.

The ratio k_s'/k_s, where k_s' is the apparent rate constant calculated as just described, is plotted as a function of frequency in Figure 40. The values of the parameters used in the calculation are indicated in the figure, and are typical of those likely to be encountered for the ferro-ferricyanide system in 1 M aqueous KCl. It is evident that, provided the uncompensated resistance is kept below 5 ohms, no more than 10% error should result from the assumptions in the methodology at frequencies below about 250 Hz. Since this is well within the limits of precision that can be expected in most electrode kinetic studies (see, for example, references 9-11), the error introduced by the method may be considered acceptable.

After wading through a few of the described error calculations, a few generalities become apparent. The most important factors contributing to the error at a

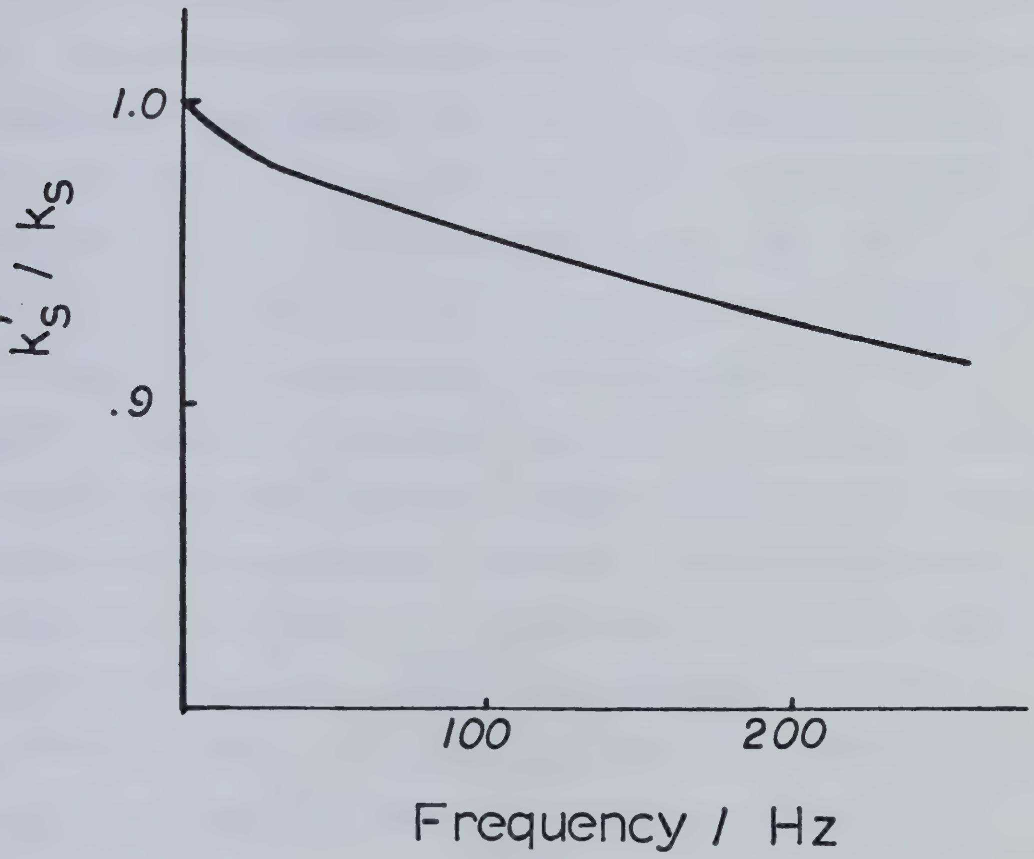

Figure 40. Ratio of apparent rate constant, k_s' , to true rate constant, k_s, as a function of frequency. Parameters used in the calculation: A = .2 cm^2; C^* = .5 mM; C_{DL} = 10 $\mu F/cm^2$; R_u = 5Ω ; k_s = .1 cm/s; D = 6 X 10^{-6} cm^2/s; ΔE = 5mV.

given frequency are the magnitude of the double layer capacitance, and the value of the uncompensated resistance. Thus, a smaller double layer capacitance will introduce less error. This is an important consideration, since the double layer capacitance in nonaqueous solvents is generally considerably less than that encountered in aqueous systems. For instance, the CH_3CN (0.1 M TBAP)/Pt interphase exhibits a double layer capacitance of ca 4 $\mu F/cm^2$ [129], while the value associated with the $C_2H_4Cl_2$ (0.2 M TBAP)/Pt interphase has been estimated at 2.5 $\mu F/cm^2$. (The latter value was obtained in this work from high frequency measurement of the electrode impedance in the absence of electroactive species, and the application of equations 4-31 and 4-32.) Values for the double layer capacitance in aqueous systems are typically 10 to 20 $\mu F/cm^2$ [25]. Hence, a larger uncompensated resistance may be more acceptable when working in nonaqueous solvents.

A second major factor is the relative magnitude of the uncompensated resistance, R_u, to the charge transfer resistance, θ. As θ increases (i.e. k_s decreases), the error inherent in the method decreases. Hence, the presence of larger uncompensated resistances is more acceptable where more sluggish charge transfer kinetics are involved.

It is evident that the inherent error always becomes greater at higher frequencies, depending on how much uncompensated resistance is present. It is recommended that the calculations just described be carried out for a particular system, before applying the method, in order to determine how much uncompensated resistance is tolerable for a particular frequency range. There is some wisdom, aside from the considerations of the error inherent in the method, in avoiding high frequencies. As Smith has noted [88], the derivative d cot ϕ/d ϕ increases sharply as ϕ decreases. Since smaller phase angles are encountered at higher frequencies, the precision with which cot ϕ values may be determined seriously deteriorates. At the same time, however, it must be kept in mind that the value of cot ϕ becomes less sensitive to the value of k_s as the frequency decreases, and greater precision is therefore required at lower frequencies.

In this work, it has been found that higher frequencies where the value of cot ϕ_s is much greater than 4 should be avoided as a result of the poor precision attainable. The lower limit on usable frequencies depends on the value of k_s, and calculation of its value from cot ϕ values less than 1.2 should probably be questioned. Of course, the precision attainable from the instruments at hand and the skill of the experimenter will both be important factors in determining a usable frequency range.

The applicability of the method to the ferro-ferricyanide system at a Pt electrode in 1 M aqueous KCl was tested, and the apparent values of the rate constant, k_s, obtained at different frequencies are collected in Table 4. The concentration of $K_4Fe(CN)_6$ was 1 mM and the uncompensated resistance present during the measurements was 3.6 ohms. The baseline extrapolation procedure was used, and the rate constants were calculated assuming a diffusion coefficient $D = 6.32 \times 10^{-6}$ cm^2/s [125]. The modulation amplitude was 6 mV and the dc potential scan rate was 5 mV/s.

There appears to be some trend to lower k_s values, as might be expected from the method employed, as the frequency increases. The average value, $k_s = 0.09 \pm 0.009$ cm/s, is in good agreement with that obtained by SMACRS, where no theoretical error is involved with the methodology.

Table 4

Standard Rate Constants for the $Fe(CN)_6^{-3}/Fe(CN)_6^{-4}$ Redox Couple Obtained by AC Voltammetry With Base-Line Extrapolation

Frequency/Hz	$k_s \times 10^2$/cm s^{-1}
93	10.3
111	8.99
143	9.36
163	8.27
199	8.06
	Ave = 9.0 ± 0.09

CHAPTER 5

STANDARD HETEROGENEOUS RATE CONSTANTS FOR SOME PORPHYRIN/PORPHYRIN CATION-RADICAL REDOX COUPLES

5.1 Experimental and Results

The method of ac voltammetry with base-line extrapolation was applied to the determination of k_s values for the redox reaction

$$P - 1e^{-} \rightleftarrows P^{+\bullet} \tag{5-1}$$

where P is $TPPH_2$ or one of its metal complexes as listed in Table 5. One-electron anodic oxidations of all of the complexes in Table 5 have previously been ascribed to cation-radical formation, as opposed to metal oxidation (see Chapter 2, and references 35 and 70). Some additional evidence for the cation-radical postulate in the case of the manganese complexes will be presented in Chapter 7.

Calculations as described in Chapter 4 were first carried out to determine an appropriate frequency range.

Table 5

Diffusion Coefficients (D), Heterogeneous Rate Constants (k_s) and AC Voltammetric Peak Potentials (E_p) for the First Oxidation of Tetraphenylporphin and Some of its Metal Complexes in $C_2H_4Cl_2$ (.2 M TBAP) at a Pt Electrode

Porphyrin	E_p/V vs SCE	$k_s \times 10^2$/cm s^{-1}	$D \times 10^6/cm^2s^{-1}$
TPP H_2	1.025	3.7 ± .2	3.6
Zn(II)TPP	.785	5.4 ± .6	3.4
(CH_3CO_2)Fe(III)TPP	.845	4.3 ± .3	1.5
ClFe(III)TPP	1.105	5.6 ± .2	2.8
(ClO_4)Mn(III)TPP	1.245	2.8 ± .2	1.9
ClMn(III)TPP	1.190	1.9 ± .2	1.8

These indicated that at frequencies below 200 Hz, no more than 10% error in the value of k_s should be introduced by the assumptions of the method employed, provided the uncompensated resistance was kept below 40 ohms. The greater value of the uncompensated resistance tolerable in these experiments, as compared to the previously discussed ferro-ferricyanide case, results from the smaller double layer capacitance associated with the Pt/$C_2H_4Cl_2$(0.2 M TBAP) interphase. In addition, both the k_s values and diffusion coefficients associated with the porphyrin oxidations are considerably smaller than those associated with the ferrocyanide system, and this also relaxes the requirement of minimum uncompensated resistance.

Before each experiment, the Pt electrode was immersed in hot concentrated nitric acid for a minimum period of 2 h. This was followed by rinsing, first, with triply distilled water, then with distilled reagent grade acetone, and finally with purified 1,2-dichloroethane. In phase and quadrature components of the ac voltammetric response were recorded, as discussed in Chapter 4, for a minimum of 6 frequencies in the range 15 to 200 Hz. The porphyrin concentrations employed were all in the range 0.5 to 1 mM with the exception of (CH_3CO_2)Fe(III)TPP, where concentrations were ca 0.2 mM due to the limited solubility of this complex in dichloroethane. The dc

potential scan range employed was 5 mV/s, and the potential modulation amplitude was 6 mV. Positive feedback compensation of solution resistance was employed to minimize R_u to a degree where stable potentiostat operation could still be maintained. The value of R_u used in subsequent calculations was experimentally determined as discussed in Chapter 4. For most cases, this was in the range 15 to 30 ohms.

Following the ac voltammetric measurements, chronocoulometric Q-t responses were obtained by stepping the applied potential to a value where the first porphyrin oxidation was diffusion controlled (ca 250 mV anodic of the ac voltammetric peak potential). The electrode was then removed from the porphyrin solution and rinsed with fresh dichloroethane. After drying, chronocoulometric curves were recorded for the oxidation of $K_4Fe(CN)_6$ in 1 M aqueous KCl. The porphyrin diffusion coefficients were determined by comparing the slope of the porphyrin chronocoulometric Q vs $t^{1/2}$ plots, normalized to concentration, with the corresponding value obtained from the ferrocyanide experiment (see Appendix 2), assuming a diffusion coefficient for ferrocyanide of 6.32×10^{-6} cm^2/s.

The entire procedure was repeated at least one more time for each porphyrin to ensure that the results were

reproducible. The diffusion coefficients, for all but one case, were reproducible within 10%. For $(CH_3CO_2)Fe(III)TPP$, the agreement between successive determinations of the diffusion coefficient was only 40%. As the diffusion coefficients enter the calculations as $D^{1/2}$, deviations of this magnitude do not seriously affect the value of k_s determined. The standard deviations associated with k_s values calculated via equation 4-11 at each individual frequency are reported in Table 5.

Also included in Table 5 are the ac voltammetric peak potentials, reported to the nearest 5 mV, for the various $P/P^{+\bullet}$ couples investigated. These are uncorrected for the presence of the liquid junction potential between the reference and working electrodes.

5.2 Discussion

The data presented here is part of a planned study of factors affecting the rate of cation radical formation for TPP complexes of a number of the first row transition metals and alkaline earths. It is hoped that eventually a deeper understanding of the mechanism underlying the electron transfer reactions of the porphyrins will be attained. Cation radicals of metalloporphyrins are believed to be important intermediates in green plant

photosynthesis, and in the action of a number of heme-containing enzymes such as the catalases and peroxidases. Aside from the biological significance of redox reactions involving porphyrin cation radical formation, such studies should be important from a more fundamental viewpoint. Because of the biological significance of the metalloporphyrins, an extensive and rapidly growing, body of literature reporting X-ray structure determinations of these compounds exists. For many cases, structures of both forms of a redox pair are available. It may be possible to arrive at correlations between charge transfer rate constants and structural changes which occur during the electron transfer process. Such correlations based on porphyrin data could well be extrapolated to other systems.

Although the data are as yet too limited to allow a great deal to be said, some comments can be made. First, all of the rate constants reported here lie in a limited range. Since all of the redox processes are associated with cation radical formation, this is to be expected. A rate constant far outside this range might well indicate that the charge transfer process involves the central metal atom rather than the porphyrin ligand, or that the charge transfer mechanism is complicated by some other factor such as specific adsorption, perhaps through an

axially bound counterion, to the electrode surface. Charge transfer reactions involving the central atom are most often considerably slower than those reported here. For instance, in a study [10] of the heterogeneous charge transfer kinetics of the redox couple XFe(III)TTP/XFe(II)TTP$^-$ (TTP = tetra(p-tolyl)porphin dianion) in CH_2Cl_2 (0.1 M TBAP), where X was one of twenty-nine axially bound counterions, an average k_s of 1.5 cm/s was found, the highest value reported being 4.8 cm/s, a full order of magnitude less than the values reported here for cation-radical formation of Fe(III)TPP complexes. Similarly, Kadish et al. [130] have reported a value of 1×10^{-3} cm/s for the redox couple Mn(III)TClPP$^+$/Mn(II)TClPP (TClPP = tetra(p-chlorophenyl)porphin dianion) in DMSO (0.1 M TBAP), and a value of 6.6×10^{-3} cm/s was estimated in this work for the analogous Mn(III)TPP$^+$/Mn(II)TPP couple by conventional cyclic voltammetry in the same solvent. (In both cases, the porphyrin counterion was chloride. This does not remain coordinated to the metal atom in DMSO, however, as noted in the introduction.)

Heterogeneous charge transfer rate constants have been reported [11] for cation radical formation of a number of octaethylporphyrin (OEP) complexes at a Pt electrode in butyronitrile (0.1 M TBAP). These appear, in

general, to be faster than those for the TPP complexes reported here, and range from ca 0.1 cm/s for complexes of simple +2 metal ions, such as Mg(II)OEP, to ca 0.4 cm/s where the metal is in a more highly oxidized state, as in the vanadyl complex OV(IV)OEP. Under the Marcus theory of electron transfer reactions [131], the reaction rate depends on the energy of solvation changes accompanying the electron transfer, as well as on the extent of internal bond reorganization of the complex which occurs during the electron transfer step. An increase in either of these factors is manifested as a decrease in the associated rate constant. For porphyrin π-cation radicals, where the charge associated with the electron transfer is highly delocalized through the aromatic ring, solvent interactions may be expected to be minimal. One can then speculate that the difference in the rates of cation radical formation for TPP and OEP complexes is due to structural differences between the two porphyrin ligands.

X-ray data indicates that, in the tetraaryl porphyrins, considerable steric interaction occurs between the ortho positions of the aromatic substituents and the β-pyrrole positions of porphyrin core, as noted in the introduction. This results in a non-planar conformation of the porphyrin nucleus with the nitrogens of adjacent

planar pyrroles positioned alternately above and below the mean porphyrin plane. The X-ray structures of Zn(II) [132] and Fe(III) [49] tetraphenylporphyrin cation radicals indicate that this distortion is more severe than in the unoxidized complexes, and it has been noted [31] that such structural deformations allow a greater degree of conjugation between the phenyl substituents and the porphyrin π-system. This in turn provides for more extensive delocalization of the positive charge in the cationic species.

On the other hand, the porphyrin nucleus in octaethylporphyrin is essentially planar [133], and it is anticipated that no departure from planarity will occur on oxidation of this ligand. The greater degree of bond deformation required to bring the phenyl substituents into conjugation in the TPP complexes may then provide a rationale for the slower rate constants observed as compared with those of the OEP complexes. Evidence was presented in Chapter 4 that the rate of oxidation of DPA is considerably less than that for perylene. In DPA, the two phenyl substituents are twisted ca 60° with respect to the anthracene nucleus [134], while perylene exists in a completely planar conformation. The slower rate constant f7r DPA oxidation might similarly result from a bond deformation required to achieve a greater degree of

conjugation between the anthracene nucleus and its phenyl substituents.

The data of Table 5 suggest that, while the metal can influence the magnitude of the rate constant associated with oxidation of the porphyrin ligand, the nature of the axially bound species is relatively unimportant. The data is as yet too limited to allow extrapolation of this observation, however.

It had been originally anticipated that some correlation might exist betwen the rate constants observed and the position of the metal within the porphyrin cavity. Fe(III) is known to lie the farthest out of the plane, Mn(III) takes an intermediate position, and Zn(II) lies in the porphyrin plane. No such correlation is apparent here. It is hoped that future studies including a greater number of metals will provide insight into how the metal affects the electron transfer rate for porphyrin oxidation. Aside from the position of the metal with respect to the porphyrin plane, metal size, electronegativity, and d electron configuration might prove to be important factors. It is interesting to note that Mn(III) is believed to interact directly with the porphyrin π-system to some extent, and this may be an important factor contributing to the slower electron transfer rates observed here for Mn(III) with respect to Fe(III) and Zn(II) complexes.

CHAPTER 6

REACTIVITY OF ZINC (II) TETRAPHENYLPORPHYRIN CATIONS TOWARD ANIONIC NUCLEOPHILES

6.1 Introduction

As noted in Chapter 1, the fifth coordination site in Fe(III) and Mn(III) porphyrins may be occupied by any of a number of possible anions. In studies of the anodic chemistry of these species, it is therefore necessary to consider the possibility that these counterions may be oxidized directly at the electrode surface, or that they may react with products of the porphyrin oxidation.

Until very recently, it was generally believed that porphyrin π-cation radicals were unreactive towards nucleophilic addition. This was based on observations that Zn(II) and Mg(II) complexes of tetraphenylporphyrin cation radicals were indefinitely stable in the presence of nucleophilic solvents such as methanol [37,135]. Similarly, in an ESR study of halide salts of Zn(II)TPP$^{+\bullet}$ [136] no evidence for halide addition to the oxidized porphyrin ring was found.

On the other hand, Zn(II)TPP^{2+} dications have been reported [37,135] to react rapidly with nucleophiles such as methanol or water to give the corresponding cationic isoporphyrin species. One possible resonance structure of Zn(II) tetraphenyl-methoxy-isoporphyrin cation is illustrated as the product of reaction 6-1.

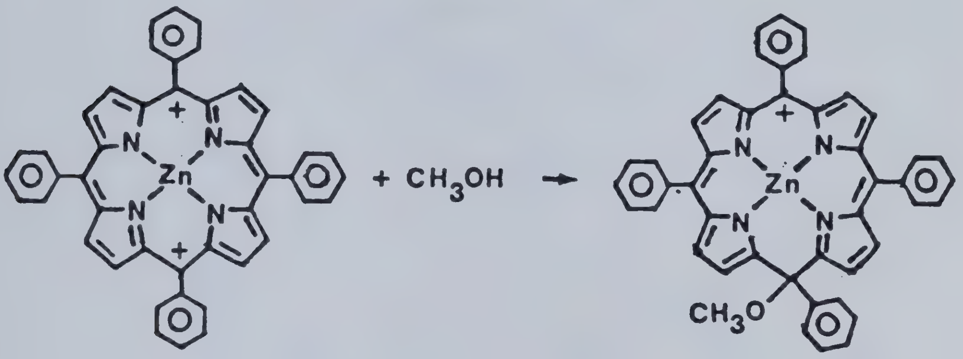

(6-1)

Such reactions with methanol or water appear to be typical of dication formation, and have been reported for Fe(III) [137] and Mg(II) [135] TPP complexes in addition to the Zn(II) case. The reaction of the dication of $TPPH_2$ with water has been observed in this laboratory by cyclic voltammetry.

Figure 41a illustrates the cyclic voltammetry of $TPPH_2$ at a Pt electrode in anhydrous dichloromethane. The peaks labelled I and II correspond respectively to formation and reduction of the cation radical, while III and IV are due to formation and reduction of the

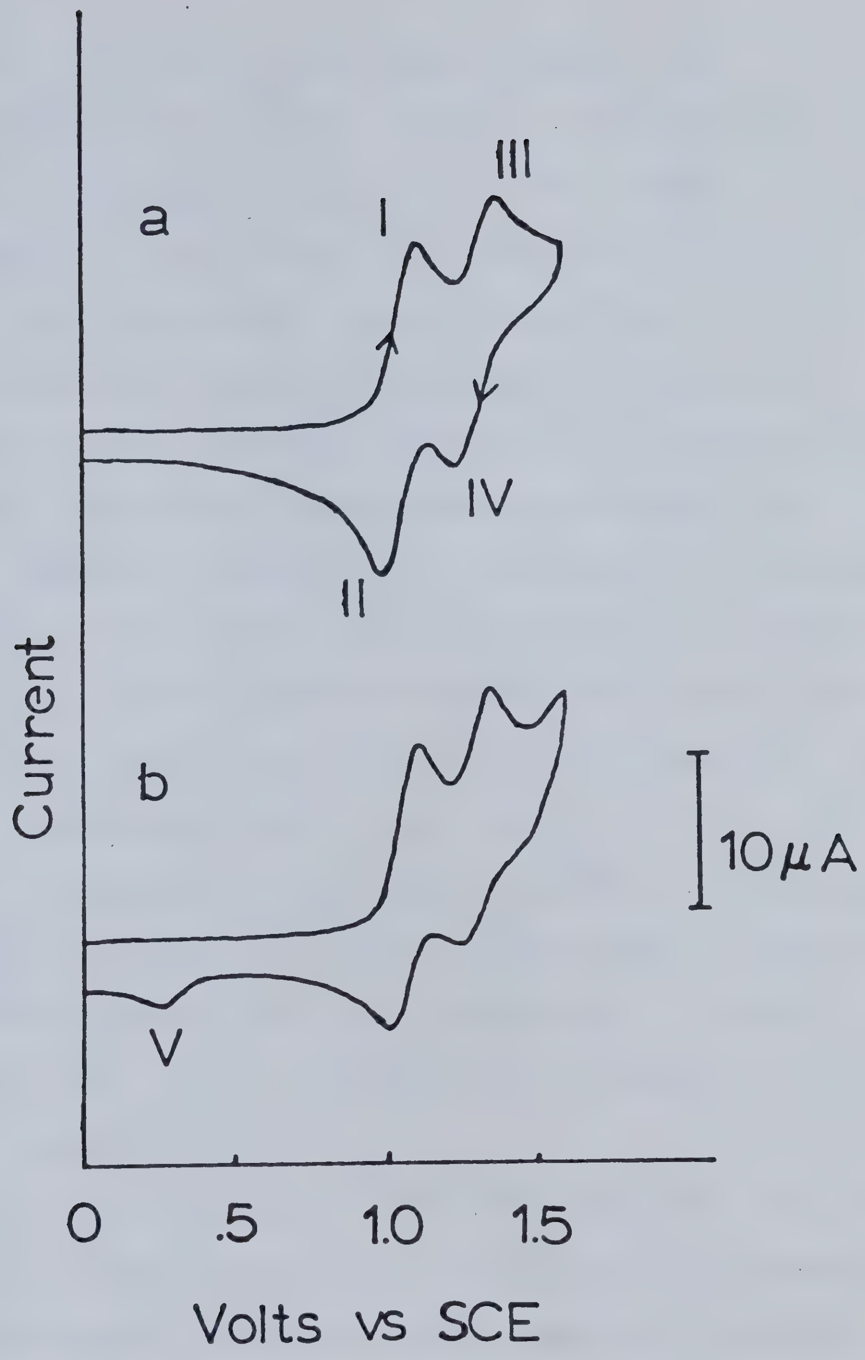

Figure 41. Cyclic voltammetry of 1 mM $TPPH_2$ in CH_2Cl_2(.1 M TBAP), υ = 300 mV/s; (a) anhydrous conditions; (b) after addition of 20 μL H_2O.

dication. For both of the redox couples, the corresponding ratio of the anodic to cathodic peak currents, $i_{p,a}/i_{p,c}$, is equal to unity, within experimental error, indicating that both the cation radical and dication are formed reversibly. In the presence of H_2O, reversible formation of the cation radical is still observed, providing the potential is kept at values cathodic of those where the dication is formed. When the potential is increased to values past the peak current for dication formation, the cathodic peak currents, IV and II, observed during the reverse sweep are reduced relative to their values in the absence of water, clearly indicating reaction between the dication and water. In addition, a new cathodic peak, V, is evident, and represents the reduction of a new species formed by the water-dication reaction. By analogy to known reactions such as 6-1, this species is assumed to be the hydroxyisoporphyrin cation.

Evans and co-workers [138] have reported that the reaction of metalloporphyrins with $Tl(CF_3CO_2)_3$ leads to the formation of trifluorocetoxyisoporphyrin cations. The initial step was ascribed to metalloporphyrin π-cation radical formation by Tl(III) oxidation. After that, the course of the reaction was less certain, and two feasible reaction paths were proposed, as in Figure 42. The first,

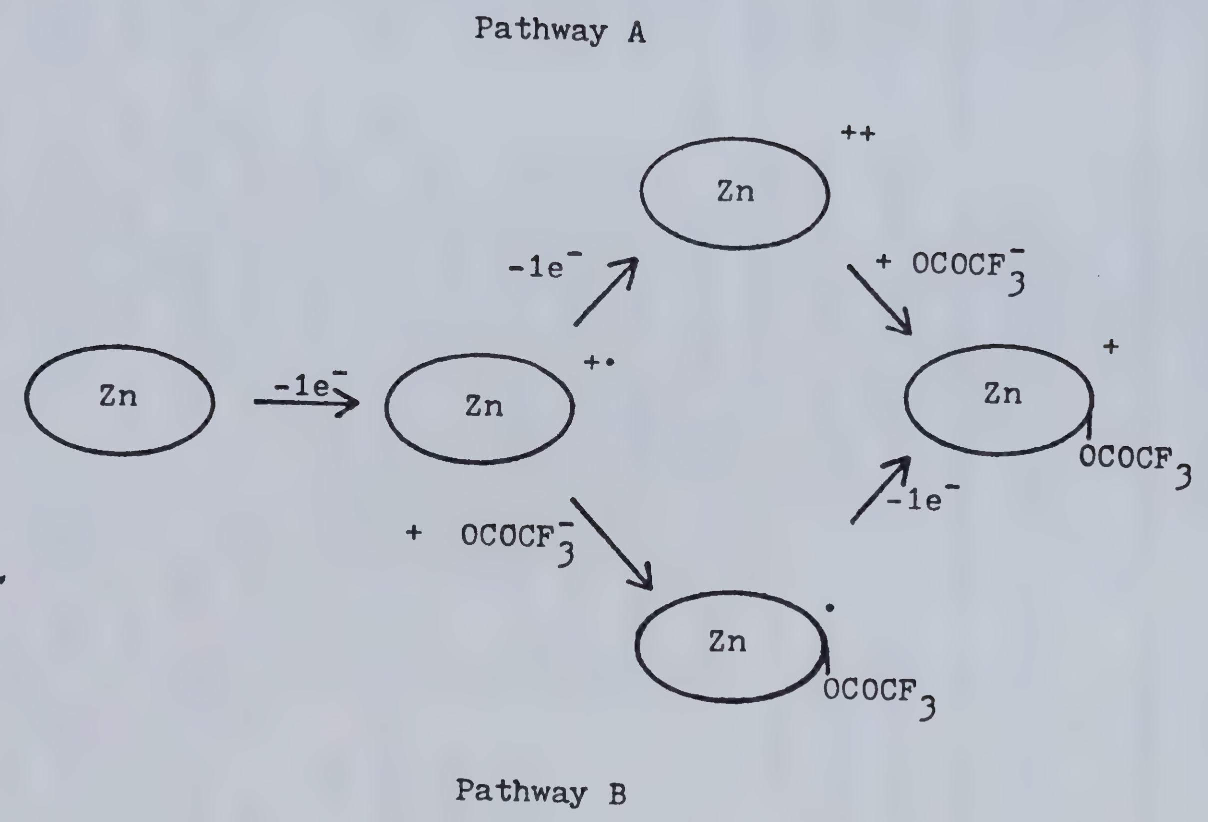
Pathway A
Zn
-1e⁻
Zn
+•
-1e⁻
Zn
++
+ OCOCF3⁻
Zn
+
OCOCF3
+ OCOCF3⁻
Zn
•
OCOCF3
-1e⁻
Pathway B

Figure 42. Suggested reaction pathways for isoporphyrin formation.

pathway A, involves reaction between the dication and trifluoroacetate ion, and is in accordance with earlier observations of the stability of cation radicals in the presence of nucleophiles. The second, pathway B, invokes reaction between trifluoroacetate and a π-cation radical, followed by subsequent oxidation to the isoporphyrin cation.

Evans et al. favoured pathway B on the basis of more recent reports that isolated metalloporphyrin π-cation radicals did indeed lead to isoporphyrin formation in the presence of neutral nucleophiles such as pyridine [139,140] or imidazole [141], or anionic species such as nitrite [142], thiocyanate, cyanide, or chloride [143].

Kadish et al. have recently examined the stability Zn(II)TPP cation radicals [70] and dications [139] in the presence of nucleophiles such as pyridine by voltammetric methods, and were able to find evidence for isoporphyrin formation only after the dication had been produced, in spite of reports by others [140,144] of the reaction between pyridine and the cation radical.

Voltammetric methodology has been applied here to determine the stability of Zn(II)TPP cation radicals in the presence of the anionic nucleophiles $CF_3CO_2^-$ and $CH_3CO_2^-$. The study was undertaken in hopes of clarifying certain anomolous behaviour observed in the anodic

voltammetry of $(CF_3CO_2)Mn(III)TPP$ and $(CH_3CO_2)Mn(III)TPP$. The relevance to the manganese porphyrins will become obvious in Chapter 7. In addition, such studies are biologically relevant, as isoporphyrins are believed to be intermediates in the formation of the bile pigments from iron porphyrins. Zn(II)TPP was chosen because the possibility of an electron transfer involving the metal is highly unlikely, and because the literature contains a great deal of spectroscopic data for this complex and its oxidized forms.

6.2 Results and Discussion

Figure 43a illustrates the cyclic voltammetry observed at anodic potentials at a Pt electrode in a solution of Zn(II)TPP in $C_2H_4Cl_2$ (0.2 M TBAP). The voltammetric waves have previously been characterized [37,139] as representing the reversible redox couples $Zn(II)TPP/Zn(II)TPP^{+}$, peaks I and II, and $Zn(II)TPP^{+\bullet}/Zn(II)TPP^{2+}$, peaks III and IV.

When small quantities of tetramethylammonium trifluoroacetate (TMATFA) are added to the solution, a new anodic peak, V, begins to appear at a potential slightly less positive than that corresponding to production of the cation radical, $Zn(II)TPP^{+\bullet}$. (Because of the limited solubility of TMATFA in dichloroethane, this was added as

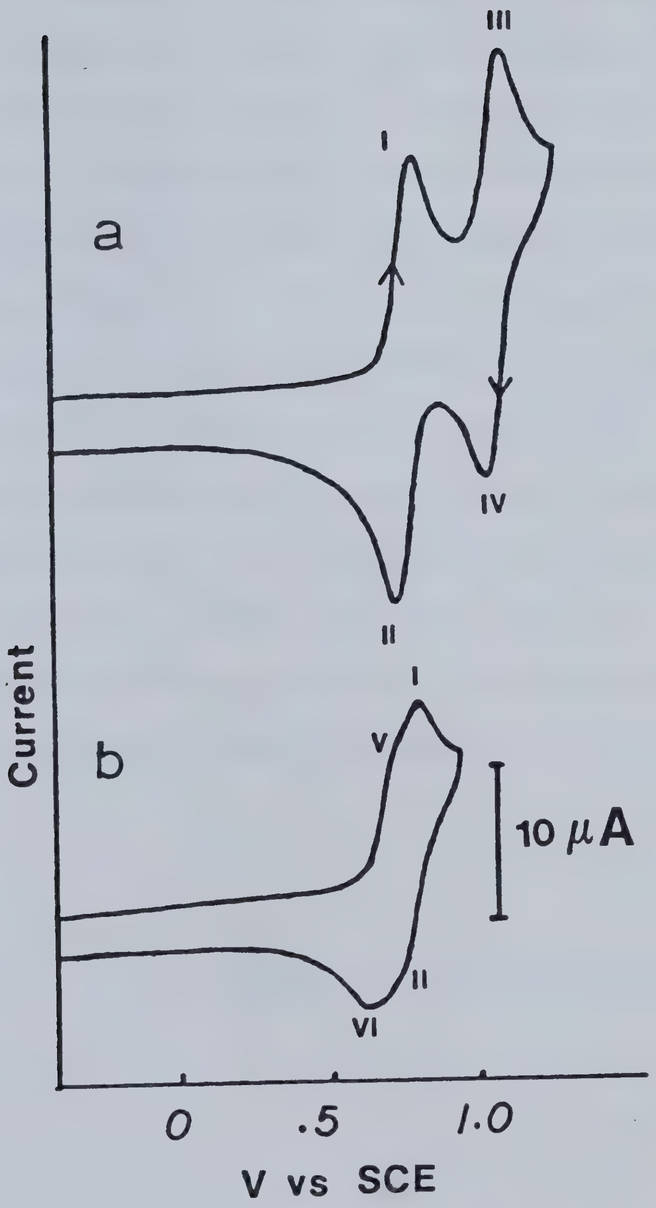

Figure 43. Cyclic voltammetry of .8 mM Zn(II)TPP in $C_2H_4Cl_2$(.2 M TBAP), ν = 100 mV/s; (a) no TMATFA added; (b) .5 mM in TMATFA.

μL injections of a 0.2 M solution in nitromethane.) A new cathodic peak, VI, coupled to the oxidation represented by peak V, is also observed. As the concentration of TMATFA is increased, peaks V and VI grow in intensity while peaks I and II disappear. These changes are complete when the ratio of the concentration of trifluoroacetate to that of the zinc porphyrin complex is unity. This suggests that the voltammetric changes are due to the formation of a 1:1 complex between trifluoroacetate ion and Zn(II)TPP. Five-coordinate complexes LZn(II)TPP, where L is a nitrogenous base such as pyridine [70], or a halide ion [136], have previously been reported. Peaks V and VI are thus ascribed to the one-electron oxidation and corresponding reduction of the anionic complex $[(CF_3CO_2)Zn(II)TPP]^-$, as in reaction 6-2.

$$[(TFA)Zn(II)TPP]^- - 1e^- \underset{VI}{\overset{V}{\rightleftharpoons}} [(TFA)Zn(II)TPP^{+\bullet}]^0 \quad (6\text{-}2)$$

$(TFA = CF_3CO_2^-)$

It is interesting to note that the cyclic voltammetric peak separation associated with formation and reduction of the cation radical in the absence of trifluoroacetate ion (ΔE_p = 70 mV at ν = 100 mV/s) is

considerably less than that observed when an excess of trifluoroacetate is present (ΔE_p = 105 mV at ν = 100 mV/s). This indicates that the apparent rate constant, k_s, associated with cation radical formation is slower for the 5-coordinate trifluoroacetate complex than for the corresponding 4-coordinate species, Zn(II)TPP. Similar observations have been reported by Kadish et al. [70] for 5-coordinate complexes between Zn(II)TPP and various nitrogenous bases. It is not clear whether or not this is due to structural changes of the porphyrin imposed by axial ligation. Adsorption of the additional ligand onto the electrode surface might also explain these results.

The ratio of the peak current for formation of the cation radical to that for the corresponding reduction is equal to unity even at sweep rates as low as 10 mV/s and when a large excess of trifluoroacetate ion is present. The cation radical is thus stable with respect to reaction with trifluoroacetate, at least under the conditions used here and on the time scale of the cyclic voltammetric experiment.

Figure 44 illustrates the cyclic voltammetric behaviour observed in the presence of excess trifluoroacetate when the potential is swept to more anodic values before reversing the direction of the sweep. When the potential sweep direction is reversed

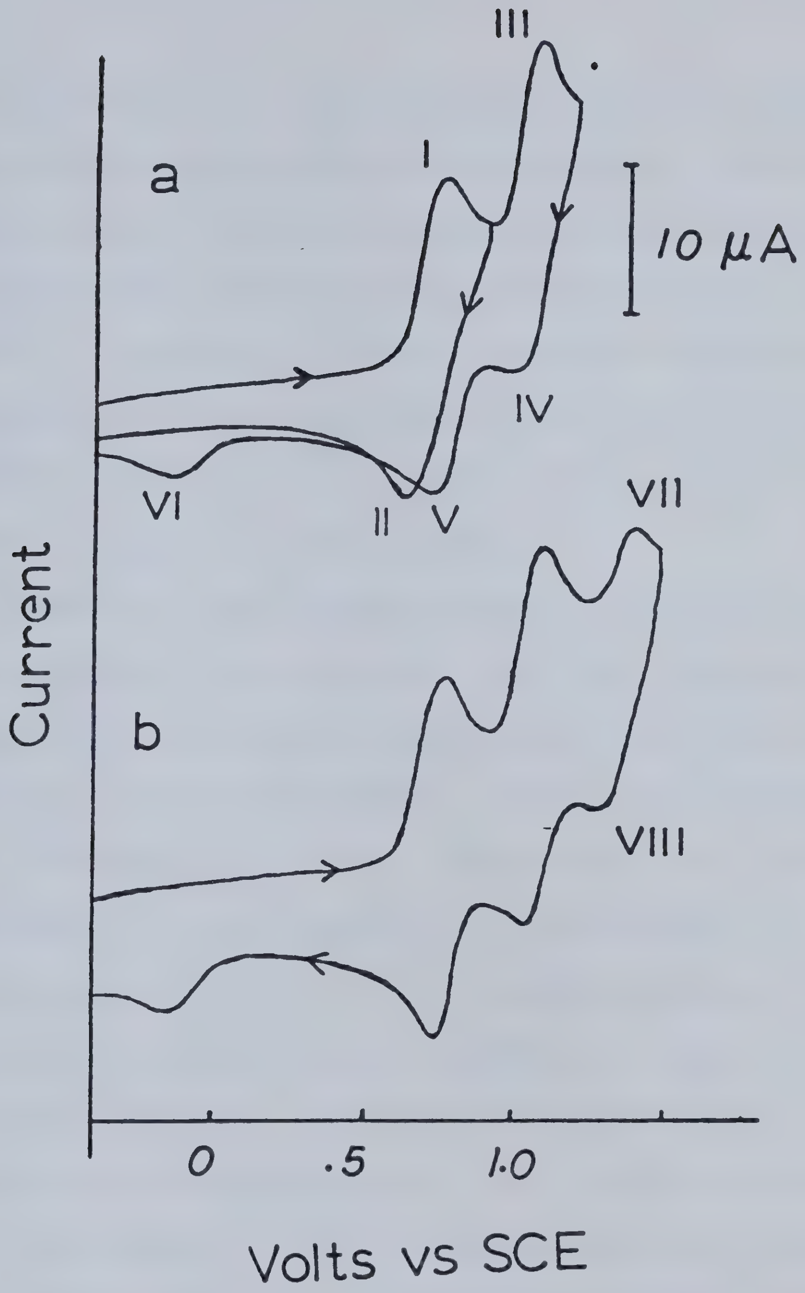

Figure 44. Cyclic voltammetry of .8 mM Zn(II)TPP in $C_2H_4Cl_2$(.2 M TBAP) containing 1.3 mM TMATFA, ν= 100 mV/s.

after formation of the dication, peak III in Figure 44a, the cathodic peak currents corresponding to reduction of cation radical and dication species, are reduced relative to the values expected if the dication formed was stable. This suggests that a reaction between the porphyrin dication and trifluoroacetate ion has occurred to give a product which is not electroactive at potentials between 0 and +1.1 volts vs SCE.

Note that the cathodic peak, V in Figure 44a, occurs at a potential more positive than that observed for reduction of the cation radical of the 5-coordinate species $[(CF_3CO_2)Zn(II)TPP]^-$. The peak potential, in fact, corresponds to that observed for the reduction of $Zn(II)TPP^{+\bullet}$ in the absence of trifluoroacetate. The reduction of the 4-coordinate cation radical is observed even when a 3-fold excess of TMATFA is present, and indicates that the dication reacts preferentially with coordinated trifluoroacetate. It is also apparent that the coordination of trifluoroacetate to the porphyrin is kinetically sluggish, as rapid kinetics associated with this step would prohibit the observation of any 4-coordinate species at the relatively slow potential scan rates used here. As the ratio of trifluoroacetate to porphyrin concentration is increased, peak V disappears, and in the presence of a 6-fold excess of

porphyrin concentration is increased, peak V disappears, and in the presence of a 6-fold excess of trifluoroacetate, only peak II is observable at potentials where cation radical reduction is expected on the reverse sweep, at least at scan rates below 500 mV/s. This observation is consistent with the assignment of peaks II and V to reduction of the 5- and 4-coordinate radical cation species, respectively.

At lower sweep rates, and when the potential scale is expanded, an inflection in the rising portion of the wave leading to peak III in Figure 44a is observed, indicating that this wave is in fact a composite of two processes. These are suggested to be the oxidation of the 5- and 4-coordinate radical cations, where the 4-coordinate species is formed as the result of a homogeneous reaction following the formation of the 5-coordinate dication, as in reaction 6-3.

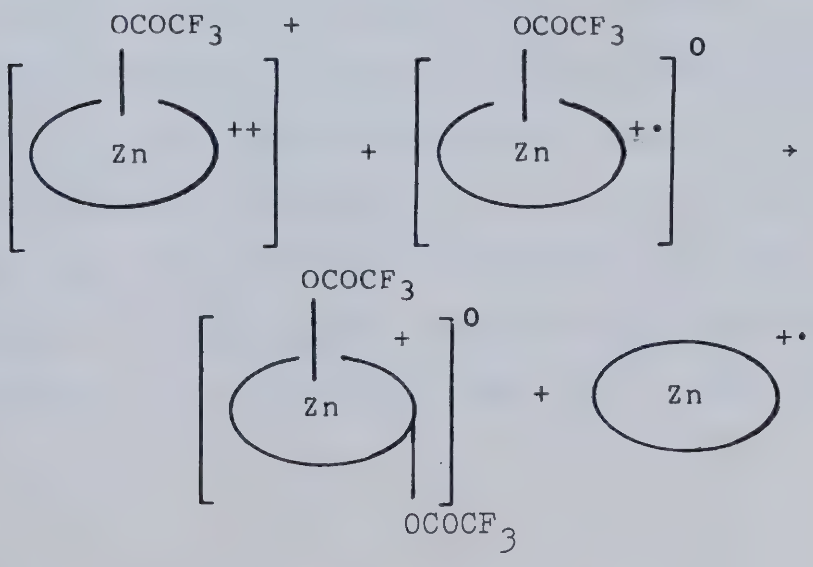

(6-3)

In order to verify that the reaction between the dication and trifluoroacetate results in isoporphyrin formation, the spectral changes associated with the oxidative processes were monitored in the thin layer spectroelectrochemical cell described in Chapter 2. All known isoporphyrins display a strong absorption at ca 875 nm in the near IR portion of the electronic absorption spectrum [3]. This is supposed to arise from interruption of the conjugation of the porphyrin π-system concurrent with isoporphyrin formation.

Spectrum 1 in Figure 45 is that observed for $[(CF_3CO_2)Zn(II)TPP]^-$ before the application of any potential to the working electrode. As the potential is gradually increased to +0.85 volts vs SCE, spectrum 2 appears, and well-defined isosbestic points are observed at 540 and 558 nm during the preceding scans (not shown in the Figure). This spectrum is in excellent agreement with those reported by others [37,135] as corresponding to Zn(II)TPP cation radicals. The appearance of the isosbestic points indicates that no reaction of the cation radical with trifluoroacetate ion occurs. As the potential is increased to +1.2 volts vs SCE, spectrum 3 is obtained. The two-band structure in the near IR is typical of isoporphyrin formation, and the spectrum appears to be essentially identical to that reported by

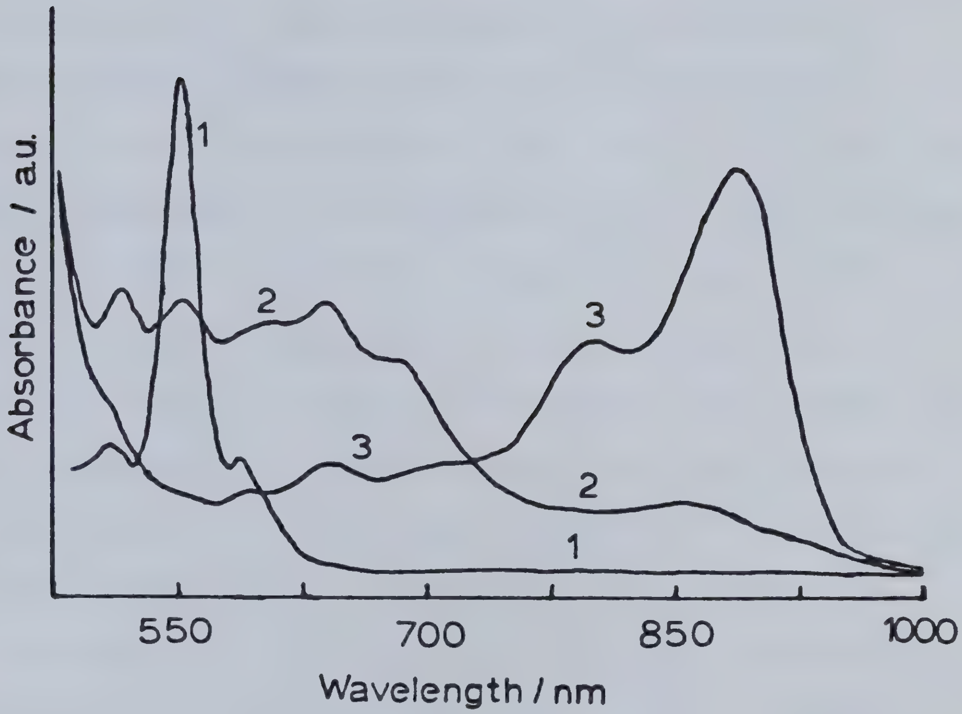

Figure 45. Spectral changes observed on oxidation of .4 mM Zn(II)TPP in $C_2H_4Cl_2$(.2 M TBAP) containing TMATFA (sat'd); (1) before the application of any applied potential; (2) E_{app} = .85 V vs SCE; (3) E_{app} = 1.2 V vs SCE.

Evans et al. [138] for the trifluoroacetoxyisoporphyrin formed by reaction of Zn(II)TPP with $Tl(CF_3CO_2)_3$.

When the potential is extended to more cathodic values on the reverse sweep of the cyclic voltammogram in Figure 44a, a new reduction peak, VI, is observed at ca -0.2 volts vs SCE. As this appears only after the dication has been formed, this may be ascribed to reduction of the isoporphyrin. The position of this peak is highly dependent on the potential scan rate, shifting more cathodically with increasing sweep rates. This is consistent with the presence of a homogeneous chemical reaction following the electron transfer step [145]. On repetitive cycling of the electrode potential between -0.5 and +1.25 volts, no anodic peak coupled to the reduction peak VI is observed at scan rates up to 1.5 V/s.

The results of the repetitive cycling experiment indicate that the reduction process at -0.2 V vs SCE results in recovery of the starting material $[(CF_3CO_2)Zn(II)TPP]^-$. When the potential is scanned repetitively between -0.4 and +1.2 V, a steady state value for the current at peak I of Figure 44a is attained after a few cycles. This is ca 30% greater, at ν = 600 mV/s, than that observed when the potential on the cathodic sweeps is stopped at +0.2 V and held at this value for the period of time which would have been required to sweep

through to -0.4 V and back again, before continuing with the next anodic sweep. This clearly indicates recovery of the starting material at the more negative potentials.

When the potential sweep is extended to more anodic values, as in Figure 44b, a new apparently 1-electron anodic peak, VII, and a corresponding reduction peak, VIII, are observed. The relative magnitude of peak VII as compared to peaks I and III decreases as the sweep rate, ν, increases. This indicates that peak VII represents the oxidation of the product of a preceding chemical reaction, and may thus be ascribed to 1-electron oxidation of the isoporphyrin. There appear to be no previous reports of isoporphyrin oxidation in the literature.

That the reaction leading to isoporphyrin formation results from the presence of the dication, and not the cation radical, is more clearly evidenced in the cyclic voltammetry obtained at the Pt thin layer electrode, as illustrated in Figure 46. Here, the potential was held constant for a few seconds at the end of the anodic sweep, to allow time for complete reaction of the dication with trifluoroacetate, before reversing the sweep direction. Note that no substantial reduction is evident on the reverse sweep until the appearance of peak IV at ca -0.1 V vs SCE. If, on the other hand, the potential is reversed before reaching values resulting in the formation of the

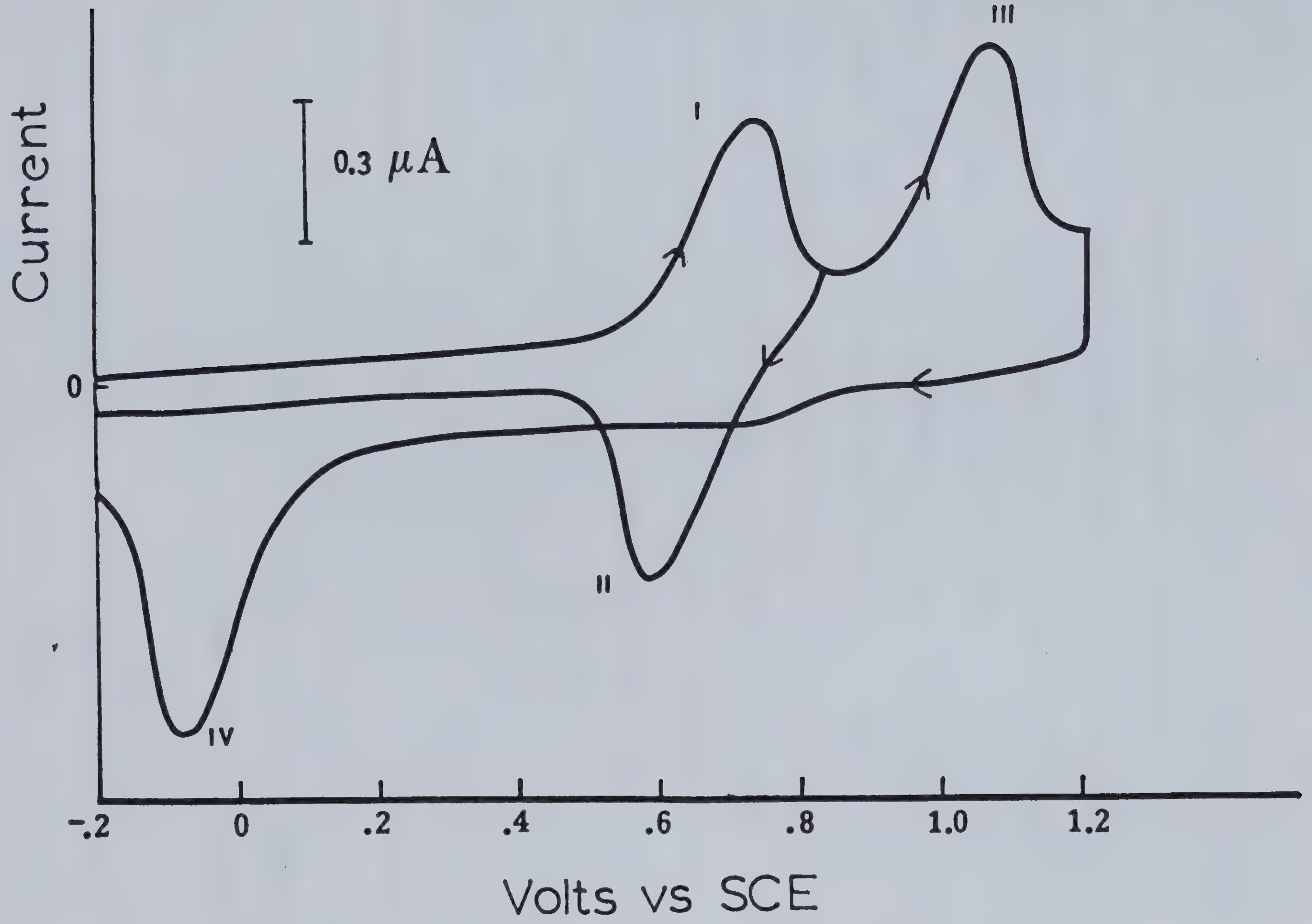

Figure 46. Cyclic voltammetry of Zn(II)TPP in $C_2H_4Cl_2$(.2 M TBAP) containing TMATFA (sat'd) at Pt thin layer electrode; ν = 100 mV/s.

dication, then the charge passed in peak I on the forward sweep is completely recovered in peak II on the reverse sweep.

It is somewhat perplexing to note that the reduction at -0.1 V, peak IV in Figure 46, corresponds to a 1-electron process. The ratio of the areas of peak I to peak IV is unity, as estimated by approximating the peaks as triangles, at all sweep rates between 10 and 100 mV/s. At 10 mV/s, the width of peak IV at half-height is 110 mV. That this reduction results in recovery of the starting material, as was suggested by the conventional cyclic voltammetric results, is substantiated by repetitive cycling at the thin layer electrode, as illustrated in Figure 47. These are the steady state cyclic voltammograms obtained on repetitive cycling between -0.5 and +1.05 V (Figure 47a) and between +0.2 and +1.05 V (Figure 47b). The substantial increase in the anodic peaks corresponding to formation of the cation radical and dication in Figure 47a, as compared to those in Figure 47b provides clear evidence that the reduction process at -0.1 V results in recovery of the starting material.

As the isoporphyrin is formed only after abstraction of two electrons from the starting material, it is difficult to see how a 1-electron reduction could result

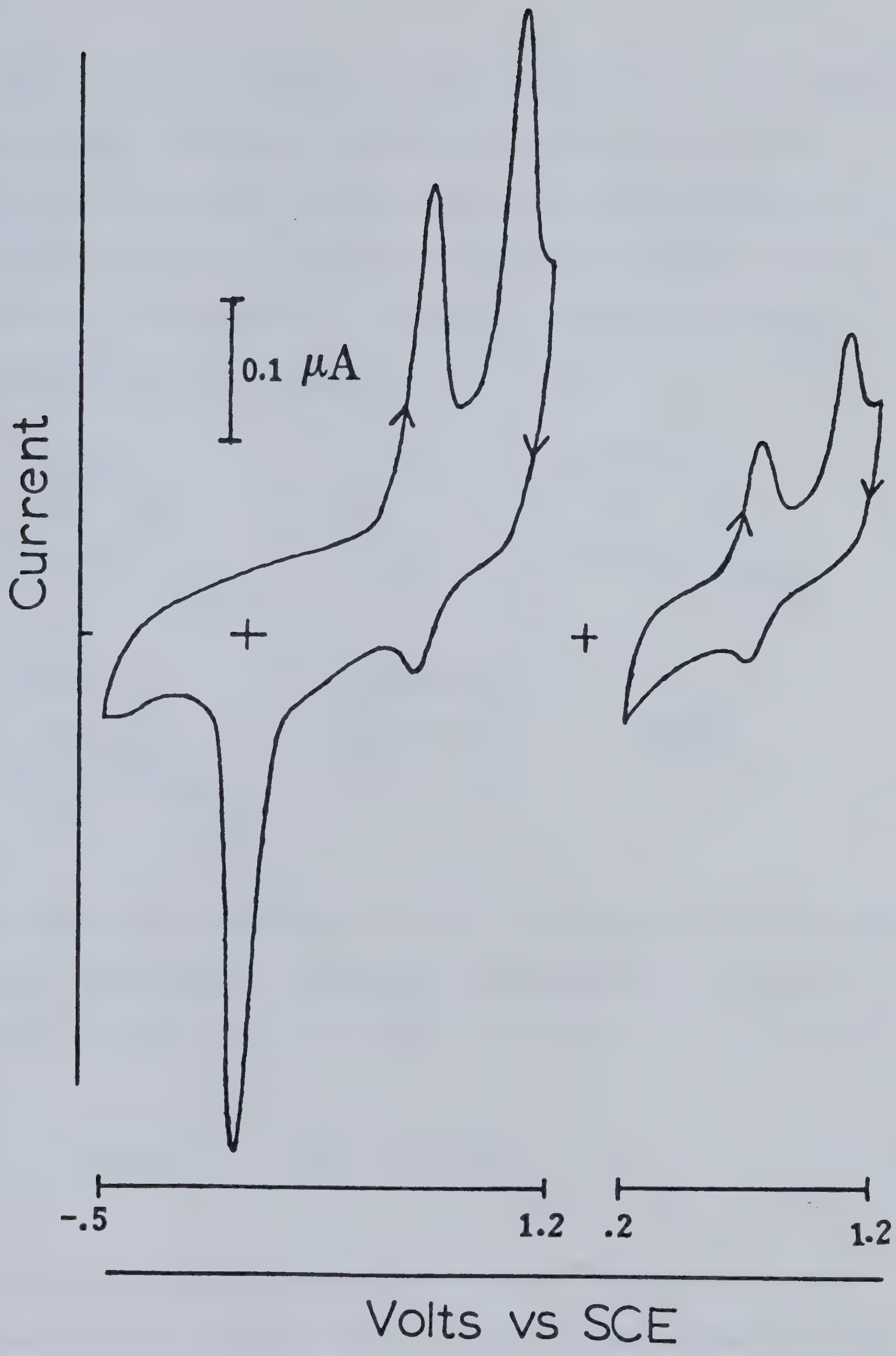

Figure 47. Steady state thin layer cyclic voltammograms for 1 mM Zn(II)TPP in $C_2H_4Cl_2$ containing TMATFA (sat'd) ν = 20 mV/s.

in the recovery of the original porphyrin. One possible route could involve a 1-electron reduction of the isoporphyrin cation to the corresponding radical, followed by elimination of a trifluoroacetoxyl radical, as in reactions 6-4 and 6-5. (Axially coordinated $CF_3CO_2^-$ has been omitted for simplicity.)

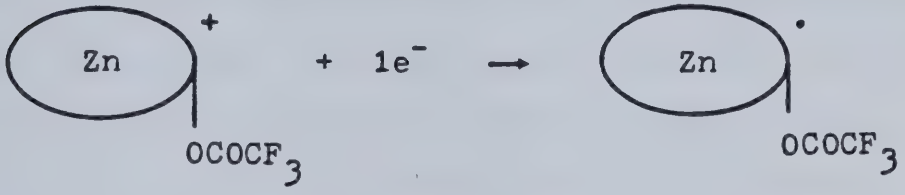

(6-4)

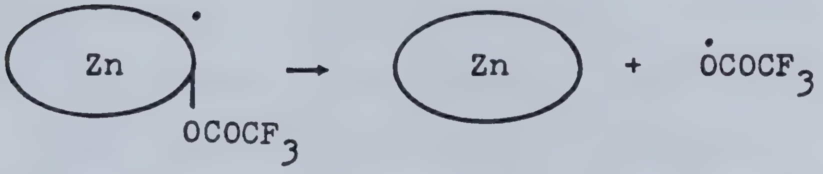

(6-5)

The resulting trifluoroacetoxyl radical would then be expected to rapidly decompose, perhaps in accordance with the well known Kolbe reaction [26], 6-6.

$$2(OCOCF_3^{\bullet}) \rightarrow 2CO_2 + CF_3CF_3 \qquad (6\text{-}6)$$

It is hoped that planned studies of the reduction of isolated isoporphyrins will clarify the nature of the mechanism by which these are reduced back to porphyrins.

A general scheme summarizing the behaviour observed here for Zn(II)TPP in the presence of excess

trifluoroacetate ion is presented in Figure 48. It should be noted that all of the 4-coordinate species in the figure can enter into additional coordination equilibria with trifluoroacetate, and some of these equilibria have been omitted in the scheme. Similarly, reaction to the isoporphyrin from the 4-coordinate dication is feasible. The trifluoroacetate incorporated into the isoporphyrin is shown as arising from the 5-coordinate cation radical. Although the voltammetric evidence suggests this is a major route, reaction between dicationic porphyrins and either solution free or other coordinated forms of trifluoroacetate is also likely to contribute.

When solutions of $(CH_3CH_2)_4N^+CH_3CO_2^-$ in dichloroethane were added to Zn(II)TPP solutions in $C_2H_4Cl_2$ (0.2 M TBAP), the qualitative voltammetric behaviour observed was identical to that for addition of TMATFA/nitromethane solutions. Hence, the same general scheme of Figure 48 applies to acetate as well as trifluoroacetate. Figure 49 illustrates the conventional cyclic voltammetry observed for Zn(II)TPP in the presence of acetate ion. Note that the effect of coordination of acetate on the porphyrin voltammetric potentials is greater than that of trifluoroacetate. Hence, the various voltammetric waves of Figure 49 arising from the oxidation of 5 and 4-coordinate species are better resolved than in

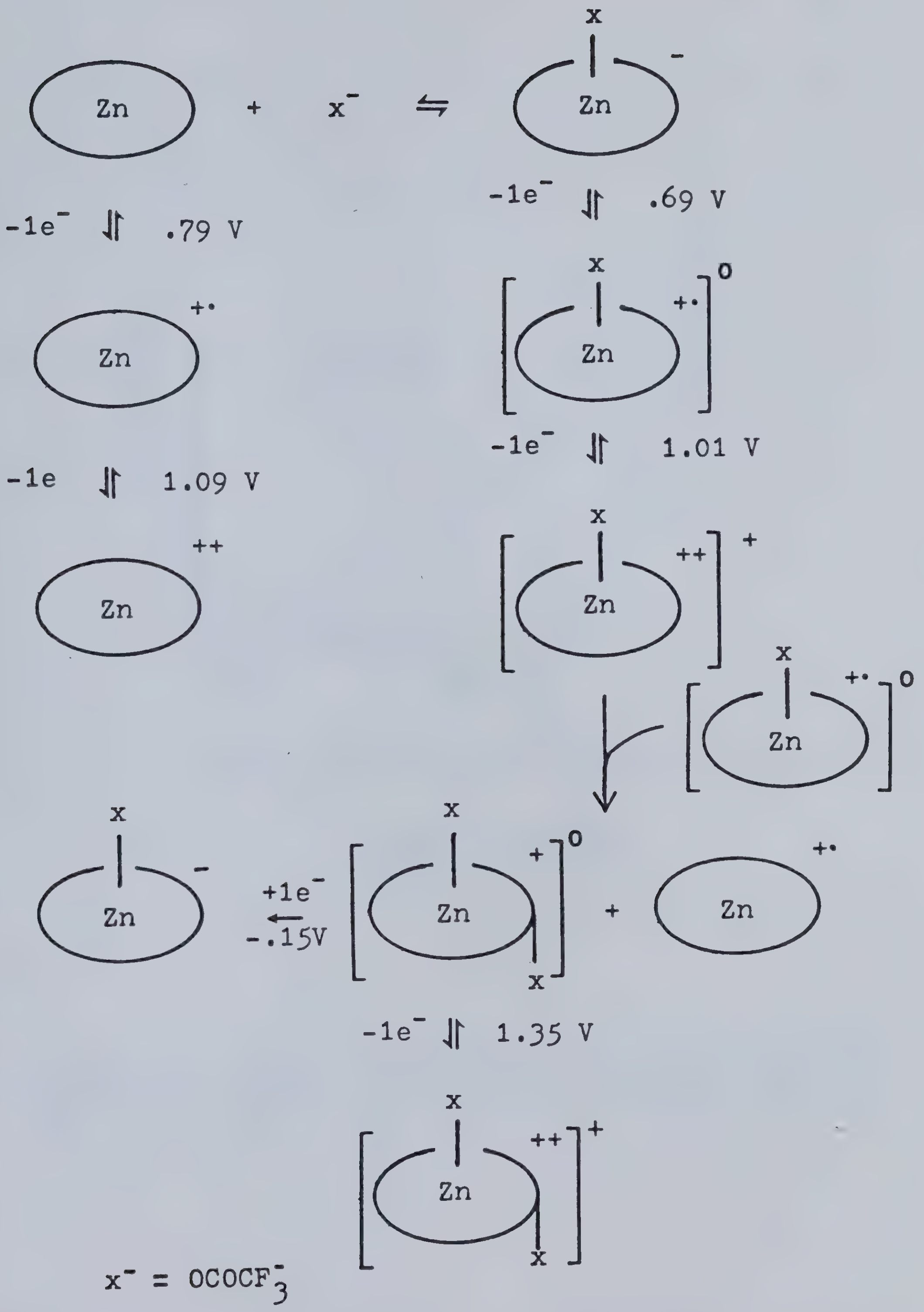
Zn
+
x⁻
⇋
x
Zn
-
-1e⁻
.79 V
-1e⁻
.69 V
+·
-1e
1.09 V
++
0
1.01 V
+
x = OCOCF₃⁻
+1e⁻
-.15V
-1e⁻
1.35 V

Figure 48. Scheme illustrating reactions of Zn(II)TPP and its oxidized forms in the presence of trifluoroacetate ion. The potentials listed were estimated as the mean of the forward and reverse peak potentials for reversible couples and as the potential at 3/4 of the peak height (ν = 100 mV/s) for irreversible processes.

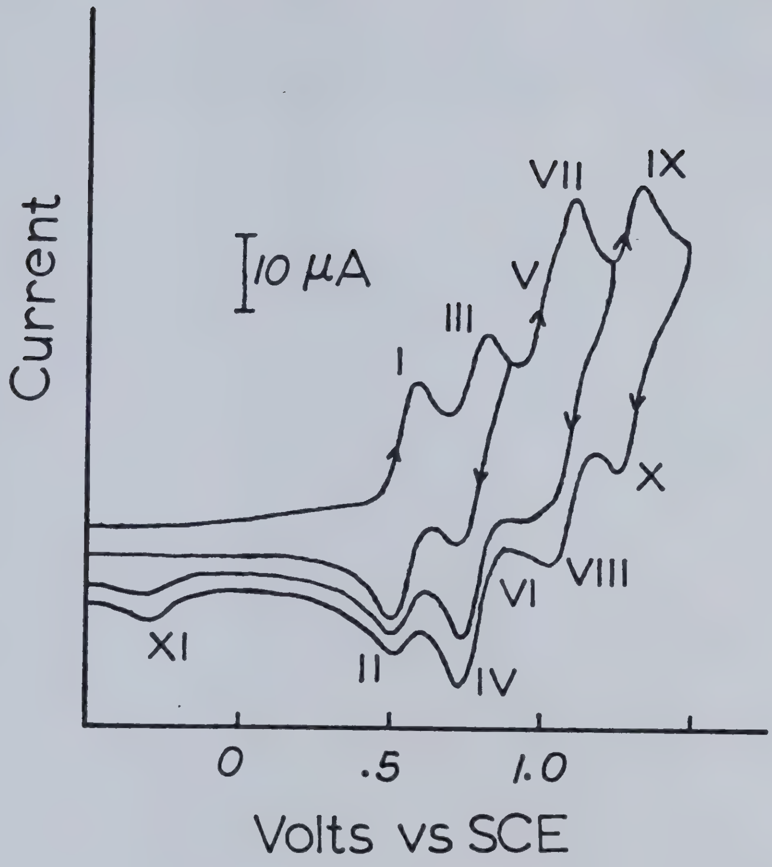

Figure 49. Cyclic voltammetry of 1 mM Zn(II)TPP in $C_2H_4Cl_2$(.2 M TBAP) containing .4 mM $(Et_4N)^+CH_3CO_2^-$, ν = 100 mV/s.

previously presented voltammograms obtained in the presence of trifluoroacetate. The assignment of the various voltammetric peaks of Figure 49 is illustrated in Figure 50.

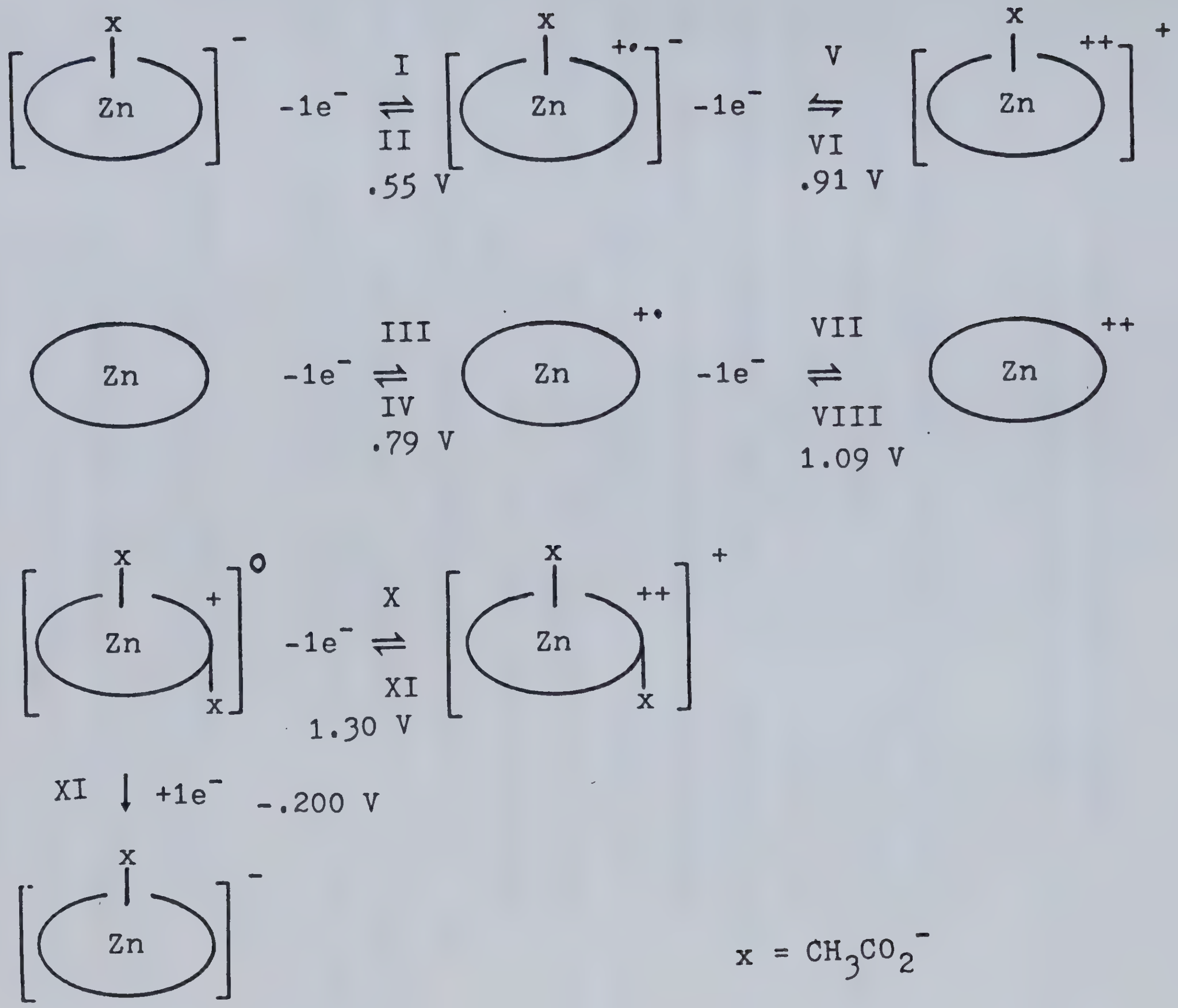
x
Zn
-1e⁻
I
II
.55 V
-1e⁻
V
VI
.91 V
III
IV
.79 V
VII
VIII
1.09 V
X
XI
1.30 V
XI
+1e⁻
-.200 V

$x = CH_3CO_2^-$

Figure 50. Assignment of voltammetric peaks of Figure 49. Potentials estimated as in Figure 48.

CHAPTER 7

ANODIC VOLTAMMETRY OF MANGANESE[III] TETRAPHENYLPORPHYRIN COMPLEXES

As the voltammetric behaviour observed for Mn(III)TPP$^+$ complexes at positive potentials with respect to SCE is highly dependent on the identity of the coordinated counterion, the various complexes studied will be discussed according to the type of voltammetric behaviour observed. Kelly et al. have shown [35] through conductivity measurements that (ClO_4)Mn(III)TPP does not ionize in $C_2H_4Cl_2$, and it will therefore be assumed throughout the following discussion that each of the counterions involved remains coordinated to the manganese atom in $C_2H_4Cl_2$ and CH_2Cl_2, except where otherwise noted.

7.1 Voltammetry of XMn(III)TPP; X = ClO_4^-, CH_3O^-

Figure 51 illustrates the cyclic voltammetric response observed for (ClO_4)Mn(III)TPP in CH_2Cl_2 (0.15 M TBAP). Two reversible cyclic voltammetric waves are observed at $E_{1/2}$ = 1.19 and 1.56 V vs SCE. No other

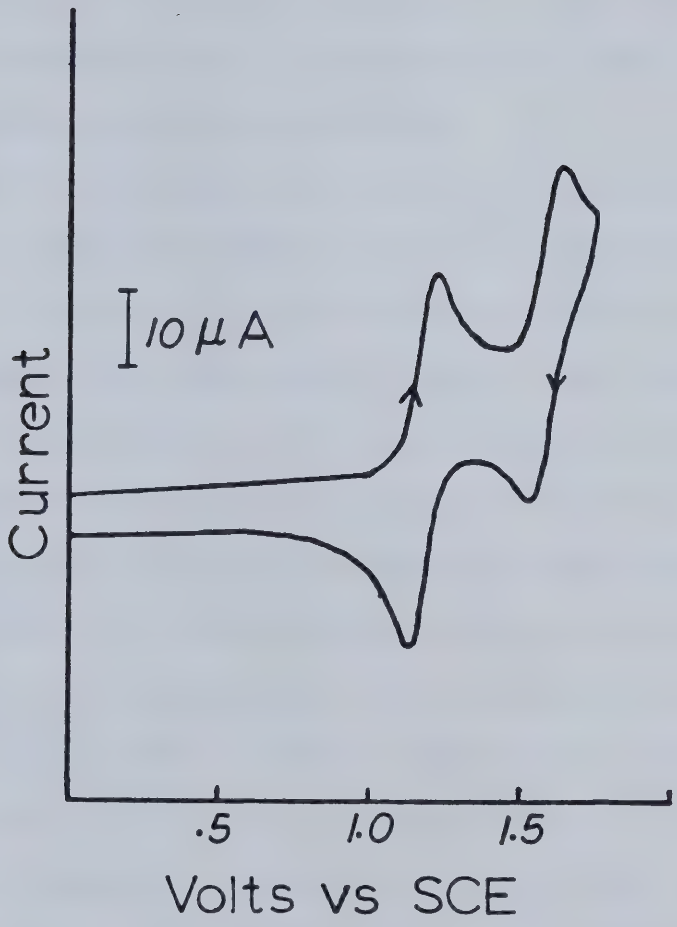

Figure 51. Cyclic voltammetry of 1.1 mM (ClO_4)Mn(III)TPP in CH_2Cl_2(0.15 M TBAP); scan rate = 100 mV/s.

voltammetric peaks are observed at potentials of up to 2.0 V. The peak separations observed for the two pairs of voltammetric peaks were in the range of 70 to 90 mV at scan rates below 300 mV/s, indicating that both processes involve 1-electron charge transfers.

Figure 52 illustrates the spectral changes observed in the thin layer spectroelectrochemical cell as the potential of the working electrode was sequentially stepped through the first anodic wave. Note the presence of several isosbestic points, indicating that only a single, stable product results from the oxidation. The decrease in intensity and broadening of the absorbance in the Soret region of the spectrum is consistent with the formation of a cation radical. The structure of the absorbance in the 500 to 700 nm region after complete electrolysis at 1.35 V is very reminiscent of that observed on 1-electron oxidation of Zn(II)TPP. The first oxidation of $(ClO_4)Mn(III)TPP$ may thus be ascribed to oxidation of the porphyrin ligand.

Attempts to observe reproducible spectral changes at potentials corresponding to the second oxidation have been unsuccessful. Isosbestic points were not observed, indicating that while the second oxidation product is apparently stable on the cyclic voltammetric time scale, it is not stable over the 3 to 10 minute time period

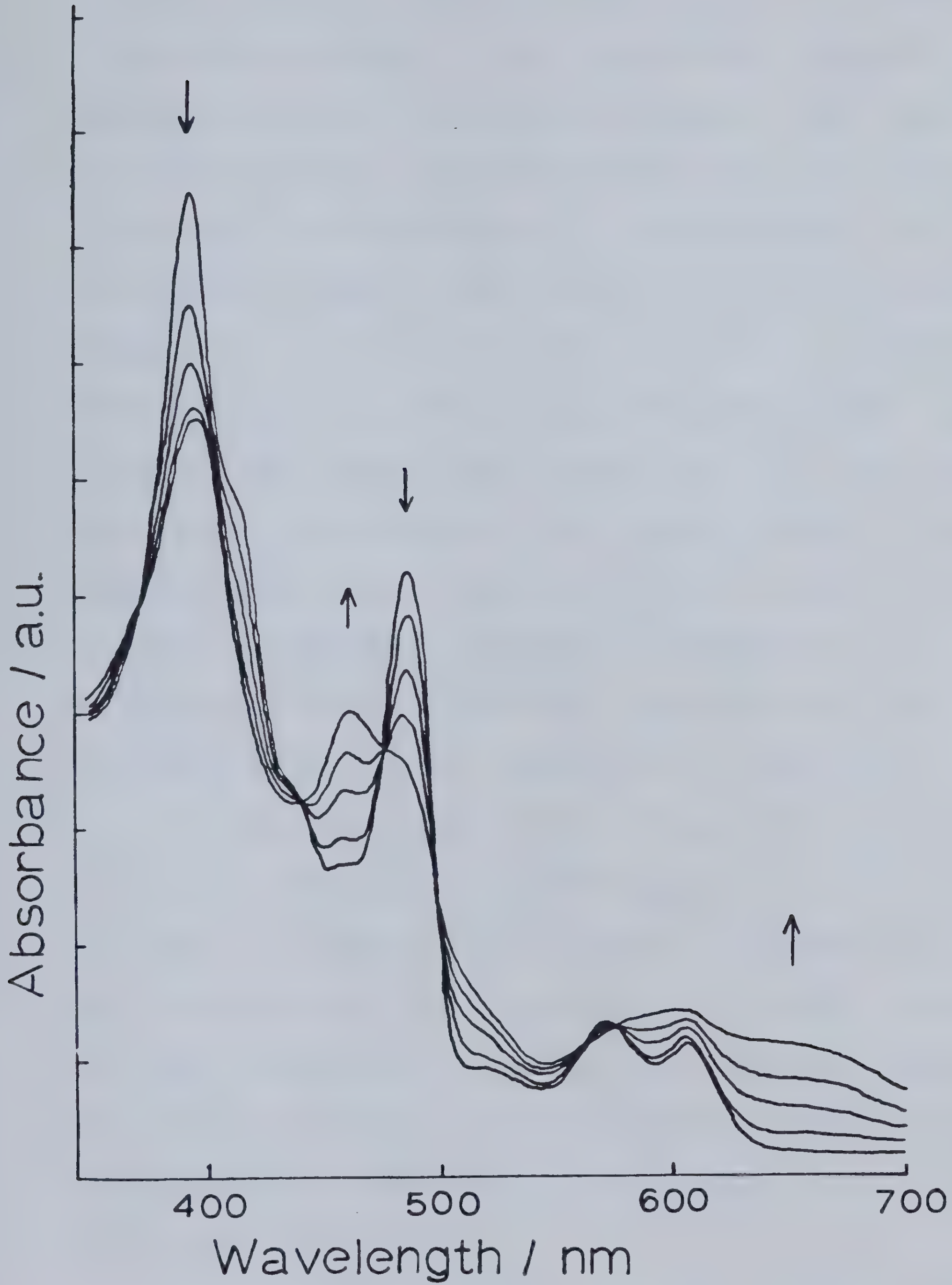

Figure 52. Spectral changes observed on 1-electron oxidation of ca 0.2 mM $(ClO_4)Mn(III)TPP$ in CH_2Cl_2 (0.2 M TBAP); final potential is 1.35 V vs SCE.

required here for spectral observation. If water is intentionally added to the electrolyte solution, then the spectral changes indicated in Figure 53 are observed. The two band structure in the near IR region of the spectrum indicates the formation of an isoporphyrin. The cyclic voltammetry observed on addition of water, or methanol, Figure 54, is similar to that presented in Chapter 5 for $TPPH_2$ in the presence of H_2O. The second wave becomes irreversible, and a new cathodic peak at less positive potentials is observed on the reverse sweep. These observations suggest that the second 1-electron oxidation of $(ClO_4)Mn(III)TPP$ results in the formation of a porphyrin dication, which may react further with water or methanol to yield the corresponding isoporphyrin.

The potential separation between the two oxidations is 0.37 V. This is consistent with the value of 0.3 ± 0.1 V noted in Chapter 1 to be typical of sequential removal of two electrons from the porphyrin ligand. On the basis of this observation, in conjunction with the spectral data, the two oxidations of $(ClO_4)Mn(III)TPP$ are ascribed to sequential formation of a porphyrin π-cation radical and π-dication.

Figure 55 illustrates the cyclic voltammetric response observed for $(CH_3O)Mn(III)TPP$ in CH_2Cl_2. Here, as with the perchlorate complex, two reversible 1-electron

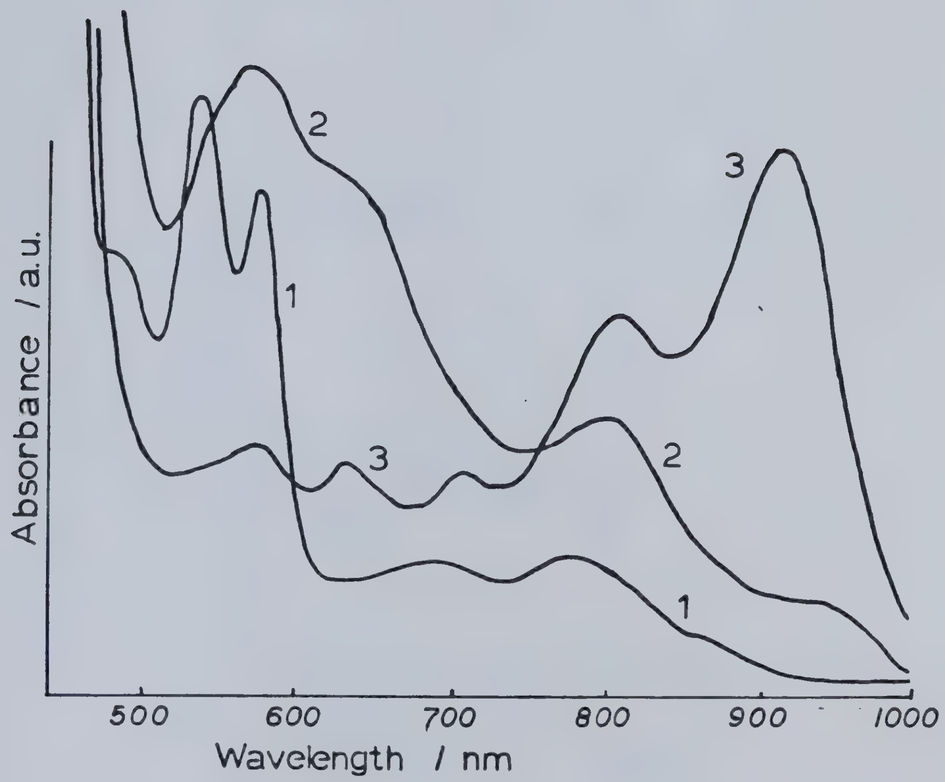

Figure 53. Spectral changes observed on oxidation of ca 0.9 mM $(ClO_4)Mn(III)TPP$ in wet CH_2Cl_2 containing (0.2 M TBAP): (1) no applied potential; (2) E_{app} = 1.25 V vs SCE; (3) E_{app} = 1.65 V vs SCE.

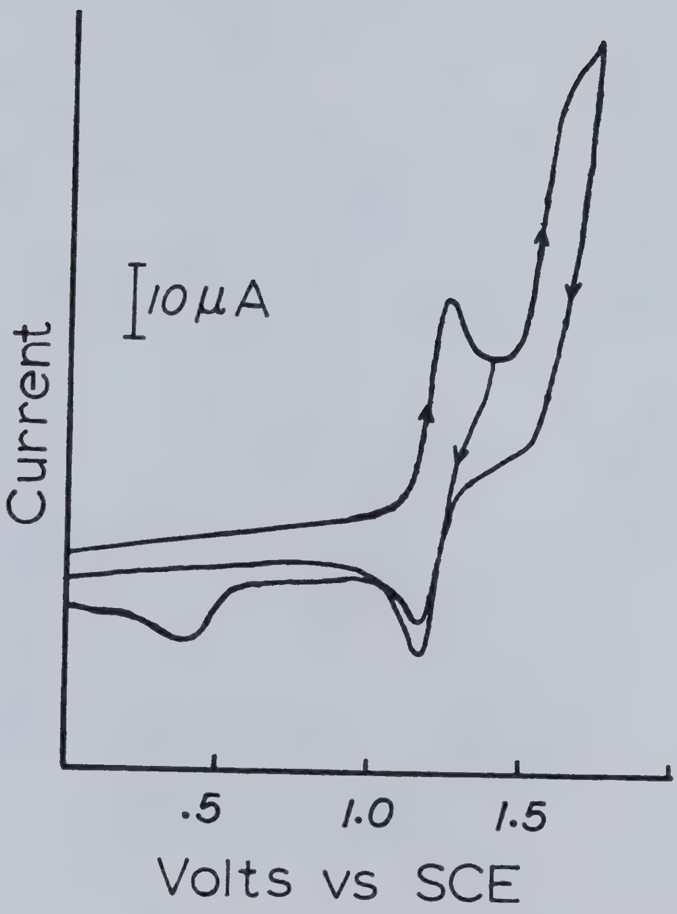

Figure 54. Cyclic voltammetry of 1.1 mM (ClO_4)Mn(III)TPP in CH_2Cl_2(0.15 M TBAP) containing ca 3 mM MeOH; scan rate = 100 mV/s.

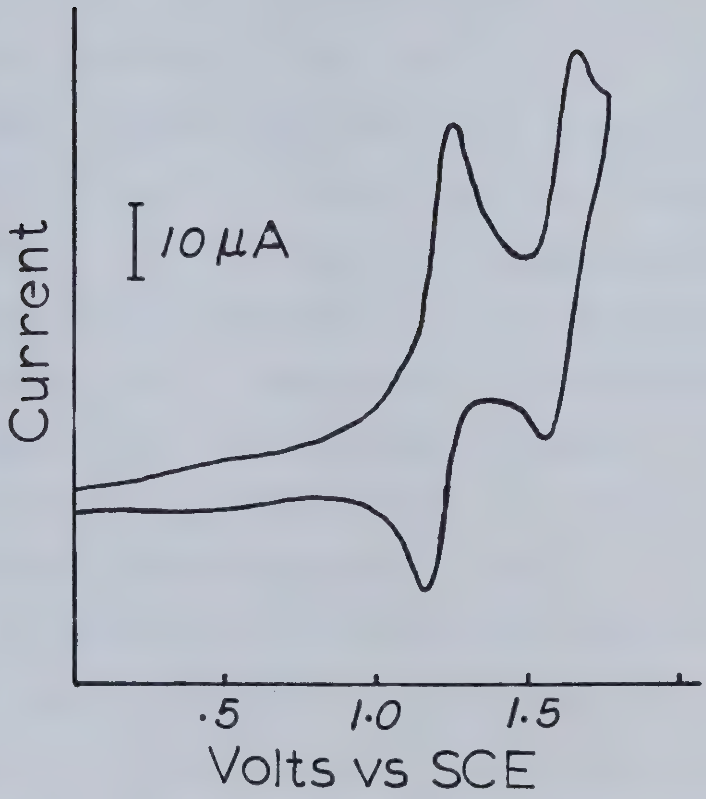

Figure 55. Cyclic voltammetry of 1.4 mM $(CH_3O)Mn(III)TPP$ in CH_2Cl_2(0.15 M TBAP); scan rate = 100 mV/s.

oxidations are indicated. The associated voltammetric half wave potentials are at $E_{1/2}$ = 1.19 and 1.56 V vs SCE. No further anodic waves are observed at potentials up to 2.0 V. The potential separation of 0.37 V between the two voltammetric processes is again in agreement with the value expected for sequential oxidation of the porphyrin ligand. In addition, the similarity of the potentials to those observed for the oxidation of (ClO_4)Mn(III)TPP suggests that the successive charge transfers lead to essentially the same products for both the perchlorate and methoxide complexes. Hence, the two oxidations of (CH_3O)Mn(III)TPP are assigned to removal of electrons from the porphyrin ligand.

The small currents at potentials below 1.0 V observed in the cyclic voltammetry of the methoxide complex are likely due to the presence of impurities. As was noted in Chapter 2, the purity of the methoxide complex is suspect.

7.2 Voltammetry of XMn(III)TPP; X = Cl^-, $CF_3CO_2^-$

Figure 56 comprises three cyclic voltammograms of ClMn(III)TPP in CH_2Cl_2 (0.15 M TBAP) obtained with different switching potentials. In contrast to the behaviour observed for the methoxide and perchlorate complexes, three well defined anodic waves are evident at

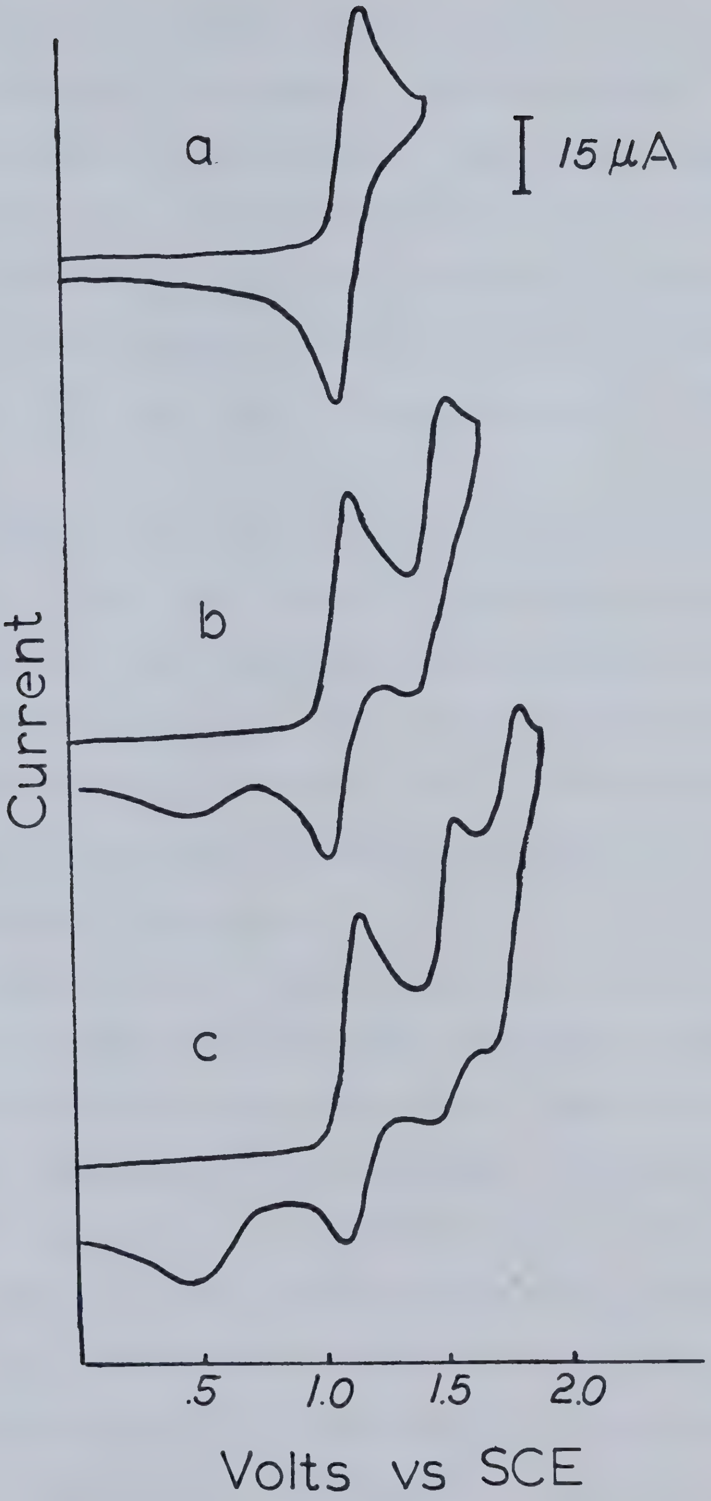

Figure 56. Cyclic voltammetry of 1.5 mM ClMn(III)TPP in CH_2Cl_2(0.15 M TBAP); scan rate = 300 mV/s.

potentials between 0 and 2.0 V vs SCE. It is clear that the very different voltammetry observed arises from the presence of the Cl^- counterion. The qualitative features of the voltammetry of the chloride complex in CH_2Cl_2 or $C_2H_4Cl_2$ are unchanged when nitromethane or nitrobenzene are used as the solvent, indicating no direct solvent participation in the reactions underlying the voltammetric response.

The first oxidation process of the chloride complex occurs at $E_{1/2}$ = 1.14 V vs SCE in methylene chloride or dichloroethane containing TBAP as supporting electrolyte, but lies at ca 30 mV less positive in nitromethane or nitrobenzene TBAP solutions. This is likely due to the different liquid junction potentials associated with the use of different solvents.

Provided that the potential of the working electrode is kept at values less positive than that corresponding to the second oxidation of ClMn(III)TPP, then the ratio of the cyclic voltammetric peak currents, $i_{p,a}/i_{p,c}$ associated with the first redox process is equal to unity at sweep rates between 20 mV/s and 1.0 V/s, indicating reversibility of the first oxidation. The peak separations observed in this range of sweep rates are between 70 and 90 mV/s, indicating a 1-electron transfer.

When the potential on the forward sweep is extended

past the second anodic peak, as in Figure 56b then the cathodic peaks coupled to the first two anodic peaks are reduced relative to the values expected if the second oxidation was reversible. In addition, a new cathodic peak at ca 0.4 V vs SCE is observed on the reverse sweep. The position of this peak is highly dependent on the sweep rate, shifting cathodically as the sweep rate is increased. On repetitive cycling, no anodic peak corresponding to the cathodic peak at 0.4 V is observed at sweep rates up to 1.0 V/s.

The repetitive cycling experiment also indicates that the new reduction process results in the recovery of starting material, or at least a product which oxidizes at similar potentials to the starting material. The steady state peak current associated with the first oxidation is 30 to 40 percent greater when the repetitive cycle includes the cathodic peak at 0.4 V than when the sweep direction on the cathodic scan is reversed before this reduction peak is reached.

As the potential on the forward scan is increased to still more anodic values, as in Figure 56c, a new at least partially reversible redox process is observed at $E_{1/2} \approx$ 1.8 V vs SCE. The third anodic peak increases relative to the first two anodic peaks as the sweep rate decreases, indicating that it results from the oxidation of a product

of a preceding homogeneous chemical reaction.

The qualitative features of the cyclic voltammetry of ClMn(III)TPP are essentially identical to those discussed in Chapter 6 for the oxidation of Zn(II)TPP in the presence of the nucleophilic anions $CF_3CO_2^-$ and $CH_3CO_2^-$. This strongly suggests that isoporphyrin formation is involved. In this case the only nucleophile present is axially ligated chloride ion. The scheme proposed to explain the observed voltammetry is illustrated in Figure 57. The presence of the perchlorate anion in this scheme arises from the supporting electrolyte.

According to the scheme of Figure 57, the second anodic wave in the cyclic voltammetry of ClMn(III)TPP must in fact represent a composite of two processes: the direct oxidation of $ClMn(III)TPP^{+\bullet}$ and the oxidation of $(ClO_4)Mn)III)TPP^{+\bullet}$ formed as a result of the homogeneous chemistry indicated in the figure. No evidence that this is the case was observed in the voltammetric experiments. No inflection in either the rising or falling portions of the second anodic voltammetric peak was observed at potential sweep rates as low as 20 mV/s. However, the half-wave potential for the second oxidation process, estimated as the potential at 3/4 of the peak height at ν = 100 mV/s, is 1.51 V vs SCE. The close proximity of this potential to the value of 1.56 V vs SCE

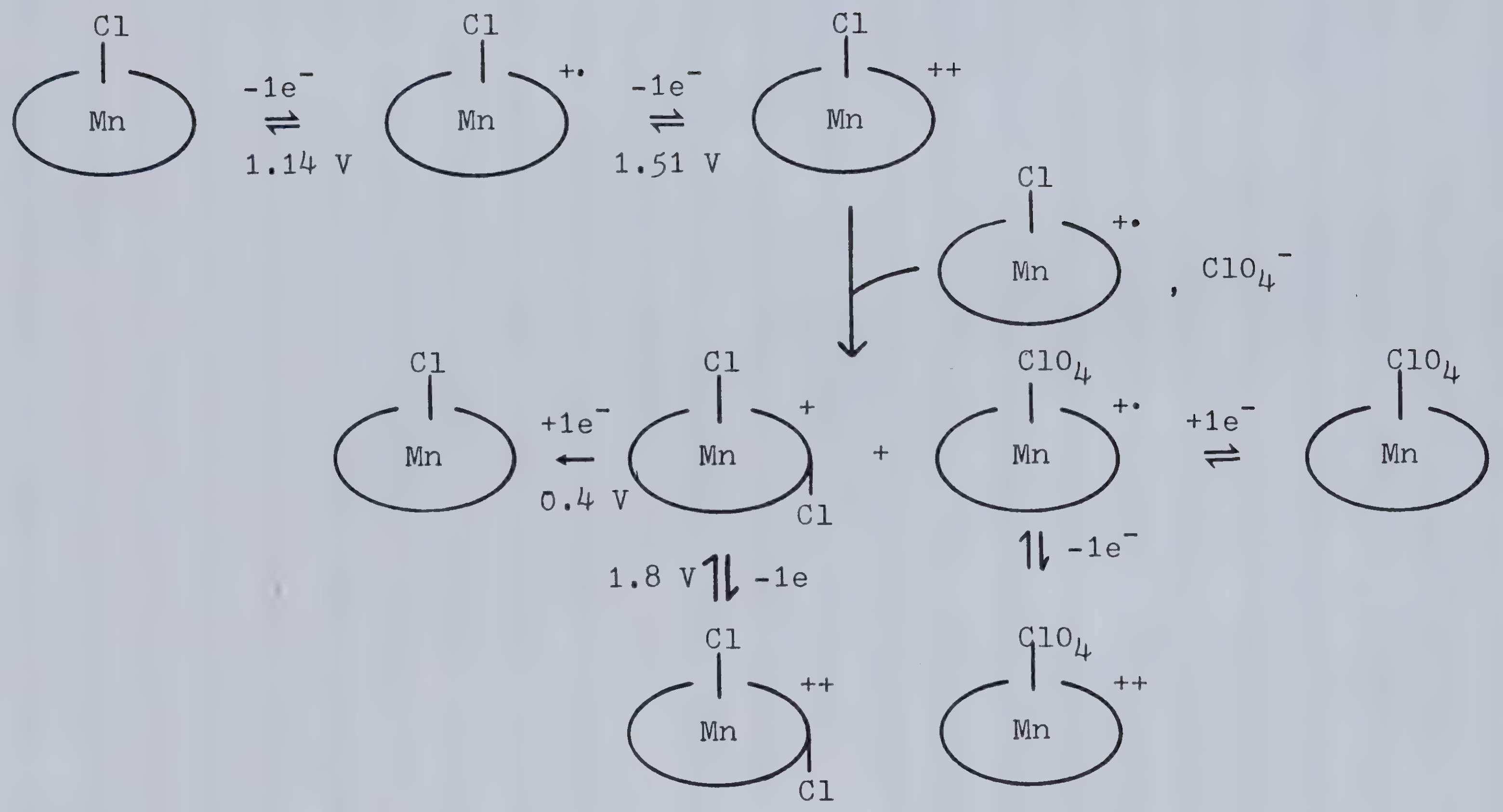

Figure 57. Possible reaction scheme for ClMn(III)TPP and its oxidized forms.

for the half wave potential associated with the second oxidation of the perchlorate complex would make these two processes very difficult to resolve. It should also be noted that the dication of the perchlorate complex could also undergo reaction with axially coordinated chloride ion to form an isoporphyrin, although this possibility has been neglected in the scheme of Figure 57. The presence of such a following chemical reaction would shift the second oxidation of the perchlorate complex to more cathodic potentials. This would make the resolution of the second oxidation of the chloride and perchlorate complexes even more difficult. In fact, when (ClO_4)Mn(III)TPP was added to solutions of ClMn(III)TPP, no indication that the second anodic peak was a composite of two processes was observed.

Some indication that the perchlorate complex is indeed formed as a result of the removal of two electrons from ClMn(III)TPP is observed in the cyclic ac voltammetry of the latter species, illustrated in Figure 58. If the dc potential scan direction on the anodic sweep is reversed before reaching potentials where the second oxidation occurs, then the peak current on the reverse sweep is equal to that of the forward sweep, as in Figure 58a, indicating that no following homogeneous reactions are associated with the first oxidation. When the anodic

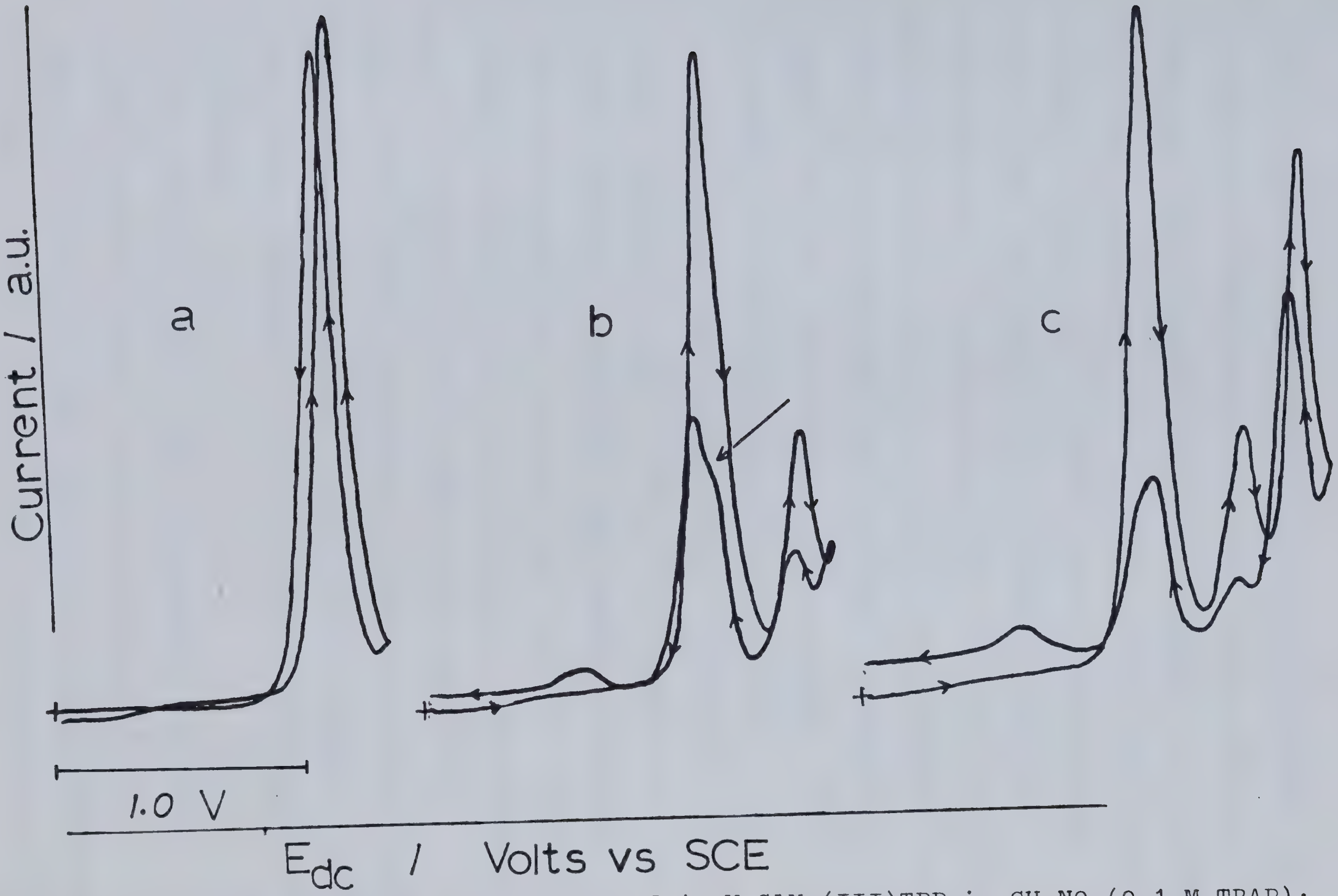

Figure 58. In-phase cyclic ac voltammetry of 1 mM ClMn(III)TPP in CH_3NO_2(0.1 M TBAP); $\omega/2\pi$ = 400 Hz; ν = 100 mV/s; ΔE = 5 mV; starting potential=0 V vs SCE.

sweep is extended past the second oxidation process, the ac voltammetric peak obtained on the reverse sweep at potentials corresponding to the first anodic wave exhibits a shoulder, indicated by the arrow in Figure 58b. The shoulder occurs at more positive potentials than the reverse peak obtained if the dc potential sweep is reversed before the second oxidation. As the potential for the first oxidation of the perchlorate complex lies at more positive potentials than that for the chloride complex, this is consistent with the formation of the perchlorate complex as indicated in Figure 57.

The reduced intensity of the ac voltammetric peak currents corresponding to removal and recapture of the second electron from the chloride complex, as compared to those associated with the first redox process, provides a clearer illustration of the irreversible nature of the second oxidation of this complex than does the conventional cyclic voltammetry. The at least partially reversible nature of the third oxidation process is also more clearly evident in the cyclic ac voltammetry, as in Figure 58c.

In order to verify that isoporphyrin formation results from the removal of two electrons from the chloride complex, the near IR spectral changes occurring on oxidation of this complex were investigated with the

thin layer optical cell described in Chapter 2. At potentials corresponding to the removal of one electron from the complex, spectrum 2 of Figure 59 is obtained. The broadening of the absorbances in the 500 to 700 nm region of the spectrum is consistent with the assignment of the first 1-electron oxidation of ClMn(III)TPP to abstraction of an electron from the porphyrin ligand. At potentials where two electrons are removed, spectrum 3 is obtained. The structure in the spectrum between 800 and 1000 nm is clearly consistent with the formation of an isoporphyrin. It should be noted, however, that the extent to which trace quantities of water might contribute to isoporphyrin formation during the longer time scales associated with this type of spectroelectrochemical experiment is difficult to assess. In support of the postulate that the isoporphyrin formed arises from the presence of axially bound chloride, and not trace impurity, it is noted that the spectral changes illustrated in Figure 59 are highly reproducible.

The cyclic voltammetric behaviour observed for ClMn(III)TPP is in sharp contrast to that illustrated in Figure 60 for ClFe(III)TPP. In the latter case, two reversible oxidations are observed. As noted in Chapter 1, the first one electron oxidation of ClFe(III)TPP has been ascribed to formation of a π-cation radical. The

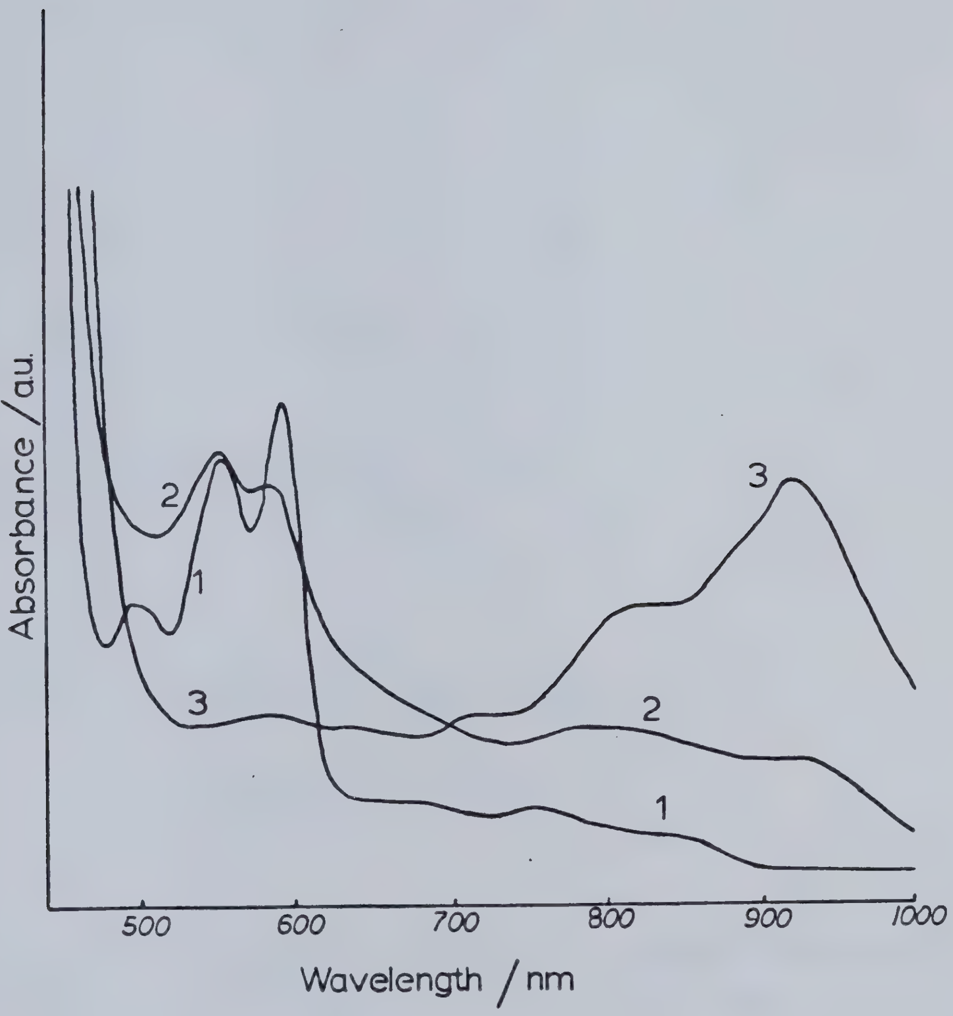

Figure 59. Spectral changes observed on oxidation of ca 0.8 mM ClMn(III)TPP in $C_2H_4Cl_2$(.2 M TBAP): (1) no applied potential; (2) E_{app} = 1.25 V vs SCE; (3) E_{app} = 1.6 V vs SCE.

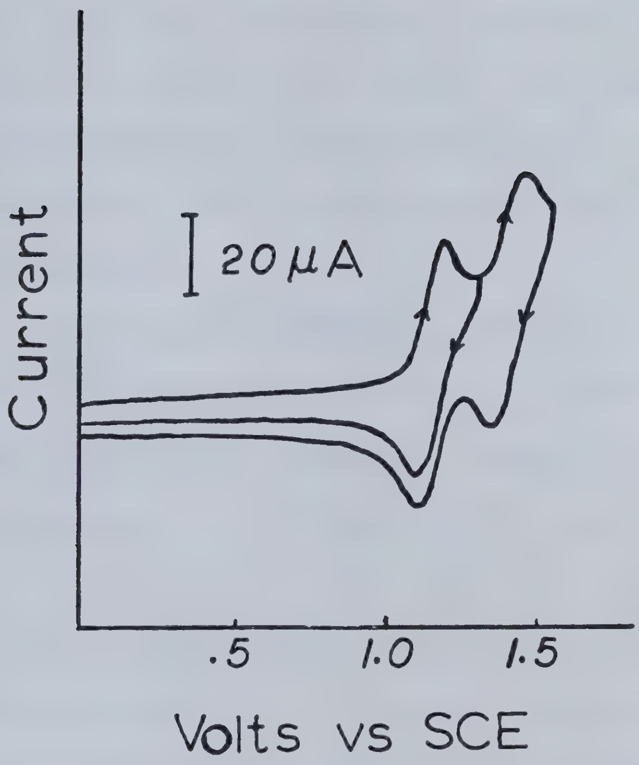

Figure 60. Cyclic voltammetry of 1.5 mM ClFe(III)TPP in CH_2Cl_2(0.1 M TBAP); scan rate = 400 mV/s.

potential separation of 0.3 V between the first two oxidations of this complex is consistent with removal of the second electron from the porphyrin ligand. Felton has shown [137] that removal of two electrons from this complex in CH_2Cl_2 leads to the formation of the methoxyisoporphyrin when methanol is present. This also suggests that the initial product of the second oxidation is a π-dication.

It may appear somewhat surprising that the tetraphenylporphyrin dication may react with chloride ion bound to a Mn(III) porphyrin complex to form the corresponding chloroisoporphyrin, but not with chloride bound to Fe(III). It was noted in Chapter 1, however, that X-ray diffraction data indicate that the axial bonding interaction in Fe(III) porphyrins is stronger than that in the corresponding Mn(III) complexes. The extra energy associated with removal of an axial chloride from the Fe(III) porphyrin, as compared to that for the analogous Mn(III) complex, might account for the apparent stability of the ClFe(III)TPP π-dication. Similarly, the extra steric interaction between axial chloride and the porphyrin nitrogens in ClMn(III)TPP, as compared to ClFe(III)TPP, may contribute to the lability of the chloride ion in the former complex.

Steric interactions are probably also responsible for

the apparent stability of the methoxide ion toward electrophilic attack by porphyrin π-dications in the complex $(CH_3O)Mn(III)TPP$. The oxygen atom in the coordinated methoxide ion is shielded above and below from close approach of an electrophile by the methyl and manganese porphyrin moieties of the complex.

Figure 61 illustrates the cyclic voltammetric behaviour observed for $(CF_3CO_2)Mn(III)TPP$ in CH_2Cl_2 (0.2 M TBAP). In this case, four anodic peaks are observed in the range 0 to 2.0 V vs SCE, as in Figure 61a. The half wave potential of the first redox couple encountered on the anodic scan is 1.17 V vs SCE. This value is consistent with those observed for the production of Mn(III) porphyrin π-cation radicals of the previously discussed complexes. The half wave potential for the second oxidation process, peak III in Figure 61, is ca 1.47 V as estimated as the potential at 75% of the peak current at ν = 100 mV/s. This is consistent with an assignment of peak III to porphyrin π-dication formation.

The mean of the potentials of peaks V and VI of Figure 61a is 1.58 V vs SCE. This is in excellent agreement with the value of 1.56 V reported in section 7.1 for the half wave potential associated with formation of the π-dication of the perchlorate complex. The presence of the perchlorate complex can be assumed to arise through

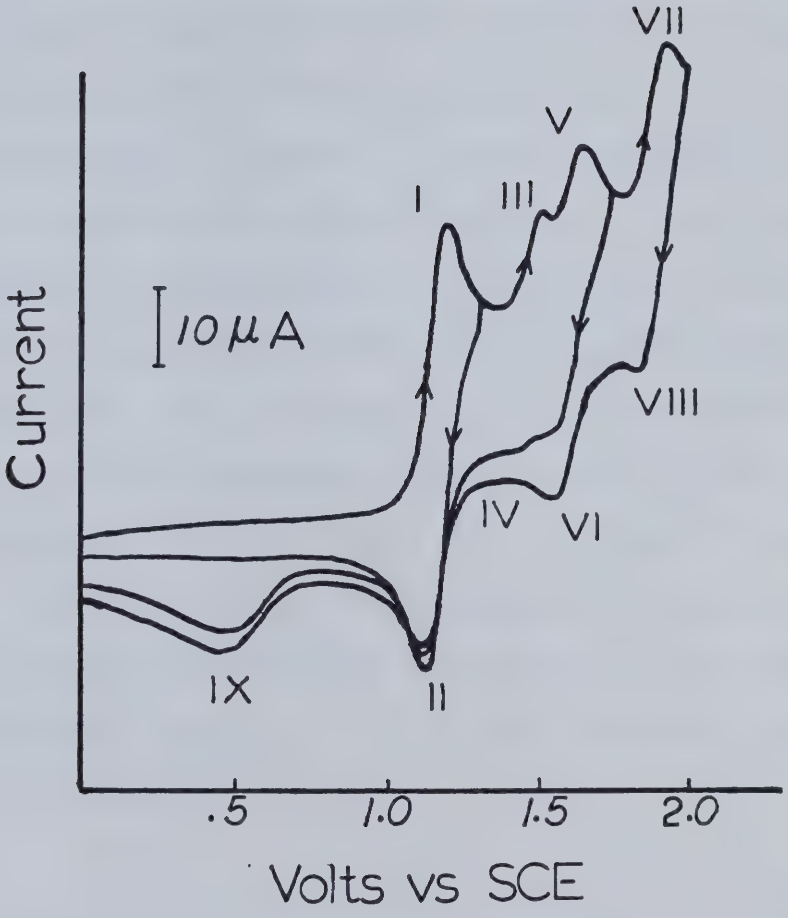

Figure 61. Cyclic voltammetry of 1.3 mM $(CF_3CO_2)Mn(III)TPP$ in CH_2Cl_2(0.2 M TBAP); scan rate = 200 mV/s.

of the perchlorate complex can be assumed to arise through removal of axially coordinated trifluoroacetate ion during formation of a trifluoroacetoxyisoporphyrin complex in a reaction scheme identical to that presented in Figure 57 for formation of the chloroisoporphyrin.

The assignment of peaks III and V to oxidation of the trifluoroacetate and perchlorate cation radical complexes, respectively, is substantiated by the cyclic voltammogram obtained for $(CF_3CO_2)Mn(III)TPP$ when a small quantity of trifluoroacetic acid is present in solution. Under these conditions peak V disappears while peak III grows proportionately. In this case, the porphyrin π-dication may react with CF_3CO_2H, as in reaction 7-1, rather than with axially coordinated trifluoroacetate, and formation of a perchlorate complex in the overall reaction scheme need not be invoked.

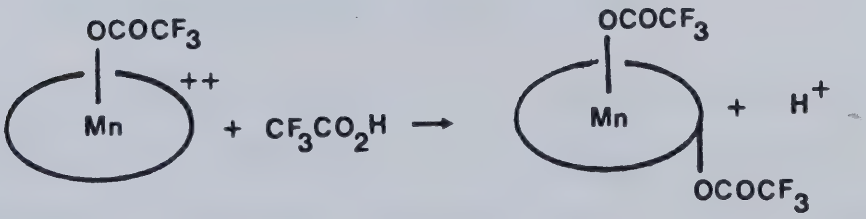

(7-1)

Further indication that isoporphyrin formation is involved in the anodic voltammetry of $(CF_3CO_2)Mn(III)TPP$ is provided by the appearance of the two voltammetric

and of the cathodic peak IX. Such peaks appear in the voltammetry of ClMn(III)TPP, and of Zn(II)TPP in the presence of $CF_3CO_2^-$ or $CH_3CO_2^-$, and appear to be very characteristic of isoporphyrin formation. The spectral changes observed in the thin layer spectroelectrochemical cell upon successive 1 electron oxidations of (CF_3CO_2)Mn(III)TPP, spectra 2 and 3, respectively, of Figure 62, are clearly consistent with the formation of a π-cation radical, followed by the appearance of an isoporphyrin at more anodic potentials. The voltammetric behaviour of (CF_3CO_2)Mn(III)TPP may be explained by a scheme identical to that presented in Figure 57 for the chloride complex, where chloride is replaced by trifluoroacetate and the potentials associated with the various redox processes are modified according to the discussion just presented.

7.3 Voltammetry of (CH_3CO_2)Mn(III)TPP

The cyclic voltammetry of (CH_3CO_2)Mn(III)TPP in CH_2Cl_2 (0.15 M TBAP) is illustrated in Figure 63. The voltammetric behaviour observed here is very different than that of the previously discussed Mn(III) porphyrin complexes. In particular, the first oxidation process at ca 1.19 V vs SCE, as in Figure 63a, is irreversible. A

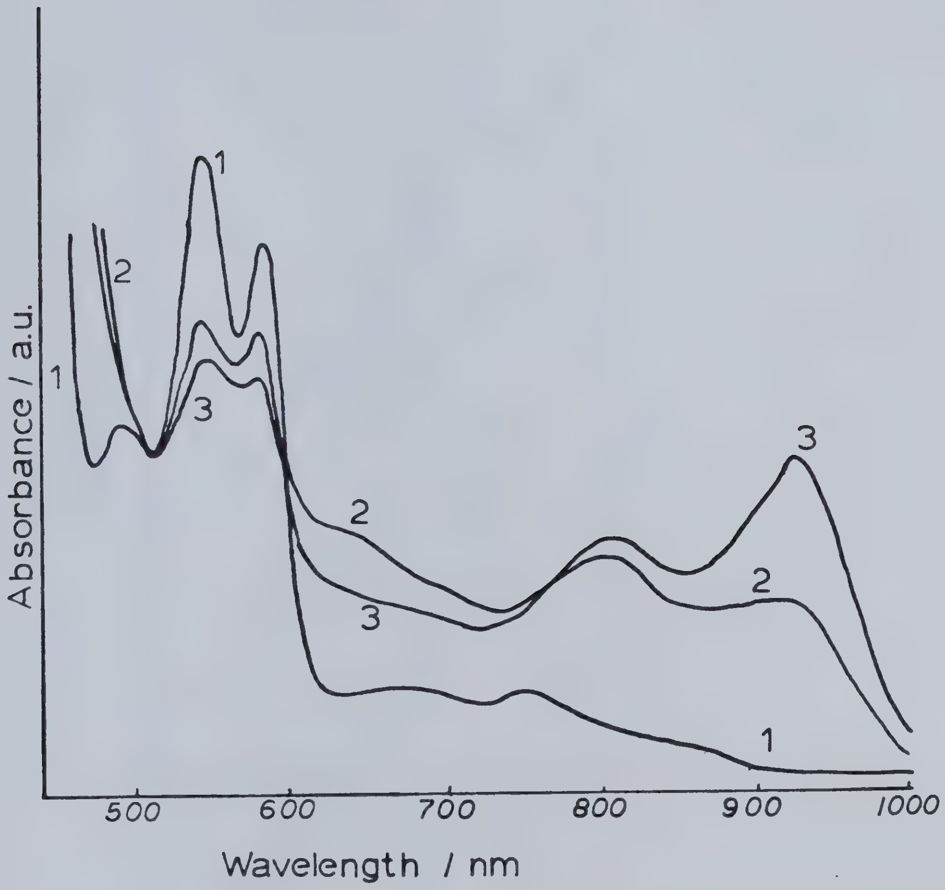

Figure 62. Spectral changes observed on successive 1-electron oxidation of ca 0.8 mM $(CF_3CO_2)Mn(III)TPP$ in CH_2Cl_2(0.2 M TBAP): (1) no applied potential; (2) E_{app} = 1.2 V; (3) E_{app} = 1.6 V vs SCE.

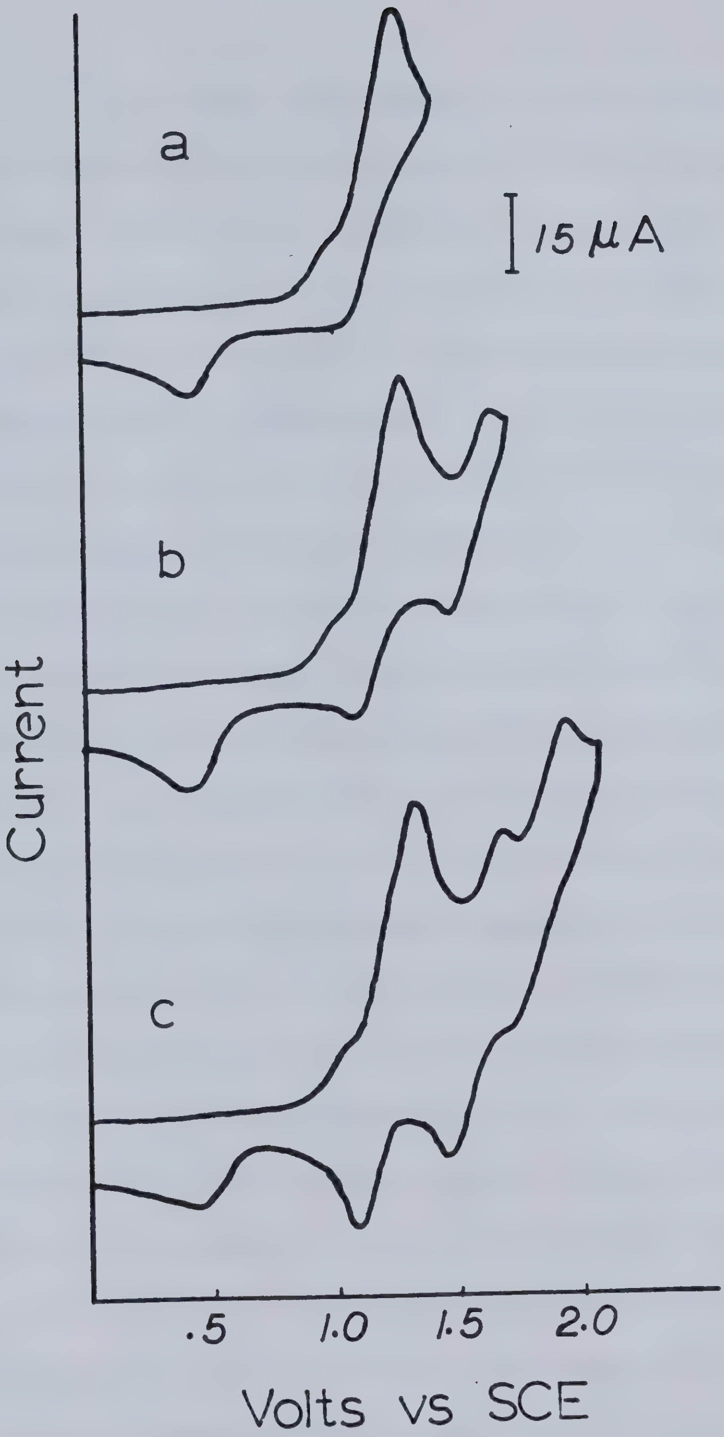

Figure 63. Cyclic voltammetry of 1.5 mM $(CH_3CO_2)Mn(III)TPP$ in CH_2Cl_2(0.15 M TBAP); scan rate = 300 mV/s.

small anodic prewave is observed on the forward sweep, and a new cathodic peak is observed on the reverse sweep at potentials of ca 0.4 V vs SCE. The prewave remained unchanged when the Pt electrode was replaced with a glassy carbon working electrode. This suggests that it is not due to adsorption phenomena. The irreversible cathodic process at ca 0.4 V is reminiscent of the reduction of isoporphyrins formed upon oxidation of the previously discussed Mn(III) porphyrin complexes. The formation of an isoporphyrin at the low potentials applied here is not consistent with the previously discussed cases, however.

When the potential on the forward sweep is extended to more anodic values, as in Figure 63b, then a second apparently reversible redox couple at $E_{1/2}$ = 1.58 V vs SCE is observable. This value is very similar to that observed for the formation and corresponding reduction of the π-dication of (ClO_4)Mn(III)TPP. The peak currents associated with this redox couple are greatly reduced relative to the peak current observed for the first oxidative process. If the potential on the forward scan is extended to still greater values, a third pair of voltammetric peaks with an associated $E_{1/2}$ value of ca 1.8 V vs SCE is evident. This is again reminiscent of the behaviour observed in previously discussed cases where isoporphyrin formation was involved.

The cyclic voltammetric behaviour observed in nitrobenzene (0.1 M TBAP) is essentially identical to that observed in CH_2Cl_2. Close inspection of the first anodic process, however, reveals two inflection points on the rising portion of the first voltammetric wave, as may be apparent in Figure 64a. On repeated cycling between 0.57 and +1.73 V vs SCE, so as to exclude the cathodic peak at ca 0.45 V, two apparently reversible redox processes are observed, as in Figure 64b. The associated half wave potentials of 1.14 and 1.47 V vs SCE corresponds to those determined in a separate experiment for the first two oxidations of (ClO_4)Mn(III)TPP in this solvent.

The cyclic voltammetric behaviour at low sweep rates obtained at the Pt thin layer electrode displays two well-defined anodic peaks at potentials corresponding to the first composite anodic process observed in the conventional cyclic voltammetric experiment. This behaviour is observed when either dichloroethane, dichloromethane, or nitrobenzene is used as solvent, and is illustrated for the former solvent in Figure 65. The cathodic peak at ca 0.6 V is associated with the anodic peak at 1.1 V. The first anodic process is followed by an apparently completely reversible process with an $E_{1/2}$ value of 1.19 V vs SCE, estimated as the mean of the forward and reverse peak potentials. This value is

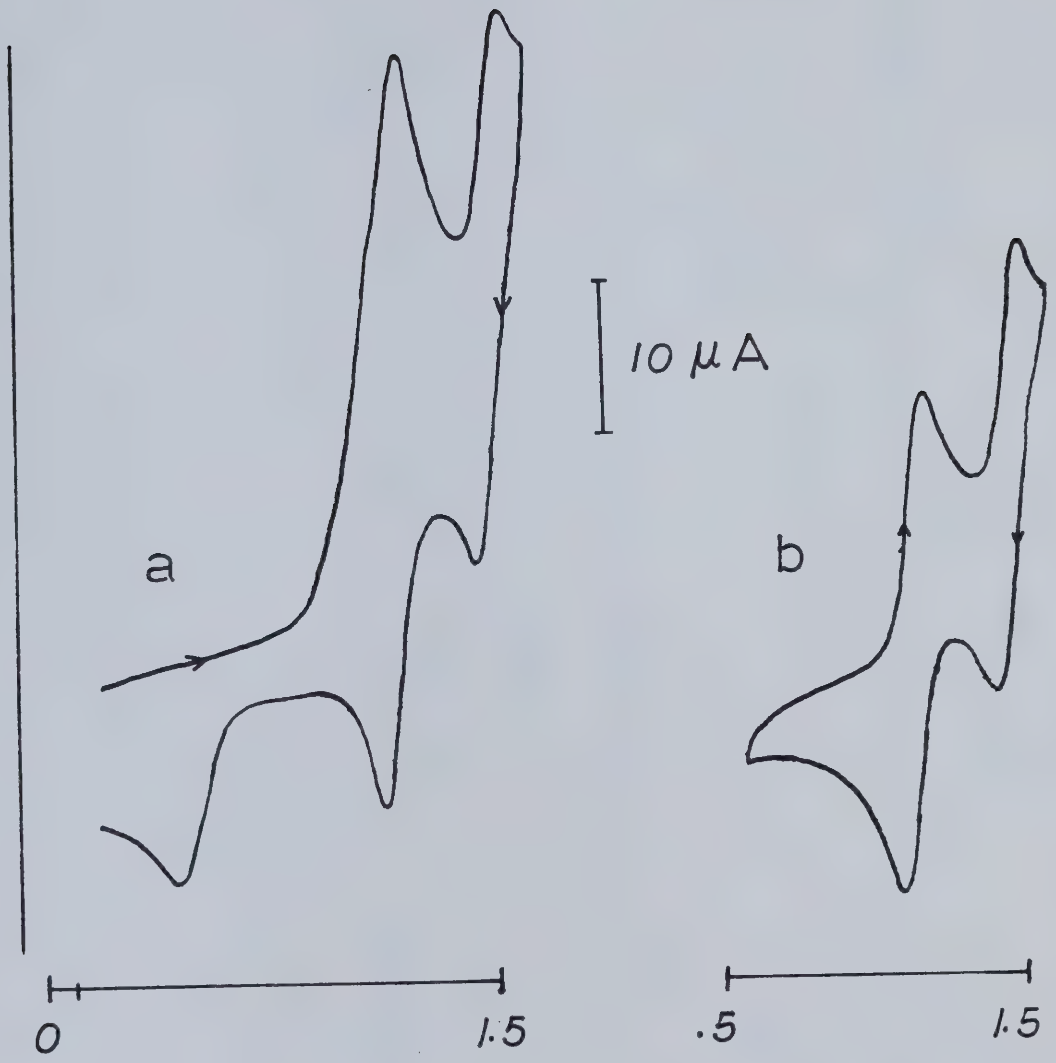

Figure 64. Cyclic voltammetry of 2 mM $(CH_3CO_2)Mn(III)TPP$ in $C_6H_5NO_2$(0.2 M TBAP); scan rate = 150 mV/s.

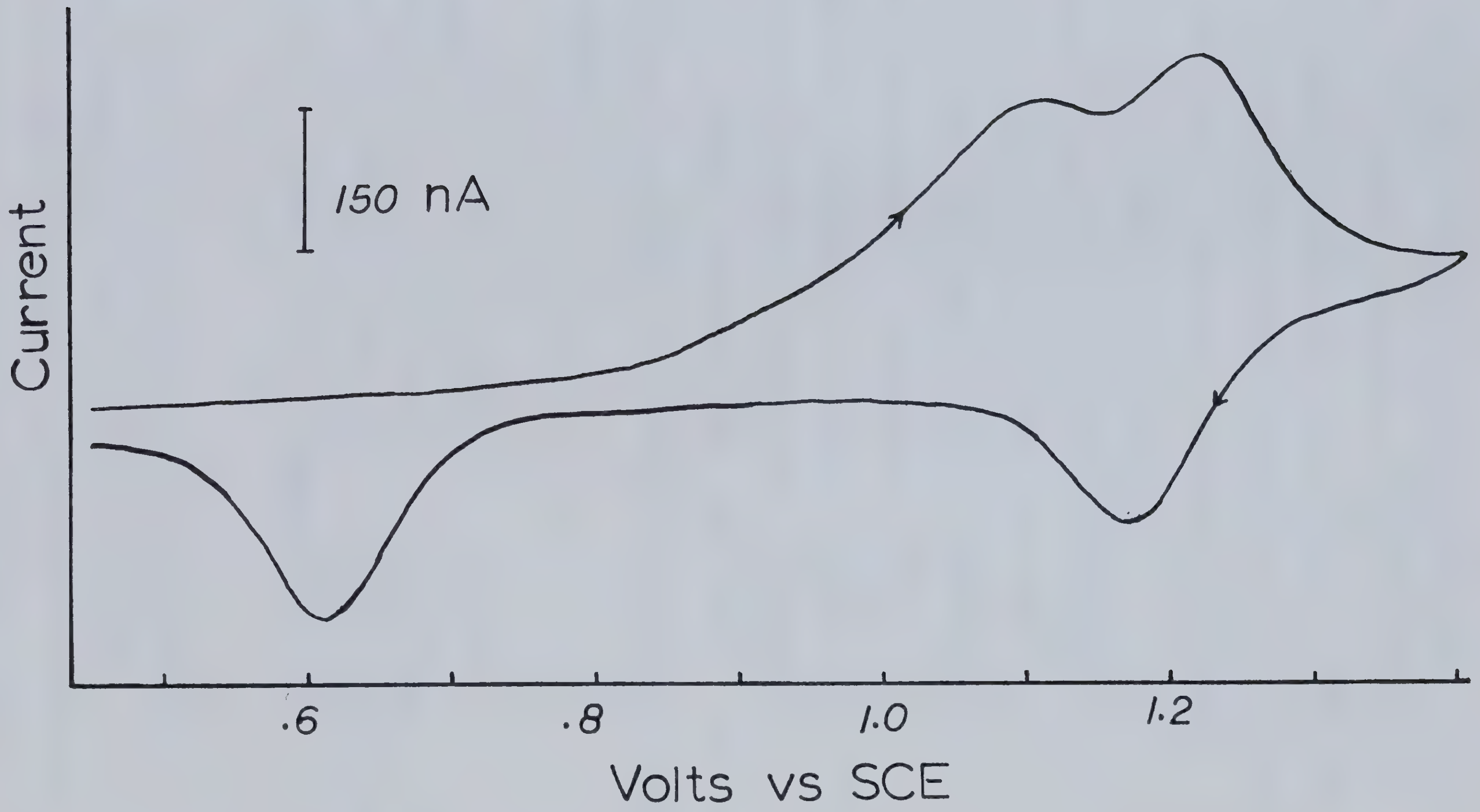

Figure 65. Thin layer cyclic voltammetry of 1.4 mM $(CH_3CO_2)Mn(III)TPP$ in $C_2H_4Cl_2$(0.2 M TBAP); scan rate = 5 mV/s.

identical to the half wave potential observed by conventional or ac cyclic voltammetry for the first oxidation of $(ClO_4)Mn(III)TPP$ in this solvent. When the thin layer volume was calibrated according to the charge required to carry out 1-electron oxidation of either $(ClO_4)Mn(III)TPP$ or $TPPH_2$, then subsequent chronocoulometry or potential scanning coulometry experiments indicated that the anodic processes illustrated in Figure 65 result in the removal of 1.5 electrons per molecule of $(CH_3CO_2)Mn(III)TPP$.

One possible mechanism which might account for both the conventional and thin layer cyclic voltammetric results is illustrated in Figure 66. The overall reaction scheme associated with the first composite anodic process is as in reaction 7-2.

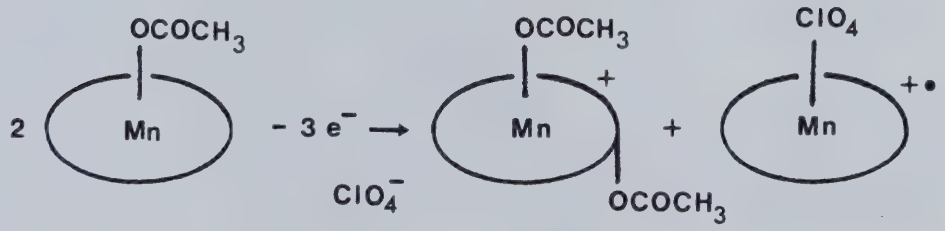

(7-2)

A scheme such as this accounts for the 1.5 electrons removed per porphyrin during the first composite oxidation. The generation of $(ClO_4)Mn(III)TPP$ accounts for the reversible couple observed in the thin layer

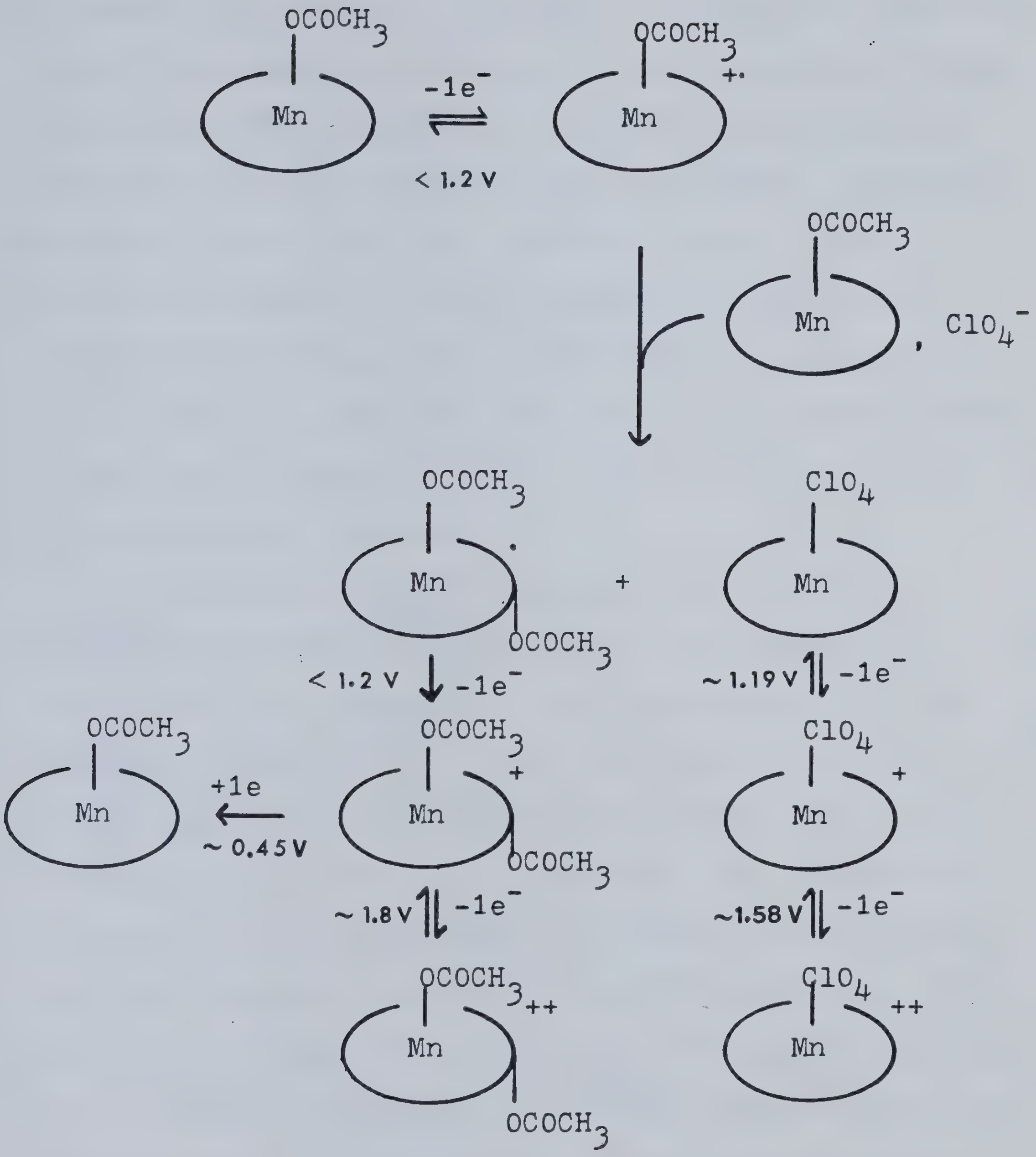
OCOCH3
Mn
-1e⁻
< 1.2 V
+·
, ClO4⁻
·
+
ClO4
< 1.2 V
-1e⁻
~1.19 V
+1e
~0.45 V
+
~1.8 V
~1.58 V
++

Figure 66. One possible scheme for reactivity of $(CH_3CO_2)Mn(III)TPP$ and oxidized forms.

voltammetry of Figure 65, and for the reversible behaviour observed on repetitive cycling in the conventional cyclic voltammogram of Figure 64b. The mechanism of Figure 66 suggests that three different species undergo 1-electron oxidation during the first composite anodic process, accounting for the inflection points observed in the voltammogram of Figure 64a. Oxidation and reduction of the isoporphyrin generated according to this scheme could account for the peaks at ca 1.8 and 0.4 V in the cyclic voltammogram of Figure 63c.

The spectral changes observed on oxidation of (CH_3CO_2)Mn(III)TPP in the thin layer spectroelectrochemical cell are consistent with the formation of the products of reaction 7-2. When the potential of the working electrode is held at 0.95 V vs SCE, where, according to the thin layer volammetry, the irreversible oxidations of the first composite anodic process should occur but oxidation of (ClO_4)Mn(III)TPP should not, then spectrum 2 of Figure 67 is obtained. The intense band at 389 nm corresponds precisely to the wavelength of maximum absorbance for (ClO_4)Mn(III)TPP. When the potential is increased to 1.3 V vs SCE, spectrum 1 of Figure 68 is observed. In the 500 to 700 nm region, this resembles the spectrum presented in section 7.1 for the π-cation radical of (ClO_4)Mn(III)TPP. At wavelengths in the 800 to 1000 nm

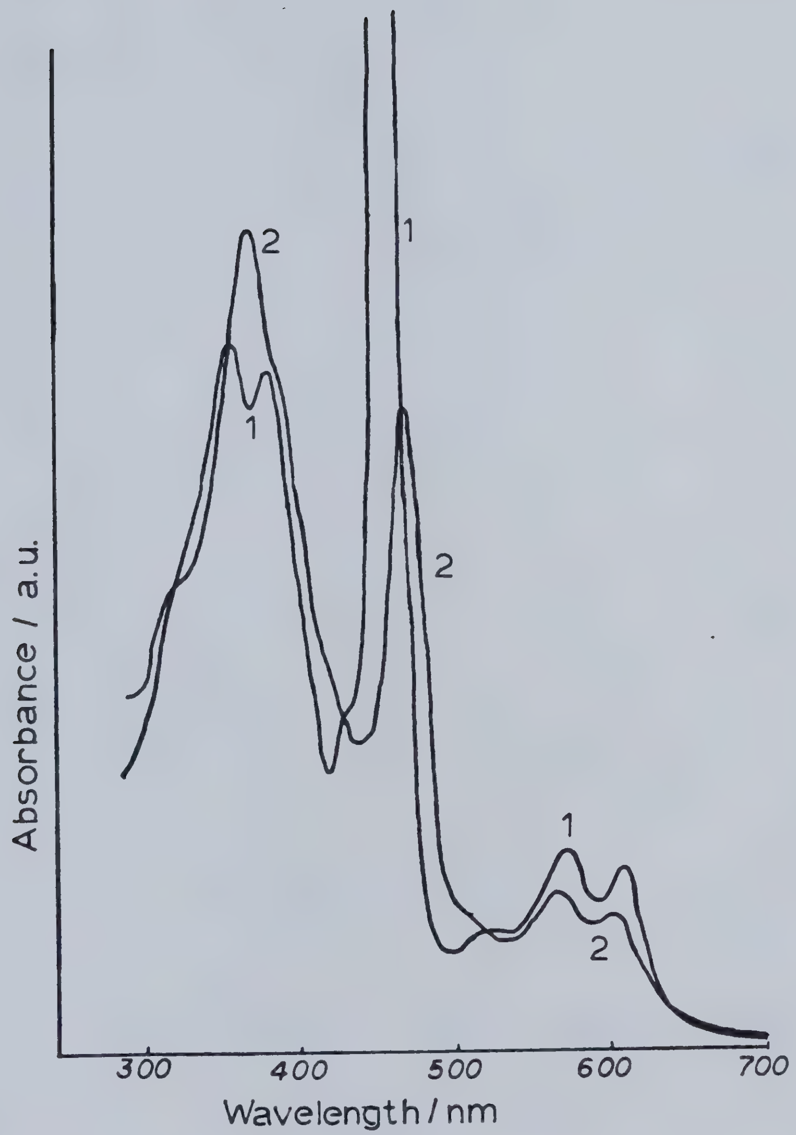

Figure 67. Spectra obtained for ca 0.2 mM $(CH_3CO_2)Mn(III)TPP$ in CH_2Cl_2(0.2 M TBAP): (1) no applied potential; (2) E_{app} = 0.95 V vs SCE.

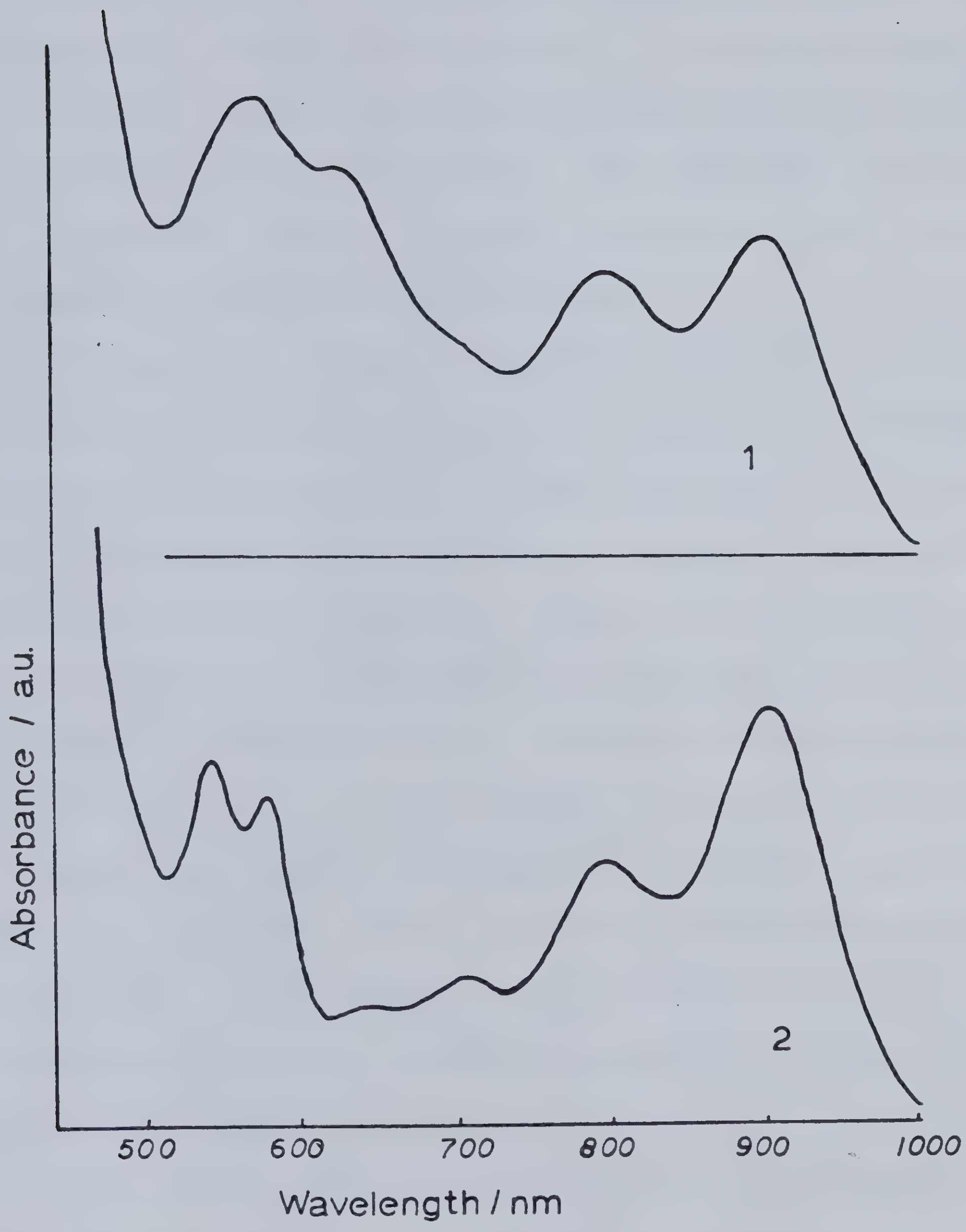

Figure 68. Spectra obtained for ca 0.8 mM $(CH_3CO_2)Mn(III)TPP$ in CH_2Cl_2(0.2 M TBAP): (1) E_{app} = 1.3 V; (2) E_{app} = 0.9 V, obtained after electrolysis at 1.3 V vs SCE.

range, the spectrum more closely resembles that of an isoporphyrin. When the potential is now stepped back to 0.9 V vs SCE, where a π-cation radical should be reduced but an isoporphyrin should not, then spectrum 2 of Figure 68 is observed. This is clearly consistent with those of isoporphyrins discussed previously.

Although the evidence presented here does favour the formation of the perchlorate and isoporphyrin complexes according to reaction 7-2, it does not constitute proof that the mechanism of Figure 66 is correct. The reaction indicated between coordinated acetate and a porphyrin π-cation radical is in apparent contradiction to the results of Chapter 5 where the cation radical of Zn(II)TPP was found to be stable in the presence of acetate. Similarly, the cyclic voltammetry of (CH_3CO_2)Fe(III)TPP, Figure 69, where two reversible oxidations are indicated suggests that neither the porphyrin π-cation radical nor the dication are powerful enough electrophiles to react with acetate coordinated to Fe(III).

The Mn(III) atom in the porphyrin cavity appears to have a unique effect in enhancing the reactivity of the coordinated acetate. It is not impossible that a short lived Mn(IV) intermediate is involved, although no spectral evidence that this might be the case has been observed. It is well known [146] that acetate ion may

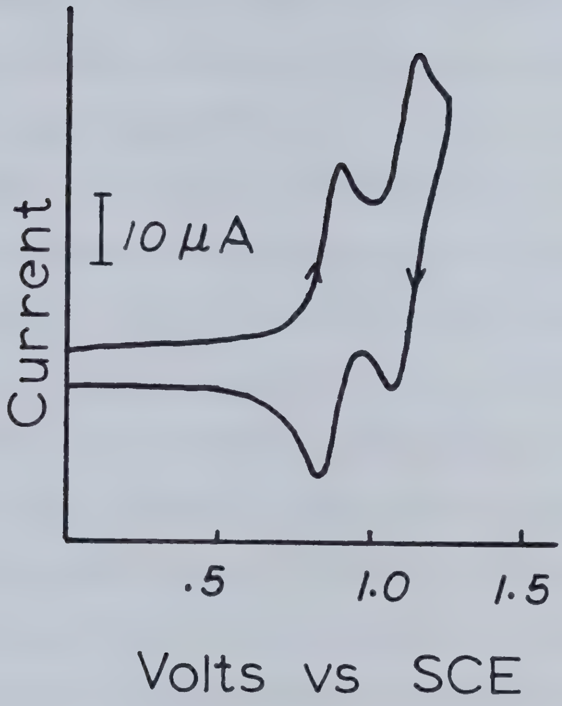

Figure 69. Cyclic voltammogram of 1mM $(CH_3CO_2)Fe(III)TPP$ in CH_2Cl_2(0.1 M TBAP); scan rate = 300 mV/s.

coordinate to metal ions in either bidentate or monodentate fashion, and that it may behave as a bridging ligand between two metal ions. The nature of the coordination of the acetate to the Mn(III) porphyrin might be an important factor in the reactivity of oxidized forms of (CH_3CO_2)Mn(III)TPP.

Beers law plots of the acetate complex in dichloroethane or chloroform are linear through the concentration 10^{-6} to 10^{-3} M, and display a zero intercept. This suggests that no dimerization reaction yielding, for instance, a bridged acetate diporphyrin species is involved. The molecular weight of the complex was determined to be 767 g/mole by vapour phase osmometry in CH_2Br_2. The formula weight of the monomer is 727 g/mole. This corroborates the Beers law evidence that no significant dimerization reaction occurs. When $(CH_3)_3CCO_2H$ was added to CH_2Cl_2 (0.15 M TBAP) solutions of (CH_3CO_2)Mn(III)TPP, the voltammetric behaviour changed from that presented in section 7.1 for the methoxide complex to a form virtually indistinguishable from that observed for the acetate complex. It was anticipated that the steric bulk of the t-butyl group in the resulting trimethylacetate complex would significantly decrease the extent to which any bridged dimer might take part in the reaction. The similarity of the cyclic voltammetry of the

acetate and trimethylacetate complexes thus suggested that such bridged species were not involved.

As noted in Chapter 2, the KBr disc IR spectrum of the acetate complex displays a strong absorbance at 1624 cm^{-1}. It is well established [147] that the C=O stretching vibration due to acetate bound in bidendate fashion occurs at wavenumbers below 1595. Hence, the acetate in $((CH_3CO_2)Mn(III)TPP$ appears to be coordinated in a normal unidentate manner. This has also been suggested to represent the mode of acetate coordination in the complex $(CH_3CO_2)Mn(III)HmP$ (HmP = hematoporphyrin dianion) by Calvin et al [148]. This assignment was similarly made on the basis of the IR spectrum.

There does not appear to be any readily advanceable explanation for the apparent enhanced tendency toward isoporphyrin formation observed in the voltammetry of $(CH_3CO_2)Mn(III)TPP$. The mechanism merits further study as it might provide insight into the reports noted in Chapter 5 of the reactions of isolated cation radicals with nucleophiles. Further study needs to be directed at characterizing the intermediates in the reaction mechanism. It is unlikely that electrochemical methodology alone will be able to provide many more clues in this regard.

7.4 Voltammetry of XMn(III)TPP; X = I^-, Br^-

Figure 70a illustrates the cyclic voltammetric behaviour observed for IMn(III)TPP in CH_2Cl_2 (0.15 M TBAP). The first anodic peak appears at 0.45 V vs SCE. This is ca 100 mV more positive than the first anodic peak observed in the cyclic voltammetry of tetramethyl ammonium iodide in this solvent, as illustrated in Figure 70b. The second anodic peaks of the two cyclic voltammograms of Figure 70 occur at identical potentials. The voltammetric behaviour of IMn(III)TPP at potentials between 0 and 1.0 V vs SCE is very clearly similar to that observed for iodide in the same potential region. Hence, the first two anodic peaks of Figure 70a are ascribed to electrochemical reactions arising from the presence of coordinated iodide, rather than to oxidation of the Mn(III) porphyrin itself. By analogy to known chemistry of I^- [97], the first anodic peak likely arises from the oxidation of coordinated I^-, resulting in the formation of I_3^-. The second anodic peak may then be ascribed to oxidation of I_3^-.

At more positive potentials, two additional reversible oxidations are observed at half wave potentials of 1.19 and 1.52 V vs SCE. These values are clearly consistent with assignment of these processes to π-cation radical and dication formation, respectively.

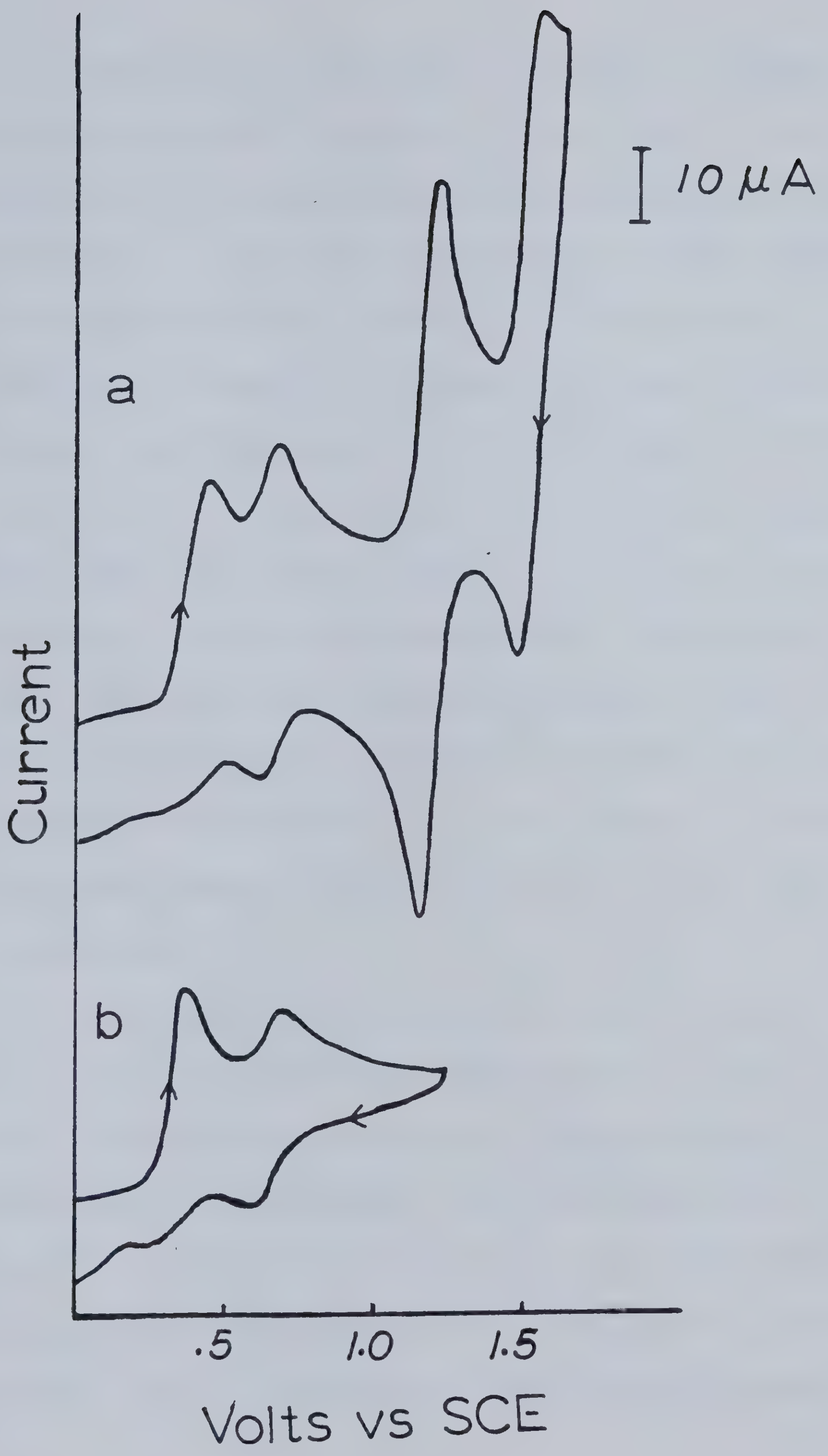

Figure 70. Cyclic voltammetry in CH_2Cl_2(0.15 M TBAP) of (a) 1 mM IMn(III)TPP, (b) $(CH_3)_4NI$; scan rate = 250 mV/s.

Figure 71 illustrates the cyclic voltammetry observed for BrMn(III)TPP in CH_2Cl_2 (0.2 M TBAP). Peak I is observed at a potential ca 80 mV more positive than that observed in a separate experiment for the oxidation of tetramethylammonium bromide in this solvent. This potential difference is consistent with that observed between the oxidation of I^- coordinated to $Mn(III)TPP^+$ and I^- added to the solution as the tetramethylammonium salt. The implication here is that peaks I and II represent the electrochemistry of coordinated bromide ion. The apparently reversible anodic peaks at more positive potentials then can be ascribed to formation of a porphyrin π-cation radical and dication, with associated half wave potentials of 1.19 and 1.52 V vs SCE, respectively.

It is interesting to note that Schardt et al. [22] have reported cyclohexyl bromide as a product when BrMn(III)TPP is reacted with iodosylbenzene in the presence of cyclohexane. The low potential at which bromide oxidizes with respect to the manganese porphyrin as observed here suggests that either Br_2 or bromine radical may be involved in the bromination reaction.

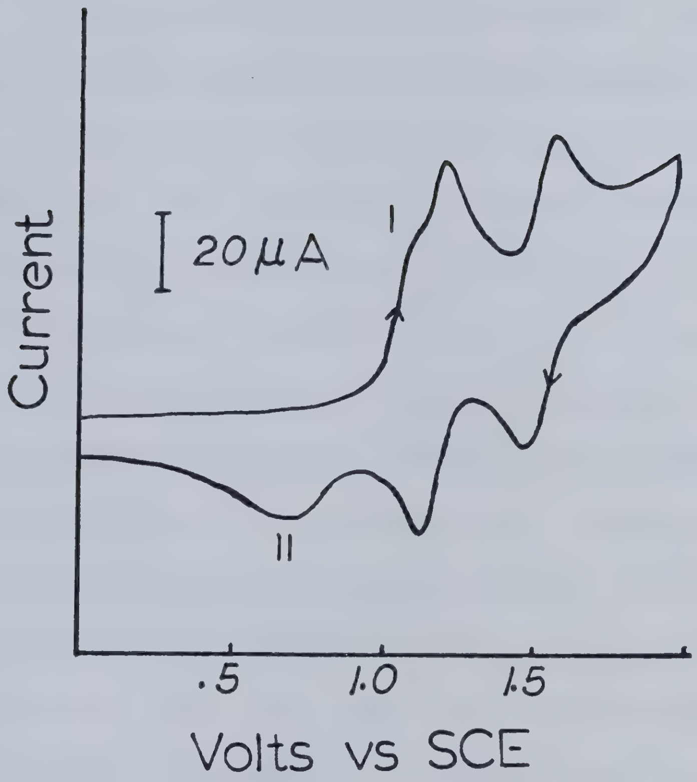

Figure 71. Cyclic voltammogram of 1.3 mM BrMn(III)TPP in CH_2Cl_2(0.2 M TBAP); scan rate = 400 mV/s.

CHAPTER 8

CONCLUDING REMARKS

The intention in this chapter is to summarize a few of the things which have, and have not, been accomplished.

The design of the thin layer cell described in Chapter 3 has led to a rapid and convenient means for determining the number of electrons involved in heterogeneous charge transfer reactions. Even in highly resistive media it is possible to use sweep rates an order of magnitude greater than those normally used in linear sweep thin layer voltammetry. This is an important consideration in the use of thin layer techniques for qualitative mechanistic diagnosis. It is hopefully apparent from this work that thin layer voltammetry is a powerful complement to conventional cyclic voltammetry in this regard.

The development of the alternating current methodologies of Chapter 4 will lead eventually, it is hoped, to some more reliable data concerning the heterogeneous charge transfer kinetics of metalloporphyrins. Although the quantitative utility of

SMACRS has been emphasized, it should not be overlooked that the method holds much promise as a qualitative tool, as well. This aspect arises through the very high degree of selectivity attainable through the combined use of ac voltammetry and spectroscopic observation. The technique has already been successfully applied by others [149] for qualitative mechanistic diagnosis in the extremely complicated voltammetric behaviour of the bilirubin molecule.

The voltammetric investigations of Chapters 6 and 7 have lead to the recognition of a cyclic voltammetric pattern which should be readily attributable in future to the involvement of isoporphyrin formation in electrochemical studies of porphyrins. In all of the cases investigated here, the presence of an isoporphyrin led to the observation of an irreversible cathodic peak in the cyclic voltammetry at potentials ca 0.6 V negative of the formation of the porphyrin π-cation radical. Similarly, a new, reversible couple is observed at potentials ca 0.3 V positive of the formation of the porphyrin π-dication.

The mechanisms associated with isoporphyrin formation have not been unequivocally established, however, and deserve more attention. Similarly, the manner in which these species are reduced back to porphyrins is uncertain,

and the single electron apparently involved in this process seems contradictory.

Concerning the manganese porphyrin complexes, it has not been possible, by varying the axial ligand, to obtain evidence for the electrochemical production of a Mn(IV) species. Even when the strongly electron donating methoxide ion is coordinated to the metal, the anodic chemistry of the complex appears to be entirely associated with the porphyrin ligand. At the same time, it now seems clear that porphyrin complexes containing high-valent manganese have been produced by others through homogeneous reactions, as noted in the introduction. In all cases where high-valent manganese porphyrins have been identified, the metal atom occurs in a 6-coodinate environment. A coordination number of 6 may be a requirement for the existence of such a species. In future studies, work might be directed at forcing the metal into a 6-coordinate configuration, perhaps through the addition of a large excess of non-oxidizable coordinating ligand, such as acetate anion. These conditions might favour the electrochemical production of a complex containing the metal in a higher oxidation state.

BIBLIOGRAPHY

1. Kevin M. Smith, Ed., "Porphyrins and Metalloporphyrins", Elsevier, Amsterdam, 1975.
2. David Dolphin, Ed., "The Porphyrins", Vols. 1-7, Academic Press, New York, 1978.
3. Jurgen-Heinrich Fuhrhop, Structure and Bonding, **18**, 1 (1974).
4. C.E. Castro in "The Porphyrins", Ed. D. Dolphin, Vol. 5, Academic Press, New York, 1978, pp. 1-52.
5. R.H. Felton, ibid, pp. 53-125.
6. D.G. Davis, ibid, pp. 127-152.
7. K.M. Kadish, L.A. Bottomley, S. Kelly, D. Schaeper, and L.R. Shiue, Bioelectrochem. and Bioeng. **8**, 213 (1981), and references therein.
8. L.A. Bottomley and K.M. Kadish, Inorg. Chem. **22**, 342 (1983), and references therein.
9. S. Ni, L. Dickens, J. Tappan, L. Constant, and D.G. Davis, Inorg. Chem. **17**, 228 (1977).
10. M.J. Richard, C.D. Shaffer, and R.F. Evilla, Electrochim. Acta **27**, 979 (1982).
11. K.M. Kadish and D.G. Davis, Ann. N.Y. Acad. Sci. **206**, 495 (1973).

12. P.A. Forshey and T. Kuwana, Inorg. Chem. **22**, 699 (1983), and references 1-18 therein.

13. J.H. Fuhrop, M. Baccouche, H. Grabow, and H. Arzoumanian, J. Mol. Cat. **7**, 245 (1980).

14. D.R. Paulson, R. Ullman, and R.B. Sloane, J.C.S. Chem. Comm., 186 (1974).

15. T. Shimidzu, T. Iyoda, and N. Kanda, J.C.S. Chem. Comm., 1206 (1981).

16. H.J. Ledon, P. Durbut, and F. Varescon, J. Am. Chem. Soc. **103**, 3601 (1981).

17. M. Perée-Fauvet and A. Gaudemer, J.C.S. Chem. Comm., 874 (1981).

18. I. Tabushi and N. Koga, J. Am. Chem. Soc. **101**, 6456 (1979).

19. J.T. Groves, R.C. Haushalter, M. Nakamura, T.E. Nemo, and B.J. Evans, J. Am. Chem. Soc. **103**, 2884 (1981).

20. J.T. Groves, W.J. Kruper, and R.C. Haushalter, J. Am. Chem. Soc. **102**, 6377 (1980).

21. J.T. Groves, W.J. Kruper, T.E. Nemo, and R.S. Myers, J. Mol. Cat. **7**, 169 (1980).

22. C.L. Hill and B.C. Schardt, J. Am. Chem. Soc. **102**, 6375 (1980).

23. B.C. Schardt, F.J. Hollander, and C.L. Hill, J. Am. Chem. Soc. **104**, 3964 (1982).

24. I. Willner, J.W. Otvos, and M. Calvin, J.C.S. Chem. Comm., 964 (1980).

25. J.O'M. Bockriss and D.M. Drazie, "Electrochemical Science", Taylor and Francis, London, 1972.

26. M.M. Baizer, "Organic Electrochemistry", Marcel Dekker, New York, 1973.

27. J. Livorness and T.D. Smith, Structure and Bonding **48**, 1 (1982).

28. M. Calvin, Can. J. Chem. **61**, 873 (1983).

29. M. Calvin, Faraday Discuss. Chem. Soc. **70**, 359 (1981).

30. I. Tabushi and S. Kojo, Tet. Letters, 1577 (1974).

31. J.L. Hoard, pp. 318-380 in Reference 1.

32. W.K. McEwen, J. Am. Chem. Soc. **58**, 1124 (1936).

33. J. Conant, B. Chev, and E. Deitz, J. Am. Chem. Soc. **56**, 2185 (1934).

34. J.W. Buchler, pp. 156-224 in Reference 1.

35. S. Kelly and K.M. Kadish, Inorg. Chem. **21**, 3631 (1982).

36. B.D. Berezin, "Coordination Compounds of Porphyrins and Phthallocyanines", Wiley-Interscience, Chichester, 1981.

37. D. Dolphin, D.J. Halko, E.C. Johnson, K. Rousseau, in "Porphyrin Chemistry Advances", F.R. Longo, Ed., Ann Arbour Science, Ann Arbor, 1979, pp. 119-141.

38. G.S. Wilson and B.P. Neri, Ann. N.Y. Acad. Sco. **206**, 568 (1973).

39. J.-H. Fuhrhop, K.M. Kadish, and D.G. Davis, J. Am. Chem. Soc. **95**, 5140 (1973).

40. A. Wolberg and J. Mannasen, Inorg. Chem. **9**, 2365 (1970).

41. A. Wolberg and J. Mannasen, J. Am. Chem. Soc. **92**, 2982 (1970).

42. D. Dolphin, T. Niem, R.H. Felton, and I. Fujita, J. Am. Chem. Soc. **97**, 5288 (1975).

43. A. Volger, H. Kunkley, and B. Rethwisch, Inorg. Chim. Acta **46**, 101 (1980).

44. E.T. Shimomura, M.A. Phillipi, H.M. Goff, W.F. Scholz, and C.A. Reed, J. Am. Chem. Soc. **103**, 6778 (1981).

45. K.M. Kadish and J.-H. Fuhrhop, Angew. Chem. **84**, 1072 (1972).

46. D. Dolphin and R.H. Felton, Accounts Chem. Res. **7**, 26 (1974).

47. R.H. Felton, G.S. Owen, D. Dolphin, and J. Fajer, J. Am. Chem. Soc. **93**, 6334 (1971).

48. M.A. Phillipi, E.T. Shimomura, and H.M. Goff, Inorg. Chem. **20**, 1322 (1981).

49. G. Buisson, A. Deronzier, E. Duée, P. Gans, J.-C. Marchon, and J.-R. Regnard, J. Am. Chem. Soc. **104**, 6793 (1982).

50. P. Gans, J.-C. Marchon, C.A. Reed, and J.-R. Regnard, Nouv. J. Chim. **5**, 203 (1981).

51. M.A. Phillipi and H.M. Goff, J. Am. Chem. Soc. **101**, 7641 (1979).

52. L.J. Boucher, Coord. Chem. Reviews **7**, 289 (1972).

53. W.R. Scheidt, Y.J. Lee, W. Lauangdiloh, K.J. Haller, K. Anzai, and K. Hatano, Inorg. Chem. **22**, 1516 (1982), and references therein.

54. J.T. Landrum, K. Hatano, W.R. Scheidt, and C.H. Reed, J. Am. Chem. Soc. **102**, 6729 (1980).

55. W.R. Scheidt and C.A. Reed, Chem. Rev. **81**, , 543 (1981).

56. L.J. Boucher and H.K. Garber, Inorg. Chem. **9**, 2664 (1970).

57. B. Gonzalez, J. Kouba, S. Yee, C.A. Reed, J.F. Kirner, and W.R. Scheidt, J.Am. Chem. Soc. **97**, 3247 (1975).

58. I. Tabushi and N. Koga, in "Biomimetic Chemistry", D. Dolphin, C. McKenna, Y. Murakami, and I. Tabushi, Eds., Adv. Chem. Ser., Am. Chem. Soc., 1980, p. 291.

59. B.B. Wayland, L.W. Olson, and Z.U. Siddiqui, J. Am. Chem. Soc. **98**, 94 (1976).

60. J.S. Valentine and A.E. Quinn, Inorg. Chem. **15**, 1997 (1976).

61. B.M. Hoffman, C.J. Weschler, and F. Basolo, J. Am. Chem. Soc. **98**, 5473 (1976).

62. P.A. Loach and M. Calvin, Biochemistry **2**, 361 (1963).

63. A. Harriman and G. Porter, J.C.S. Faraday II **75**, 1532 (1979).

64. I. Tabushi and N. Koga, Tet. Letters, 5017 (1978).

65. I. Tabushi and S. Kojo, Tet. Letters, 305 (1975).

66. B.C. Schardt, F.J. Hollander, and C.L. Hill, J.C.S. Chem. Comm., 765 (1981).

67. J.T. Groves and T. Takahashi, J. Am. Chem. Soc. **105**, 2073 (1983).

68. J.W. Buchler, C. Dreher, K.-L. Lay, Y.J.A. Lee, and W.R. Scheidt, Inorg. Chem. **22**, 888 (1983).

69. A.D. Adler, R.F. Longo, F. Kampas, and J. Kim, J. Inorg. Nucl. Chem. **32**, 2443 (1970).

70. K.M. Kadish, L.R. Shiue, R.K. Rhodes, and L.A. Bottomley, Inorg. Chem. **20**, 1274 (1981).

71. P.R. Gaughan, D.F. Shriver, and L.J. Boucher, Proc. Nat. Acad. Sci., USA **72**, 433 (1975).

72. J.W. Buchler, Vol. 1, pp. 390-483 in Reference 2.

73. A. Cornu and R. Massot, Eds., "A Compilation of Mass Spectral Data", Heyden and Sons, Ltd., London, 1966.

74. L.J. Boucher, Ann. N.Y. Acad. Sci. **206**, 409 (1973).

75. H.L. Goering, T.D. Nevitt, and E.F. Silversmith, J. Am. Chem. Soc. **77**, 4042 (1955).

76. R.N. Adams, "Electrochemistry at Solid Electrodes", Marcel Dekker, New York, 1969.

77. J.A. Riddick and E.E. Toops, Jr., "Organic Solvents", in 'Technique of Organic Chemistry', Vol. 7, A. Weissberger, Ed., Interscience, New York, 1955, pp. 409-417.

78. A.J. Bard and L.R. Faulkner, "Electrochemical Methods, Fundamentals and Applications", John Wiley and Sons, New York, 1980.

79. A.J. Bard and K.S.V. Santhanam, in "Electroanalytical Chemistry", Vol. 4, A.J. Bard, Ed., Marcel Dekker, New York, 1970, pp. 215-315.

80. A.T. Hubbard and F.C. Anson, ibid, pp. 129-214.

81. B. Breyer and H.H. Bauer, "Alternating Current Polarography and Tensammetry", in 'Chemical Analysis', Vol. 13, P.J. Elving and I.M. Kolthoff, Eds., Wiley-Interscience, New York, 1963.

82. G.M. Tom and A.T. Hubbard, Anal. Chem. **43**, 671 (1971).

83. D.T. Sawyer and J.L. Roberts, Jr., "Experimental Electrochemistry for Chemists", Wiley-Interscience, New York, 1974.

84. I.B. Goldberg and A.J. Bard, J. Electroanal. Chem. **38**, 314 (1972).

85. D.M. Oglesby, S.H. Omang, and C.N. Reilly, Anal. Chem. **37**, 1312 (1965).

86. J.A. Christiansen and M. Pourbaix, Proc. 17th IUPAC Meeting, Stockholm, 1953, p. 83.

87. A.T. Hubbard and F.C. Anson, Anal. Chem. **38**, 58 (1966).

88. D.E. Smith, in "Electroanalytical Chemistry", Vol. 1, A.J. Bard, Ed., Marcel Dekker, New York, 1966, pp. 1-155.

89. I.B. Goldberg, A.J. Bard, and S.W. Feldberg, J. Phys. Chem. **76**, 2550 (1972).

90. I.B. Goldberg and A.J. Bard, J. Phys. Chem. **75**, 3281 (1971).

91. D.M. Oglesby, L.B. Anderson, B. McDuffie, and C.N. Reilly, Anal. Chem. **37**, 1317 (1965).

92. M. Fleischman, D. Pletcher, and A. Rafinski, J. Electroanal. Chem. **38**, 323 (1972).

93. M. Fleischman, D. Pletcher, and A. Rafinski, J. Electroanal. Chem. **38**, 329 (1972).

94. E. Laviron, J. Electroanal. Chem. **87**, 31 (1978).

95. A.I. Popov and D.H. Geske, J. Am. Chem. Soc. **80**, 1340 (1958).

96. F.C. Anson, Anal. Chem. **38**, 54 (1966).

97. D. Britz, J. Electroanal. Chem. **88**, 309 (1978).

98. A. Bewick, Electrochim. Acta **13**, 825 (1968).

99. A.M. Bond, R.J. O'Halloran, I. Ruzic, and D.E. Smith, Anal. Chem. **48**, 872 (1976).

100. A.M. Bond, R.J. O'Halloran, I. Ruzic, and D.E. Smith, Anal. Chem. **50**, 216 (19978).

101. J.H. Sluyters and M. Sluyters-Rehbach, in "Electroanalytical Chemistry", Vol. 4, A.J. Bard, Ed., Marcel Dekker, New York, 1970, pp. 1-128.

102. D.D. Macdonald and M.C.H. McKubre, in "Modern Aspects of Electrochemistry", Vol. 14, J.O'M. Bockriss, B.E. Conway, and R.E. White, Eds., Plenum Press, New York, 1982, pp. 61-150.

103. A.M. Bond, R.J. O'Halloran, I. Ruzic, and D.E. Smith, J. Electroanal. Chem. **90**, 381 (1978).

104. J.E.B. Randles, Disc. Faraday Soc. **1**, 11 (1947).

105. D.E. Smith, Crit. Rev. Anal. Chem. **2**, 247 (1971).

106. R. de Levie, in "Advances in Electrochemistry and Electrochemical Engineering", Vol. 6, P. Delahay, Ed., Interscience, New York, 1967, pp. 329-398.

107. J.O'M. Bockriss, E. Gileadi, and K. Muller, J. Chem. Phys. **44**, 1445 (1966).

108. A. Bewick, M. Fleischmann, and M. Lila, Electrochim. Acta **1**, 83 (1959).

109. M.D. Ryan and G.S. Wilson, Anal. Chem. **54**, 20R (1982).

110. T. Kuwana and N. Winograd, in "Electroanalytical Chemistry", Vol. 7, A.J. Bard, Ed., Marcel Dekker, New York, 1974.

111. W.R. Heineman, Anal. Chem. **50**, 390A (1978).

112. A.W.B. Aylmer-Kelly, A. Bewick, P.R. Cantrill, and A.M. Tuxford, Disc. Faraday Soc. **56**, 96 (1973).

113. A. Bewick, J. Mellor, and S. Pons, Electrochim. Acta **23**, 77 (1978).

114. A. Bewick and A.M. Tuxford, J. Electroanal. Chem. **46**, 255 (1973).

115. S. Pons and S.B. Khoo, Electrochim. Acta **27**, 1161 (1982).

116. S. Pons and S.B. Khoo, J. Am. Chem. Soc. **104**, 3845 (1982).

117. A. Bewick, J. Mellor, and S. Pons, Electrochim. Acta **25**, 931 (1980).

118. E.E. Bancroft, H.N. Blount, and F.M. Hawkridge, Anal. Chem. **53**, 1862 (1981).

119. N. Winograd, H.N. Blount, and T. Kuwana, J. Phys. Chem. **73**, 3456 (1969).

120. H. Malmstadt, C. Enke, and S. Crouch, "Electronics and Instrumentation for Scientists", Benjamin/Cummings, Reading, Massachusetts, 1981.

121. L.M. Peter, W. Durr, P. Bindra, and H. Gerischer, J. Electroanal. Chem. **71**, 31 (1976).

122. J. Kawiak, T. Jedral, and Z. Galus, J. Electroanal. Chem. **145**, 163 (1983).

123. J. Kuta and E. Yeager, J. Electroanal. Chem. **59**, 110 (1975).

124. J.M. Hale, in "Reactions of Molecules at Electrodes", N.S. Hush, Ed., Wiley-Interscience, New York, 1971.

125. M. Von Stackelberg, M. Pilgrim, and W. Toome, Z. Elektrochim. **57**, 342 (1953).

126. M.E. Peover and B.S. White, J. Electroanal. Chem. **13**, 93 (1967).

127. N. Koizumi and S. Aoyagui, J. Electroanal. Chem. **55**, 452 (1974).

128. R.L. McCreery, R. Pruiksma, and R. Fagan, Anal. Chem. **51**, 749 (1979).

129. B.S. Pons, Ph.D. Thesis, University of Southamption, 1979.

130. K.M. Kadish, M. Sweetland, and J.S. Cheng, Inorg. Chem. **17**, 2795 (1978).

131. R.A. Marcus, J. Phys. Chem. **67**, 853 (1963).

132. L.D. Spaulding, P.G. Eller, J.A. Bertrand, and R.H. Felton, J. Am. Chem. Soc. **96**, 982 (1974).

133. J.W. Lauher and J.A. Ibers, J. Am. Chem. Soc. **95**, 5148 (1973).

134. B. Tinland, Theor. Chim. Acta **11**, 385 (1968).

135. D. Dolphin, Z. Muljiani, K. Rousseau, D.C. Borg, J. Fajer, and R.H. Felton, Ann. N.Y. Acad. Sci. **206**, 177 (1973)

136. J. Fajer, D.C. Borg, A. Forman, R.H. Felton, L. Vegh, and D. Dolphin, Ann. N.Y. Acad. Sci. **206**, 349 (1973).

137. J.A. Guzinski and R.H. Felton, J.C.S. Chem. Comm., 715 (1973).

138. J.A.S. Cavaleiro, B. Evans, and K. Smith, in "Porphyrin Chemistry Advances", F.R. Longo, Ed., Ann Arbor Science, Ann Arbor, 1979, pp. 335-362.

139. K.M. Kadish and R.K. Rhodes, Inorg. Chem. **20**, 2961 (1981).

140. G.H. Barnett, B. Evans, K.M. Smith, S. Besecke, and J.-H. Fuhrhop, Tet. Letters, 4009 (1976).

141. S. Besecke, G.H. Barnett, B. Evans, K.M. Smith, and J.-H. Fuhrhop, Angew. Chem. **88**, 616 (1976).

142. G.H. Barnett and K.M. Smith, J.C.S. Chem. Comm., 772 (1974).

143. B. Evans and K.M. Smith, Tet. Letters, 3079 (1977).

144. H.J. Shine, A.G. Padilla, and S.M. Wu, J. Org. Chem. **44**, 4069 (1979).

145. R.S. Nicholson and I. Shain, Anal. Chem. **36**, 706 (1964).

146. F.A. Cotton and G. Wilkinson, "Advanced Inorganic Chemistry", 4th Ed., John Wiley and Sons, New York, 1980, pp. 170-172.

147. N.W. Alcock, V.M. Tracy, and T.C. Waddington, J.C.S. Dalton, 2238 (1976).

148. A. Yamamoto, L.K. Philips, and M. Calvin, Inorg. Chem. **7**, 847 (1968).

149. J.R. Pradko, M.Sc. Thesis, University of Alberta, 1983.

150. R.S. Nicholson, Anal. Chem. **37**, 1351 (1965).

APPENDIX 1

APPENDIX 1

BACKGROUND INFORMATION ON ELECTRODE KINETICS

The following discussion is intended to provide a very brief introduction to some of the basic concepts of electrode kinetics, and to define some of the terminology used in the bulk of the thesis. The treatment follows that of Bard and Faulkner [78]. Their book is recommended for a more complete presentation of the material presented here and in Appendices 2 and 3, and may be consulted for references to the original literature.

Current has units of coulombs, in essence electrons, per second. While a net electrolysis occurs at the surface of an electrode, each of the electrons transferred between the electrode and the electroactive species represents the occurence of a single electron transfer reaction. The current therefore provides a direct measurement of the instantaneous rate of the heterogeneous charge transfer process.

If one considers a simple uncomplicated reduction process, as in equation A1-1

$$Ox + ne^- \underset{k_b}{\overset{k_f}{\rightleftharpoons}} Red \qquad (A1\text{-}1)$$

where Ox and Red represent the oxidized and reduced forms of a redox pair, and n is the number of electrons involved in converting one form to the other, the rate of the reaction, and hence the current, is controlled by a physical and a chemical process. The chemical process has to do with the kinetics, i.e. the magnitude of the forward and reverse rate constants, k_f and k_b respectively, of the charge transfer process itself. The physical process involves the rate at which the electroactive species arrives at the surface of the electrode.

The rates, or currents, associated with the forward and reverse reactions indicated in equation A1-1 are given by

$$i_f = nFAk_f C_{Ox} \qquad (A1\text{-}2)$$

and

$$i_b = nFAk_b C_R \qquad (A1\text{-}3)$$

where C_{Ox} and C_R are the concentrations of Ox and Red at the electrode surface and A is the electrode area. Note

that if these have units of moles/cm^3, then the rate constants k_f and k_b must have units of cm/s.

Consider the case where the electrode interface is in equilibrium with a solution in which the bulk concentrations of Ox and Red, C_{Ox}^* and C_R^*, are equal. The condition of equilibrium implies that the surface concentrations equal those in the bulk solution. The electrode potential under these conditions is equal to the formal potential, E°, of the redox couple. The rates of the forward and reverse reactions are equal under these equilibrium conditions, so that $i_f = i_b$. Since $C_{Ox} = C_R$, it follows that

$$k_f = k_b = k_s \qquad \text{(A1-4)}$$

where k_s, the standard rate constant, is defined under the equilibrium conditions discussed.

If a potential E, negative with respect to E°, is now applied to the electrode, then the system is no longer at equilibrium and a net cathodic current results. The rate constants associated with the forward and reverse reactions are now given by

$$k_f = k_s \exp(-\alpha nF(E-E°)/RT) \qquad \text{(A1-5)}$$

$$k_b = k_s \exp(\beta nF(E-E°)/RT) \qquad \text{(A1-6)}$$

The charge transfer coefficient, α, expresses the fraction of the applied potential difference, E-E°, which goes to increasing the forward, by convention the cathodic, reaction. Similarly, $\beta = 1-\alpha$ may be considered as the fraction of the potential difference which affects a decrease in the rate of the anodic reaction.

The magnitude of the resulting net current is given by

$$i_{net} = i_f - i_b \qquad \text{(A1-7)}$$

Substitution of equations A1-5 and A1-6 into A1-2 and A1-3, followed by inclusion of the resulting expressions for i_f and i_b in A1-7 leads to

$$i_{net} = nFAk_s(C_{Ox} \exp(-\alpha nF(E-E°)/RT) - C_R \exp(\beta nF(E-E°)/RT)) \qquad \text{(A1-8)}$$

This equation is frequently referred to as the complete current-potential characteristic, and it, or one of its variations, forms the basis of all modern electrode kinetic theory.

Note that the concentrations in equation A1-8 are surface concentrations, and not those in the solution bulk. If the rate of the charge transfer step itself is very large, so that equilibrium between the electrode potential and the surface concentrations may be attained instantly, then the current which results from the application of some potential depends entirely on the rate at which the electroactive species arrive at the electrode surface. Where the mass transport of the electroreactant to the electrode from the solution bulk arises solely through diffusion under a concentration gradient, then the derivation of the current requires the solution of Ficks laws. For a net reduction, where diffusion of Ox is the factor limiting the magnitude of the current, these may be expressed as

$$-J_{Ox}(x,t) = D_{Ox}\frac{\partial\, C_{Ox}(x,t)}{\partial t} \qquad \text{(A1-9)}$$

and

$$\frac{\partial C_{Ox}(x,t)}{\partial t} = D_{Ox}\frac{\partial^2 C_{Ox}(x,t)}{\partial t^2} \qquad \text{(A1-10)}$$

The flux, $J_{Ox}(x,t)$, is the net mass transfer rate of Ox at a given time, t, at some distance, x, into the solution from the electrode surface. D_{Ox} is the diffusion

coefficient of Ox. The magnitude of the current, for a diffusion controlled reduction process, is given by

$$i = -nFA\ J_{Ox}(0,t) \qquad \text{(A1-11)}$$

The solution of these partial derivative expressions requires the establishment of certain initial and boundary conditions. These are specific to the particular experiment being performed. For the case where the electrode potential is stepped from a value where no net current flows to a value where the electrolysis reaction is diffusion controlled, and where only Ox is initially present in solution, then the familiar Cottrell equation, A1-12, results.

$$i(t) = \frac{nFAD_{Ox}^{1/2}C_{Ox}^{*}}{(\pi t)^{1/2}} \qquad \text{(A1-12)}$$

The inverse time dependence of the magnitude of the current on the square root of time is typical of diffusion control of the electrode reaction.

A second limiting case arises when the rate of mass transport is very great with respect to the charge transfer kinetics. Under these conditions linear relationships between the logarithm of the current and the applied potential frequently result. Such relations are typical of sluggish charge transfer kinetics.

APPENDIX 2

APPENDIX 2

CHRONOCOULOMETRY

In the simplest form of the chronocoulometric experiment, as applied in this work, only one form of a redox couple is initially present in solution. The electrode potential is then pulsed from some initial value, E_1, to a value, E_2, where electrolysis of the electroreactant occurs at a diffusion controlled rate. E_2 is generally selected to lie a minimum of 100 mV on the other side of voltammetric half-wave potential from E_1. The charge resulting from the faradaic process is then simply given by integration of the Cottrell equation, A1-12, yielding

$$Q(t) = \frac{2nFAD^{1/2}C^{*}t^{1/2}}{\pi^{1/2}} \qquad \text{(A2-1)}$$

where D and C* are the diffusion coefficients and bulk concentration of the electroreactant.

There will, in general, be a contribution to the response arising from the current required to charge the double layer capacitance. In the absence of uncompensated

$$Q(t) = \frac{2nFAD^{1/2}C^{*}t^{1/2}}{\pi^{1/2}} + Q_{DL} \qquad \text{(A2-2)}$$

If the charge-time transient is recorded, and then replotted as a function of $t^{1/2}$, the slope of the resulting line allows calculation of the diffusion coefficient of the electroreactant provided the electrode area is known. Alternatively, if the diffusion coefficient is known, then the electrode area may be determined. The porphyrin diffusion coefficients reported in Chapter 5 were calculated from the chronocoulometric Q vs $t^{1/2}$ slope after calibration of the electrode area with 1 M KCl solutions of $K_4Fe(CN)_6$. The results of a typical chronocoulometric experiment for the oxidation of ferrocyanide are illustrated in Figure 72.

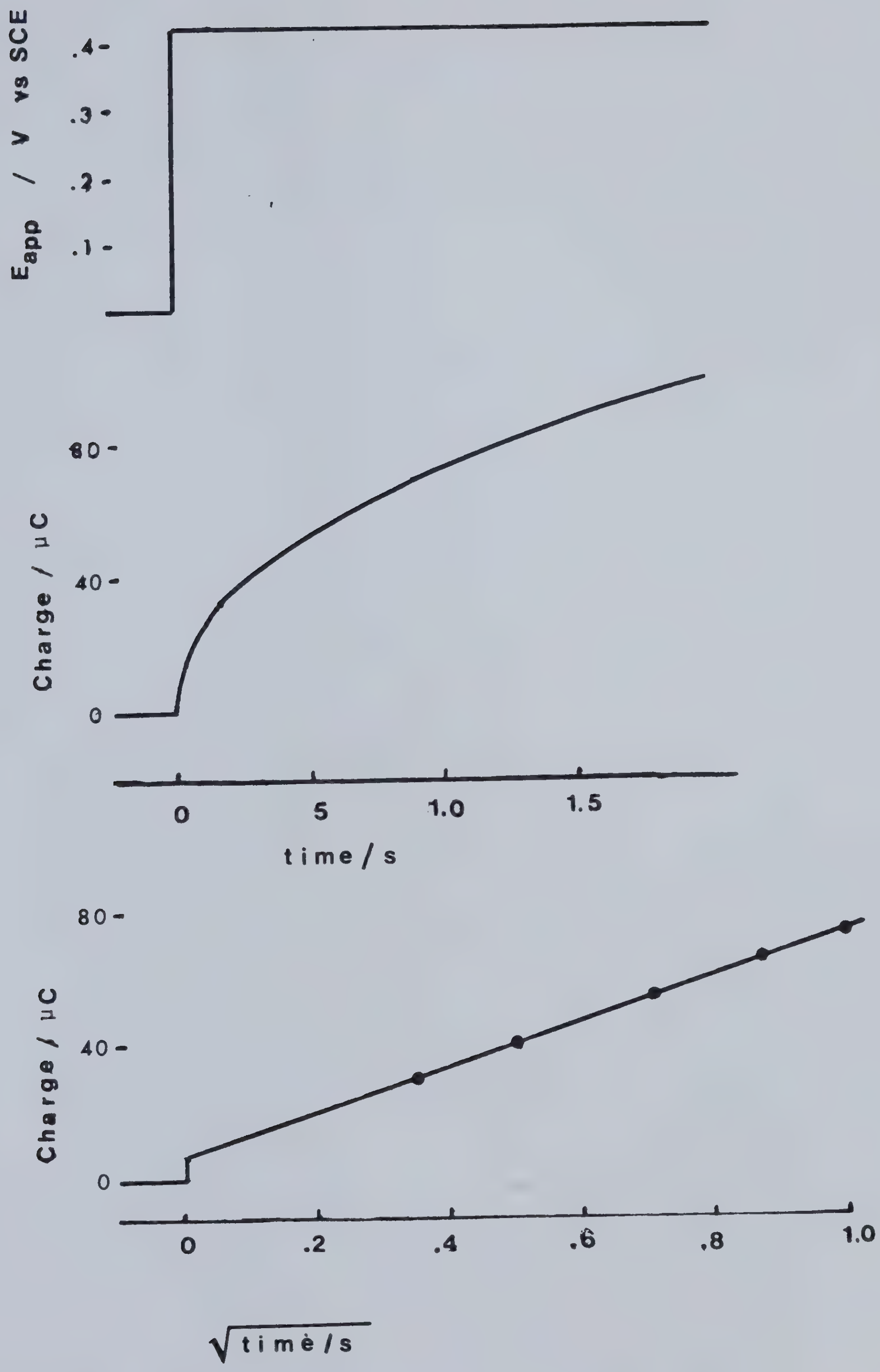

Figure 72. Chronocoulometry of 1.14 mM K_4FeCN_6 in 1 M KCl.

APPENDIX 3

APPENDIX 3

CYCLIC VOLTAMMETRY

In conventional cyclic voltammetry, only one form of a redox couple is initially present in solution. The potential of the working electrode is then swept linearly from a value where this form is stable to a value where the other form of the redox pair is favoured.

If the charge transfer kinetics associated with the redox couple are rapid, the relative concentrations of the oxidized and reduced forms of the redox pair at the electrode surface must vary with the potential in accordance with the Nernst equation. Hence, as the working electrode potential nears the formal potential of the redox couple, a current must flow in order that the ratio of concentrations of the two forms at the electrode surface may be maintained at that dictated by Nernstian equilibrium. The current will continue to increase with the applied potential until, at some point past the formal potential, the surface concentration of the redox form initially present falls essentially to zero. The current will now be controlled by the rate at which this species diffuses to the electrode surface from the solution bulk. As the region in which the electroreactant has been

depleted extends farther and farther out into the solution, the magnitude of the current will decay.

At some point well past the formal potential of the redox couple, generally 100 mV or more, the direction of the potential scan is reversed. The behaviour of the current observed on the reverse scan may be explained by the same qualitative reasoning as that used for the forward sweep. Now, however, the other form of the redox couple predominates at the electrode surface and for some distance out into the solution bulk.

No closed-form solution for the current-potential curve obtained in the cyclic voltammetric experiment exists. The present understanding of cyclic voltammetry comes, for the most part, from computer evaluations of the cyclic voltammetric response, and, in particular, those presented in the classic work of Nicholson and Shain [145]. These authors were able to provide quantitative characterization of the cyclic voltammetric response for a variety of electrode mechanisms.

In the case where the electrolysis occurs at a diffusion controlled rate, the forward and reverse peak potentials will be separated by 59/n mV at 25°C. The mean of these two potentials is frequently used to estimate the reversible half wave potential of the redox couple. The peak current on the forward sweep increases linearly with

the square root of the scan rate, and the magnitudes of the forward and reverse peak currents are equal.

Determination of the magnitude of the reverse peak current is not straightforward. The baseline from which this current is measured is the decaying portion of the forward peak. Several techniques for experimental determination of the peak current ratio have been proposed. The method used in this work was apparently first suggested by Reinmuth (unpublished) and is discussed in reference 78. The cyclic voltammetric current is recorded as a function of time, rather than potential. As time and potential are linearly related, the peak on the forward sweep is equivalent to that obtained in the conventional experiment. At the end of the forward sweep, however, the scan direction is not reversed, but held constant. The decaying current is then recorded as a function of time. The experiment is then repeated and, this time, the scan direction is reversed at the end of the forward sweep. The reverse peak current is now recorded under the decaying baseline established in the first experiment. The method is illustrated in Figure 73 for the first oxidation of $(CF_3CO_2)Mn(III)TPP$ in CH_2Cl_2 (0.15 M TBAP). The method is readily extendable to determination of the forward and reverse peak currents associated with successive charge transfers.

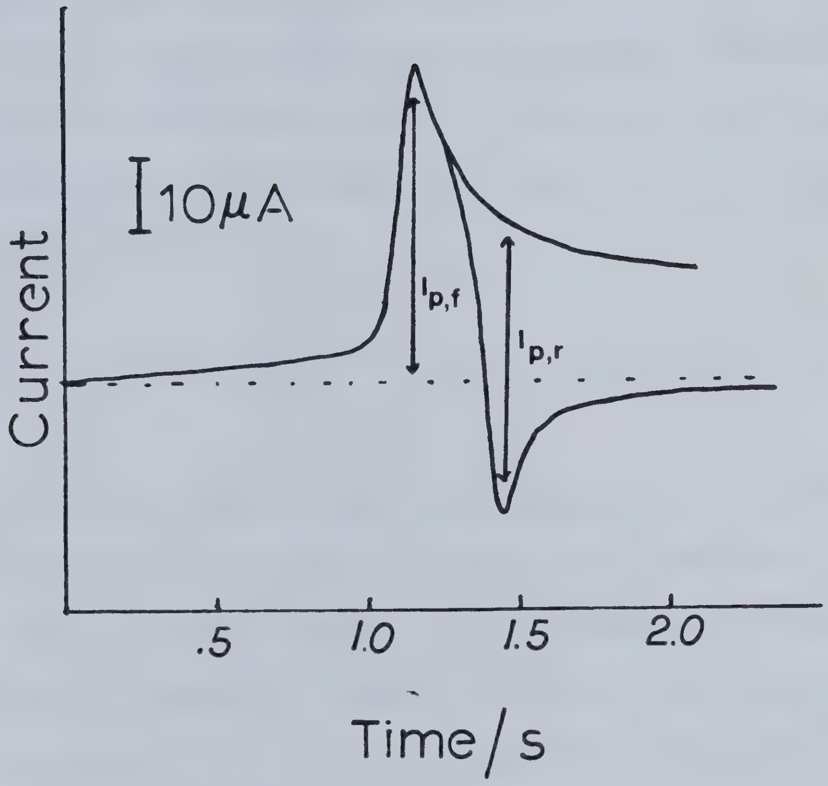

Figure 73. Cyclic voltammogram of 1 mM $(CF_3CO_2)Mn(III)TPP$ in CH_2Cl_2(0.15 M TBAP), recorded in Y-T mode illustrating method of determining forward and reverse peak currents; ν = 100 mV/s.

If the charge transfer reaction is kinetically sluggish, then the forward and reverse peak currents need not necessarily be equal. In addition, the peak potential separation, ΔE_p, will be greater than the 59/n mV predicted for the purely diffusion controlled case. The increase in ΔE_p may be used to determine the standard rate constant of the redox couple. Nicholson [150] has tabulated numerically generated values of a dimensionless parameter, Ψ, given by

$$\Psi = (\frac{D_{Ox}}{D_R})^{\alpha/2}\ k_s(D_{Ox}\pi\ \nu\ nF/RT)^{-1/2} \qquad \text{(A3-1)}$$

This function depends only on $n\Delta E_p$, which in turn increases as the potential sweep rate increases. The peak separation yields a value of Ψ by comparison with Nicholson's tables. Equation A3-1 is then used to calculate k_s. It is often assumed that $D_{Ox} = D_R$, and, in this case, the value of the charge transfer coefficient, α, need not be known.

When an irreversible chemical reaction, yielding an electro-inactive product, follows the charge transfer step, the ratio of the cyclic voltammetric forward and reverse peak currents will be less than unity, the exact value depending largely on the potential sweep rate and the rate constant associated with the homogeneous

reaction. For a reduction, the presence of the following chemical reaction will cause the forward peak to shift to more anodic potentials at lower sweep rates. The direction of the potential shift is reversed where the forward peak represents an oxidation.

The effects of other types of mechanisms on the cyclic voltammetric response where homogeneous reactions are coupled to the charge transfer process are detailed in references 78 and 145.

APPENDIX 4

APPENDIX 4

THE PROGRAM "THNLAY"

This is a Fortran listing of the program used to calculate the thin layer voltammetric curves presented. The geometry assumed in this version is the radial concentric configuration. The parameters which must be supplied are as follows:

NIN = the number of volume increments to be assumed in the calculation.

RAD = the radius of the electrode, in cm.

RHO = the solution resistivity, in ohm-cm.

DL = the thickness of the thin layer cavity.

DREF = the distance of the Luggin tip from the edge of the working electrode, in cm.

CON = the concentration of electroactive species, in moles/cm^3.

POT = the working electrode potential at the beginning of the scan, E-E° in Volts.

DPOT = the potential increments for which you wish the current to be calculated, in Volts.

SCNRT = the potential scan rate, in Volts/s.

These are entered initially in a separate file according to the format statements 19 and 29.

The output of the program is a table of values, as follows:

POT = the potential of the working electrode, E-E°, in Volts.

HACUR = the theoretical current, in amps, calculated assuming no solution resistance.

ESTTRUCUR = an estimate, in amps, of the true current.

KOUNT = the number of iterations involved in calculating the estimate.

```
      FUNCTION TLC(POT,VOL,SCNRT,CON)
      XPRG=38.944*POT
      XPNT=EXP(XPRG)
      XPRT=XPNT/(1.0+XPNT)**2
      TLC=XPRT*3.7576E06*SCNRT*CON*VOL
      RETURN
      END
      SUBROUTINE RADGEO(V,R,TVOL,NIN,RAD,RHO,DL,DREF)
      DIMENSION R(20),V(20)
      PI=3.1416
      DX=RAD/FLOAT(NIN)
      TVOL=RAD**2*DL*PI
      RFF=RAD+DREF
      RADN=RAD
      RNRM=RHO/(2.*PI*DL)
      VNEW=TVOL
      DO 10 I=1,NIN,1
      R(I)=RNRM*ALOG(RFF/RADN)
      RFF=RADN
      RADN=RADN-DX
      VOL=RADN**2*PI*DL
      V(I)=VNEW-VOL
      VNEW=VOL
   10 CONTINUE
      RETURN
      END
      SUBROUTINE CURR(HACUR,TCUR,KOUNT,TVOL,V,R,POT,SCNRT,CON,NIN)
      DIMENSION CUR(20)
      DIMENSION R(20),V(20)
      TCUR=TLC(POT,TVOL,SCNRT,CON)
      HACUR=TCUR
```

```
      KOUNT=1
   11 ENEW=POT-TCUR*R(1)
      VOL=V(1)
      CUR(1)=TLC(ENEW,VOL,SCNRT,CON)
      C=TCUR-CUR(1)
      DO 30 J=2,NIN,1
      ENEW=ENEW-C*R(J)
      VOL=V(J)
      CUR(J)=TLC(ENEW,VOL,SCNRT,CON)
      C=C-CUR(J)
   30 CONTINUE
      KOUNT=KOUNT+1
      IF(KOUNT,GT.10) GO TO 12
      T=TCUR-ABS(C)
      TEST=T/TCUR
      IF(TEST.GT.0.999) GO TO 12
      TCUR=TCUR-C
      GO TO 11
   12 RETURN
      END
      DIMENSION R(20),V(20)
      READ(5,19) NIN,RAD,RHO,DL,DREF,CON
   19 FORMAT(I3,4F8.5,1PE10.2)
      READ(5,29) POT,DPOT,SCNRT
   29 FORMAT(3F10.6)
      CALL RADGEO(V,R,TVOL,NIN,RAD,RHO,DL,DREF)
      DP=ABS(2.*POT)/DPOT
      NPOT=IFIX(DP)+2
      WRITE(6,39)
   39 FORMAT(' ','POTENTIAL',3X,'HACUR',7X,'ESTTRUCUR',3X,'KOUNT')
      DO 50 K=1,NPOT,1
      CALL CURR(HACUR,TCUR,KOUNT,TVOL,V,R,POT,SCNRT,CON,NIN)
```

```
      WRITE(6,49) POT,HACUR,TCUR,KOUNT
      POT=POT+DPOT
   50 CONTINUE
   49 FORMAT(1PE12.4,1PE12.4,1PE12.4,I3)
      STOP
      END
```

B30392